THEORETICAL AND EXPERIMENTAL INVESTIGATION OF DESPIN CONTROL OF MASSIVE SPACE DEBRIS BY TETHERED SPACE TUG

JUNJIE KANG

A DISSERTATION SUBMITTED TO
THE FACULTY OF GRADUATE STUDIES
IN PARTIAL FULFILLMENT OF THE REQUIREMENTS
FOR THE DEGREE OF

DOCTOR OF PHILOSOPHY

GRADUATE PROGRAM IN
EARTH AND SPACE SCIENCE AND ENGINEERING
YORK UNIVERSITY
TORONTO, ONTARIO
NOVEMBER 2020

© JUNJIE KANG, 2020

Abstract

This doctoral research investigates the problem of despin control of the massive uncooperative rotating target by the tethered space tug in the post-capture phase. Theoretical and experimental studies are conducted to achieve the objective in three parts: dynamics characterization, control strategy design, and experimental validation. The mathematical formulation of the rotating target captured by tethered space tug is modeled in free space to investigate the pure despin motion. It is extended into the central gravitational field to investigate the coupled dynamics between the tethered system's orbital and attitude motion during the despin process. Despin control strategies are proposed with the practical constraints to achieve the purpose of despinning the target's rotation to a permissible level and ensure the system's safety together for orbital maneuvering operation. The advanced nonlinear control techniques are employed to address the tethered space system's underactuation and stability to improve performance. First, a unified control framework of tether tension for a simplified dumbbell model is proposed to precisely control the tether deployment and retrieval. The asymptotic stability of the control framework is proved rigorously. It is improved as a robust sliding mode controller to attenuate the effect of the possible uncertainties and disturbances. Second, a passivity-based nonlinear model predictive control law is designed to handle the constraints on the inputs and states analytically. The tethered system's passivity is revealed and incorporated into nonlinear model predictive control implementation to guarantee the asymptotic stability. Finally, the orbital maneuvering of the rotating target after despun is studied analytically with the non-singularity orbital elements in numerical simulation and validated experimentally in a zero-gravity environment provided by a custom-built spacecraft simulator air-bearing platform.

Dedication

I dedicate my dissertation work to my family.

Acknowledgements

"If I have seen further, it is by standing upon the shoulders of giants."

-Isaac Newton

I would like to express my sincere appreciation to those who have contributed to this dissertation during this doctoral journey. This research work would not have been possible without the encouragement and support.

First and foremost, I would like to extend my heartfelt and sincere gratitude to my supervisor and mentor, Prof. George Z. H. Zhu, for providing me an opportunity to complete my Ph.D. dissertation. I appreciate his contributions of time and constructive suggestions to make my work productivity. His scientific guidance, continuing support, and constant optimism encourage me to be better at what I do. I benefit greatly from his insightful feedback, rigorous academic attitude, and an excellent example.

I am extremely grateful to my supervisor committee members, Dr. Dan Zhang and Dr. Franz Newland, for the insightful comments and important suggestions in my research evaluation's annual meetings, which inspired me to bring my work to a higher level.

I would also like to acknowledge my fellow group members and friends, Dr. Gangqi Dong, Dr. Gangqiang Li, Dr. Peng Li, Mr. Latheepan Murugathasan, Mr. Udai Bindra, Mr. Chonggang Du, Mr. Lucas Santaguida, and many others for companionship, rewarding academic exchanges, and many interesting conversations.

Last but not least, I wish to thank my beloved family for believing in me and supporting me all the way. I would like to thank my parents and parents-in-law for their wise counsel and sympathetic ear. You are always there for me. I would like to thank my brothers for being part of my foundation and all of the advice and wise words. I would especially like to express my love and gratitude to my wife, Qian Li, for her great companion, constant support, warm encouragement, and never-ending patience in my life. I also would like to thank my dearest daughter, Cynthia, for bringing me unlimited happiness and pleasure.

Thank you, everyone, for your support during my Ph.D. study; I wish you all the best.

Table of Contents

List of Tables

List of Figures

List of Main Symbols

$\mathbf{F}$	=	Thrust Vector on Tug, N
F_t	=	Tangential Thrust along Tether, N
F_n	=	Thrust Normal to Tether, N
C	=	Coriolis/Centrifugal Force Matrix
G	=	Gravity Force Matrix
J	=	Inertia Momentum of Target, kgm^2
K	=	Kinetic Energy
l	=	Tether Length, m
L	=	Lagrangian Energy
m_1	=	Mass of Space Tug, kg
m_2	=	Mass of Space Target, kg
M	=	Inertia Matrix
r	=	Radius of Target, m
$\mathbf{R}$	=	Position Vector of System's CM in Inertial Frame
$\bar{T}$	=	Tether Tension, N
T	=	Dimensionless Tether Tension
u_t	=	Dimensionless Tangential Thrust along Tether
u_n	=	Dimensionless Thrust Normal to Tether
U	=	Potential Energy

α	=	Rotation Angle of Target, rad
θ, β	=	Tether Libration Angle, rad
λ	=	Inertial Ratio
ξ	=	Dimensionless Tether Length or Length Ratio
ω	=	Angular Velocity of Target, rad/s
Ω	=	Angular Velocity of Orbital Frame, rad/s
τ	=	Dimensionless Time

List of Abbreviations

3D	=	3-Dimensional
ABT	=	Air-bearing Testbed
ADR	=	Active Debris Removal
ARM	=	Asteroid Redirect Mission
CM	=	Center of Mass
DAQ	=	Data Acquisition
DOF	=	Degree of Freedom
ESA	=	European Space Agency
FOC	=	Fractional-Order Control
GA	=	Genetic Algorithm
GEO	=	Geostationary Earth Orbit
IR LED	=	Infrared Light Emitting Diode
LEO	=	Low Earth Orbit
LVLH	=	Local-Vertical Local-Horizontal
MPC	=	Model Predictive Control
NMPC	=	Nonlinear Model Predictive Control
PBMPC	=	Passivity-Based Model Predictive Control
PD	=	Proportional Derivative
SMC	=	Sliding Mode Control

SS	=	Spacecraft Simulator
TSS	=	Tethered Spacecraft System

Chapter 1 INTRODUCTION AND JUSTIFICATION

Summary: This chapter introduces and reviews the applications and research activities of the space tethered system. It provides the research objectives of this dissertation and presents the methodologies of research. In the end, we outline the layout of this dissertation and provide a full list of publications out of the doctoral study

1.1 Backgrounds

In 1957, the launch of 'Sputnik 1', first artificial satellite of the world, inaugurated the space age. After that, more than 10,000 satellites have been sent into space for various purposes, such as communications, navigation, and Earth observation, in 60 years of space exploration. Currently, there are about 5,720 satellites still in space, about 2,900 are functioning, and others are defunct [1]. The defunct satellites, around half of all, can divide into space debris, which comes from the collisions and explosions of satellites, and other fragmentation events. There are around 27,000 space debris in the low earth orbit (LEO) and the geostationary earth orbit (GEO) objects, see Figure 1.1, which are regularly tracked by the United States Space Surveillance Networks. Space debris is heavily threatening our spacecraft, satellites, and

International Space Station (ISS), and the rising of the population increases the potential danger. [2, 3] Thus, the issue of cleaning up the space debris is getting really important.

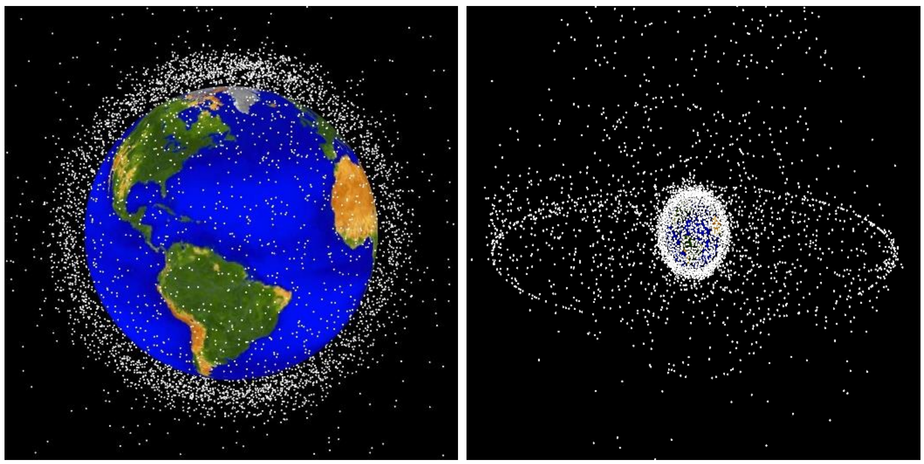

(a) (b)

Figure 1.1 Distribution of catalogued objects in space[1]

(a) LEO region; (b) GEO region

Earth has suffered many times of Near-Earth-Objects (NEOs) impacts in the last two century. [4]. Most of them are asteroids, called as Near-Earth Asteroids (NEAs). As of September, 2020, over 23,000 NEAs are known, 2,100 of which are considered as potentially hazardous for sufficiently large and close to Earth [5]. Asteroids with a diameter of 7 meters enter the Earth's atmosphere about every five years, but its kinetic energy as much as the atomic bomb dropped on Hiroshima. Asteroids with a smaller size, 4 meters' diameter,

[1] Retrieved from https://www.orbitaldebris.jsc.nasa.gov/photo-gallery/ in July 2020

enter the atmosphere more frequently once per year. Thus, to protect our planet from hitting or reduce the damage, NASA is working on tracking and predicting the near-earth asteroids [6]. In recent, scientific and commercial interests have been drawn on the Asteroids, referred to as Asteroid Retrieval Mission (ADM) [7, 8]. To explore the clues to life on Earth, NASA launched a spacecraft, OSIRIS-REx, to bring the asteroid's samples of Bennu to Earth in September 2016. [9]

To reduce the potential collision risk of spacecraft with debris, many approaches have been devoted to space debris removal, such as space robotic arm, space tether, gripper mechanism, and some contactless approaches [10, 11]. Among them, space tether technology is one of the most appealing approaches for the advantages of the promising properties of lightweight and high flexibility [10]. As well, space tether technology is considered as one feasible approach to capture and return the asteroid, or collect a sample on the asteroid's surface.[12]

Space tether, as a potential technology, has received much attention on debris removal or asteroid retrieval by researchers.[11] The main operations of space tether can be divided into three steps, drawn in Figure 1.2. First, capture the space targets [2] with a tethered spacecraft. Then, reduce the rotation of targets before removing/redirecting. Finally, maneuver the targets

[2] Space debris and asteroids are called as targets.

by firing the thrust on the spacecraft.

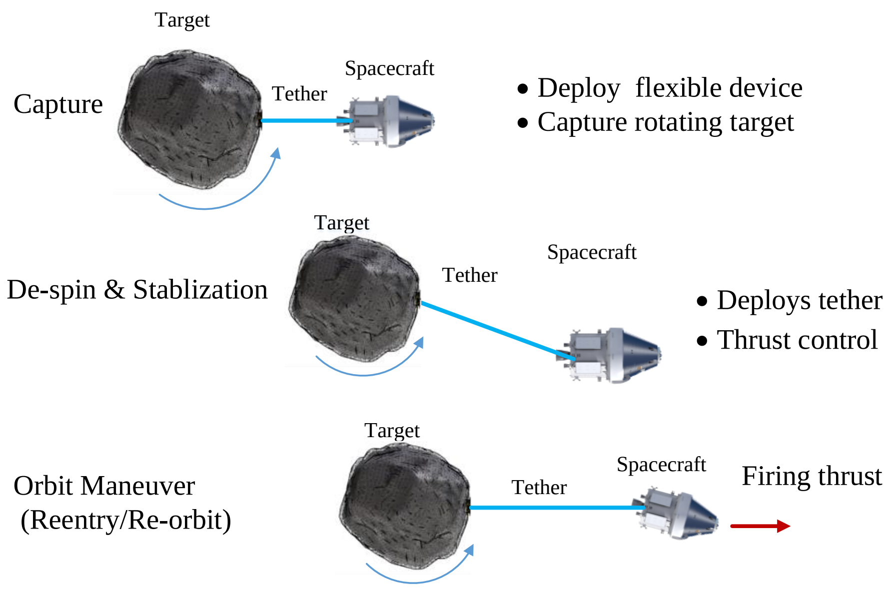

Figure 1.2 Operations of space target removal by space tether

Many countries spent a great number of efforts on space missions verifying the potential of the space tether applications, including the National Aeronautics and Space Administration (NASA) in the USA, European Space Agency (ESA), Canadian Space Agency(CSA), and Japan Aerospace Exploration Agency (JAXA), and also some space companies and universities. Many pioneering works of the space tether have been made for various purposes, such as Electrodynamics Tether Deorbit, Artificial Microgravity Generation, and Tether Propulsion. The previous space tether missions are listed in the Table 1.1.[13-15]

Table 1.1 List of space tether missions

Year	Mission	Agency	Orbit	Length	Status
1966	Gemini 11	NASA	LEO	30 m	Successfully deployed
1966	Gemini 12	NASA	LEO	30 m	Successfully deployed
1980	TEP1	NASA	Suborbital	500 m	Partially deployed (38 m)
1981	TEP2	NASA/ISAS	Suborbital	500 m	Partially deployed (65 m)
1983	Charge-1	NASA/ISAS	Suborbital	500 m	Successfully deployed
1985	Charge-2	NASA/ISAS	Suborbital	500 m	Successfully deployed
1989	Oedipus-A	CSA/NASA	Suborbital	958 m	Successfully deployed
1992	Charge-2B	NASA	Suborbital	500 m	Successfully deployed
1992	TSS-1	NASA/ISA	LEO	260 m	Partially deployed and retrieved.
1993	PMG	NASA	LEO	500 m	Successfully deployed
1993	SEDS-1	NASA	LEO	20 km	Successfully deployed
1995	Oedipus-C	CSA/NASA	Suborbital	958 m	Successfully deployed
1996	TSS-1R	NASA/ISA	LEO	19.6 km	Tether broke
1996	TiPS	NRO/NRL	LEO	4 km	Successfully deployed

1997	YES	T. U. Delft	GTO	35 km	Not deployed
1998	ATEx	NRL	LEO	6 km	Partial deployed
2000	PicoSAT1.0	Aerospace Corp.	LEO	30 m	Successfully deployed
2000	PicoSAT1.1	Aerospace Corp.	LEO	30 m	Successfully deployed
2003	ProSEDS	NASA	LEO	15 km	Not deployed
2007	MAST	NASA	LEO	1 km	Fail to deploy
2007	YES 2	T. U. Delft	LEO	30 km	Fully deployed
2008	Cute-1.7 +APDI	Tokyo Tech	LEO	10 m	Fail to deploy
2009	STARS	Kagawa U	LEO	10 m	Deployed
2010	T-Rex	JAXA	Suborbital	300 m	Deployed
2014	STARS-2	Kagawa U	Suborbital	350 m	Not confirmed
2017	KITE	JAXA	LEO	700 m	Fail to deploy
2018	STARS-Me	JAXA	LEO	10 m	Fail to deploy
2019	TEPCE	NRL	LEO	1 k m	Deployed
2020	DESCENT	LASSONDE, YORK U	LEO	100 m	Deployment not reported yet

1.2 Justification of Research

Tethered space system (TSS) consists of the spacecraft and targets connected by space tether orbiting in space. The dynamics motion of TSS is usually very complex because of the flexibility issue of tether and the orbital coupling effect. The tether's flexibility will cause the high-frequency oscillations in tether, and the orbital coupling effect will induce the Coriolis force resulting tether libration while tether deploying or retrieving. The fast tumbling of the target makes the dynamic motions even complicated since it will result in the tethered system winding around onto the target and spacecraft, leading to instability of the TSS. Thus, in this dissertation, the focuses are drawn on the two main aspects of dynamics and control of the tethered spacecraft system: deployment/retrieval of TSS and its application to large rotating targets removal.

1.2.1 Tether Deployment/Retrieval Control

1.2.1.1 Challenges of Tension Control

Tether deployment/retrieval is fundamental for space tether mission's success, which suffers from the following challenges:[16, 17]

(i) **Underactuation**. The tethered spacecraft systems are usually only equipped with an active reel in/out mechanism to control tether deployment and retrieval. Only tether length can be actuated while the tether libration angle is not. Thus, the tether deployment/retrieval of TSS becomes underactuated when the tension is the only control input used to achieve precise positioning.

(ii) **Constraints.** During the deployment and retrieval process, two practical constraints should be considered, positive tension, and libration angle. The tension in the tether should be maintained positive. Otherwise, the tether becomes slack, which means the dynamics model is invalid and would result the failure of operation. The libration angle is usually set to within 90 degrees to prevent the tether from wrapping around the spacecraft or target.

(iii) **Measurement Limitations.** In practical situations, we do not have enough sensors to measure all the states, such as libration angle and libration angular velocity in the tethered CubeSat missions. Thus, the controller should be designed in manner of the partial state feedback based on the measurement requirement.

1.2.1.2 Limitations of Existing Studies

To date, many control schemes have been developed to tackle the control problem of the tether deployment and retrieval with considering the system's underactuation and constraints, which is particularly difficult to design a controller satisfies the requirements and guaranteeing asymptotic stability [16]. Most existing control schemes require the full state feedback, both the actuated states (tether length and velocity) and underactuated states (tether libration angle and angular velocity). Moreover, some existing controllers are only Lyapunov bounded stable instead of asymptotically stable for precise allocation. Optimal control based techniques are also employed, however they are computationally heavy and difficult to implement onboard [18]. In addition, the existing disturbances in practical mission requires the robust controller to handle the disturbance while system is underactuated. Some researchers used sliding mode control to achieve asymptotic stability, but it will raise the well-known chattering phenomenon, which leads to the undesirable high-frequency oscillation.

1.2.2 Large Space Target Removal by TSS

1.2.2.1 Challenges

Space tether technology is a promising approach to remove the large space debris and retrieve an asteroid. However, challenges exist for the dynamics and control of combined systems, which can be summarized as: [19-21]

(i) **Tumbling/Spinning**. Targets in space are usually rotating persistently. It will cause the acute libration motion after the targets are captured by the tethered space system, which may even cause the tether winding around the target and be slack. Thus, it is necessary to reduce the rotation rate of the target to a small admissible region for removal.

(ii) **Underactuation**. The space targets are captured by the flexible tethered device, such as the space net or gripper. They are not able to directly control the target's attitude because only the force is applied to the targets by the flexible tethers. Thus, the combined system is underactuated due to fewer control inputs than system's degrees of freedom.

(iii) **Constraints.** Same as in deployment/retrieval control, the tether should be kept taut to avoid the slack-taut-slack phenomena, which will result in tether's fatigue and break out. It also might cause the system's vibration. Moreover, the libration motion should limit within 90 degrees to prevent the tether from winding around the targets.

1.2.2.2 Limitations of Existing Studies

Many researches are dedicated to analyzing the dynamics of debris removal while considering the captured targets with small rotation energy, which will not cause tether winding around. Researches focused on the problem of de-tumbling/despinning the targets in an ideal free-floating space while ignoring the gravitational field [22]. As a result, the dynamic coupling of orbit and the TSS's motions is not addressed. The dynamic motion of the combined rotating tethered system might become instable while the rotating angular velocity of the system approaching orbital angular velocity might induce the system's resonance and cause chaotic motions. Some works designed the virtual controller for simulation studies, but this is not applicable in real situations.[23] Thus, appropriate control strategies should be designed to ensure the system's stability during the de-tumbling/despinning phase. The operational constraints of the positive tension and libration angle should also be guaranteed. Furthermore, the effectiveness of most current studies is only validated by numerical simulations. Experimental verification of removing large targets by TSS is still needed.

1.3 Objectives of Proposed Research

To address the existing challenges and limitations, this dissertation works on the dynamic behavior and control of TSS and its application to remove or retrieve the large rotating space targets. Therefore, the research objectives of this study are presented as follows:

(i) Develop the mathematical models of the tethered spacecraft system in despinning and orbital maneuvering, respectively to characterize the dynamic behaviors of tethered systems.

(ii) Study the control problem of the underactuated tethered system to despin the rotation space targets and simultaneously stabilize the tether's libration under the constraints.

(iii) Investigate attitude stabilization and libration suppression during the orbit maneuvering.

(iv) Validate the effectiveness of the proposed control strategy through experimental system on the air-bearing platform.

1.4 Methodology of Approach

This dissertation's methodology of approach begins with the dynamic modeling of the tethered spacecraft systems, including the dumbbell model and the rigid-body attitude model. Lagrange formulation and Newton's Second Law are employed to derivate the dynamic equations of motion.

To achieve the stabilization of the underactuated TSS, passivity-based control (PBC) theory is utilized to propose a unified framework for tethered system deployment and retrieval for accurate known model. In real mission, tethered system always perturbed by the unknown disturbance. Thus, to solve the disturbance attenuation problem, SMC is combing with the fractional-order control to improve the controller's dynamic performance. Then, to investigate the despin control of the rotating target for removal/redirect operation, simple control strategies are designed in free space and extended into the circular orbit. The indirect Lyapunov method, linearization technique around the equilibrium, is used to analyze the stability. Furthermore, to guarantee the asymptotic stability and deal with constraints, model predictive control (MPC) method is implemented with combing passivity-based control, where a passivity constraint is added to remove the terminal constraint of MPC.

The orbital propagation of the rotating target towed by the tethered space tug is described non-singularly by the modified Gaussian Elements. Then, simple control strategies are proposed to stabilize both the space target's attitude motion and tug's attitude motion, and suppress the tether libration. Finally, the effectiveness and reliability of the tethered space tug are demonstrated on a custom-built ground testbed that consists of air-bearing spacecraft simulator on a granite table.

1.5 Outline of this Dissertation

The dissertation includes eight chapters. Chapter 1 gives an introduction and justification. Chapter 2 provides a detailed review of the literature about stabilization control of the tethered spacecraft system, despinning of rotating target after capture, and target's orbit maneuvering. Chapter 3 develops the tethered system's various mathematical formulations for studying the tether deployment/retrieval and despinning the target in different scenarios. Chapter 4 focuses on the tension control problem of the underactuated tethered system's deployment and retrieval and rigorous stability analysis, and the robust control design to handle the disturbance. Chapter 5 includes the parametric analysis and control strategies of despinning the rotating target by tethered spacecraft. Chapter 6 focuses on the orbital maneuvering of the rotating target. Chapter 7 validates the tethered system's feasibility and effectiveness to maneuver the rotating target in a microgravity environment provided by the ground air-bearing testbed. Finally, Chapter 8 summarizes the contributions of this research and states the potential future research aspects.

1.6 List of Publications

The following is a full list of peer-reviewed journals publications associated with this dissertation.

1. **Kang, J.**, Zhu, Z H., A unified energy-based control framework for tethered spacecraft deployment. *Nonlinear Dynamics*, 2019, 95 (2): 1117-1131. (Reference Paper A)

   Doi: 10.1007/s11071-018-4619-x

2. **Kang, J.**, Zhu, Z H., Dynamics and control of de-spinning giant asteroids by small tethered spacecraft. *Aerospace Science and Technology*, 2019, 94: 105394.(Reference Paper B)

   Doi: 10.1016/j.ast.2019.105394

3. **Kang, J.**, Zhu, Z H., De-spin of massive rotating space object by tethered space tug. *Journal of Guidance, Control, and Dynamics*, 2018, 41 (11): 2463-2469. (Reference Paper C)

   Doi: 10.2514/1.G003584

4. **Kang, J.**, Zhu, Z H., Wang, W., et al. Dynamics and De-spin control of massive target by single tethered space tug. *Chinese Journal of Aeronautics*, 2019, 32 (3):653-659. (Reference Paper D)

   Doi: 10.1016/j.cja.2019.01.002

5. **Kang, J.**, Zhu, Z H, Wang, W., et al. Fractional order sliding mode control for tethered satellite deployment with disturbances. *Advances in Space Research*, 2017, 59 (1): 263-273. (Reference Paper E)

   Doi: 10.1016/j.asr.2016.10.006

6. **Kang, J.**, Zhu, Z H., Hamiltonian Formulation and Energy-based Control for Space Tethered System Deployment and Retrieval. *Transactions of the Canadian Society for Mechanical Engineering*, 2019, 43 (4): 463-470. (Reference Paper F)

   Doi: 10.1139/tcsme-2018-0215

7. **Kang, J.**, Zhu, Z H., Analytical and Experimental Investigation of Stabilizing Rotating Uncooperative Target by Tethered Space Tug, Submitted to *IEEE Transactions on Aerospace and Electronic Systems*, (under review)

Chapter 2 LITERATURE REVIEW

Summary: In this chapter, we review the literatures of TSS dynamics and control as well as despin and maneuver of a rotating target by tethered spacecraft.

2.1 Tether Deployment/Retrieval

In the past decades, a large number of efforts have been devoted to achieve the successful tether deployment/ retrieval for space tether mission. Due to the overall flexibility, the dynamic equations of TSS are usually with very complex forms. Thus, in order to study the dynamics and control of the deployment/retrieval of TSS, the TSS is usually modeled as a dumbbell model [17], where the tether is treated as a rigid rod. The advantage of rigid tether assumption is that we can understand the overall tethered system's motion in space for preliminary mission design.[24] On the contrary, the rigid tether assumption cannot reflect the possible tether deformations and libration motions because it ignores the tether's flexibility, which should be considered for accurate analysis in the practical mission.[13]

New challenge arises from the non-propellant design in TSS deployment/retrieval, where the TSS becomes underactuated [16]. A great deal of controllers have been proposed to achieve the tether deployment/retrieval for the fast, precise, and stable purposes. For instance, a tension controller in terms of tether length and velocity is designed by Rupp to deploy the tether with the tether libration suppressed [25]. Fujii and Ishijima developed a Lyapunov-like mission function based controller to deploy and retrieve the tether with bounded stability [26]. Further, Vadali designed a tension controller based on the system's energy to study the deployment and retrieval in the orbital plane at the local vertical and local horizon (LVLH) with the asymptotic stability [27]. It was extended to three-dimensional motion with an out-plane thrust [28]. Later, Pradeep utilized linearization technique to prove the linear tension controller's asymptotic stability around the equilibrium for planar TSS [29], and Kumar and Pradeep extended the controller into three-dimensional TSS [30]. Recently, Sun and Zhu further expanded the linear integer-order tension control scheme into a linear fractional-order (FOC) type for the purpose of fast and stable deployment and retrieval [31, 32]. Besides, sliding mode control theory, which can avoid finding the Lyapunov function, was implemented in tether deployment/retrieval to attenuate the external disturbances [33-36]. Ma et al. designed an adaptive type of sliding mode controller with the consideration of the input saturation based on the linearized system's equations, and the effectiveness is shown by implementing it to the original nonlinear system [33]. Wang et al. studied the tether deployment in an elliptical orbit with adaptive sliding mode control to track a designed nominal trajectory, and the stability is analyzed by linearization technique around the equilibrium. As is well known, the local asymptotic stability can only be ensured near the equilibrium due to the linearization. Thus, the control gains should be selected to ensure a large enough region of attraction in the practical implementation. To deal with the positive tension constraint, Wen et al. proposed a positive tension controller and proved its asymptotic stability [37]. The proposed controller is implemented in the space tether tug's stabilization with a velocity free form [38].

Additionally, most of the preceding controllers need full-state feedback, both the actuated states and unactuated states. However, the requirement of full-state feedback increases the unduly burdensome need and the cost of TSS for full-state measurement [38]. Hence, controllers with partial-state feedback are highly desirable in practical use, as mentioned in Ref. [25, 29, 37], where only the actuated states are measured to use. Moreover, most controllers only achieved Lyapunov bounded stability instead of asymptotic stability, thus, tethered payload will be only allocated near the desired position with errors, which will affect the operations like tether-aid capture. In order to ensure the asymptotic stability, finding an appropriate Lyapunov function are required. However, finding such Lyapunov function is usually not easy because it mainly depends on the designer's experience [29]. Although the use of SMC techniques can avoid the difficulty to construct a Lyapunov function, it will cause the well-known chattering problems [39], which may induce the undesirable high-frequency oscillations of tether. It should be pointed out that SMC in an underactuated system is much trickier than in a fully actuated system because it is difficult to define a sliding mode manifold to stabilize the both actuated and unactuated states. There are some control schemes for tether deployment/retrieval using optimal control or optimization method [40-43], where the deployment/retrieval control problem is converted to a constraint two-point boundary value optimization problem. The positive tension and libration motion constraints are handled simultaneously. However, they are with heavy computation to implement for on-board computer.

To address these limitations and challenges on tether deployment/retrieval control, we will present a unified energy-based tension control framework to accomplish the precise deployment/retrieval of TSS [44] with only partial-state feedback. And, the practical positive tether tension and passive deployment constraints [45] are considered for the controller implementation. Asymptotic stability of the proposed control framework will be theoretically proved through the Lyapunov theory and LaSalle Invariance Principle. Furthermore, a sliding mode controller with fractional order with coupled two layers sliding manifold is designed to deal with the uncertainty of

TSS and external disturbances [39] and ensure the asymptotic stability.

2.2 Large Rotating Target Removal by TSS

Asteroid retrieval and space debris removal have received a great deal of interest to maintain the long-term sustainable use of the outer space [10, 12, 46]. Space tether technology in ARM and ADR includes capture, despin, and orbit maneuver. Capture methods contains the stiff connection, like space robot [47, 48], and the flexible connection, such as the tethered net [49, 50] and gripper [51, 52]. Stiff capture by space robot has the advantages of straightforward operation with stiff composition, while they are limited to small size targets and in the short distance. However, TSS with a flexible mechanism can be used for different sizes of targets and in a long-distance. Many flexible capture mechanisms are designed and tested successfully in the Refs. [11, 12].

Asteroids and large space debris are usually rotating with huge kinetic energy [53], which will cause the tether wrapping around the targets while directly towing. Therefore, it is essential to reduce the rotation of the target into a small admissible level. This process is called targets despin or de-tumble. Much efforts on targets despin and de-tumble have been made. Fedor et al. designed a Yo-Yo despin mechanism to despin rocket in 1961 [54]. The rocket's spinning kinetic energy is de-spun by deploying the pre-wound tether. Holt and

James proposed an innovative concept to despin small asteroids by a tethered nanosatellite system, which deploys the nanosatellite from the asteroid to bring the asteroid's angular momentum to the nanosatellite [55]. Notably, Aslanov made a lot of outstanding work on the large debris removal with tethered space tug [56-59]. He analyzed the effect on dynamic motions caused by the atmospheric drag, flexible appendages, and rotation of debris. Then, Yudintsev and Aslanov modified the classical Yo-Yo mechanism from [54] to de-tumble the space debris [20]. O'Connor et al. explored the debris de-tumbling by a special designed inflatable open-net and proposed an wave-based controller [60, 61]. Besides, Wang and Meng studied the dynamic stabilization of the space debris towed by the tether. They focused on the twist suppression by the active tether length regulation [62] at first. Then, they presented an approach to control the target's attitude motion by special movable tethered attachment device [63]. It can generate the desired torque to de-tumble the targets by actively adjusting the attachment. However, the installment of such device onto an uncooperative rotating target is a challenge. Similar research of the moving attachment are reported in the Refs. [64] and [65]. To de-tumble the rotating space debris, Sun et al. proposed a strategy by actively switching tension similar as the bang-bang control, where the tension is discontinuous [66]. A precise dynamic modelling for tethered tug captured space debris is established in the Ref. [23], in which the virtual controller is given to achieve the target's attitude stabilization for simulation purpose. Besides, the multi-tether system is compared with the single-tether system [67-69]. Hovell et al. compared single and multiple tethers connected configuration to damp out the rotation of the debris through the viscoelasticity of tethers in both simulation and experiment. [70-72] Multiple tether connected configuration shows a significant superiority of fast debris despinning. It should be noted that despin/de-tumble the rotation of the target by the tether's material damping is very challenging for the massive target with huge kinetic energy because it may require very long time or fail to despun/de-tumble. To address the challenge of despinning and removing a massive rotating target, Kang and Zhu investigated the despin dynamics of a massive asteroid by a small tethered spacecraft [73] and proposed several control strategies to actively despin the massive asteroid in free-space [74] and in the central gravitational field [22]. Wen and Jin designed an optimal control law to despin the target by MPC method [75].

However, the control problem of the despinning large target by TSS still remains open due to its underactuation and complex state/input constraints. Compared with traditional control methods, MPC performs as a simple and powerful tool to cope with state/input constraints [76]. MPC is implemented with the quasi-linearization technique for space tether deployment/retrieval and space target despin in the Refs. [75, 77], where the linearization improves the online computation speed. MPC is combined with SMC method to suppress TSS's libration in the Ref. [78]. Notably, in order to guarantee the closed-loop system stability, a terminal cost is usually included in MPC, which leads to the small local neighborhood stability [76]. To circumvent the local linearization and terminal cost, the control Lyapunov function based MPC (CLMPC) is proposed to guarantee the stability. However, CLMPC needs to define a Lyapunov function while making it decrease with the control action, which is not easy to find for an underactuated system. As an alternative, Raff presented the concept of passivity-based MPC (PBMPC) to guarantee the closed-loop system stability [79], and later Tahirovic et al. implemented it for the mobile robot navigation [80]. Inspired by this concept, we will present a novel MPC based on a passivity framework and apply to despin the rotating asteroid by TSS with the stability and constraints guaranteed.

Orbit maneuver of the debris using tethered tug system has attracted a lot of attention [21, 38, 81-88]. Jasper et al. studied the debris removal by the tethered tug with a colossal thrust and the discretized tether dynamics [21, 81, 82]. Input shaping methodology is designed to stabilize the TSS during orbit transfer. Linskens et al. investigated the dynamics, guidance, and control of active space debris removal by TSS [83], and the Linear-Quadratic Regulator (LQR) and SMC are applied to stabilize the tug's attitudes. In order to keep the tether from slackness during orbit transfer, Wen et al. designed a positive tension constraint controller with the point-mass model [38] Further, Liu proposed a new controller based on the small-gain theorem to ensure the closed-loop system input-to-state stable with the point-mass model too [84]. Zhong et al. studied the stabilization problem of the space debris towed by TSS during orbital transfer through optimal control method [85-87]. Sun and Zhong studied the libration suppression of TSS with the help of electrodynamic force in orbital maneuver [88].

2.3 Tether Experimental Validation on Air-Bearing Platform

Ground experimental validation of space tether technology is critical to bring the space tether into space operations. To validate the relevant space applications, the ground facilities should be developed to produce a zero-gravity environment to mimic the tether in space.

Air-bearing platform has been proved on its excellent performance to produce the zero-gravity on a smooth granite table [89]. Chung et al. verified the three tethered satellites in a line formation on the air-bearing table in Space Systems Laboratory of Massachusetts Institute of Technology. The proposed linear and nonlinear controllers are both verified on the platform (SPHERES) [90, 91]. Yu et al. validated tether deployment on the custom-built air-bearing platform at Nanjing University of Aeronautics and Astronautics (NUAA) with an analytical velocity control law [92]. Pang et al. verified the chaotic control of TSS's libration motion on the air-bearing platform at NUAA [93]. Hovell et al. proceeded the experimental verification of passive despinning of sub-tether and single tether connection on the air-bearing platform in Spacecraft Robotics and Control Lab. at Carleton University [71]. Among these experimental systems, the air-bearing platform provided a good simulation of zero-gravity environments and near zero-friction.

In Chapter 7, we will set up an experimental system on the air-bearing table to validate the tethered space tug on ground. In the experimental validation, we verify the concept of tethered space tug for orbital maneuvering and demonstrate effectiveness of the proposed control strategy to remove an uncooperative rotating target.

Chapter 3 MATHEMATICAL MODELING OF TETHERED SYSTEM

Summary: This chapter presents dynamic models of TSS in this dissertation. Beginning with the simple mass point model, we establish dynamic models with consideration of the attitude motions of the target and spacecraft, as well as the orbital propagation. The materials in this chapter have been published in the Reference papers A-F.

3.1 Dumbbell Model for Tethered System Deployment/Retrieval

Consider two end bodies as lumped mass points, and tether is massless and inextensible [38, 39, 75]. TSS in Earth's orbit, see Figure 3.1, can be treated as a standard dumbbell model. Considering the orbital motion of TSS moves in a planar circular orbit. As a result, the motion of TSS includes the orbital motion of the system's center of mass (CM) and the local motion about the CM in the orbital coordinate frame. The orbital coordinate frame (O-xyz) is fixed at the CM of system. Oy-axis is along the orbital radius and pointing to the center of Earth. Ox-axis is perpendicular to the Oy-axis and located in the orbital plane along the orbital velocity's direction. Oz-axis completes the coordinate frame with the right-hand rule.

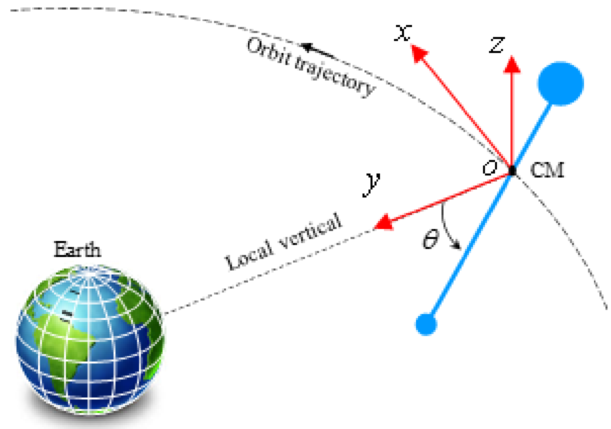

Figure 3.1 Schematic of TSS in orbital coordinate frame.

3.1.1 Lagrangian Formulation

The kinetic (K) energy of the TSS can be calculated as

$$
\begin{aligned}
K &= \frac{1}{2}\left(m_1\mathbf{R}_1'^2 + m_2\mathbf{R}_2'^2\right) \\
&= \frac{1}{2}\left[m_1\left(\mathbf{R}' + \mathbf{r}_1'\right)^2 + m_2\left(\mathbf{R}' + \mathbf{r}_2'\right)^2\right] \\
&= \frac{1}{2}\left(m_e\mathbf{R}'^2 + m_1\mathbf{r}_1'^2 + m_2\mathbf{r}_2'^2\right) \\
&= \frac{1}{2}\left[(m_1 + m_2)R^2\Omega^2 + m_e l^2\left(\theta' + \Omega\right)^2 + m_e l'^2\right]
\end{aligned}
\tag{3.1}
$$

where $\mathbf{R}_1$ and $\mathbf{R}_2$ denote the position vectors of the space tug and target from the Earth center in the inertial frame, respectively. $\mathbf{r}_1$ and $\mathbf{r}_2$ denote the local position vectors of the space tug and target in the orbital frame. The prime $(\ )'$ denotes the time derivative with respect to t. R denotes the module of orbital radius of the system. l represents the tether length and θ represents the libration angle of tether. Ω is the orbital angular velocity. $m_e = m_1 m_2/\left(m_1 + m_2\right)$

is the equivalent mass with m_1 and m_2 being the masses of the space tug and target, respectively.

Further, the potential (U) energy of TSS is derived as,

$$\begin{aligned} U &= -\frac{\mu m_1}{R_1} - \frac{\mu m_2}{R_2} \\ &= -\frac{\mu m_1}{|\mathbf{R}+\mathbf{r}_1|} - \frac{\mu m_2}{|\mathbf{R}+\mathbf{r}_2|} \\ &\approx -(m_1+m_2)R^2\Omega^2 + 0.5 m_e l^2 \Omega^2 \left(1-3\cos^2\theta\right) \end{aligned} \tag{3.2}$$

where the following Taylor series is used in Eq. (3.2),

$$\begin{aligned} \frac{1}{|\mathbf{R}+\mathbf{r}_s|} &= \frac{1}{R}\left[\left(1+\frac{x_s}{R}\right)^2 + \left(\frac{y_s}{R}\right)^2\right]^{-\frac{1}{2}} \\ &\approx \frac{1}{2R}\left[2-2\frac{y_s}{R}+2\left(\frac{y_s}{R}\right)^2 - \left(\frac{x_s}{R}\right)^2\right] \end{aligned} \tag{3.3}$$

Here, $x_s = r_s \sin\theta$ and $y_s = r_s \cos\theta$. The subscript is defined as $s = \{1,2\}$. It should be pointed out the potential energy in Eq.(3.2) is approximated due to $R \gg l$.

Then, the equations of TSS's dynamic motions can be derived by Lagrange's Equation with the $L = K - U$,

$$\begin{aligned} & l'' - l[\theta'^2 + 2\theta'\Omega + 3\Omega^2\cos^2\theta] = -\frac{\bar{T}}{m_e} \\ & l^2\theta'' + 2ll'(\Omega+\theta') + \frac{3}{2}l^2\Omega^2\sin 2\theta = 0 \end{aligned} \tag{3.4}$$

where $\bar{T}$ denotes the tether tension.

For the sake of convenience, Eq. (3.4) is recast into a dimensionless form,

$$\begin{aligned} &\ddot{\xi}-\xi[(1+\dot{\theta})^2-1+3\cos^2\theta]=-T \\ &\xi^2\ddot{\theta}+2\xi\dot{\xi}(1+\dot{\theta})+\frac{3}{2}\xi^2\sin 2\theta=0 \end{aligned} \tag{3.5}$$

by the following dimensionless variables,

$$\xi=l/l_n \quad T=\bar{T}/(m_e l_n \Omega^2) \quad \tau=\Omega t \quad \dot{(\ )}=d(\ )/d\tau$$

where l_n denotes a nominal tether length, T denotes the dimensionless tension, and τ denotes the dimensionless time(true anomaly). It is worth noting that tether length should satisfy the physical constraint $\xi_{\max}\geq\xi\geq\xi_{\min}>0$ to avoid singularity in Eq.(3.5).

Rewrite the dynamic motion Eq. (3.5) into classical form,

$$M(x)\ddot{x}+C(x,\dot{x})\dot{x}+G(x)=u \tag{3.6}$$

where $x=\mathrm{col}(\xi,\theta)$ denotes the state variable and $u=\mathrm{col}(-T,0)$ denotes the dimensionless control input. $M(x)$ is the mass matrix, $C(x,\dot{x})$ is the matrix resulting from Coriolis and Centrifugal effects, $G(x)=\partial U_0(x)/\partial x$ is gravity term, and $U_0(x)$ denotes the dimensionless potential energy of TSS,

$$U_0(x)=-\frac{3}{2}\xi^2\cos^2\theta \qquad (3.7).$$

$$M(x)=\begin{bmatrix}1 & 0\\ 0 & \xi^2\end{bmatrix}\quad C(x,\dot{x})=\begin{bmatrix}0 & -\xi\left(\dot{\theta}+2\right)\\ \xi\left(\dot{\theta}+2\right) & \xi\dot{\xi}\end{bmatrix}\quad G(x)=\begin{bmatrix}-3\xi\cos^2\theta\\ \frac{3}{2}\xi^2\sin 2\theta\end{bmatrix}$$

The following properties are summarized as:

Property 1. The inertia matrix $M(x)$ is positive definite and bounded, $\|M(x)\|\le\zeta$, ζ is a positive constant.

Property 2. $\dot{M}(x)-2C(x,\dot{x})$ is a skew-symmetric matrix.

$$\dot{x}^T\left(\dot{M}(x)-2C(x,\dot{x})\right)\dot{x}=\dot{x}^T\begin{bmatrix}0 & 2\xi\left(\dot{\theta}+2\right)\\ -2\xi\left(\dot{\theta}+2\right) & 0\end{bmatrix}\dot{x}=0 \tag{3.8}$$

Property 3. There exists a positive constant k_g that the gravity vector satisfies $\left\|\frac{\partial G(x)}{\partial x}\right\|\le k_g$.

Then, an energy function is given as,

$$\begin{aligned}E(x,\dot{x})&=\frac{1}{2}\dot{x}^T M(x)\dot{x}+U_0(x)\\ &=\frac{1}{2}\dot{\xi}^2+\frac{1}{2}\xi^2\dot{\theta}^2-\frac{3}{2}\xi^2\cos^2\theta\end{aligned} \tag{3.9}$$

and its time derivative is,

$$
\begin{aligned}
\dot{E} &= \dot{x}^T M\ddot{x} + \frac{1}{2}\dot{x}^T \dot{M}\dot{x} + \dot{U}_0 \\
&= \frac{1}{2}\dot{x}^T\left(\dot{M} - 2C\right)\dot{x} - \dot{x}^T G + \dot{x}^T u + \dot{U}_0 \\
&= \dot{x}^T u
\end{aligned} \tag{3.10}
$$

Integrating the both sides of Eq. (3.10) in $[0,\tau]$, one obtains the equation of energy balance,

$$E(\tau) - E(0) = \int_0^\tau \dot{x}(\xi)^{\mathrm{T}} u(\xi) d\xi \tag{3.11}$$

Assume U_0 is bounded from below C, then $E - C \geq 0$. Obviously, from Eq.(3.11), TSS is lossless with the input u and output $\dot{x}$, if the storage function is $S = E - C$. Thus, one can obtain the following passivity,

Property 4. (Passivity) TSS in Eq. (3.5) is passive if the input action $u = v - \beta(\dot{x})$ with the mapping $v \mapsto \dot{x}$ and a storage function $V \geq 0$ that satisfies the following condition

$$\underbrace{V[x(\tau), \dot{x}(\tau)] - V[x(0), \dot{x}(0)]}_{\text{Stored energy}} = \underbrace{\int_0^\tau \dot{x}(\xi)^{\mathrm{T}} v(\xi)\,\mathrm{d}\xi}_{\text{Supplied energy}} - \underbrace{d\left(\dot{x}(\tau)\right)}_{\text{Dissipated energy}} \tag{3.12}$$

where the dissipation energy function is positive, such that, $d\left(\dot{x}(\tau)\right) = \int_0^\tau \beta\left(\dot{x}(\xi)\right)^{\mathrm{T}} v(\xi)\,\mathrm{d}\xi \geq 0$.

3.1.2 Hamiltonian Formulation

In the section, we will derive the system's equations by Hamiltonian formulation. As in Hamiltonian mechanics, the coordinate (q, p) is used to describe the system's motion instead of $(q,\dot{q})$ in Lagrangian.

The generalized momentum $p=\mathrm{col}\left(p_\xi, p_\theta\right)$ is obtained as,

$$p_\xi = \frac{\partial L_0}{\partial \dot{\xi}} = \dot{\xi} \tag{3.13}$$

$$p_\theta = \frac{\partial L_0}{\partial \dot{\theta}} = \xi^2\left(\dot{\theta}+1\right) \tag{3.14}$$

Applying the Legendre transformation, one can obtain the Hamiltonian function as follows,

$$\begin{aligned} H(q,p) &= \dot{q}^T p - L_0\left(q,\dot{q}(q,p)\right) \\ &= \frac{1}{2}\dot{\xi}^2 + \frac{1}{2}\xi^2\dot{\theta}^2 - \frac{3}{2}\xi^2\cos^2\theta \\ &= \frac{1}{2}p_\xi^2 + \frac{\xi^2}{2}\left(\frac{p_\theta}{\xi^2}-1\right)^2 + U\left(q\right) \end{aligned} \tag{3.15}$$

where the normalized Lagrangian is $L_0(x,\dot{x}) = \frac{1}{2}\dot{\xi}^2 + \frac{1}{2}\xi^2\left[\left(\dot{\theta}+1\right)^2 + 3\cos^2\theta - 1\right]$.

Recall the Hamilton equations,

$$\begin{bmatrix} \dot{q} \\ \dot{p} \end{bmatrix} = \begin{bmatrix} 0^{2\times2} & I^{2\times2} \\ -I^{2\times2} & 0^{2\times2} \end{bmatrix} \begin{bmatrix} \dfrac{\partial H}{\partial q} \\ \dfrac{\partial H}{\partial p} \end{bmatrix} + \begin{bmatrix} 0^{2\times1} \\ u \end{bmatrix} \tag{3.16}$$

Then, the dynamics of motion of TSS can be expressed as,

$$
\begin{aligned}
&\ddot{\xi} = \xi\left(\dot{\theta}+1\right)^2 - \xi + 3\xi\cos^2\theta - T \\
&\xi^2\ddot{\theta} + 2\xi\dot{\xi}\left(\dot{\theta}+1\right) = -3\xi^2\sin\theta\cos\theta
\end{aligned}
\tag{3.17}
$$

Then, taking the time derivative of H yields that

$$
\begin{aligned}
\dot{H}(q,p) &= \frac{\partial^T H}{\partial q}\dot{q} + \frac{\partial^T H}{\partial p}\dot{p} \\
&= \left(\frac{\partial^T H}{\partial q}, \frac{\partial^T H}{\partial p}\right)\begin{pmatrix} & I \\ -I & \end{pmatrix}\left(\frac{\partial^T H}{\partial q}, \frac{\partial^T H}{\partial p}\right)^T + \frac{\partial^T H}{\partial p}u \\
&= \frac{\partial^T H}{\partial p}u = -\frac{\partial H}{\partial p_\xi}T = -\dot{\xi}T
\end{aligned}
\tag{3.18}
$$

Equation (3.18) indicates the energy balance property of TSS, where the energy's changing in the Hamiltonian quantity equals to the power supply. Relation shown in Eq.(3.18) is actually identical to the TSS's passivity defined in Eq.(3.10). Moreover, it is quite straightforward to reveal the intrinsic property of TSS by the Hamiltonian formulation [94].

3.2 Modeling of Tethered Despin System

3.2.1 Dynamic Motion of TSS without Orbital Effect

Considering a massive rotating target is captured by a single tether and connected to a small spacecraft, as shown in Figure 3.2. The tether is assumed to be massless and inextensible. The tethered system moves in the orbital plane. As the first step, we ignore the gravitational field and assume that the tethered despin system is rotating in a free space. The target is treated as rigid body with mass m_2 and inertia momentum J. The space tug is simplified as a lumped mass with a mass m_1, $m_1 \ll m_2$. The tether which connects target and spacecraft is with the constant length l. Further, due to $m_1 \ll m_2$, it is reasonable to assume the center of mass (CM) of the tethered despin system is at the massive target's center and the center of rotation is same as the center of mass of the target during the despin process.

Inertial coordinate system OXY is defined with its origin fixed at the CM of the target. The tether connection point at the target is with distance r to the massive target's CM. The target is rotating around the principal axis through CM with an angular velocity ω vertical to the plane XOY.

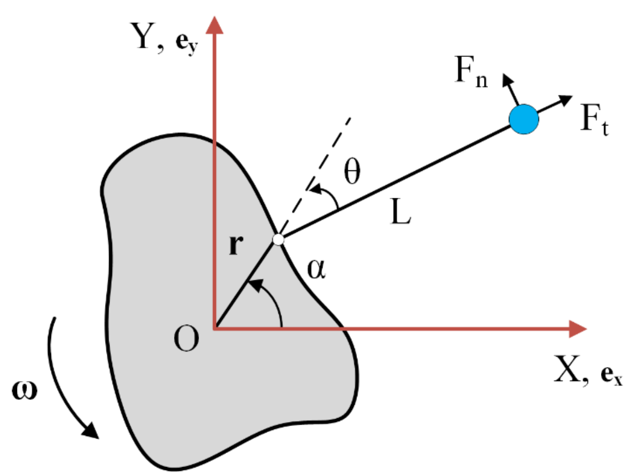

Figure 3.2 Sketch of spinning target and tethered spacecraft.

Then, the position of the spacecraft $\mathbf{R}_1$ in OXY with respect to the CM system is given as,

$$\mathbf{R}_1 = x_1\mathbf{e}_\mathbf{x} + y_1\mathbf{e}_\mathbf{y} = \mathbf{R}_2 + \mathbf{L} \tag{3.19}$$

$$\mathbf{R}_2 = x_2\mathbf{e}_\mathbf{x} + y_2\mathbf{e}_\mathbf{y} = r\cos\alpha\mathbf{e}_\mathbf{x} + r\sin\alpha\mathbf{e}_\mathbf{y} \tag{3.20}$$

$$\mathbf{L} = l\cos(\alpha+\theta)\mathbf{e}_\mathbf{x} + l\sin(\alpha+\theta)\mathbf{e}_\mathbf{y} \tag{3.21}$$

where $\mathbf{R}_2$ denotes the position vector of tether connection point on the target. α denotes the rotation angle of the vector $\mathbf{R}_2$ to the OX-axis. $\left(\mathbf{e}_\mathbf{x}, \mathbf{e}_y\right)$ denote the unit vectors of OX and OY. θ is the angle from the tether to the vector $\mathbf{R}_2$, i.e. tether libration angle.

Accordingly, one can calculate the spacecraft's velocity and acceleration as follows,

$$\begin{aligned} \mathbf{v}_1 = \dot{\mathbf{R}}_1 = & -\left[r\dot{\alpha}\sin\alpha + l\sin\left(\alpha+\theta\right)\left(\dot{\alpha}+\dot{\theta}\right)\right]\mathbf{e}_\mathbf{x} \\ & +\left[r\dot{\alpha}\cos\alpha + l\cos\left(\alpha+\theta\right)\left(\dot{\alpha}+\dot{\theta}\right)\right]\mathbf{e}_\mathbf{y} \end{aligned} \tag{3.22}$$

$$\begin{aligned} \mathbf{a}_1 = \ddot{\mathbf{R}}_1 = & -\begin{bmatrix} l\sin\left(\alpha+\theta\right)\left(\ddot{\alpha}+\ddot{\theta}\right) + r\ddot{\alpha}\sin\alpha + r\dot{\alpha}^2\cos\alpha \\ +l\cos\left(\alpha+\theta\right)\left(\dot{\alpha}+\dot{\theta}\right)^2 \end{bmatrix}\mathbf{e}_\mathbf{x} \\ & +\begin{bmatrix} l\cos\left(\alpha+\theta\right)\left(\ddot{\alpha}+\ddot{\theta}\right) + r\ddot{\alpha}\cos\alpha - r\dot{\alpha}^2\sin\alpha \\ -l\sin\left(\alpha+\theta\right)\left(\dot{\alpha}+\dot{\theta}\right)^2 \end{bmatrix}\mathbf{e}_\mathbf{y} \end{aligned} \tag{3.23}$$

Then, the following equations are represented,

$$J\ddot{\alpha} = \overline{T}r\sin\theta \tag{3.24}$$

$$m_1\mathbf{a}_1 = \left[(F_t-\bar{T})\cos(\alpha+\theta)-F_n\sin(\alpha+\theta)\right]\mathbf{e}_\mathbf{x} + \left[(F_t-\bar{T})\sin(\alpha+\theta)+F_n\cos(\alpha+\theta)\right]\mathbf{e}_\mathbf{y} \tag{3.25}$$

where $\bar{T}$ denotes the tension in tether and (F_t, F_n) are the vectoring thrust along and perpendicular to the tether.

Substituting Eqs. (3.19)-(3.23) into (3.25) yields,

$$\begin{aligned}&-r\sin\alpha\ddot{\alpha}-r\cos\alpha\dot{\alpha}^2-l\sin(\alpha+\theta)(\ddot{\alpha}+\ddot{\theta})-l\cos(\alpha+\theta)(\dot{\alpha}+\dot{\theta})^2\\&=\frac{1}{m_1}\left[(F_t-\bar{T})\cos(\alpha+\theta)-F_n\sin(\alpha+\theta)\right]\end{aligned} \tag{3.26}$$

$$\begin{aligned}&r\cos\alpha\ddot{\alpha}-r\sin\alpha\dot{\alpha}^2+l\cos(\alpha+\theta)(\ddot{\alpha}+\ddot{\theta})-l\sin(\alpha+\theta)(\dot{\alpha}+\dot{\theta})^2\\&=\frac{1}{m_1}\left[(F_t-\bar{T})\sin(\alpha+\theta)+F_n\cos(\alpha+\theta)\right]\end{aligned} \tag{3.27}$$

Arranging the Eqs. (3.26) and (3.27), one has,

$$r\sin\theta\ddot{\alpha}-r\cos\theta\dot{\alpha}^2-l(\dot{\alpha}+\dot{\theta})^2=\frac{1}{m_1}(F_t-\bar{T}) \tag{3.28}$$

$$r\cos\theta\ddot{\alpha}+r\sin\theta\dot{\alpha}^2+l(\ddot{\alpha}+\ddot{\theta})=\frac{1}{m_1}F_n \tag{3.29}$$

Arrange the above equations and write in terms of $\omega=\dot{\alpha}$ and angle θ, such that,

$$
\begin{aligned}
\dot{\omega} &= \frac{m_1 r \sin\theta\left[r\omega^2\cos\theta + l\left(\omega+\dot{\theta}\right)^2\right] + F_t r \sin\theta}{J + m_1 r^2 \sin^2\theta} \\
\ddot{\theta} &= -\left(1+\frac{r}{l}\cos\theta\right)\dot{\omega} - \frac{r}{l}\omega^2\sin\theta + \frac{1}{m_1 l}F_n
\end{aligned}
\tag{3.30}
$$

$$
\bar{T} = \frac{m_1\left[r\omega^2\cos\theta + l\left(\omega+\dot{\theta}\right)^2\right] + F_t}{1 + m_1 r^2 \sin^2\theta / J}
\tag{3.31}
$$

Define the dimensionless variables to normalize the above differential equations,

$$
\tau = \omega_0 t\,,\ \lambda = J\big/\left(m_1 r^2\right),\ \xi = l/r\,, \eta = \omega/\omega_0
$$

$$
u_t = F_t\big/\left(m_1 r \omega_0^2\right),\ u_n = F_n\big/\left(m_1 r \omega_0^2\right),\ T = \bar{T}\big/\left(m_1 r \omega_0^2\right)
$$

Then, Eq. (3.30) is represented in the dimensionless forms as follows,

$$
\begin{aligned}
\eta' &= \frac{\sin\theta\left(\cos\theta\eta^2 + \xi\left(\eta+\theta'\right)^2\right) + u_t\sin\theta}{\lambda + \sin^2\theta} \\
\theta'' &= -\left(1+\frac{1}{\xi}\cos\theta\right)\eta' - \frac{1}{\xi}\sin\theta\eta^2 + \frac{u_n}{\xi}
\end{aligned}
\tag{3.32}
$$

where $(\ )' = \mathrm{d}(\ )/\mathrm{d}\tau$ and ω_0 denotes the target's initial angular velocity.

The above dynamic equations (3.28) and (3.29) are established while the target is assumed fixed at the center of mass. The free-floating model can be derived as follows,

The position and acceleration relations can be rewritten as,

$$\begin{aligned} x_0 + r\cos\alpha + l\cos(\alpha+\theta) = x_1 \\ y_0 + r\sin\alpha + l\sin(\alpha+\theta) = y_1 \end{aligned} \tag{3.33}$$

$$\begin{aligned} m_2\ddot{x}_0 = T\cos\theta\cos\alpha \\ m_2\ddot{y}_0 = T\cos\theta\sin\alpha \end{aligned} \tag{3.34}$$

$$\begin{aligned} m_1\ddot{x}_1 = (F_t - T)\cos(\alpha+\theta) - F_n\sin(\alpha+\theta) \\ m_1\ddot{y}_1 = (F_t - T)\sin(\alpha+\theta) + F_n\cos(\alpha+\theta) \end{aligned} \tag{3.35}$$

where (x_0, y_0) and (x_1, y_1) are the target's and spacecraft's coordinates in the inertial frame.

Then, substituting Eqs. (3.33) and (3.34) into Eq. (3.35), one has,

$$\begin{aligned} &-r\sin\alpha\ddot{\alpha} - r\cos\alpha\dot{\alpha}^2 - l\sin(\alpha+\theta)(\ddot{\alpha}+\ddot{\theta}) - l\cos(\alpha+\theta)(\dot{\alpha}+\dot{\theta})^2 \\ &= \frac{1}{m_1}\left[(F_t - T)\cos(\alpha+\theta) - F_n\sin(\alpha+\theta)\right] - \frac{T\cos\theta\cos\alpha}{m_2} \end{aligned} \tag{3.36}$$

$$\begin{aligned} &r\cos\alpha\ddot{\alpha} - r\sin\alpha\dot{\alpha}^2 + l\cos(\alpha+\theta)(\ddot{\alpha}+\ddot{\theta}) - l\sin(\alpha+\theta)(\dot{\alpha}+\dot{\theta})^2 \\ &= \frac{1}{m_1}\left[(F_t - T)\sin(\alpha+\theta) + F_n\cos(\alpha+\theta)\right] - \frac{T\cos\theta\sin\alpha}{m_2} \end{aligned} \tag{3.37}$$

It is easy to find an extra term $T\cos\theta\cos\alpha/m_2$ in Eq.(3.36) compared with Eq. (3.28), and $T\cos\theta\cos\alpha/m_2$ in Eq. (3.37) compared with Eq. (3.29). Due to the mass relation $m_2 \gg m_1$, these two terms are negligibly small. Hence, one can reasonably ignore them when the main interest focuses on despinning the target.

If the tether length is variable, the dynamic motion equations can be obtained as in the Ref. [74],

$$
\begin{aligned}
&\ddot{l} + r\sin\theta\ddot{\alpha} - r\cos\theta\dot{\alpha}^2 - l(\dot{\alpha}+\dot{\theta})^2 = \left(F_t - \bar{T}\right)/m_1 \\
&r\cos\theta\ddot{\alpha} + r\sin\theta\dot{\alpha}^2 + 2\dot{l}(\dot{\alpha}+\dot{\theta}) + l(\ddot{\alpha}+\ddot{\theta}) = F_n/m_1 \\
&J\ddot{\alpha} = \bar{T}r\sin\theta
\end{aligned} \tag{3.38}
$$

One can further represent the equations into the dimensionless form as,

$$
\begin{aligned}
&\xi'' = -\sin\theta\eta' + \cos\theta\eta^2 + \xi\left(\eta+\theta'\right)^2 + (u_t - T) \\
&\eta' = T\sin\theta/\lambda \\
&\theta'' = -\left(1 + \frac{1}{\xi}\cos\theta\right)\eta' - \frac{1}{\xi}\sin\theta\eta^2 + \frac{u_n}{\xi}
\end{aligned} \tag{3.39}
$$

3.2.2 Dynamic Motion of TSS in Circular Orbit

In this section, a massive spinning asteroid is modeled in a central gravitational field. Assume the large target (asteroid) is captured by a small tethered spacecraft, as shown in Figure 3.3. Tether is assumed to be rigid and massless. Consider target as a rigid body with mass m_2 and inertia momentum J. The small spacecraft is treated as particle with mass m_1 due to $m_2 \gg m_1$. The tether connects two body is with length l. The distance from tether connection point to the asteroid's center of mass (CM) is r. Due $m_2 \gg m_1$, it is reasonable to assume the CM of system is located at the CM of the massive asteroid [22]. Further, the motion of the TSS is assumed to limit in the orbital plane. The massive asteroid is spinning about the principal axis perpendicular to the orbital plane. Orbital frame is denoted as $Ox_oy_oz_o$ as shown in Figure 3.3. The origin O is fixed at the CM of the massive asteroid. The Ox_o-axis is along the orbital radius. The Oy_o-axis is along the direction of the orbital velocity of system. The Oz_o-axis completes a right-hand coordinate frame.

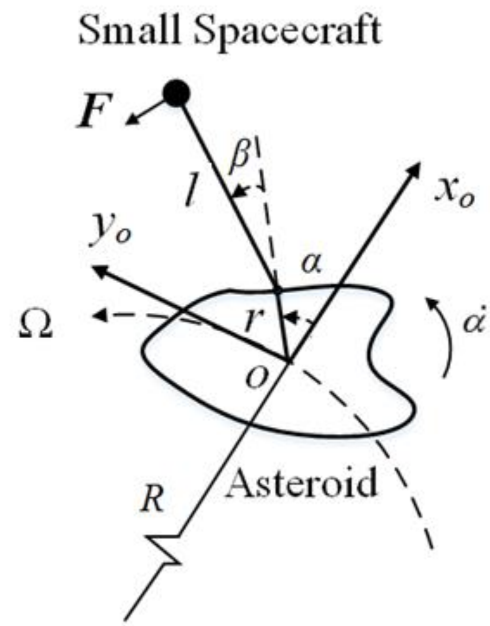

Figure 3.3 Spinning target with TSS in a circular orbit

According to the above assumptions, the system's kinetic energy is obtained as,

$$K = \frac{1}{2} m_1 \mathbf{v}_1 \cdot \mathbf{v}_1 + \frac{1}{2} m_2 \mathbf{v}_2 \cdot \mathbf{v}_2 + \frac{1}{2} J \left(\dot{\alpha} + \Omega \right)^2 \tag{3.40}$$

where $\mathbf{v}_2$ denotes the system's orbital velocity and $\mathbf{v}_1$ denotes the small spacecraft velocity's. Ω denotes the orbital angular velocity and α denotes the asteroid's attitude which is defined as the angle from the Ox_o-axis to $\mathbf{r}$.

Represent $\mathbf{v}_1$ and $\mathbf{v}_2$ in the orbital frame, such that,

$$\mathbf{v}_2 = \dot{\mathbf{R}}_2 = R\Omega\,\mathbf{j} \tag{3.41}$$

$$\mathbf{v}_1 = \dot{\mathbf{R}}_1 = d\left(R\mathbf{i} + \mathbf{r}_1\right)/dt \tag{3.42}$$

$$\mathbf{r}_1 = x_1\mathbf{i} + y_1\mathbf{j} = \left[r\cos\alpha + l\cos\left(\alpha+\beta\right)\right]\mathbf{i} + \left[r\sin\alpha + l\sin\left(\alpha+\beta\right)\right]\mathbf{j} \tag{3.43}$$

where $\mathbf{R}_1$ and $\mathbf{R}_2$ denote the spacecraft's position and asteroid's position, respectively. R denotes the orbital radius of system and β denotes the tether libration angle from $\mathbf{r}$ to the tether. $(\mathbf{i}, \mathbf{j})$ are the unit vectors of Ox_o-axis and Oy_o-axis. The small spacecraft's coordinates in the O-$x_oy_oz_o$ can be represented as $x_1 = r\cos\alpha + l\cos\left(\alpha+\beta\right)$ and $y_1 = r\sin\alpha + l\sin\left(\alpha+\beta\right)$.

Substituting Eq. (3.43) into Eq.(3.42) leads,

$$\begin{aligned}\mathbf{v}_1 = &\left\{\begin{aligned}&-r\sin\dot{\alpha} - l\sin\left(\alpha+\beta\right)\left(\dot{\alpha}+\dot{\beta}\right) + \dot{l}\cos\left(\alpha+\beta\right)\\ &-\left[r\sin\alpha + l\sin\left(\alpha+\beta\right)\right]\Omega\end{aligned}\right\}\mathbf{i}\\ &+\left\{\begin{aligned}&\left[R + r\cos\alpha + l\cos\left(\alpha+\beta\right)\right]\Omega + r\cos\alpha\dot{\alpha}\\ &+l\cos\left(\alpha+\beta\right)\left(\dot{\alpha}+\dot{\beta}\right) + \dot{l}\sin\left(\alpha+\beta\right)\end{aligned}\right\}\mathbf{j}\end{aligned} \tag{3.44}$$

Accordingly, the expression of v_1^2 is obtained as,

$$
\begin{aligned}
\mathbf{v}_1^2 &= R^2\Omega^2 + r^2\dot{\alpha}^2 + l^2\left(\dot{\alpha}+\dot{\beta}\right)^2 + \dot{l}^2 + r^2\Omega^2 + l^2\Omega^2 \\
&+2r\dot{\alpha}l\cos\beta\left(\dot{\alpha}+\dot{\beta}\right) + 2r\dot{\alpha}\dot{l}\sin\beta + 2r^2\dot{\alpha}\Omega \\
&+2r\dot{\alpha}l\Omega\cos\beta + 2l\left(\dot{\alpha}+\dot{\beta}\right)r\Omega\cos\beta + 2l\left(\dot{\alpha}+\dot{\beta}\right)l\Omega \\
&+2\dot{l}r\Omega\sin\beta + 2rl\Omega^2\cos\beta + 2R\Omega r\cos\alpha\Omega \\
&+2R\Omega l\cos\left(\alpha+\beta\right)\Omega + 2R\Omega r\cos\alpha\dot{\alpha} \\
&+2R\Omega l\cos\left(\alpha+\beta\right)\left(\dot{\alpha}+\dot{\beta}\right) + 2R\Omega\dot{l}\sin\left(\alpha+\beta\right)
\end{aligned}
\tag{3.45}
$$

Next, the system's potential energy is denoted as,

$$
U = -\frac{\mu m_1}{\left|\mathbf{R}_1\right|} - \frac{\mu m_2}{\left|\mathbf{R}_2\right|} = -\frac{\mu m_2}{R} - \frac{\mu m_1}{\left|\mathbf{R}+\mathbf{r}+\mathbf{l}\right|} \tag{3.46}
$$

where μ denotes the gravitational constant of Earth. Due to $R \gg l > r$, the second term in Eq.(3.46) can be approximated by Tayler expansion,

$$
\begin{aligned}
-\frac{1}{\left|\mathbf{R}+\mathbf{r}+\mathbf{l}\right|} &= -\frac{1}{2R}\left[2 - 2\frac{x_1}{R} - \left(\frac{x_1}{R}\right)^2 - \left(\frac{y_1}{R}\right)^2 + \frac{3}{2}\left(\frac{x_1}{R}\right)^2 + O^3(0)\right] \\
&\approx -\frac{1}{R} + \frac{x_t}{R^2} - \frac{x_t^{\,2}}{R^3} + \frac{y_t^{\,2}}{2R^3}
\end{aligned}
\tag{3.47}
$$

Thus, the tethered system's potential energy is simplified as,

$$
\begin{aligned}
U &\approx -\frac{\mu(m_1+m_2)}{R} + \frac{\mu m_1}{R^2}\left[r\cos\alpha + l\cos\left(\alpha+\beta\right)\right] \\
&-\frac{\mu m_1}{R^3}\left[r\cos\alpha + l\cos\left(\alpha+\beta\right)\right]^2 + \frac{\mu m_1}{2R^3}\left[r\sin\alpha + l\sin\left(\alpha+\beta\right)\right]^2
\end{aligned}
\tag{3.48}
$$

Combining Eqs.(3.40)-(3.48), one obtains the system's Lagrangian as,

$$
\begin{aligned}
L &= K - U \\
&= \frac{m_2}{2} R^2 \Omega^2 + \frac{m_1}{2} v_1^2 + \frac{J}{2} (\Omega + \dot{\alpha})^2 \\
&+ \frac{\mu(m_1 + m_2)}{R} - \frac{\mu m_1}{R^2} \left[r \cos\alpha + l \cos(\alpha + \beta) \right] \\
&+ \frac{\mu m_1}{R^3} \left[r \cos\alpha + l \cos(\alpha + \beta) \right]^2 - \frac{\mu m_1}{2R^3} \left[r \sin\alpha + l \sin(\alpha + \beta) \right]^2
\end{aligned}
\tag{3.49}
$$

Recall the Lagrange's equation,

$$
\frac{\mathrm{d}}{\mathrm{d}t} \left(\frac{\partial L}{\partial \dot{q}} \right) - \frac{\partial L}{\partial q} = Q \tag{3.50}
$$

where $q = \mathrm{col}\{l, \alpha, \beta\}$ are generalized coordinates and Q are the corresponding generalized forces.

Substituting the kinetic and potential energy into Eq. (3.50)yields,

$$
m_1 \ddot{l} + m_1 r \ddot{\alpha} \sin\beta + m_1 f_l \left(l, \dot{l}, \alpha, \dot{\alpha}, \beta, \dot{\beta} \right) = -\bar{T} \tag{3.51}
$$

$$
\begin{aligned}
& m_1 r \sin\beta \ddot{l} + \left(J + m_1 r^2 + m_1 l^2 + 2 m_1 r l \cos\beta \right) \ddot{\alpha} + m_1 \left(l^2 + r l \cos\beta \right) \ddot{\beta} \\
& + m_1 f_\alpha \left(l, \dot{l}, \alpha, \dot{\alpha}, \beta, \dot{\beta} \right) = F l + F r \cos\beta
\end{aligned}
\tag{3.52}
$$

$$
m_1 l^2 \left(\ddot{\alpha} + \ddot{\beta} \right) + m_1 r l \cos\beta \ddot{\alpha} + m_1 f_\beta \left(l, \dot{l}, \alpha, \dot{\alpha}, \beta, \dot{\beta} \right) = F l \tag{3.53}
$$

where $\bar{T}$ denotes the tether tension, F denotes the thrust force along tether's tangent direction.

The expressions f_α and f_β are given as follows,

$$f_l\left(l,\dot{l},\alpha,\dot{\alpha},\beta,\dot{\beta}\right)=-r\cos\beta\dot{\alpha}^2-2r\Omega\cos\beta\dot{\alpha}-l\left(\dot{\alpha}+\dot{\beta}\right)^2-2l\Omega\left(\dot{\alpha}+\dot{\beta}\right)$$
$$-3r\Omega^2\cos\alpha\cos\left(\alpha+\beta\right)-3l\Omega^2\cos^2\left(\alpha+\beta\right) \tag{3.54}$$

$$\begin{aligned}f_\alpha\left(l,\dot{l},\alpha,\dot{\alpha},\beta,\dot{\beta}\right)=&-2rl\sin\beta\dot{\alpha}\dot{\beta}-rl\sin\beta\dot{\beta}^2-2rl\Omega\sin\beta\dot{\beta}\\&+2r\cos\beta\dot{l}\left(\dot{\alpha}+\dot{\beta}+\Omega\right)+2l\dot{l}\left(\dot{\alpha}+\dot{\beta}+\Omega\right)\\&+3r^2\Omega^2\sin\alpha\cos\alpha+3rl\Omega^2\sin\alpha\cos\left(\alpha+\beta\right)\\&+3rl\Omega^2\cos\alpha\sin\left(\alpha+\beta\right)+3l^2\Omega^2\sin\left(\alpha+\beta\right)\cos\left(\alpha+\beta\right)\end{aligned} \tag{3.55}$$

$$\begin{aligned}f_\beta\left(l,\dot{l},\alpha,\dot{\alpha},\beta,\dot{\beta}\right)=&\,rl\sin\beta\dot{\alpha}^2+2rl\Omega\sin\beta\dot{\alpha}+2l\dot{l}\left(\dot{\alpha}+\dot{\beta}+\Omega\right)\\&+3rl\Omega^2\cos\alpha\sin\left(\alpha+\beta\right)+3l^2\Omega^2\sin\left(\alpha+\beta\right)\cos\left(\alpha+\beta\right)\end{aligned} \tag{3.56}$$

For the sake of simplicity, we normalize the above dynamic equations by the following dimensionless variables:

$$\lambda=J/(m_1r^2),\ \xi=l/r,\ T=\bar{T}/(m_1r\dot{\alpha}_0{}^2),\ u=F/(m_1r\dot{\alpha}_0{}^2),$$

$$\tau=\dot{\alpha}_0t,\ \bar{\Omega}=\Omega/\dot{\alpha}_0\ \text{and}\ \dot{(\ )}=\dot{\alpha}_0()'=\dot{\alpha}_0d(\ )/d\tau$$

where $\dot{\alpha}_0$ denotes the massive target's initial angular velocity.

Thus, the dimensionless dynamics equations are presented as,

$$\xi''+\alpha''\sin\beta+\tilde{f}_\xi\left(\xi,\xi',\alpha,\alpha',\beta,\beta'\right)=-T \tag{3.57}$$

$$\begin{aligned}&\sin\beta\xi''+\left(\lambda+1+\xi^2+2\xi\cos\beta\right)\alpha''+\left(\xi^2+\xi\cos\beta\right)\beta''\\&+\tilde{f}_\alpha\left(\xi,\xi',\alpha,\alpha',\beta,\beta'\right)=u\xi+u\cos\beta\end{aligned} \tag{3.58}$$

$$\left(\xi^2+\xi\cos\beta\right)\alpha''+\xi^2\beta''+\tilde{f}_\beta\left(\xi,\xi',\alpha,\alpha',\beta,\beta'\right)=u\xi \tag{3.59}$$

and $\tilde{f}_\xi$, $\tilde{f}_\alpha$ and $\tilde{f}_\beta$ are expressed as,

$$\tilde{f}_\xi = -\cos\beta\alpha'^2 - 2\cos\beta\bar{\Omega}\alpha' - \xi\left(\alpha'+\beta'\right)^2 - 2\xi\bar{\Omega}\left(\alpha'+\beta'\right)$$
$$-3\bar{\Omega}^2\cos\alpha\cos\left(\alpha+\beta\right) - 3\xi\bar{\Omega}^2\cos^2\left(\alpha+\beta\right) \tag{3.60}$$

$$\tilde{f}_\alpha = -2\xi\sin\beta\alpha'\beta' - \xi\sin\beta\beta'^2 - 2\xi\sin\beta\bar{\Omega}\beta'$$
$$+2\cos\beta\xi'\left(\alpha'+\beta'+\bar{\Omega}\right) + 2\xi\xi'\left(\alpha'+\beta'+\bar{\Omega}\right)$$
$$+3\bar{\Omega}^2\sin\alpha\cos\alpha + 3\xi\bar{\Omega}^2\sin\alpha\cos\left(\alpha+\beta\right)$$
$$+3\xi\bar{\Omega}^2\cos\alpha\sin\left(\alpha+\beta\right) + 3\xi^2\bar{\Omega}^2\sin\left(\alpha+\beta\right)\cos\left(\alpha+\beta\right) \tag{3.61}$$

$$\tilde{f}_\beta = \xi\sin\beta\alpha'^2 + 2\xi\sin\beta\bar{\Omega}\alpha' + 2\xi\xi'\left(\alpha'+\beta'+\bar{\Omega}\right)$$
$$+3\xi\bar{\Omega}^2\cos\alpha\sin\left(\alpha+\beta\right) + 3\xi^2\bar{\Omega}^2\sin\left(\alpha+\beta\right)\cos\left(\alpha+\beta\right) \tag{3.62}$$

3.3 Dynamic Motion of TSS during Orbital Maneuvering

3.3.1 Non-Singular Orbital Elements

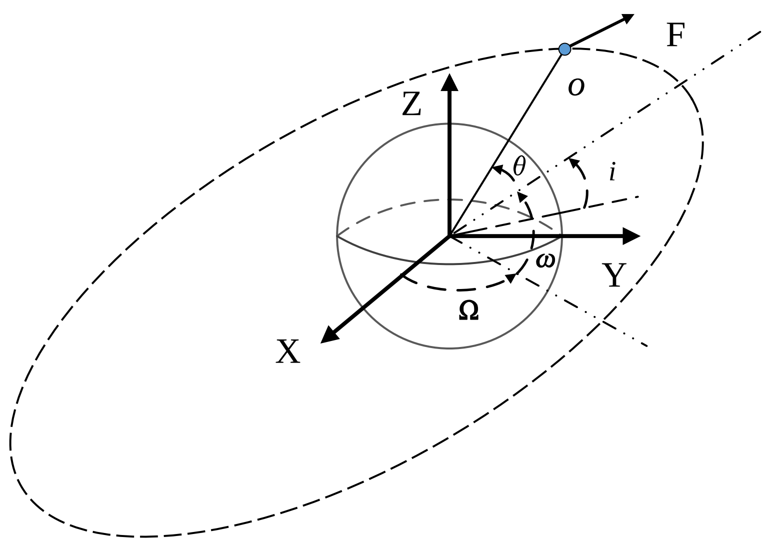

Figure 3.4 Sketch of the orbital elements

The disturbed motion of the space target in orbiting the earth can be written as,

$$\frac{d^2}{dt^2}\mathbf{r}_o+\frac{\mu}{r_o^3}\mathbf{r}_o=\frac{\mathbf{F}}{m} \tag{3.63}$$

where $\mathbf{r}_0$ denotes the position vector to Earth center in the inertial frame. m denotes the mass of the space target, μ is the gravitational parameter of Earth, the symbol $\frac{d}{dt}()$ denotes the time derivative of vector in inertial frame, and $\mathbf{F}$ is a constant perturbation force acting on the mass point.

Then, one can write the Eq.(3.63) in the Gaussian form of variational equations with classical orbital elements $(a, e, i, \Omega, \omega, \theta)$, as shown in Figure 3.4, as follows,

$$\begin{aligned}
&\frac{d}{dt}a=2a^2e\sin v\left(\frac{S}{\kappa\sqrt{p}}\right)+2a^2\frac{p}{r}\left(\frac{T}{\kappa\sqrt{p}}\right)\\
&\frac{d}{dt}e=p\sin v\left(\frac{S}{\kappa\sqrt{p}}\right)+p\left(\cos v+\cos E\right)\left(\frac{T}{\kappa\sqrt{p}}\right)\\
&\frac{d}{dt}i=r\cos\left(v+w\right)\left(\frac{W}{\kappa\sqrt{p}}\right)\\
&\frac{d}{dt}w=-\frac{p\cos v}{e}\left(\frac{S}{\kappa\sqrt{p}}\right)+\frac{r+p}{e}\left(\frac{T}{\kappa\sqrt{p}}\right)-r\sin\left(v+w\right)\cot i\left(\frac{W}{\kappa\sqrt{p}}\right)\\
&\frac{d}{dt}\Omega=\frac{r\sin\left(v+w\right)}{\sin i}\left(\frac{W}{\kappa\sqrt{p}}\right)\\
&\frac{d}{dt}\theta=\frac{\sqrt{1-e^2}}{e}\left[\left(p\cos v-2er\right)\left(\frac{S}{\kappa\sqrt{p}}\right)-\left(r+p\right)\sin v\left(\frac{T}{\kappa\sqrt{p}}\right)\right]
\end{aligned} \tag{3.64}$$

where (S,T,W) is the perturbed acceleration along: S in the radial direction, T in orbital plane perpendicular to S, and W completes the right hand coordinates.

$$p = a\left(1-e^2\right) \quad r = \frac{p}{1+e\cos v} \quad \kappa^2 = \mu \quad \dot{v} = \frac{\kappa\sqrt{p}}{r^2} \quad \cos E = \frac{e+\cos v}{1+e\cos v}$$

It is easy to find that Eq.(3.64) is singular if the eccentricity or inclination is zero. Thus, the non-singular orbital elements $(a, e_1, e_2, q_1, q_2, \lambda)^{\mathrm{T}}$ are adopted from [95],

$$\begin{pmatrix} a \\ e_1 \\ e_2 \\ q_1 \\ q_2 \\ \lambda \end{pmatrix} = \begin{pmatrix} a \\ e\cos(\omega+\Omega) \\ e\sin(\omega+\Omega) \\ \tan(i/2)\cos\Omega \\ \tan(i/2)\sin\Omega \\ \Omega+\omega+\theta \end{pmatrix} \tag{3.65}$$

The corresponding perturbed differential equations can be obtained as,

$$\begin{cases} \dfrac{da}{dt} = \dfrac{2a^2}{h}\left[\left(e_1\sin\lambda - e_2\cos\lambda\right)\tilde{a}_x + w\tilde{a}_y\right] \\ \dfrac{de_1}{dt} = \dfrac{p}{hw}\left\{w\sin\lambda\tilde{a}_x + \left[\left(w+1\right)\cos\lambda + e_1\right]\tilde{a}_y - \left(q_1\sin\lambda - q_2\cos\lambda\right)e_2\tilde{a}_z\right\} \\ \dfrac{de_2}{dt} = \dfrac{p}{hw}\left\{-\cos\lambda\tilde{a}_x + \left[\left(w+1\right)\sin\lambda + e_2\right]\tilde{a}_y + \left(q_1\sin\lambda - q_2\cos\lambda\right)e_1\tilde{a}_z\right\} \\ \dfrac{dq_1}{dt} = \dfrac{p}{2hw}\left(1+q_1^{\,2}+q_2^{\,2}\right)\cos\lambda\tilde{a}_z \\ \dfrac{dq_2}{dt} = \dfrac{p}{2hw}\left(1+q_1^{\,2}+q_2^{\,2}\right)\sin\lambda\tilde{a}_z \\ \dfrac{d\lambda}{dt} = \dfrac{w^2}{p^2}h + \dfrac{p}{hw}\left(q_1\sin\lambda - q_2\cos\lambda\right)\tilde{a}_z \end{cases} \tag{3.66}$$

where $(\tilde{a}_x, \tilde{a}_y, \tilde{a}_z)^{\mathrm{T}}$ denote the components of the perturbing acceleration $\tilde{\mathbf{a}} = \mathbf{F}/m$ expanded in the orbital frame along (S, T, W). Variables p, w, and h are calculated as below,

$$\begin{cases} p = \left(1 - e_1^{\ 2} - e_2^{\ 2}\right) a \\ w = 1 + e_1 \cos\lambda + e_2 \sin\lambda \\ h = \sqrt{\mu p} \end{cases} \tag{3.67}$$

It should be noted that the corresponding six perturbed differential equations are singularity free as long as the inclination angle $-\pi < i < \pi$. It works for the special cases such as, circular orbit $e = 0$ or geostationary orbit $i = 0$.

3.3.2 Dynamic Motion of TSS in Orbital Frame

Consider an uncooperative large rotating space target in the perturbed Keplerian Orbit captured and connected to the tethered space tug as shown in Figure 3.5. The space tug with mass m_1 and large space target with mass m_2 are all treated as rigid body. Two single elastic tethers (l_{21}, l_{22}) with material damping are anchored to the edges (P_{21}, P_{22}) of the space target using the triangle attachment architecture and the main tether l_1 is connected to the surface of space tug at P_1. All tethers converge together to the connection C. A main tether is considered as rigid with variable length. Tethers are all assumed to be massless. The following coordinate frames are defined to describe the tethered system's dynamics,

Inertial frame $\mathcal{F}_I$ (E-XYZ): The origin E is at the center of the Earth. The X-axis is along the orbital radius pointing to the vernal equinox. The Z-axis is perpendicular to the orbit plane. The Y-axis completes a right-hand coordinate frame.

Orbital frame $\mathcal{F}_o$ (O-xyz): The origin O is located at the center of mass (CM) of the tethered system, which should satisfy $m_1\mathbf{r}_1 + m_2\mathbf{r}_2 + m_c\mathbf{r}_c = \left(m_1 + m_2 + m_c\right)\mathbf{r}_0$, $\mathbf{r}_{1,2,c}$ are the position vectors to the Earth's center in the inertial frame. The Ox_o-axis is along the orbital radius. The Oy_o-axis is along the direction of the orbital velocity of system.

Body frame $\mathcal{F}_b$ (O_1-$x_1y_1z_1$ and O_2-$x_2y_2z_2$): The origins O_1 and O_2 are located at the center of the tug and target, respectively. The three axes of the body frame are along with their principle moments of inertial of tug and target. In current research, it is assumed that the motion of TSS is limited in the orbital plane. The large space target and space tug are all rotating about its principal axis perpendicular to the orbital plane.

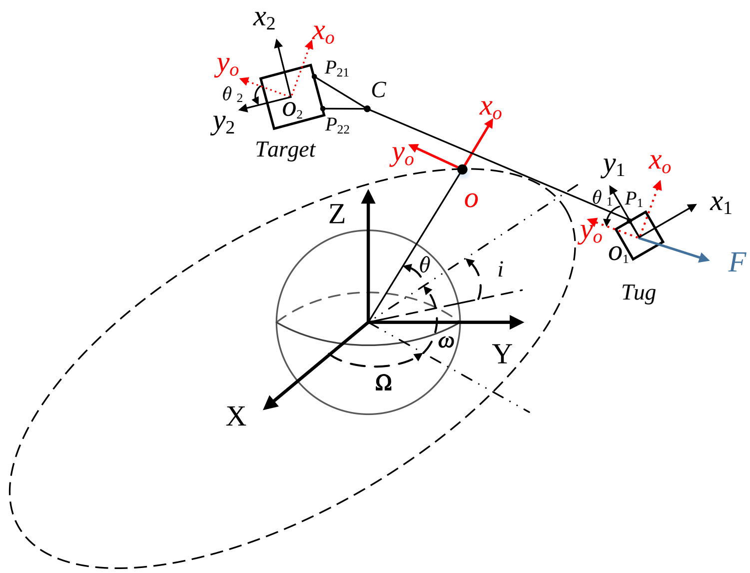

Figure 3.5 Sketch of tethered system maneuvering in the orbital plane

To establish the dynamic motions in the orbital frame $\mathcal{F}_o$ after the dynamic motion of the CM of system obtained. The positions of the tug, target, and connection are presented as follows,

$$\begin{aligned}
\mathbf{r_1} &= \mathbf{r}_o + \boldsymbol{\rho}_1 = (r_o + x_1)\mathbf{e}_x + y_1\mathbf{e}_y \\
\mathbf{r_2} &= \mathbf{r}_o + \boldsymbol{\rho}_2 = (r_o + x_2)\mathbf{e}_x + y_2\mathbf{e}_y \\
\mathbf{r}_c &= \mathbf{r}_o + \boldsymbol{\rho}_c = (r_o + x_c)\mathbf{e}_x + y_c\mathbf{e}_y
\end{aligned} \tag{3.68}$$

where $\boldsymbol{\rho}_1, \boldsymbol{\rho}_2, \boldsymbol{\rho}_c$ are the position vectors in the orbital frame $\mathcal{F}_o$. $\mathbf{e}_x, \mathbf{e}_y$ are the unit vectors of the x-axis and y-axis in $\mathcal{F}_o$.

Accordingly, the motion of the tug, target, and connection are obtained as,

$$\frac{d^2}{dt^2}\mathbf{r_1} = \frac{d^2}{dt^2}\mathbf{r}_o + \frac{d^2}{dt^2}\boldsymbol{\rho}_1 = \left(\mathbf{G_1} + \mathbf{F} + \mathbf{T}_1\right)/m_1$$
$$\frac{d^2}{dt^2}\mathbf{r_2} = \frac{d^2}{dt^2}\mathbf{r}_o + \frac{d^2}{dt^2}\boldsymbol{\rho}_2 = \left(\mathbf{G_2} - \mathbf{T}_{21} - \mathbf{T}_{22}\right)\Big/m_2 \tag{3.69}$$
$$\frac{d^2}{dt^2}\mathbf{r}_c = \frac{d^2}{dt^2}\mathbf{r}_o + \frac{d^2}{dt^2}\boldsymbol{\rho}_c = \left(\mathbf{G}_c + \mathbf{T}_{21} + \mathbf{T}_{22} - \mathbf{T}_1\right)\Big/m_c$$

where $\mathbf{T}_1$ denotes the tether tension in the main tether. $\mathbf{T}_{21}$ and $\mathbf{T}_{22}$ denote the tether tensions in the tether CP_{21} and CP_{22} of the triangle connection, respectively. $\mathbf{G}_s$, $s = 1, 2, c$, is the gravitational force of each body from Earth, which could be calculated as follows,

$$\mathbf{G}_s = -\frac{\mu m_s}{r_s^3}\mathbf{r}_s \approx -\frac{\mu m_s}{r_0^2}[(1-2x_s/\mathrm{r}_o)\mathbf{e}_x + (y_s/\mathrm{r}_o)\mathbf{e}_y]$$
$$= -\frac{\mu m_s}{\mathrm{r}_o^3}\mathbf{r}_o - \frac{\mu m_s}{r_o^2}[(-2x_s/\mathrm{r}_o)\mathbf{e}_x + (y_s/\mathrm{r}_o)\mathbf{e}_y] \tag{3.70}$$

Combing Eqs.(3.69) and (3.70), the following differential equations can be derived,

$$\frac{d^2}{dt^2}\boldsymbol{\rho_1} = -\frac{\mu}{r_o^3}\left(-2x_1\mathbf{e}_x + y_1\mathbf{e}_y\right) + \frac{\mathbf{T}_1 + \mathbf{F}\left(m_2 + m_c\right)/m}{m_1}$$
$$\frac{d^2}{dt^2}\boldsymbol{\rho}_2 = -\frac{\mu}{r_o^3}\left(-2x_2\mathbf{e}_x + y_2\mathbf{e}_y\right) - \frac{\mathbf{T}_{21} + \mathbf{T}_{22} + \mathbf{F}m_2/m}{m_2} \tag{3.71}$$
$$\frac{d^2}{dt^2}\boldsymbol{\rho}_c = -\frac{\mu}{r_o^3}\left(-2x_c\mathbf{e}_x + y_c\mathbf{e}_y\right) + \frac{\mathbf{T}_{21} + \mathbf{T}_{22} - \mathbf{T}_1 - \mathbf{F}m_c/m}{m_c}$$

Next, the dynamic motions in rotating frame in relation with inertial frame are written as below,

$$\frac{d^2}{dt^2}\boldsymbol{\rho}_j = \ddot{\boldsymbol{\rho}}_j + \dot{\boldsymbol{\omega}}_{\mathbf{o}} \times \boldsymbol{\rho}_j + \boldsymbol{\omega}_{\mathbf{o}} \times \left(\boldsymbol{\omega}_{\mathbf{o}} \times \boldsymbol{\rho}_j\right) + 2\boldsymbol{\omega}_{\mathbf{o}} \times \dot{\boldsymbol{\rho}}_j \tag{3.72}$$

Thus, the relative motions in $\mathcal{F}_o$ can be obtained by substituting Eq.(3.71) into (3.72), such that,

$$\begin{bmatrix} \ddot{x}_1 \\ \ddot{y}_1 \end{bmatrix} = \begin{bmatrix} \alpha y_1 + 2\omega_o \dot{y}_1 + \omega_o{}^2 x_1\left(1+\dfrac{2}{w}\right) + \dfrac{\mathbf{T}_1 + \mathbf{F}\left(m_2+m_c\right)/\left(m_1+m_2+m_c\right)}{m_1}\mathbf{e}_x \\ -\alpha \mathrm{x}_1 - 2\omega_o \dot{x}_1 + \omega_o{}^2 y_1\left(1-\dfrac{1}{w}\right) + \dfrac{\mathbf{T}_1 + \mathbf{F}\left(m_2+m_c\right)/\left(m_1+m_2+m_c\right)}{m_1}\mathbf{e}_y \end{bmatrix} \tag{3.73}$$

$$\begin{bmatrix} \ddot{x}_2 \\ \ddot{y}_2 \end{bmatrix} = \begin{bmatrix} \alpha y_2 + 2\omega_o \dot{y}_2 + \omega_o{}^2 x_2\left(1+\dfrac{2}{w}\right) - \dfrac{\mathbf{T}_{21} + \mathbf{T}_{22} + \mathbf{F}m_2/\left(m_1+m_2+m_c\right)}{m_2}\mathbf{e}_x \\ -\alpha \mathrm{x}_2 - 2\omega_o \dot{x}_2 + \omega_o{}^2 y_2\left(1-\dfrac{1}{w}\right) - \dfrac{\mathbf{T}_{21} + \mathbf{T}_{22} + \mathbf{F}m_2/\left(m_1+m_2+m_c\right)}{m_2}\mathbf{e}_y \end{bmatrix} \tag{3.74}$$

$$\begin{bmatrix} \ddot{x}_c \\ \ddot{y}_c \end{bmatrix} = \begin{bmatrix} \alpha y_c + 2\omega_o \dot{y}_c + \omega_o{}^2 x_c\left(1+\dfrac{2}{w}\right) + \dfrac{\mathbf{T}_{21} + \mathbf{T}_{22} - \mathbf{T}_1 - \mathbf{F}m_c/\left(m_1+m_2+m_c\right)}{m_c}\mathbf{e}_x \\ -\alpha \mathrm{x}_c - 2\omega_o \dot{x}_c + \omega_o{}^2 y_c\left(1-\dfrac{1}{w}\right) + \dfrac{\mathbf{T}_{21} + \mathbf{T}_{22} - \mathbf{T}_1 - \mathbf{F}m_c/\left(m_1+m_2+m_c\right)}{m_c}\mathbf{e}_y \end{bmatrix}$$

(3.75)

where ω_o denotes the magnitude of the orbital angular velocity, α denotes the derivative of ω_o,

$$\begin{aligned} \boldsymbol{\omega}_o &\approx \omega_o\, \mathbf{e}_z = \frac{w^2}{p^2} h \mathbf{e}_z \\ \alpha &= \dot{\omega}_o = -2\left(e_1 \sin\lambda - e_1 \cos\lambda\right)\omega_o{}^2 / w \end{aligned} \tag{3.76}$$

Then, the attitude motions of the space tug and target can be obtained as,

$$\begin{bmatrix} \ddot{\theta}_1 \\ \ddot{\theta}_2 \end{bmatrix} = \begin{bmatrix} -\alpha + \left(\mathbf{P}_1 \times \mathbf{T}_1\right)/I_1 + M_c \\ -\alpha + \left(\mathbf{P}_{21} \times \mathbf{T}_{21} + \mathbf{P}_{22} \times \mathbf{T}_{22}\right)/I_2 \end{bmatrix} \tag{3.77}$$

where θ_1 and θ_2 denote the attitude angles of space tug and target, which are the rotation angle between body frame $\mathcal{F}_b$ and orbital frame $\mathcal{F}_o$. M_c is the control torque of the space tug. I_1 and I_2 are the principle axis inertial momentum of two body. $\mathbf{P}_1 = O_1P_1 \bullet \mathrm{R}\left(\theta_1\right)$, $\mathbf{P}_{21} = O_2P_{21} \bullet \mathrm{R}\left(\theta_2\right)$ and $\mathbf{P}_{22} = O_2P_{22} \bullet \mathrm{R}\left(\theta_2\right)$ are the level arm of each tether tension. $\mathrm{R}\left(*\right)$ represents the rotation matrix as below,

$$\mathrm{R}\left(*\right) = \begin{bmatrix} \cos\left(*\right) & -\sin\left(*\right) \\ \sin\left(*\right) & \cos\left(*\right) \end{bmatrix} \tag{3.78}$$

The tensions in the elastic tethers with material damping are calculated as,

$$\begin{aligned} &\mathbf{T}_{21,22} = T_{21,22}\,\mathbf{l}_{21,22}/l_{21,22} \\ &T_{21,22} = \begin{cases} c_k\left(l_{21,22} - l_{20}\right) + c_v \dot{l}_{21,22} & ,T_{21,22} > 0 \\ 0 & ,else \end{cases} \end{aligned} \tag{3.79}$$

where $T_{21,22}$ are the magnitudes of tether tension $\mathbf{T}_{21,22}$. $l_{21,22}$ are the magnitudes of tether length and $\mathrm{l}_{21,22}$ are the vectors of tether length, c_k and c_v denote the tether stiffness and material damping, respectively, and l_{20} is the original length of elastic tethers.

Chapter 4 Tension Control for Deployment and Retrieval

Summary: This chapter presents the tension control for underactuated tether deployment and retrieval. Frist, a unified control framework is presented for the purpose of precise and fast control for the nominal accurate known model. Then, a robust approach of sliding mode control plus fractional order approaching law is designed to reject the external disturbance for the tethered system under unknown perturbations. This chapter interpolates material from three published papers by the authors in Reference papers A, E, and F. All variable symbols in this chapter refer to definitions in Section 3.1.

4.1 Passivity-Based Control for Underactuated TSS

This section aims to address the underactuated TSS control problem to achieve the tether deployment/retrieval with suppressing the tether libration angle. The controller is designed to ensure the asymptotic stability of the closed-loop system with only the actuated states measurement. Besides, the underactuated states are regulated by the interconnection of the system's nonlinear coupling, see Figure 4.1.

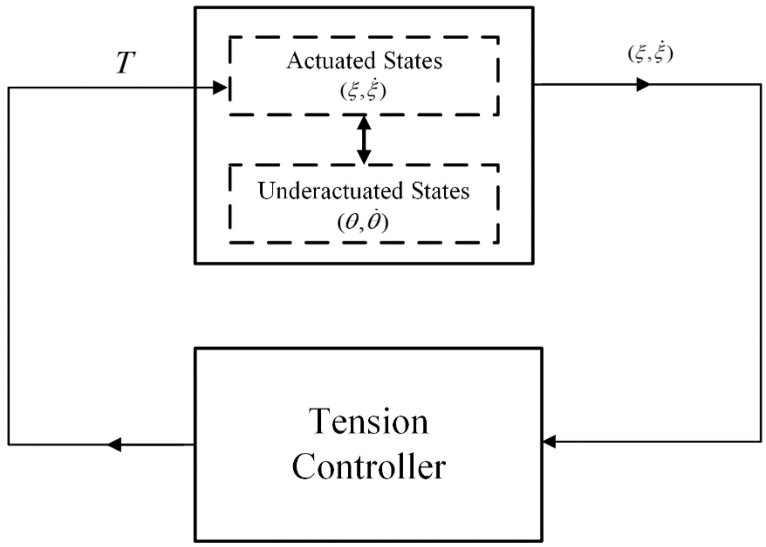

Figure 4.1 Block diagram of the TSS under tension control

4.1.1 Equilibrium and Controllability Analysis

TSS is with multiple equilibria which should be first determined for the stabilization the tether deployment/retrieval.

Recall Eq.(3.5) and set the first and second order derivatives to zero, then one has

$$\begin{pmatrix} -3\xi\cos^2\theta \\ \frac{3}{2}\xi^2\sin 2\theta \end{pmatrix} = \begin{pmatrix} -T \\ 0 \end{pmatrix} \tag{4.1}$$

Then, it is easy to obtain the equilibria as,

$$\theta = k\pi, \xi = \xi_e \text{ and } \theta = (k+1/2)\pi, \xi = \xi_e,\ k \in \mathbb{Z} \tag{4.2}$$

where ξ_e is tether length at equilibrium state. $T = 3\xi\cos^2\theta$ is the static balance force. The equilibria at $\theta = k\pi$ are stable, while the equilibria at $\theta = (k+1/2)\pi$ are not, which can be shown by the phase portraits of tethered system.

Fixing the tether length, the solution of the libration can be obtained as,

$$\ddot{\theta} + \frac{3}{2}\sin 2\theta = 0 \tag{4.3}$$

Integrate Eq.(4.3) with time,

$$\dot{\theta} = \pm\sqrt{(h - 3\sin^2\theta)} \tag{4.4}$$

where $h = \dot{\theta}^2 + 3\sin^2\theta$ is a metric of Hamiltonian of the pendular motion of the constant length of the tethered space system. We sketch the phase portraits of Eq.(4.3) in $\theta - \dot{\theta}$ plane with various Hamiltonian h, see Figure 4.2. The equilibria are periodical and isolated. The equilibria of the libration motion at $\theta = k\pi$ are the center points while the saddle points at $\theta = (k+1/2)\pi$. The libration motions periodically oscillate around zero, which is within $\pi/2$ when $3 > h \geq 0$. It indicates that the TSS does not flip over. Otherwise, the libration motion of TSS flips over when $h \geq 3$. $h = 3$ is the boundary of starting to flip over.

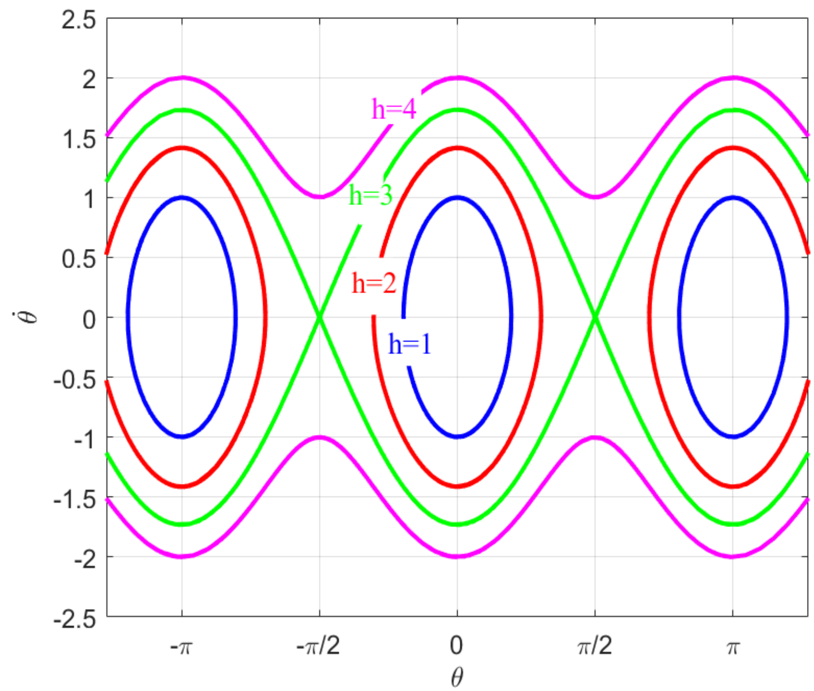

Figure 4.2 Phase portraits of TSS's libration

To test the controllability TSS, Eq.(3.6) is written into the state space form,

$$\frac{\mathrm{d}}{\mathrm{d}\tau}\begin{bmatrix}\mathbf{x}\\ \dot{\mathbf{x}}\end{bmatrix}=\begin{bmatrix}\dot{\mathbf{x}}\\ -\mathbf{M}^{-1}(\mathbf{x})[\mathbf{C}(\mathbf{x},\dot{\mathbf{x}})\dot{\mathbf{x}}+\mathbf{G}(\mathbf{x})]+\begin{bmatrix}-T\\ 0\end{bmatrix}\end{bmatrix} \tag{4.5}$$

Define $\delta\mathbf{x}=\mathbf{x}-\mathbf{x_e}$, $\delta\dot{\mathbf{x}}=\dot{\mathbf{x}}-\dot{\mathbf{x}}_\mathbf{e}$, and $\delta T=-T+3\xi_e$. Linearizing Eq. (4.5) at the equilibria $\{\mathbf{x}_\mathbf{e}^T,\dot{\mathbf{x}}_\mathbf{e}^T\}=\{\xi_e,k\pi,0,0\}$ yields,

$$\frac{\mathrm{d}}{\mathrm{d}\tau}\begin{Bmatrix}\delta\mathbf{x}\\ \delta\dot{\mathbf{x}}\end{Bmatrix}=\mathbf{A}\begin{Bmatrix}\delta\mathbf{x}\\ \delta\dot{\mathbf{x}}\end{Bmatrix}+\mathbf{B}\delta T \tag{4.6}$$

where,

$$\mathbf{A}=\begin{bmatrix}0 & 0 & 1 & 0\\ 0 & 0 & 0 & 1\\ 3 & 0 & 0 & 2\xi_e\\ 0 & -3 & -\dfrac{2}{\xi_e} & 0\end{bmatrix} \text{ and } \mathbf{B}=\begin{bmatrix}0\\0\\1\\0\end{bmatrix}$$

Then, one can obtain the controllability matrix as,

$$\mathbf{Co}=\begin{bmatrix}\mathbf{B} & \mathbf{AB} & \mathbf{A}^2\mathbf{B} & \mathbf{A}^3\mathbf{B}\end{bmatrix}=\begin{bmatrix}0 & 1 & 0 & -1\\ 0 & 0 & -\dfrac{2}{\xi_e} & 0\\ 1 & 0 & -1 & 0\\ 0 & -\dfrac{2}{\xi_e} & 0 & \dfrac{8}{\xi_e}\end{bmatrix} \tag{4.7}$$

Thus, it is easy to verify $\operatorname{Rank}(C)=4$. Thus, under only tension input, the deployment/retrieval of TSS is controllable.

4.1.2 Controller Design and Stability Analysis

To achieve the regulation of the underactuated TSS, Energy shaping methodology will be adopted. The basic prerequisite for energy shaping is to construct an artificial potential energy function that makes the closed-loop system's total potential energy to be the minimums at the desired equilibria. Furthermore, to achieve the asymptotic stability, a damping term should be injected to dissipate the total energy of system towards the minimums.

A unified framework of the passivity-based controller in Figure 4.3 is proposed as,

$$T = T_a + T_d \tag{4.8}$$

where $T_a = \dfrac{\partial U_a}{\partial \xi}$ is the force corresponds to potential energy shaping part, and $T_d = \partial\Phi(\dot{\xi})/\partial\dot{\xi}$ represents the dissipation to stabilize the TSS. $U_a = U_s + U_r$ is the constructed artificial potential energy function.

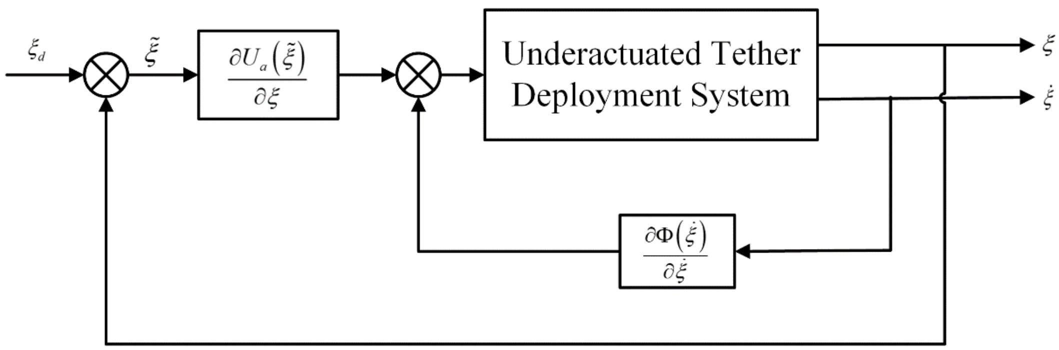

Figure 4.3 Block diagram of the tension controller

The artificial potential energy function $U_a(\xi)$ is defined as,

$$U_a = U_r + U_s \tag{4.9}$$

where $U_r := f_r(\xi)$ is a positive definite energy function and $U_s := f_s(\xi)$ is a quasi-potential energy function. These two energy functions are required to satisfy two following conditions,

$$\arg_{\theta}\left[\min(U_s - U_0)\right] = k\pi \quad (k \in \mathbb{Z}) \tag{4.10}$$

$$\arg_{\xi}\left[\min\left(U_a - U_0\big|_{\theta=k\pi}\right)\right] = \xi_d \tag{4.11}$$

where U_0 is defined in Eq. (3.7) and $\xi_d \subseteq \xi_e$ is the desired tether length at the equilibria.

It is obvious that the potential energy U_0 is related to the tether tension T_0 at the equilibrium,

$$T_0 = \frac{\partial U_0}{\partial \xi} \tag{4.12}$$

Moreover, the tension in Eq.(4.8) should equal T_0, at the desired equilibrium states of TSS $(\xi, \theta, \dot{\xi}, \dot{\theta}) = (\xi_d, k\pi, 0, 0)$. Thus, this equilibrium condition is equivalent to the extreme condition, subject to the following condition

$$\frac{\partial (U_a - U_0)}{\partial \xi} = 0 \quad iff\ \xi = \xi_d \text{ and } \theta = k\pi \tag{4.13}$$

Finally, the dissipation function $\Phi(\dot{\lambda})$ in Eq.(4.8) is constructed with the conditions of $\frac{\partial \Phi}{\partial \dot{\xi}}\Big|_{\dot{\xi}=0} = 0$ and $\dot{\xi}\frac{\partial \Phi}{\partial \dot{\xi}} > 0, \forall \dot{\xi} \neq 0$ to achieve an asymptotically stable of tether deployment/retrieval.

Theorem 1. The closed-loop TSS Eq.(3.6) under the proposed unified framework controller Eq. (4.8) will asymptotically stabilize to the desired equilibria, $(\xi, \dot{\xi}, \theta, \dot{\theta}) = (\xi_d, k\pi, 0, 0)$.

To prove the asymptotic stability of the closed-loop system, a Lyapunov function candidate is defined as follows,

$$V = H + U_a = \frac{1}{2}\dot{x}^T M\dot{x} + U_t \tag{4.14}$$

which is bounded form below because the potential energy U_t is lower bounded and the kinetic energy $\frac{1}{2}\dot{x}^T M\dot{x}$ is global positive definite. Then, taking the derivative of the Lyapunov function V yields,

$$\dot{V} = \dot{H} + \dot{U}_a = -\dot{\xi}T + \frac{\partial U_a}{\partial \xi}\dot{\xi} = -\dot{\xi}\frac{\partial \Phi}{\partial \dot{\xi}} \leq 0 \tag{4.15}$$

It is obvious that $V \leq V(0)$, $V \in \mathcal{L}_\infty$ because the $\dot{V}$ is semi-negative definite due to the definition of $\Phi(\dot{\xi})$. One has $\dot{V} = 0$ only when $\dot{\xi} = 0$. Thus, the closed-loop system is stable in the sense of Lyapunov.

Due to $V \in \mathcal{L}_\infty$, one has,

$$\xi, \dot{\xi}, \dot{\theta} \in \mathcal{L}_\infty \tag{4.16}$$

However, one cannot get the $\theta \in \mathcal{L}_\infty$ because the state θ in V is a trigonometric function ($U_0(x) = -\frac{3}{2}\xi^2 \cos^2\theta$). Thus, the LaSalle's Invariance Principle is not directly possible to use. To circumvent such difficulty, new variables are introduced as,

$$y=\begin{pmatrix}\xi\\ \dot{\xi}\\ \cos\theta\\ \sin\theta\\ \dot{\theta}\end{pmatrix}=\begin{pmatrix}y_1\\ y_2\\ y_3\\ y_4\\ y_5\end{pmatrix} \tag{4.17}$$

Eq. (3.6) of TSS's motion is rewritten as,

$$\begin{aligned}
&\dot{y}_1 = y_2\\
&\dot{y}_3 = -y_4 y_5\\
&\dot{y}_4 = y_3 y_5\\
&\begin{pmatrix}\dot{y}_2\\ \dot{y}_5\end{pmatrix}=\begin{pmatrix}1 & 0\\ 0 & y_1^2\end{pmatrix}^{-1}\left\{\begin{bmatrix}0 & y_1\left(y_5+2\right)\\ -y_1\left(y_5+2\right) & -y_1 y_2\end{bmatrix}\begin{pmatrix}y_2\\ y_5\end{pmatrix}+\begin{pmatrix}3y_1 y_3^2-T\\ 3y_1^2 y_3 y_4\end{pmatrix}\right\}
\end{aligned} \tag{4.18}$$

The Hamiltonian function can be represented as

$$H=\frac{1}{2}\begin{pmatrix}y_2\\ y_5\end{pmatrix}^{\mathrm{T}}\begin{pmatrix}1 & 0\\ 0 & y_1^2\end{pmatrix}\begin{pmatrix}y_2\\ y_5\end{pmatrix}-\frac{3}{2}y_1^2 y_3^2 \tag{4.19}$$

Then, representing the Lyapunov function candidate V respect to y yields,

$$V=H+U_a=\frac{1}{2}\begin{pmatrix}y_2\\ y_5\end{pmatrix}^{\mathrm{T}}\begin{pmatrix}1 & 0\\ 0 & y_1^2\end{pmatrix}\begin{pmatrix}y_2\\ y_5\end{pmatrix}-\frac{3}{2}y_1^2 y_3^2+U_a \tag{4.20}$$

Take the derivative of the Lyapunov function V,

$$\dot{V}=\dot{H}+\dot{U}_a=-T\dot{y}_1+\frac{\partial U_a}{\partial y_1}\dot{y}_1 \tag{4.21}$$

Recalling the tension controller in Eq.(4.8), one has

$$T = \frac{\partial U_a}{\partial y_1} + \frac{\partial \Phi}{\partial \dot{y}_1} \dot{y}_1 \tag{4.22}$$

Substitute the Eq.(4.22) into Eq.(4.21),

$$\dot{V} = -\frac{\partial \Phi}{\partial \dot{y}_1} \dot{y}_1 \leq 0 \tag{4.23}$$

Thus, V decreases monotonically and y_1, y_2, y_3, y_4, y_5 are all bounded. $\dot{V} = 0$ only if $\dot{y}_1 = y_2 \equiv 0$ which implies $y_1 \equiv c_1$, where c_1 is a positive constant.

Recalling the Eq.(4.21), one can obtain that $\dot{H} \equiv 0$ and H is constant. Therefore, the fourth formula of Eq.(4.18) and Eq.(4.19) become

$$y_1^2(y_5^2 - 3y_3^2) \equiv c_2 \tag{4.24}$$

$$y_1(y_5^2 + 2y_5 + 3y_3^2) = T \equiv c_3 \tag{4.25}$$

where $T \equiv c_3$ is obtained from Eq.(4.22), U_a is constant when $y_1 \equiv c_1$, and c_2, c_3 are constant. Thus, one has,

$$y_5{}^2 + y_5 = c_4 \equiv (c_3 c_1 - c_2)/(2c_1^2) \tag{4.26}$$

where c_4 is constant. Hence, y_5 is constant due to y_5 is the solution of the Eq.(4.26). Then,

$$\dot{y}_5 \equiv 0 \tag{4.27}$$

Introducing $y_2 \equiv 0$ and $y_5 \equiv 0$ into the last equation of Eq. (4.18), one can obtain,

$$y_3 y_4 \equiv 0 \tag{4.28}$$

Equation (4.28) has two solutions: $(y_3, y_4) = (0, \pm 1)$ and $(y_3, y_4) = (\pm 1, 0)$ due to $y_3^2 + y_4^2 = 1$. Substituting the solutions into of Eq.(4.18) leads to $y_5 = c_5 = 0$.

Define the set Ω as

$$\Omega = \left\{ \mathbf{y} \in \mathbb{R}^5 \mid V(\mathbf{y})\big|_{t=t_0} \geq V(\mathbf{y}), y_3^2 + y_4^2 = 1 \right\} \tag{4.29}$$

and $W = \left\{ \mathbf{y} \in \mathbb{R}^5 \mid \dot{V} = 0 \right\}$ as the largest invariant set contained in Ω. Thus, W contains two cases:

Case 1: $$(y_1, y_2, y_3, y_4, y_5) = (c_1^h, 0, 0, \pm 1, 0) \tag{4.30}$$

Case 2: $$(y_1, y_2, y_3, y_4, y_5) = (c_1^v, 0, \pm 1, 0, 0) \tag{4.31}$$

where the tether length $y_1 = c_1^h$ corresponds to $(y_3, y_4) = (\pm 1, 0)$ at the local horizontal direction ($\sin\theta = \pm 1$) and the tether length $y_1 = c_1^v$ corresponds to $(y_3, y_4) = (0, \pm 1)$ at the local vertical direction ($\cos\theta = \pm 1$).

The horizontal equilibrium states $(y_1, y_2, y_3, y_4, y_5) = (c_1^h, 0, 0, 1, 0)$ and $(y_1, y_2, y_3, y_4, y_5) = (c_1^h, 0, 0, -1, 0)$ are unstable. Considering any small perturbation of $\varepsilon \neq 0$ on y_3, from Eq.(4.20), there exists $(y_1, y_2, y_3, y_4, y_5) = (c_1^h, 0, \varepsilon, \sqrt{1-\varepsilon^2}, 0)$ and $V_\varepsilon = -\frac{3}{2}(c_1^h)^2 \varepsilon^2 + U_a(c_1^h) < U_a(c_1^h)$. As V is non-increasing, the trajectory of system will move away from $(y_1, y_2, y_3, y_4, y_5) = (c_1^h, 0, 0, 1, 0)$. Thus, this equilibrium is unstable. Similarly, the other equilibrium $(y_1, y_2, y_3, y_4, y_5) = (c_1^h, 0, 0, -1, 0)$ is unstable.

The vertical equilibrium states $(y_1, y_2, y_3, y_4, y_5) = (c_1^v, 0, 1, 0, 0)$ and $(y_1, y_2, y_3, y_4, y_5) = (c_1^v, 0, -1, 0, 0)$ are stable. Note that $\mathcal{U}$ denote the union of two vertical equilibriums set $\mathcal{U}_+ = \{y \mid y = (c_1^v, 0, 1, 0, 0)\}$ and $\mathcal{U}_- = \{y \mid y = (c_1^v, 0, -1, 0, 0)\}$. Obviously, $V = -\frac{3}{2}(c_1^v)^2 y_3^2 + U_a(c_1^v)$ has the minimums only if $y_3^2 = 1$. Therefore, the states in the neighborhood of $\mathcal{U}_+$ will converge to $\mathcal{U}_+$. This implies the states in $\mathcal{U}_+$ are locally asymptotically stable. Similarly, the states in the neighborhood of $\mathcal{U}_-$ will converge to $\mathcal{U}_-$. Consequently, we can denote the stable solution set as $\mathcal{U} = \left\{\mathbf{y} \in \Omega \middle| \dot{V} = 0, y_3^2 = 1\right\}$, and the largest invariant set W will asymptotically converge to $\mathcal{U}$.

Additionally, solutions in $\mathcal{U}$ are required to satisfy Eq.(4.11), such that,

$$\frac{\partial(U_r + U_s - U_0|_{\theta=k\pi})}{\partial y_1} = 0, \quad \frac{\partial^2(U_r + U_s - U_0|_{\theta=k\pi})}{\partial {y_1}^2} > 0 \quad iff \quad y_1 = \xi_d \tag{4.32}$$

Obviously, there must exist $y_1 = \xi_d = c_1$, and the stable solution set can be expressed as $\mathcal{U}=\left\{\mathbf{y}\in\Omega \middle| (y_1,y_2,y_3,y_4,y_5)=(\xi_d,0,\pm1,0,0)\right\}$. Based on the LaSalle's Invariance Principle, the trajectory of the closed-loop system in Eq. (3.6) will approach to the largest invariant set W as $t\to\infty$, and asymptotically converge to $\mathcal{U}$. We complete the proof of the Theorem 1.

4.1.3 Construction of Controllers

Based on the unified framework of controller, we can construct distinct types of controllers. For instance, four types of controller are given as follows,

1. Linear PD with gravity compensation (LPDgc),

$$T_1 = 3\xi + k_{p1}\tilde{\xi} + k_{v1}\dot{\xi}\,,\ k_{p1} > 0, k_{v1} > 0 \tag{4.33}$$

2. Linear PD with desired gravity compensation (LPDdgc),

$$T_2 = 3\xi_d + k_{p2}\tilde{\xi} + k_{v2}\dot{\xi}\,,\ k_{p2} > 3, k_{v2} > 0 \tag{4.34}$$

3. Trigonometric PD with gravity compensation (TPD),

$$T_3 = 3\xi + k_{p3}\arctan(\tilde{\xi}) + k_{v3}\arctan(\dot{\xi})\,,\ k_{p3} > 0, k_{v3} > 0 \tag{4.35}$$

4. Hyperbolic PD with gravity compensation (HPD),

$$T_4 = 3\xi + k_{p4}\tanh(\tilde{\xi}) + k_{v4}\tanh(\dot{\xi})\,,\ k_{p4} > 0, k_{v4} > 0 \tag{4.36}$$

The corresponding the potential energy functions are listed,

$$U_{t1} = -\frac{3}{2}\xi^2 \cos^2\theta + \frac{3}{2}\xi^2 + \frac{1}{2}k_{p1}\tilde{\xi}^2 \tag{4.37}$$

$$U_{t2} = -\frac{3}{2}\xi^2 \cos^2\theta + \frac{3}{2}\xi_d^2 + 3\xi_d\tilde{\xi} + \frac{1}{2}k_{p2}\tilde{\xi}^2 \tag{4.38}$$

$$U_{t3} = -\frac{3}{2}\xi^2 \cos^2\theta + \frac{3}{2}\xi^2 + k_{p3}[\tilde{\xi}\arctan(\tilde{\xi}) - \frac{1}{2}\ln(1+\tilde{\xi}^2)] \tag{4.39}$$

$$U_{t4} = -\frac{3}{2}\xi^2 \cos^2\theta + \frac{3}{2}\xi^2 + k_{p4}\ln(\cosh\tilde{\xi}) \tag{4.40}$$

These total potential energy functions are illustrated in Figure 4.4 with the $\xi_d = 1$ and $k_{p1} = k_{p2} = k_{p3} = k_{p4} = 8$. As is clear from Figure 4.4, they have similar trends and the isolated minimums ($\min(U_t) = 0$), which are denoted by the red spots. ξ

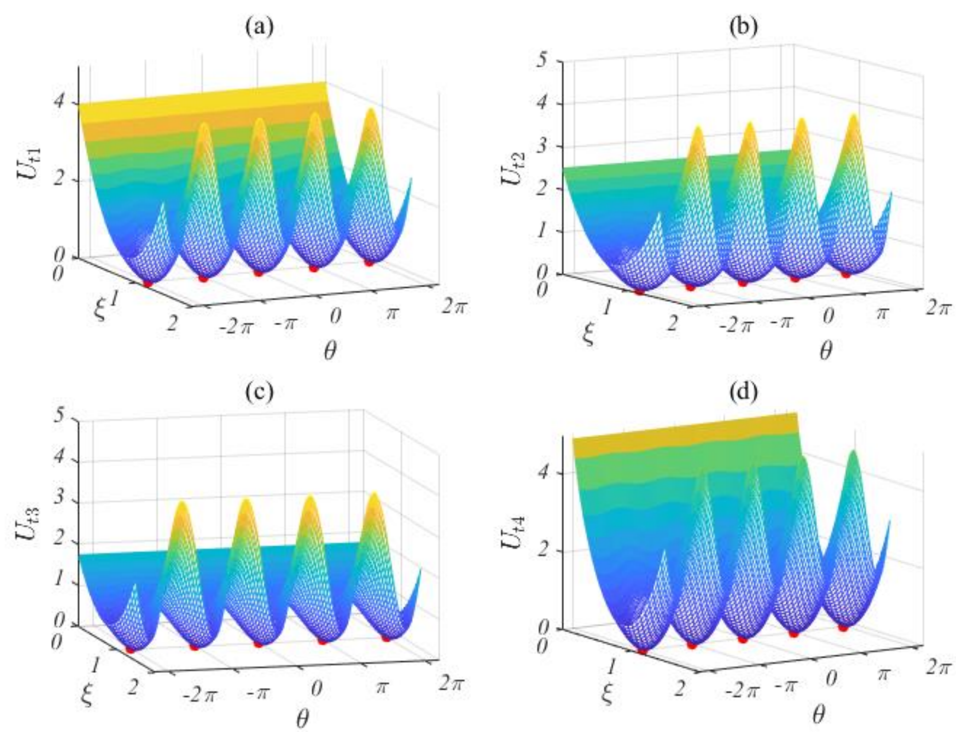

Figure 4.4 The potential energy functions

Remark 1: The term $3\xi = \partial U_s / \partial \xi$ in the controller 1, 3 and 4 comes from the quasi-potential energy U_s. It is to compensate the static balance force at $\theta = k\pi, \dot{\theta} = 0$. To dominate the static balance force at $\theta = k\pi, \dot{\theta} = 0$ and $\xi = \xi_d$, one can replace 3ξ by $3\xi_d$. As a result, the parameter k_p in potential function must satisfy $k_p > 3$.

Remark 2: Although only four controllers are presented, it is easy to construct other types of tension controller with the proposed unified framework in Eq.(4.8), where the asymptotic stability will be guaranteed by Theorem 1.

4.1.4 Simulations and Discussion

4.1.4.1 Validation of Different Controllers

To demonstrate the effectiveness of the proposed unified framework of tension controller, both tether deployment and retrieval process will be verified by numerical simulations.

First, the tether deployment process is carried on with the initial state $(\xi_0, \dot{\xi}_0, \theta_0, \dot{\theta}_0) = (0.01, 0.5, 0, 0)$ and the desired state $(\xi_d, \dot{\xi}_d, \theta_d, \dot{\theta}_d) = (1, 0, 0, 0)$.

The gains of the controllers are given in Table 4.1. The simulation results are drawn in Figure 4.5. All controllers successfully achieve the tether deployment to desired position with asymptotic stability and they perform remarkably similar performances.

Table 4.1 Controller gains

Controller	k_p	k_v
LPDgc	2	4
LPDdgc	4	4
TPD	2	4
HPD	2	4.5

It can be seen in Figure 4.5, all states converge to the desired position. Figure 4.5 (a) shows that all controllers achieve the deployment to the desired length within 1.5 orbits very quickly. However, settling time of each controller is different, which are 0.66, 0.74, 1.11, and 1.25 orbits for the LPDgc, HPD, TPD, and LPDdgc controller, respectively. The LPDgc is with a minor overshoot of tether length during deployment. LPDdgc controller with a bigger gain on the linear feedback of tether length error slows down the tether deployment, which avoid that small overshooting. Nonlinear feedback controller, HPD and TPD, achieve a slightly better performance than LPDdgc without overshooting. Tether deployment velocity are plotted in Figure 4.5 (b). They are all smooth and satisfy the positive constraint apart from LPDgc. As shown in Figure 4.5 (c), libration angles are similar with the maximum magnitude smaller than 0.88 rad. The tether librates a negative angle due to the action of Coriolis force at the beginning, and finally converge to 0 rad. This is because that the Coriolis force decreases and the gravity force increases as the tether deployment. Figure 4.5 (d) shows the angular velocities of tether libration, which finally converge to zero with the tether deployment. Tether tension are given in the Figure 4.6. They are continuous and smooth, and satisfy the positive tension constraint during the deployment. Finally, tether tensions asymptotically converge to the static balance force $T_0 = 3$. In short, simulation results show all proposed controllers based on the unified framework effectively achieve the deployment of TSS.

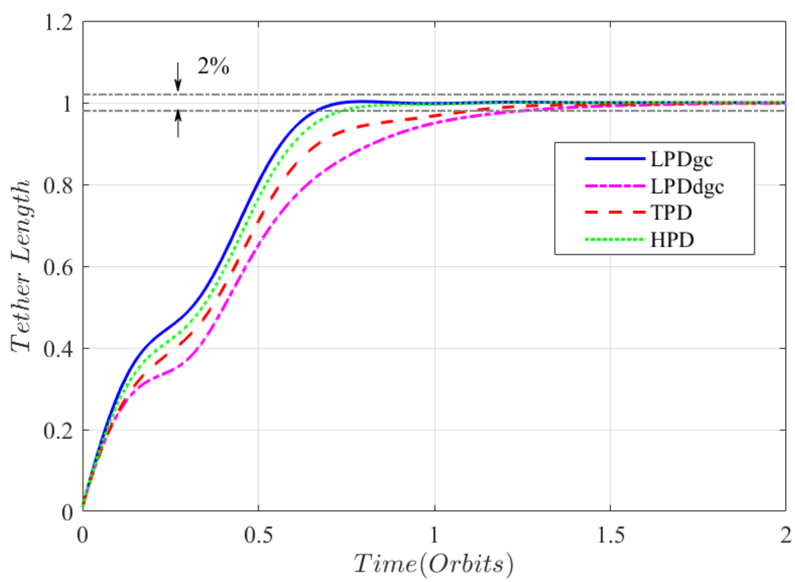

(a)

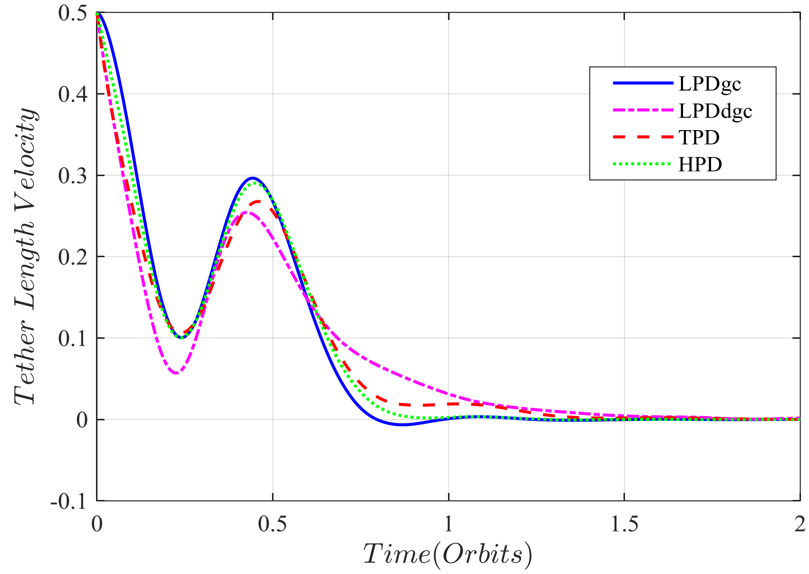
LPDgc
LPDdgc
TPD
HPD
Tether Length Velocity
Time(Orbits)

(b)

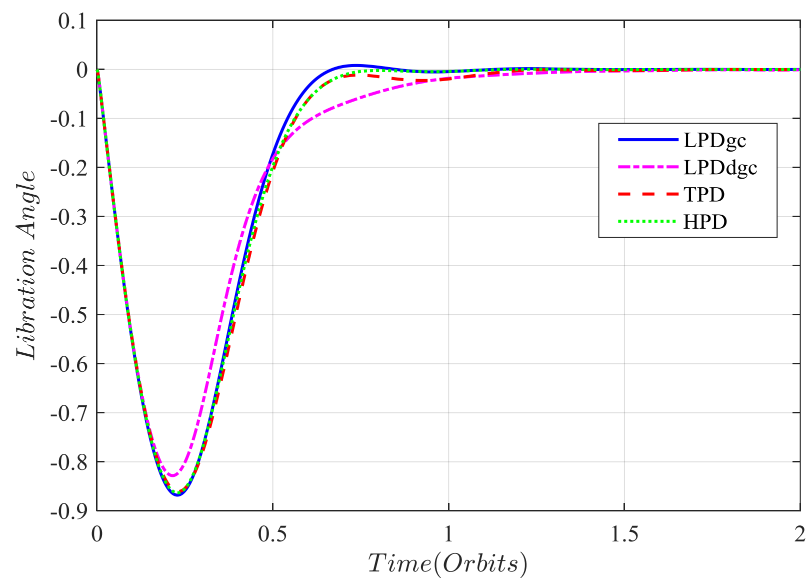
LPDgc
LPDdgc
TPD
HPD
Libration Angle
Time(Orbits)

(c)

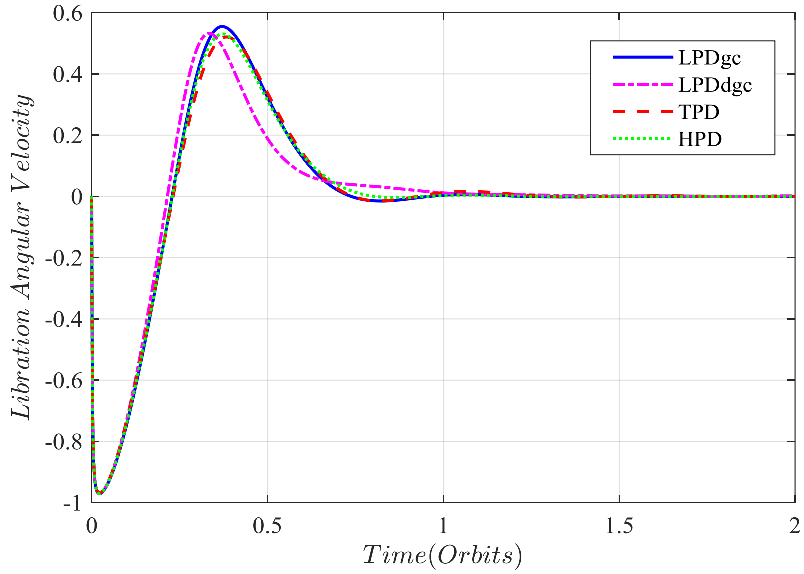

(d)

Figure 4.5 Time histories of states during deployment

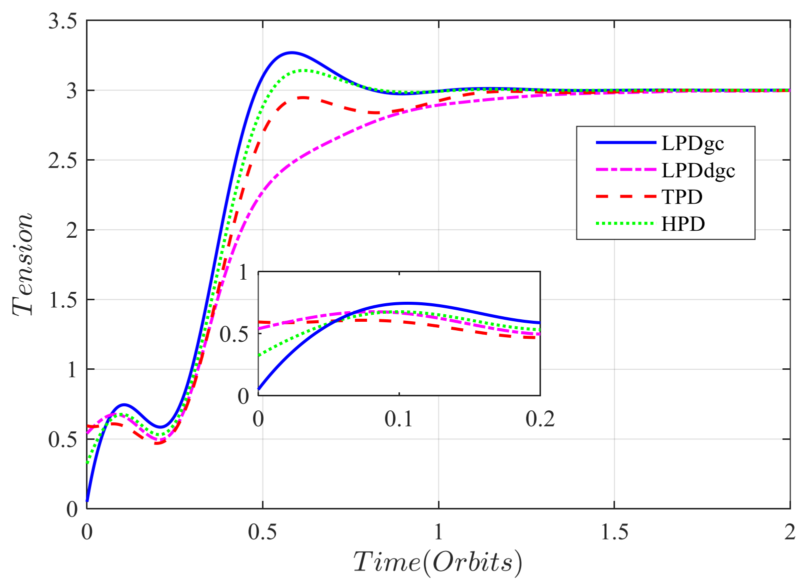

Figure 4.6 Tether tensions during deployment.

Next, the tether retrieval process is simulated with the initial condition $(\xi_0, \dot{\xi}_0, \theta_0, \dot{\theta}_0) = (1, 0, 0, 0)$ and the desired state $(\xi_d, \dot{\xi}_d, \theta_d, \dot{\theta}_d) = (0.01, 0, 0, 0)$. Here, for sake of briefness, only controller 1 (LPDgc) and 2 (LPDdgc) are used in the retrieval process. The control gains are chosen as $\left(k_p, k_v\right) = (1, 4)$ and $\left(k_p, k_v\right) = (4.5, 4)$ for controllers 1 and 2, respectively. The results of the tether length and libration angle are presented in Figure 4.7 and Figure 4.8. Figure 4.7 indicates the tether is successfully retrieved while the tether libration angle is effectively suppressed by both two controllers. However, the positive tether libration angle is found during retrieval while negative for deployment. This is because the direction of Coriolis force in retrieval is opposite to the one in deployment. As shown in Figure 4.9, the tether tension is always positive during entire retrieval process.

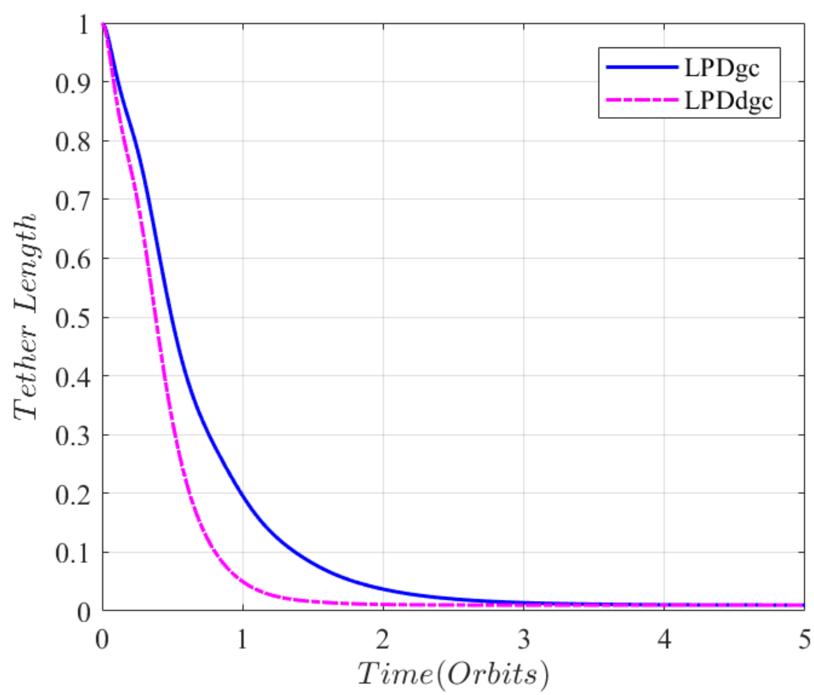

Figure 4.7 Tether length during retrieval

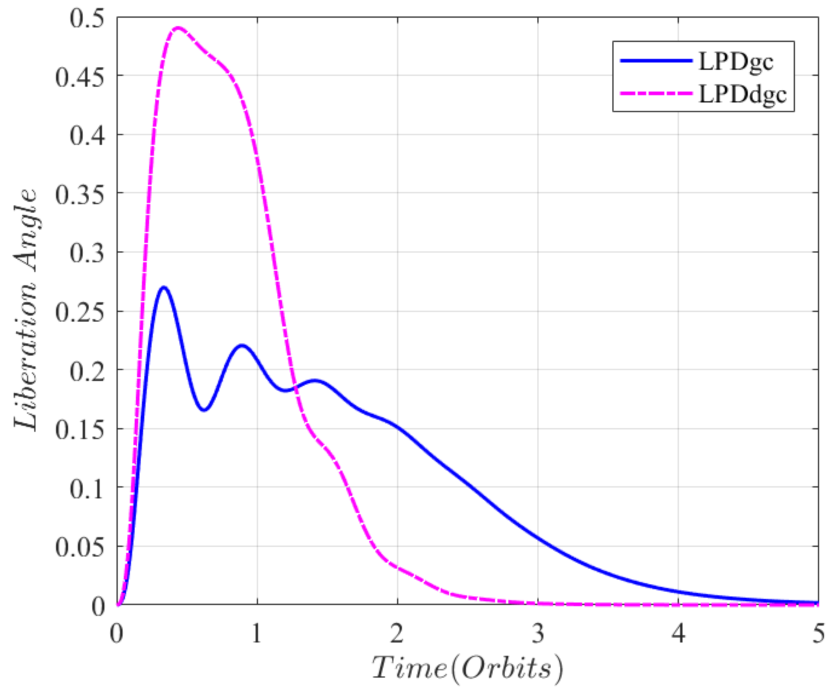

Figure 4.8 Libration angle during retrieval

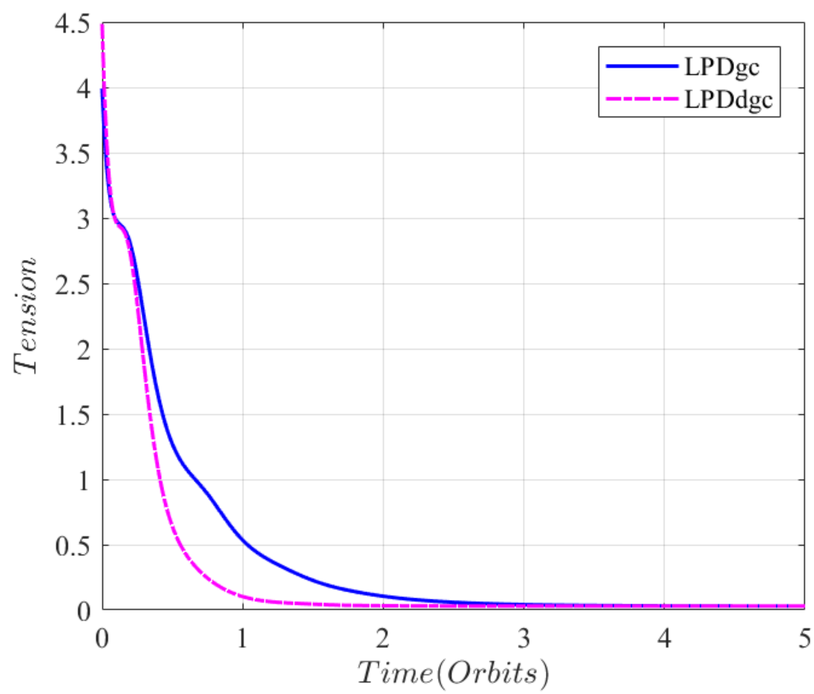

Figure 4.9 Tether tension during retrieval

As shown in the simulation results of deployment and retrieval, the proposed controllers perform the asymptotic stability, which agrees with the theoretical analysis.

4.1.4.2 Initial Condition Uncertainties

To guarantee the performance and safety of practical situation, the uncertainties of TSS's initial condition should be analyzed. For instance, only the LPDdgc is used to demonstrate the controller's robust. A wide range of initial conditions, $\xi_0 = 0.01$, $\dot{\xi}_0 \in [0, 8]$, $\theta_0 \in [-\pi/2, \pi/2]$, $\dot{\theta}_0 \in [-2, 2]$ are considered to study the convergence of controllers and estimate the region of attraction. In total, there exist 136161 initial conditions as follows,

$$\begin{array}{ll} \xi_0 = 0.01 & \dot{\xi}_0 = 0.1(a-1) \\ \theta_0 = -\dfrac{\pi}{2} + \dfrac{\pi}{40}(b-1) & \dot{\theta}_0 = -2 + 0.1(c-1) \end{array} \tag{4.41}$$

where $a = 1 \sim 81$, $b = 1 \sim 41$, $c = 1 \sim 41$ and the control gains LPDdgc controller are $k_{p2} = 5, k_{v2} = 4$ for numerical simulations in ten orbits.

The final tether length and libration angle are plotted in Figure 4.10, where each circle represent one initial condition. For all of the different initial conditions, the final results converge to the vertical equilibria, $\theta = k\pi, k \in \mathbb{Z}$, $\xi_d = 1$. In the practical space missions, the allowable operation point is usually at the LVLH $(\xi_d, \dot{\xi}_d, \theta_d, \dot{\theta}_d) = (1,0,0,0)$, and the maximum tether libration less is smaller than $\pi/2$ to prevent TSS from flipping over. To this end, the region of attraction to the allowable equilibrium is estimated with the contraction the set of the initial condition. The obtained initial conditions are $\xi_0 = 0.01$, $\dot{\xi}_0 \in [0, 1.7]$, $\theta_0 \in [-\pi/20, 19\pi/40]$ and $\dot{\theta}_0 \in [-2, 1.2]$, and the distribution final lengthen and maximum tether libration are depicted in Figure 4.11. All initial conditions of the above set converge to $(\xi_d, \dot{\xi}_d, \theta_d, \dot{\theta}_d) = (1,0,0,0)$ with the maximum tether libration smaller than $\pi/2$.

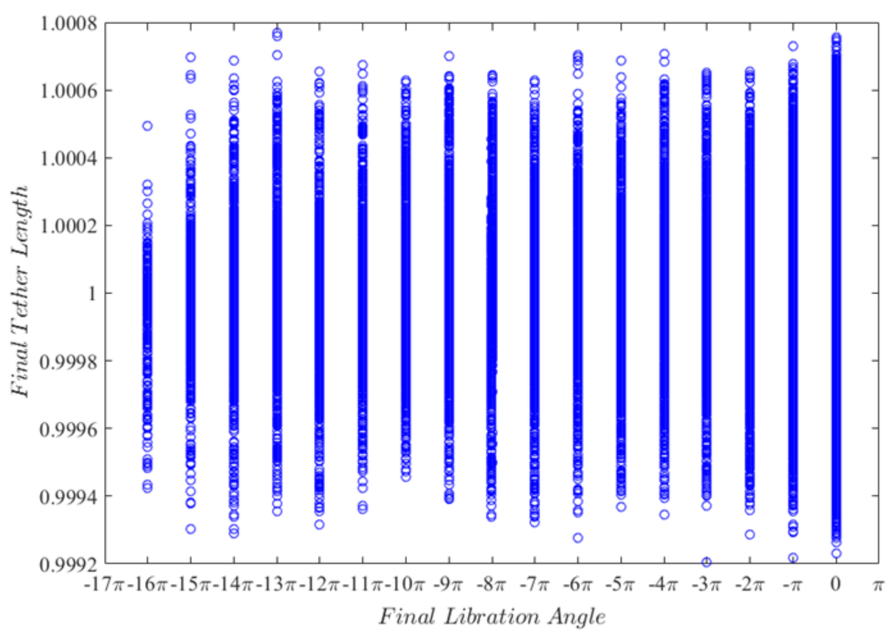

Figure 4.10 Final tether lengths and libration angles

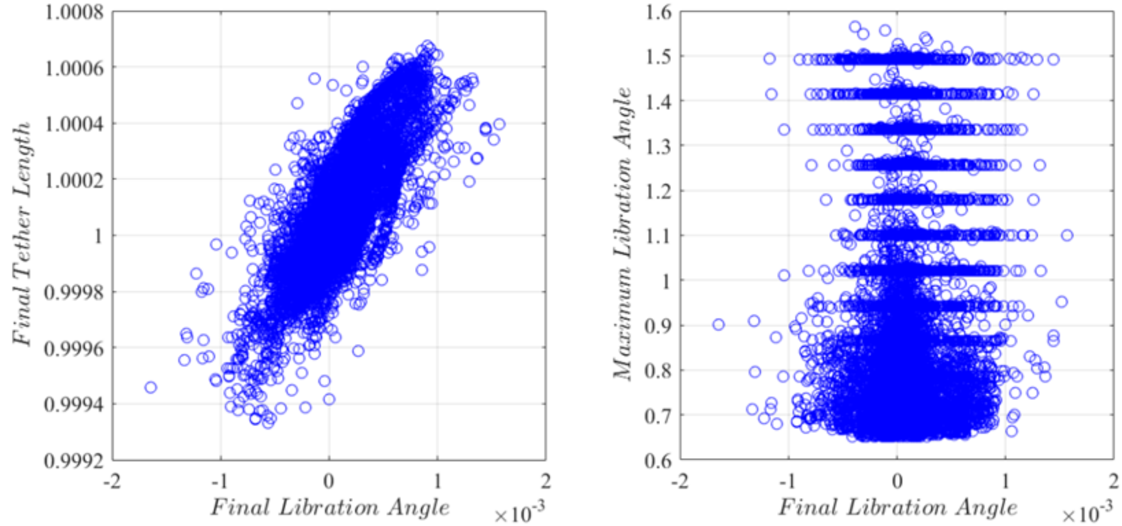

Figure 4.11 Distribution of final tether length, libration angle, and maximum libration angle

4.1.4.3 Positive Constraints on Tether Tension and Velocity

In most of space tether missions, the passive tether deployment mechanism is adopted, which leads to two constraints as following,

$$T \geq 0 \text{ and } \dot{\xi} \geq 0 \tag{4.42}$$

As one way to enforce these constraints, the parameters of the tension controllers are tuned with optimization algorithm. A cost function is given as follows,

$$I = \int_0^{t_f} \tau[a(\xi - \xi_d)^2 + b\theta^2]d\tau \tag{4.43}$$

where a, b are the adjustable weights and t_f is final time of optimization.

The optimization problem for parameters becomes

$$\begin{gathered} \text{Minimize} : I \\ \text{Subject to} : T \geq 0 \,, \dot{\xi} \geq 0 \end{gathered} \tag{4.44}$$

Here, we will show how to obtain better performance by tuning the control gains with Genetic Algorithm. For instance, the LPDdgc controller is used with an initial guess of gains at $(k_p, k_v) = (5,4)$. The initial condition of system starts at $(\xi_0, \dot{\xi}_0, \theta_0, \dot{\theta}_0) = (0.01, 0.7, 0, 0)$. Three acceptable errors are considered as:

(a). non-negative tension and almost non-overshoot;

(b). non-negative tension and velocity constraints with $(\left|\min \dot{\xi}\right| > 10^{-6})$;

(c). non-negative tension and velocity constraints with $(\left|\min \dot{\xi}\right| > 10^{-3})$.

Results of the optimized control gains are given in Table 4.2, where optimization is conducted for two orbits.

Table 4.2 Control gains of controllers after optimization

Constraints	(k_{p2}, k_{v2})
$T \geq 0$ and overshoot $\sigma = (\xi - \xi_d) / \xi_d \leq 2\%$	(5.0587, 3.8722)
$T \geq 0$, $\dot{\xi} \geq 0$, and tight tolerance $(\left|\min \dot{\xi}\right| > 10^{-6})$	(4.7199, 3.8545)
$T \geq 0$, $\dot{\xi} \geq 0$, and low tolerance $(\left|\min \dot{\xi}\right| > 10^{-3})$	(4.8186, 3.8065)

The simulation results of LPDdgc with optimal gains in Table 4.2 are drawn in Figure 4.12. For all three cases, the tether is deployed to desired position very quickly and stably. A shown in Figure 4.12 (a), tether lengths are all stabilized to 1 within one orbit. The profiles of libration angles are plotted in Figure 4.12 (b), and similar trends can be found in these three cases. Next, Tether deployment velocity and libration angular velocity are sketched in Figure 4.12 (c) and (d), where the velocities of tether are smooth and finally converge to zero. Tether tensions are drawn in the Figure 4.13, where all tensions keep positive in the deployment process. Consequently, the constraints of tension and tether velocity can be tackled by tuning the gains of controller.

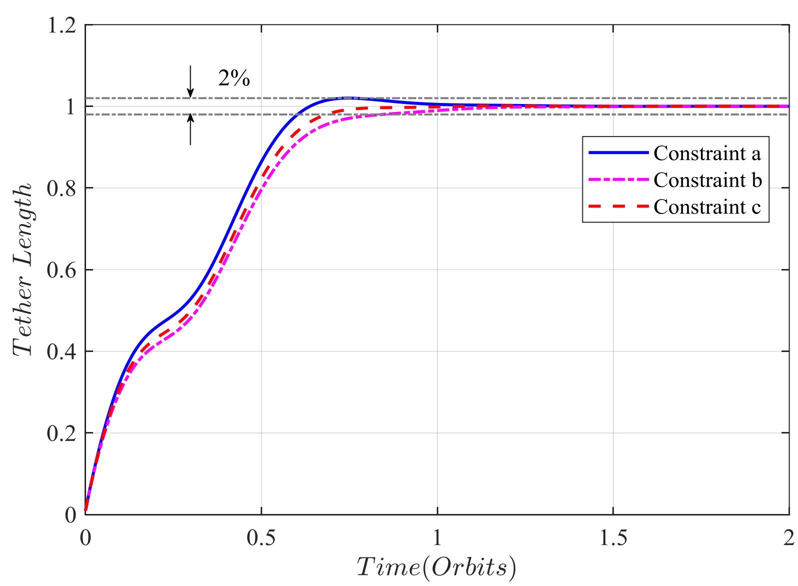

(a)

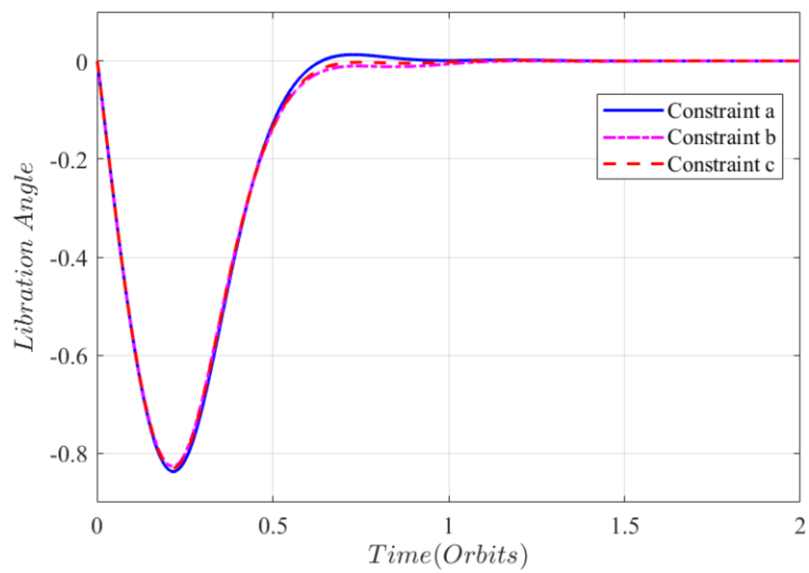

Constraint a
Constraint b
Constraint c
Libration Angle
Time(Orbits)

(b)

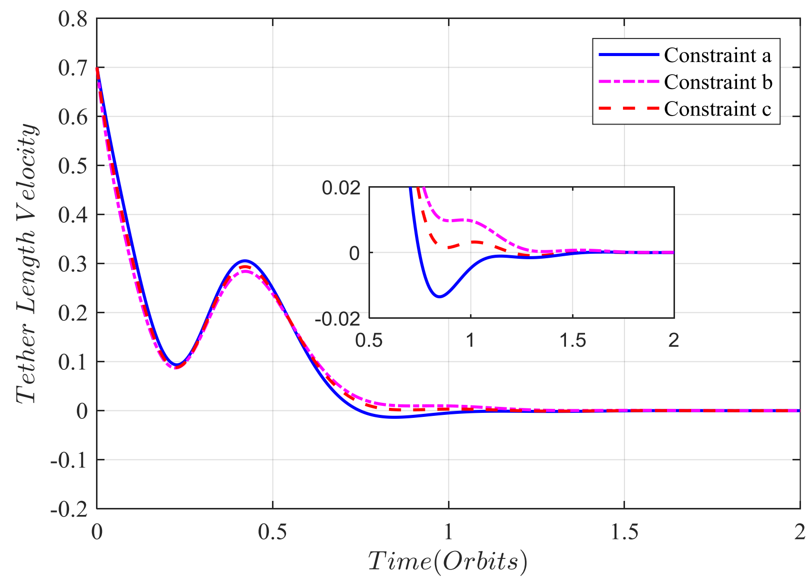

Constraint a
Constraint b
Constraint c
Tether Length Velocity
Time(Orbits)

(c)

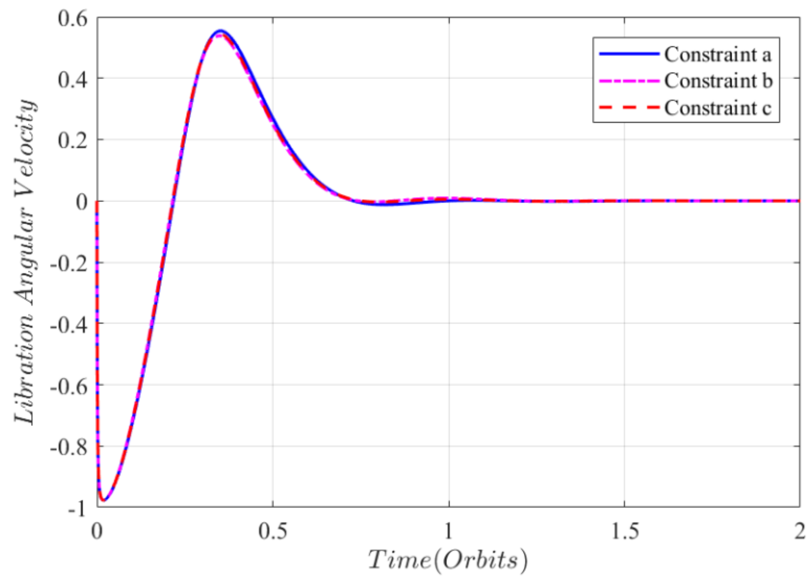

(d)

Figure 4.12 Time histories of states under constraints

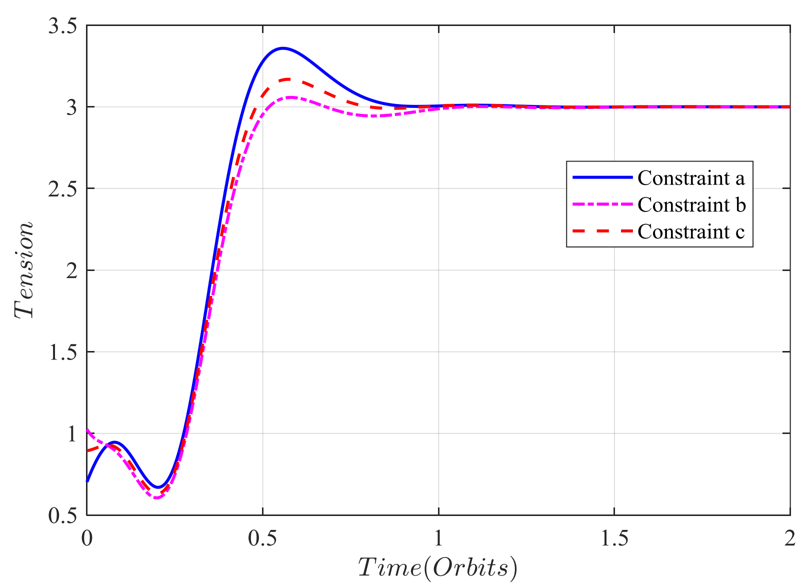

(e)

Figure 4.13 Tensions under constraints

4.2 Fractional-Order Sliding Mode Control

In this section, a fractional-order sliding mode controller is proposed to address the possible existing uncertainties and disturbances of TSS in practical missions to ensure the fast and stable deployment. Recalling the TSS's equations in Eq. (3.5) and applying the transformation,

$$x_1 = \xi - 1,\ x_2 = \dot{\xi},\ x_3 = \theta,\ x_4 = \dot{\theta}$$

one can shift the system's equilibrium to $x_{1e} = x_{2e} = x_{3e} = x_{4e} = 0$, such that,

$$\begin{aligned} \dot{x}_1 &= x_2 \\ \dot{x}_2 &= f(x) - T \\ \dot{x}_3 &= x_4 \\ \dot{x}_4 &= g(x) \end{aligned} \tag{4.45}$$

where

$$f(x) = (1+x_1)(1+x_4)^2 - (1+x_1) + 3(1+x_1)\cos^2 x_3$$

$$g(x) = -2\frac{x_2}{1+x_1}(1+x_4) - 3\cos x_3 \sin x_3$$

Next, with the model's uncertainty Δf and the external disturbances to control input ΔT, Eq. (4.45) is represented as,

$$\begin{aligned} x_1' &= x_2 \\ x_2' &= f(x) + d - T \\ x_3' &= x_4 \\ x_4' &= g(x) \end{aligned} \tag{4.46}$$

where $d \triangleq \Delta f + \Delta T$ denotes the total disturbance. Assume that the disturbance d has the upper bound, $\|d\| \le \eta$. To attenuate the disturbance's effect on TSS, a fractional-order sliding mode control law will be proposed in next section.

4.2.1 Sliding Mode Controller Design

Due to the underactuation of TSS, the most difficult task is to design a sliding manifold that can undertake the convergence of all modes (λ, θ). Thus, we design a sliding manifold contains two sub-manifolds, s_θ and s_ξ. The sub-manifolds correspond to the libration and length of TSS, respectively,

$$s_\theta = x_3 \tag{4.47}$$

$$z = \frac{c_3}{c_1} s_\theta \tag{4.48}$$

$$s_\xi = c_1 D^{1-\alpha}(x_1 - z) + c_2 D^{1-\alpha} x_2 \tag{4.49}$$

where α denotes the fractional-order operator with $\alpha \in (0,1)$ and $c_i, i = 1 \sim 3$ are all positive numbers.

The intermediate state z in Eq. (4.49) interconnects two sub-manifolds together and transfers the equilibrium, $x_1 = 0$, $x_2 = 0$ to $x_1 = z$, $x_2 = 0$. Note that, $s_\theta = 0$ indicates $z = 0$ from Eq. (4.48). The sub-manifold $s_\xi = 0$ will approach to zero as the sub-manifold s_θ goes to zero. As a result, all states will be steered to the equilibrium.

Apply the fractional operator D^{α} to s_{ξ} Eq. (4.49) and then combine with Eq. (4.46), such that,

$$D^{\alpha} s_{\xi} = c_1 (x_1' - z') + c_2 x_2' = c_1 x_2 + c_2 f - c_3 x_4 + c_2 u + c_2 d \tag{4.50}$$

Then, the fractional-order sliding mode controller is designed as,

$$\begin{cases} u = u_{eq} + u_{sw} \\ u_{eq} = -\dfrac{1}{c_2}[c_1 x_2 + c_2 f(x) - c_3 x_4] \\ u_{sw} = -\left[k \operatorname{sign}\left(s_{\xi}\right) + \delta s_{\xi} \right] \end{cases} \tag{4.51}$$

where u_{eq} is the equivalent input and u_{sw} is switch reaching function. k and δ are parameters to guarantee the existence and convergence of SMC.

4.2.2 Stability Analysis

In order to analyze the stability of TSS under the proposed controller, a positive Lyapunov function candidate is given as

$$V = s_{\xi}^{\ 2} \tag{4.52}$$

Applying the fractional operator D^{α} to both sides of Eq. (13) yields,

$$\begin{aligned} D^{\alpha} V &= s_{\xi} D^{\alpha} s_{\xi} + \sum_{i=1}^{\infty} \frac{\Gamma(1+\alpha)}{\Gamma(1-i+\alpha)\Gamma(1+i)} D^{i} s_{\xi} D^{\alpha-i} s_{\xi} \\ &\le s_{\xi} D^{\alpha} s_{\xi} + \left| \sum_{i=1}^{\infty} \frac{\Gamma(1+\alpha)}{\Gamma(1-i+\alpha)\Gamma(1+i)} D^{i} s_{\xi} D^{\alpha-i} s_{\xi} \right| \end{aligned} \tag{4.53}$$

Considering the inequality $\left|\sum_{i=1}^{\infty}\frac{\Gamma(1+\alpha)}{\Gamma(1-i+\alpha)\Gamma(1+i)}D^{i}sD^{\alpha-i}s\right|\le\gamma|s|$ in Ref. [96], where γ is a positive constant, and substituting Eqs. (4.51), (4.47)-(4.49) into Eq. (4.53), one has,

$$\begin{aligned} D^{\alpha}V &\le s_{\xi}[c_1x_2+c_2f-c_3x_4+c_2u+c_2d]+\gamma\left|s_{\xi}\right| \\ &=-c_2s_{\xi}[\mathrm{ksign}(\mathrm{s}_{\xi})+\delta s_{\xi}-d]+\gamma\left|s_{\xi}\right| \\ &\le c_2\left(\eta+\frac{\gamma}{c_2}-k\right)\left|s_{\xi}\right| \end{aligned} \tag{4.54}$$

Taking $k>\eta+\gamma/c_2$, then $D^{\alpha}V<0$. Thus, the trajectory of TSS will reach the sliding manifold $s_{\xi}=0$ and remain on it. If the sliding manifold is reached, then one has $D^{\alpha}s_{\xi}=c_1\dot{x}_1+c_2\dot{x}_2-c_3\dot{x}_3=0$, which can be written as,

$$\dot{x}_2=-\frac{c_1}{c_2}x_2+\frac{c_3}{c_2}x_4 \tag{4.55}$$

Putting Eq. (4.55) into Eq. (4.46) and linearizing the governing equations at the equilibrium point, $x_{1e}=x_{2e}=x_{3e}=x_{4e}=0$, it leads to

$$\begin{bmatrix}\dot{x}_2\\ \dot{x}_3\\ \dot{x}_4\end{bmatrix}=\begin{bmatrix}-c_1/c_2 & 0 & c_3/c_2\\ 0 & 0 & 1\\ -2 & -3 & 0\end{bmatrix}\begin{bmatrix}x_2\\ x_3\\ x_4\end{bmatrix} \tag{4.56}$$

The characteristic polynomial equation of Eq. (4.56) is

$$\lambda^3 + \frac{c_1}{c_2}\lambda^2 + \left(3 + \frac{c_3}{c_2}\right)\lambda + \frac{3c_1}{c_2} = 0 \tag{4.57}$$

It is easy to know the roots of Eq. (4.57) are $\mathrm{Re}\left(\lambda_{1,2,3}\right) < 0$ if $c_{1,2,3} > 0$. Accordingly, the state variables (x_2 , x_3 and x_4) are asymptotically stable and will go to zero. Then, one can get $x_1 = 0$ due to $s_\xi = 0$. Thus, all state variables will stabilize to zero asymptotically. That is to say, the TSS under the proposed fractional-order sliding mode control law is asymptotically stable.

4.2.3 Simulation and Discussion

There are two approaches to proceed the numerical implementation of the fractional operator: direct and indirect discretization [97]. Among them, the rational filter based Crone method is one of the widely used approach, where the fractional operator D^α is approximated by a filter s^α defined over a specified frequency range (ω_b, ω_h), such as,

$$D^\alpha = s^\alpha \approx K \frac{\prod_{i=1}^{N} s + \omega_i'}{\prod_{j=1}^{N} s + \omega_j} \tag{4.58}$$

$$\omega_i' = \omega_b \left(\frac{\omega_h}{\omega_b}\right)^{\frac{i + N + \frac{1}{2}(1-\alpha)}{2N+1}} \tag{4.59}$$

$$\omega_j = \omega_b \left(\frac{\omega_h}{\omega_b} \right)^{\frac{j+N+\frac{1}{2}(1+\alpha)}{2N+1}} \tag{4.60}$$

where N denotes the order of approximation and $K = \omega_h^{\alpha}$ is a gain term with fractional order power. In the simulation, we take the frequency range within $(\omega_b, \omega_h) = (10^{-2}, 10^{4})$. The order of approximation is chosen as $N = 5$ because of the small truncation error after 5 order.

To reduce the chattering phenomenon of SMC caused by the sign function in Eq.(4.51). A so-called bound lawyer function as follows is used to replace the sign function,

$$\mathrm{sat}\left(\frac{s_\xi}{\varepsilon}\right) = \begin{cases} \mathrm{sign}\left(\frac{s_\xi}{\varepsilon}\right) & \text{if } \left|\frac{s_\xi}{\varepsilon}\right| \geq 1 \\ \frac{s_\xi}{\varepsilon} & \text{if } \left|\frac{s_\xi}{\varepsilon}\right| < 1 \end{cases} \tag{4.61}$$

where $\varepsilon = 0.01$.

To examine the effectiveness of the proposed fractional-order sliding mode (FOSM) tension controller, numerical simulations are run. For comparison purpose, three control methods, the standard integer order sliding mode (SM) tension controller, the PD controller in Ref.[29] and the fractional-order PD (FOPD) tension control in Ref.[31] are adapted with the same parameters. The initial conditions of TSS are set at $x_1(0) = -0.99$, $x_2(0) = 0.5$,

$x_3(0) = 0$, $x_4(0) = 0$.

4.2.3.1 Influence of Fractional Order

Parameters of sliding mode manifold are set as $c_1 = 1$, $c_2 = 1$, $c_3 = 0.8$ in this case. The gains in the switching control law are $k = 0.4$ and $\delta = 0.2$ for the SM and FOSM control laws. The fractional-order in FOC is $\alpha = 0.5$. $d(\tau) = 0.2\sin(\pi\tau)$ is used to simulate the total disturbance.

To investigate the fractional-order's influence, varying fractional orders α = 0.1, 0.3, 0.5, 0.7, 0.9 are used to FOSM tension controller' comparison. The simulation results of tether length and rate are drawn in Figure 4.14 (a) and (b). It is easy to find that all controllers with different fractional-order successfully achieve the fast tether deployment in about 1.5 orbits with the disturbance suppressed. As shown in Figure 4.14 (c) and (d), the pitch (libration) angle and the angular velocity of tether stabilize to zero at the final stage of deployment. Furthermore, with a larger fractional-order, the deployment of TSS performs slightly faster and the max magnitude of the libration angle of tether decreases. As an example, the pitch angle of tether is about 0.7 rad with the fractional-order $\alpha = 0.9$, in contrast it is 0.8 rad with the fractional order $\alpha = 0.1$. As shown in the simulation results, the fractional-order of the FOSM have positive impacts on the close-loop system's performance.

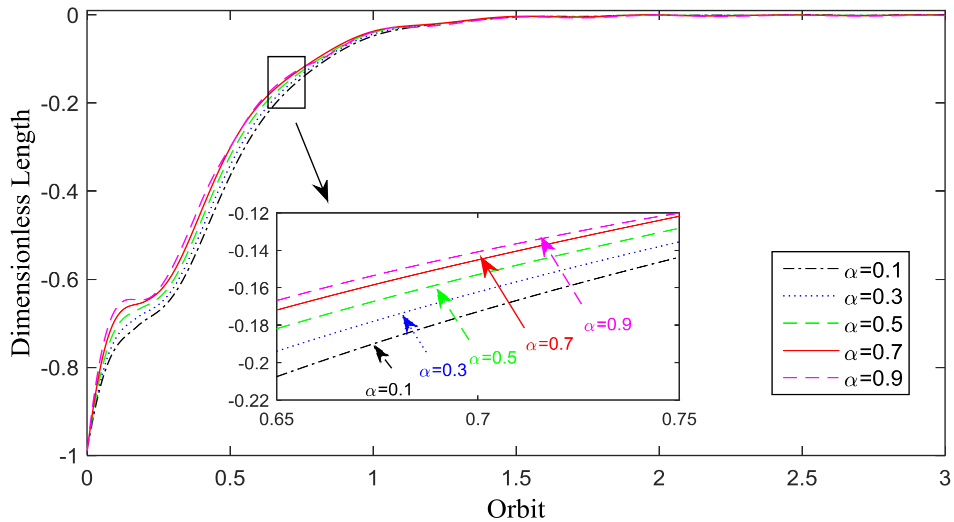

Dimensionless Length
Orbit
α=0.1
α=0.3
α=0.5
α=0.7
α=0.9

(a)

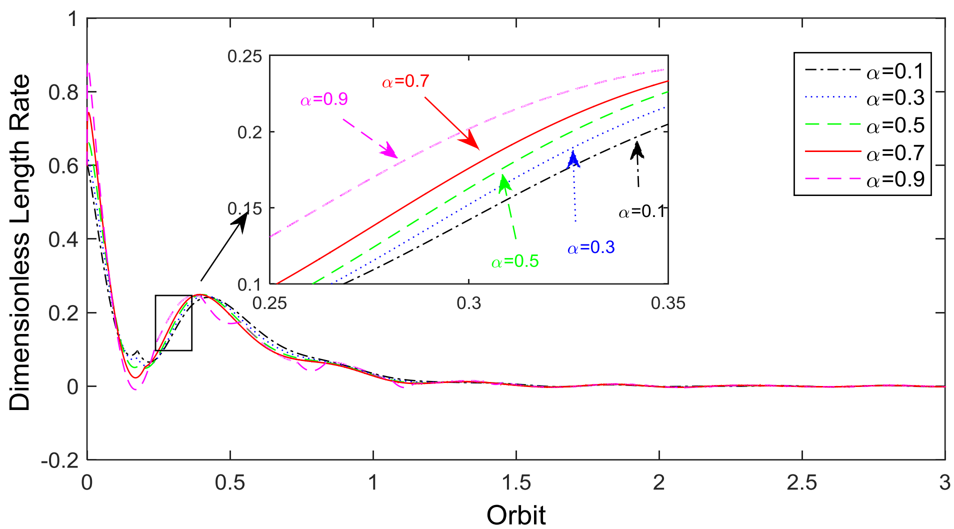

Dimensionless Length Rate
Orbit
α=0.1
α=0.3
α=0.5
α=0.7
α=0.9

(b)

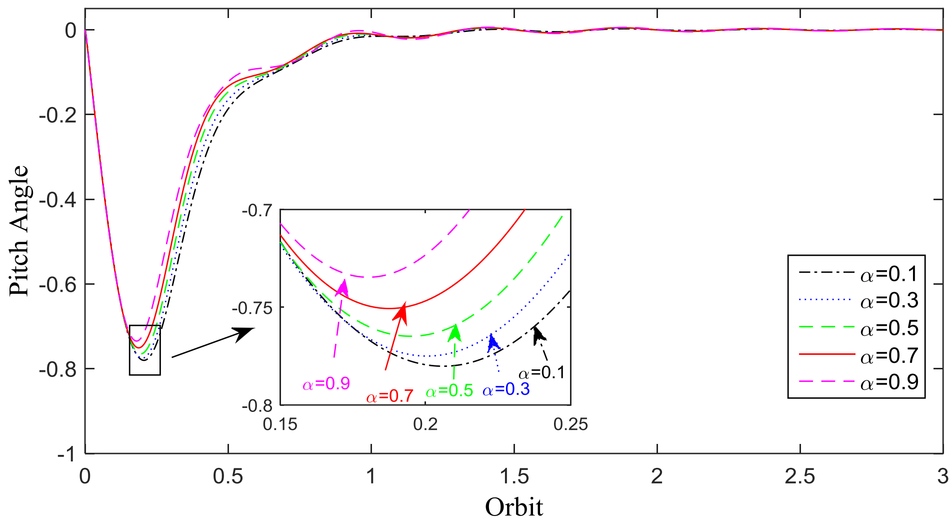

(c)

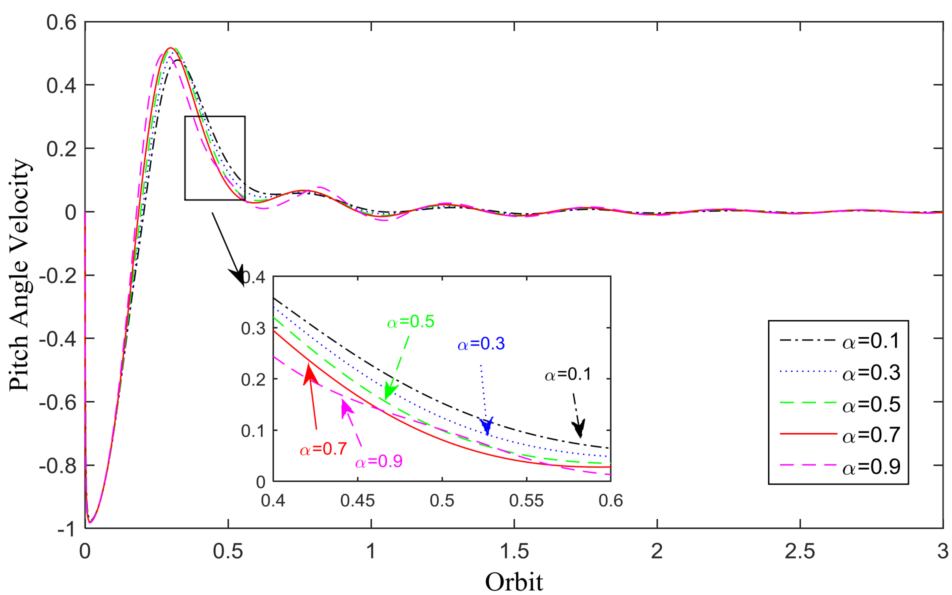

(d)

Figure 4.14 Time histories of states for different fractional-orders.

4.2.3.2 Influence of Sliding Sub-Manifold s_θ

It is worth to mention that all parameters of sliding mode manifold has the effects on the performance of controllers. However, from the expressions of two sub-sliding manifolds, one knows the c_1 and c_2 mainly affect the tether length, and the c_3 affects on the tether libration angle. To study the effect of c_3 in sliding manifold s_θ on TSS, c_1 and c_2 are set as $c_1 = 1$, $c_2 = 1$ same as in Section 4.2.3.1. The different c_3 from 0.7 to 1.5 will be compared. The gains in the switching control law are $k = 0.4$ and $\delta = 0.2$ control laws. The fractional-order of FOC is $\alpha = 0.5$. The total disturbance $d(\tau) = 0.2\sin(\pi\tau)$ is used in the simulation case. Simulation results for the different c_3 are shown in Figure 4.14. As shown in Figure 4.14 (a), tether lengths converge to the steady state quickly and the convergence rate is much faster with small the parameter c_3, where the convergence time reduces from 2 to 1.5 orbits as the parameter c_3 decreases from 1.5 to 0.7. On the contrary, the maximum of pitch angle presents quite the opposite tendency as shown in Figure 4.14 (c). For instance, the max magnitude of the pitch angle is 0.8 rad with $c_3 = 0.7$ and reduces to 0.6 rad with $c_3 = 1.5$. As are clear from Figure 4.14 (b) and (d), the tether length velocity and pitch angular velocity converge to near zero around 1.5 orbits. In conclusion, the parameter c_3 has a remarkable effect on the TSS with proposed fractional-order sliding mode control law.

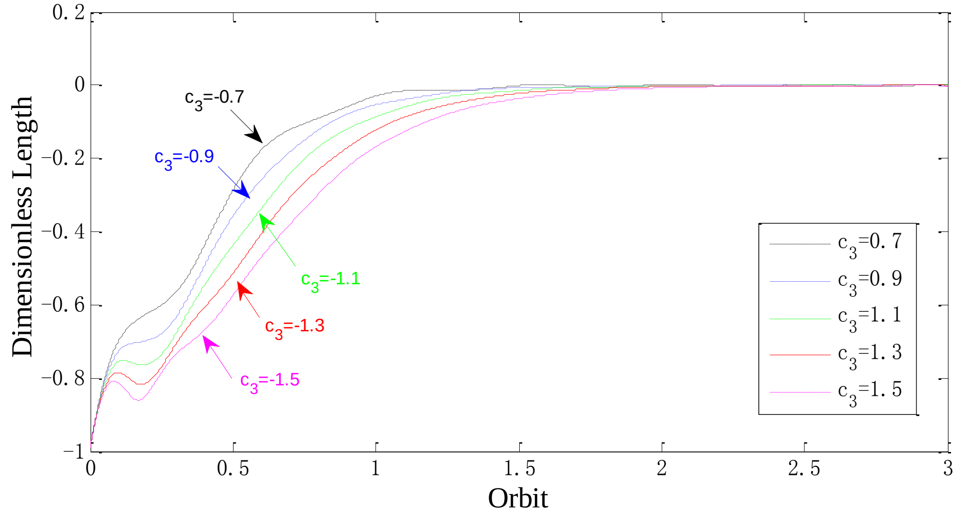

Dimensionless Length
Orbit
c3=-0.7
c3=-0.9
c3=-1.1
c3=-1.3
c3=-1.5
c3=0.7
c3=0.9
c3=1.1
c3=1.3
c3=1.5

(a)

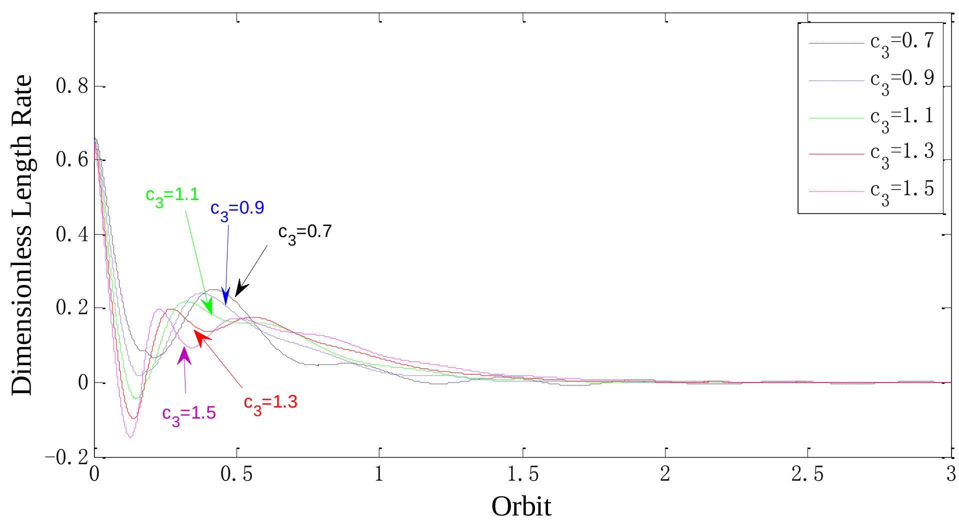

Dimensionless Length Rate
Orbit
c3=1.1
c3=0.9
c3=0.7
c3=1.5
c3=1.3
c3=0.7
c3=0.9
c3=1.1
c3=1.3
c3=1.5

(b)

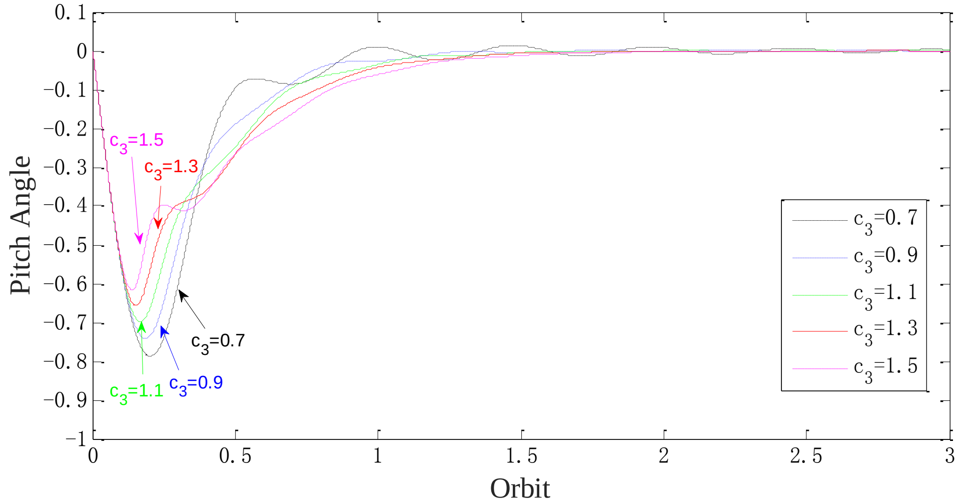

(c)

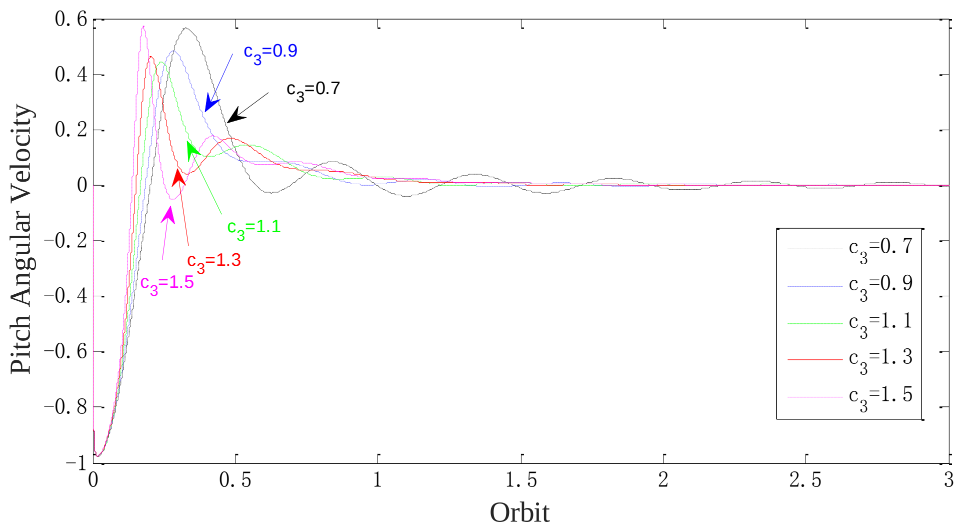

(d)

Figure 4.15 Time histories of states for different c_3

4.2.3.3 Comparisons with Other Control Methods

In this case, the effectiveness of proposed FOSM controller is compared with three different control laws (PD, FOPD, SM), where the parameters of the

PD and FOPD controller are the same as in Refs. [29] and [31]. Simulation results are presented in Figure 4.16 (a-d), respectively. Figure 4.16 (a) shows that the SM and FOSM controllers perform better than PD and FOPD controllers for disturbance attenuation. It is clear to find that PD and FOPD control laws are very vulnerable to disturbance because they cannot suppress the oscillations in tether length caused by the disturbance. However, SM and FOSM control schemes perform better robust to suppress the disturbance than the PD and FOPD. Moreover, as Figure 4.16 (a) and (c) show FOSM controller shows better performance of small settling-time and tether angle in comparison with the classical integer-order SM controller. Figure 4.16 (b) and (d) present same trend in the tether length velocity and angular velocity. Thus, we can conclude that FOSM controller is with better robust performance than the controllers of PD, FOPD and SM.

To further verify the effectiveness of disturbance suppression in a large frequency range, a composite disturbance that combines low and high frequencies is given as follows,

$$d_1(\tau) = 0.2\left[\sin(\pi\tau) + \sin(100\pi\tau)\right] \tag{4.62}$$

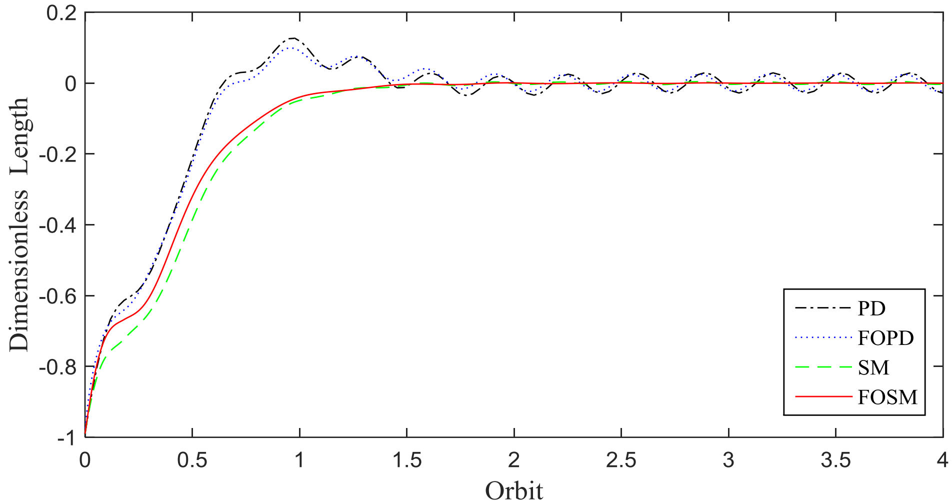

0.2
0
-0.2
-0.4
-0.6
-0.8
-1
0
0.5
1
1.5
2
2.5
3
3.5
4
Orbit
Dimensionless Length
PD
FOPD
SM
FOSM

(a)

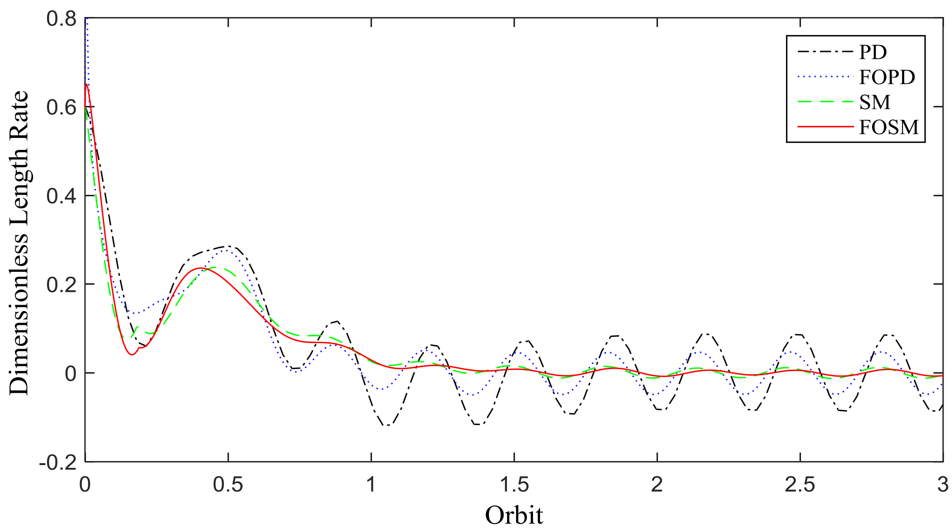

0.8
0.6
0.4
0.2
0
-0.2
0
0.5
1
1.5
2
2.5
3
Orbit
Dimensionless Length Rate
PD
FOPD
SM
FOSM

(b)

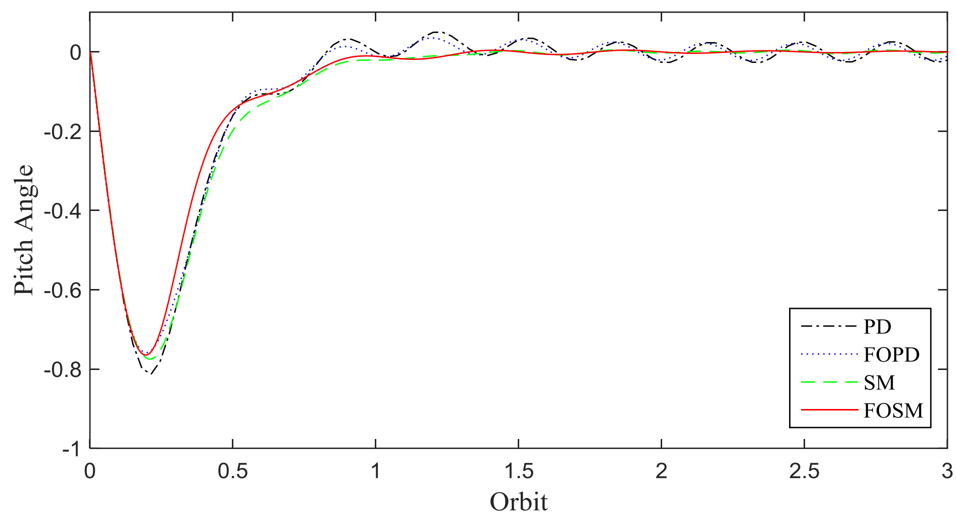

(c)

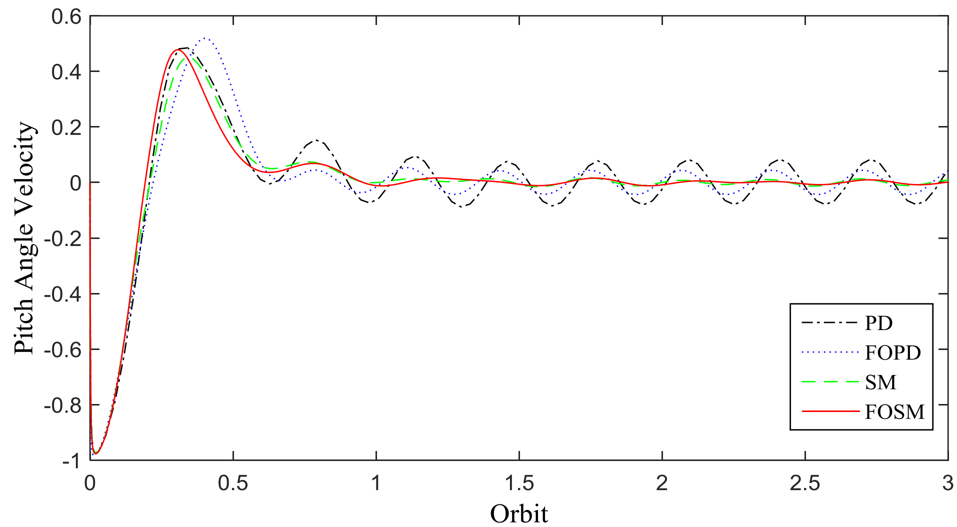

(d)

Figure 4.16 Comparisons of different control methods

As Figure 4.17 shows the tether tension is always continuous and positive, which indicates tether is always taut during the entire deployment in presence of the disturbance. Moreover, tether tension performs the same frequency oscillations as in the composite disturbance with low and high frequency, where two modes of oscillation frequency of tension are shown in Figure 4.17. The green line represents the composite frequency oscillation and red line represents the low frequency oscillation. The simulation results of tether length and angle are similar as those in Figure 4.16, thus not shown.

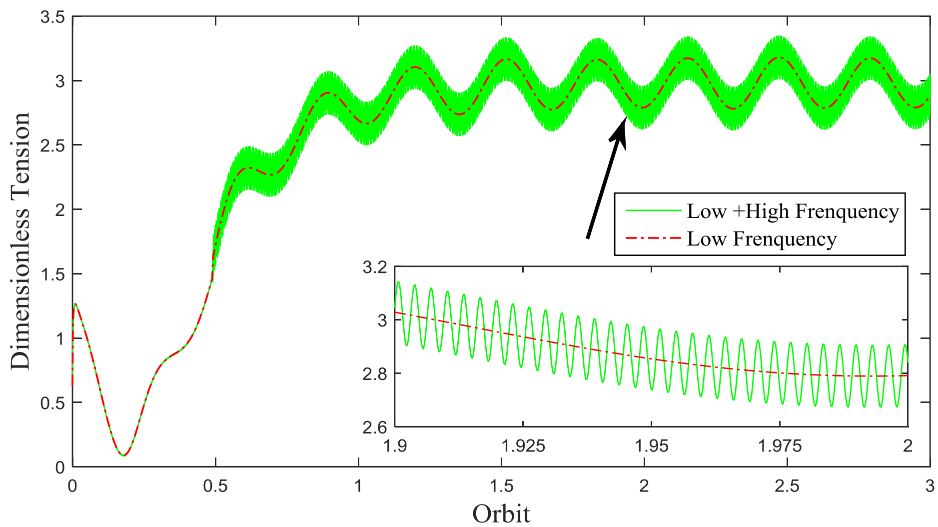

Figure 4.17. Time history of tether tension

In summary, a robust fractional-order sliding mode controller is proposed to address the problem of unknown disturbance in TSS deployment. Compared with other classical control methods, the effectiveness and robustness of the proposed FOSM controller are demonstrated by simulation.

Chapter 5 DESPIN ROTATING TARGET BY TETHERED SPACECRAFT SYSTEM

Summary: The focus of this chapter is on studying the rotating target despin. First, a parametric study of the physical parameters is investigated. Then, different despin control strategies are designed with considering the operational constraints. Further, dynamics and control of the despinning with considering the orbital motion's effect is given. Finally, a passivity based MPC is proposed to stabilize the underactuated TSS under the input and state constraints. Part of theatrical and simulation results has been published in reference paper B, C and D. All variable symbols in this chapter refer to the definitions in Section 3.2.

5.1 Parametric Study of System's Physical Parameters

As shown in the normalized tethered system model in Eq.(3.32), we can find that the system's dynamic behaviors highly depend on two dimensionless variables: inertial ratio and length ratio, corresponding to the system's physical parameters, which further affecting the despin efficiency. Also, the magnitude of thrust significantly affects the despin efficiency. Thus, it is very necessary to study parameters' impacts on the target despin.

5.1.1 Controller Design and Stability around Equilibrium

Before conducting the parametric study, the admissible equilibrium and simple control strategy should be studied first. To determine the admissible equilibrium of the system in Eq. (3.30), we can study the $\theta-\theta'$ phase portraits of tether angle subject to the operational constraint as following,

$$|\theta|<\frac{\pi}{2} \quad T=\frac{\left(\cos\theta\eta^2+\xi\left(\eta+\theta'\right)^2\right)+u_t}{1+\frac{1}{\lambda}\sin^2\theta}>0 \tag{5.1}$$

First, assume the target is rotating with a small constant angular velocity. Then, one can reduce Eq. (3.30) to,

$$\theta''=-\sin\theta\eta^2/\xi \tag{5.2}$$

The phase portraits of θ are plotted in Figure 5.1 with different ξ and η based on Eq.(5.2). As is clear from Figure 5.1, all trajectories of different ξ and η preforms similar trends, which shows the $\left(\theta,\dot{\theta}\right)=(0,0)$ is the stable center equilibrium and $\left(\theta,\dot{\theta}\right)$ = $(\pm\pi,0)$ are unstable saddles. Thus, $(\eta,\theta,\theta')=(\eta_d,0,0)$ is the unique admissible equilibrium of the system due to the operational constraint $|\theta|\leq\pi/2$, where η_d denotes the desired angular velocity of the target.

Next, we propose a despin control law to despin the target angular velocity to η_d. For sake of convenience, we define an error state $e_\eta = \eta - \eta_d$ to shift the equilibrium to zero. Then, one can convert the Eq. (3.30) as

$$\begin{aligned} e'_\eta &= \frac{\sin\theta\left[\left(e_\eta+\eta_d\right)^2\cos\theta+\xi\left(e_\eta+\eta_d+\theta'\right)^2+u_t\right]}{\lambda+\sin^2\theta} \\ \theta'' &= -\left(1+\frac{1}{\xi}\cos\theta\right)e'_\eta-\frac{1}{\xi}\left(e_\eta+\eta_d\right)^2\sin\theta+\frac{u_n}{\xi} \end{aligned} \tag{5.3}$$

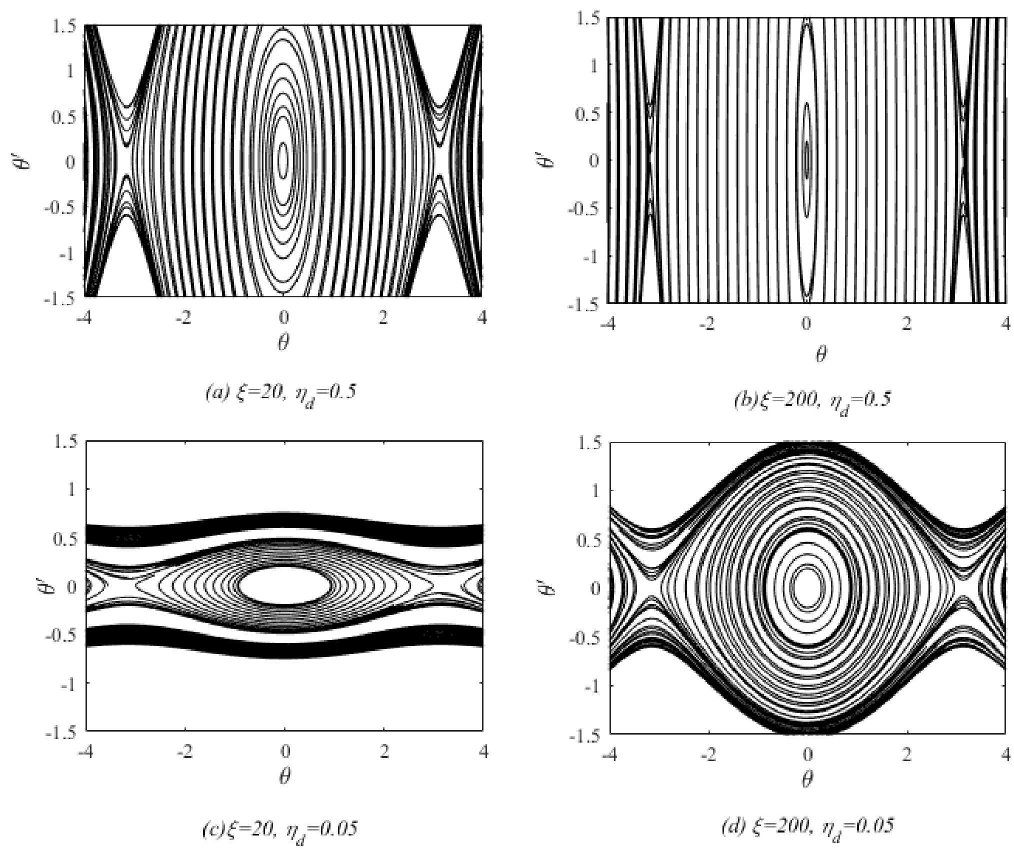

Figure 5.1 Phase planes of TSS at different values of ξ and η.

Linearizing the nonlinear Eq.(5.3) at zero yields

$$\begin{bmatrix} e'_\eta \\ \theta' \\ \theta'' \end{bmatrix} = \begin{bmatrix} 0 & \dfrac{(1+\xi)\eta_d^{\ 2}+u_t}{\lambda} & 0 \\ 0 & 0 & 1 \\ 0 & -\left(1+\dfrac{1}{\xi}\right)\dfrac{(1+\xi)\eta_d^{\ 2}+u_t}{\lambda}-\dfrac{\eta_d^{\ 2}}{\xi} & 0 \end{bmatrix} \begin{bmatrix} e_\eta \\ \theta \\ \theta' \end{bmatrix} + \begin{bmatrix} 0 \\ 0 \\ \dfrac{u_n}{\xi} \end{bmatrix} \tag{5.4}$$

Seen from the above Eq. (5.4), e_η only depends on u_t while the θ depends on u_t and u_n. Thus, one can decouple two inputs by taking $u_t = c \geq 0$ as a positive constant to satisfy the positive tension constraint in Eq. (5.1). Then, u_n is the only input to determine.

Further, simple proportional-derivative controller is proposed as follows,

$$\begin{aligned} u_t &= \mathrm{c} \\ u_n &= -k_1\left(e_\eta\right) - k_2\theta - k_3\theta' \end{aligned} \tag{5.5}$$

where k_i (i = 1, 2, 3) denote control gains.

After substituting Eq.(5.5) into Eq.(5.4), one has

$$\begin{bmatrix} e'_\eta \\ \theta' \\ \theta'' \end{bmatrix} = \begin{bmatrix} 0 & \dfrac{(1+\xi)\eta_d^{\ 2}+c}{\lambda} & 0 \\ 0 & 0 & 1 \\ -\dfrac{k_1}{\xi} & -\left(1+\dfrac{1}{\xi}\right)\dfrac{(1+\xi)\eta_d^{\ 2}+c}{\lambda}-\dfrac{\eta_d^{\ 2}}{\xi}-\dfrac{k_2}{\xi} & -\dfrac{k_3}{\xi} \end{bmatrix} \begin{bmatrix} e_\eta \\ \theta \\ \theta' \end{bmatrix} \tag{5.6}$$

It is easy to obtain the characteristic polynomials of Eq. (5.6) as,

$$s^3 + \frac{k_3}{\xi}s^2 + \left[p\left(1+\frac{1}{\xi}\right)+\frac{1}{\xi}\eta_d^{\ 2}+\frac{k_2}{\xi}\right]s + \frac{k_1}{\xi}p = 0 \tag{5.7}$$

where $p=\frac{(1+\xi)\eta_d^{\ 2}+c}{\lambda}$. According to the Routh–Hurwitz stability criterion, the following inequality

$$k_1>0;\ \ k_3>0;\ \ k_3\left[p(1+\xi)+\eta_d^{\ 2}+k_2\right]-k_1\xi p>0 \tag{5.8}$$

should hold to guarantee the stability of the equilibrium.

If $k_2>0$ and $k_3(1+\xi)>k_1\xi$, the inequality (5.8) always holds true. Therefore, the closed-loop system will be locally asymptotical stable at the equilibrium $(e_\eta,\theta,\theta')=(0,0,0)$, which means the target's spinning velocity converges to η_d. It is worth noting that the setting $\eta_d=0$ leads the complete despin to zero.

5.1.2 Simulation and Discussion

As discussed before, we should investigate the effects of thrust magnitude, inertial ratio, and length ratio on despin efficiency. Thus, three simulation scenarios with different inertial ratio, different length ratio, and different thrust will be conducted in the subsequent study.

In all simulation cases, the initial conditions are same at $(\eta,\theta,\theta')=(1,0,0)$. Target's initial angular velocity $\omega_0=0.02rad/s$ is from Ref.[74] and the time scale is normalized by the target's rotation period $T_0=2\pi/\omega_0$. Finally, the controller gains $k_1=k_2=k_3=1$ are given for all simulation cases.

5.1.2.1 Effect of Tangent Thrust u_t

In this case, inertial ratio is $\lambda = 2000$ and length ratio is $\xi = 10$. Then, different tangent thrust $u_t = 0.1, 1, 10, 100$ are compared in simulations. As shown in the Figure 5.2 (a-e), all the states converge to zero as expected. Figure 5.2 (a) shows the despin times decreases significantly from 10,000 to 20 cycles with the magnitude of the u_t increase from 0.1 to 100. The tether libration angle converges to zero from 10000 to 20 cycles with u_t from 0.1 to 100 as well, shown in Figure 5.2 (b). However, the angular velocity of tether libration decrease to zero around 15 cycles for all values of u_t, see Figure 5.2 (c). Tether tensions are plotted in Figure 5.2 (d), where all tensions quickly approach to the magnitude of the thrust u_t. In Figure 5.2 (e), the normal thrust u_n goes to zero quickly and its magnitude is smaller than 1, $|u_n| \leq 1$. Thus, one conclude that the tangent thrust has a significant effective on despin. The target can be quickly despun for a sufficient capacity of thrust at the tug.

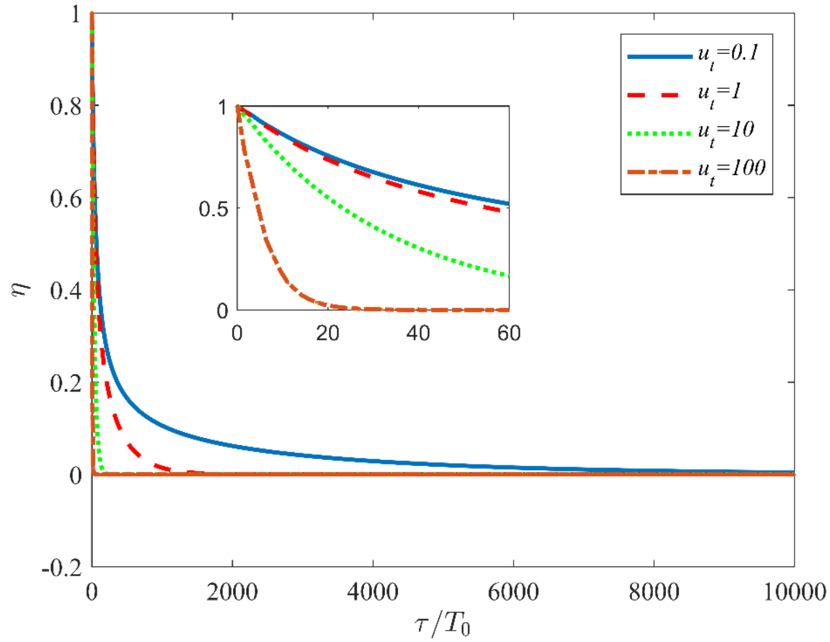

u_t=0.1
u_t=1
u_t=10
u_t=100
η
τ/T_0

(a)

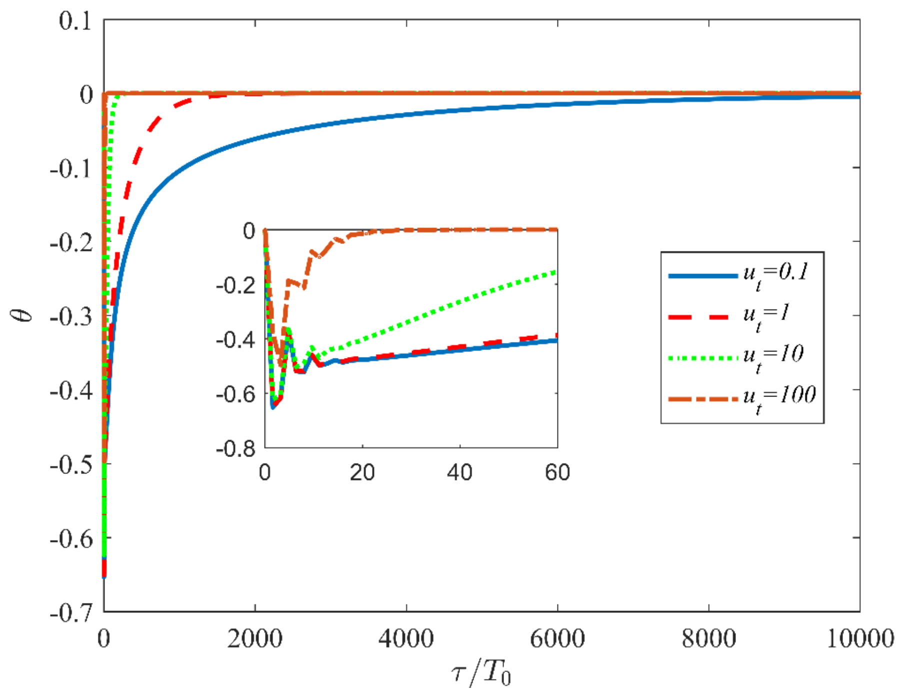

u_t=0.1
u_t=1
u_t=10
u_t=100
θ
τ/T_0

(b)

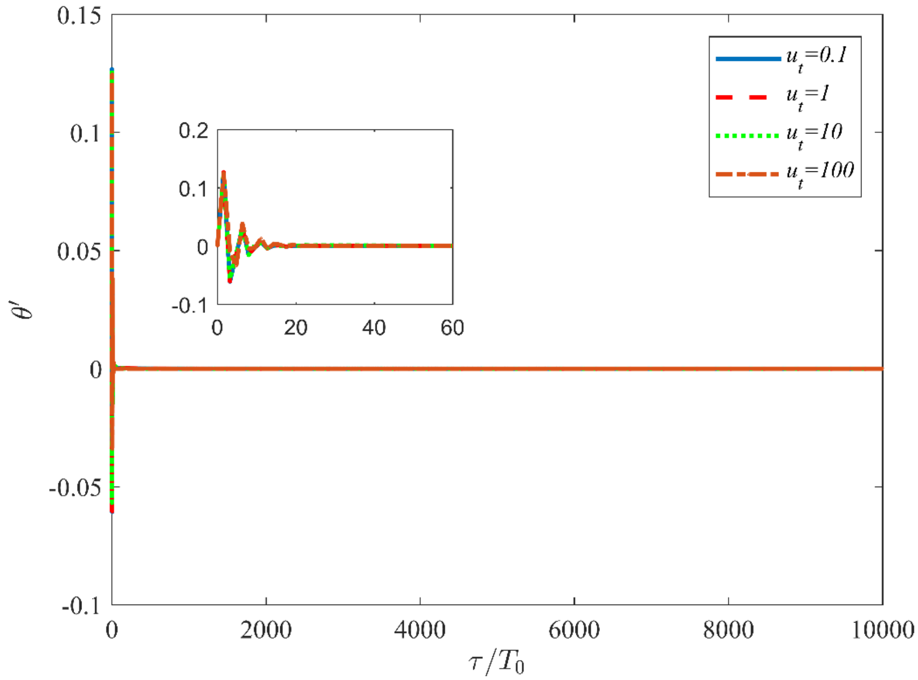
0.15
0.1
0.05
0
-0.05
-0.1
θ'
0
2000
4000
6000
8000
10000
τ/T_0
u_t=0.1
u_t=1
u_t=10
u_t=100
0.2
0.1
0
-0.1
0
20
40
60

(c)

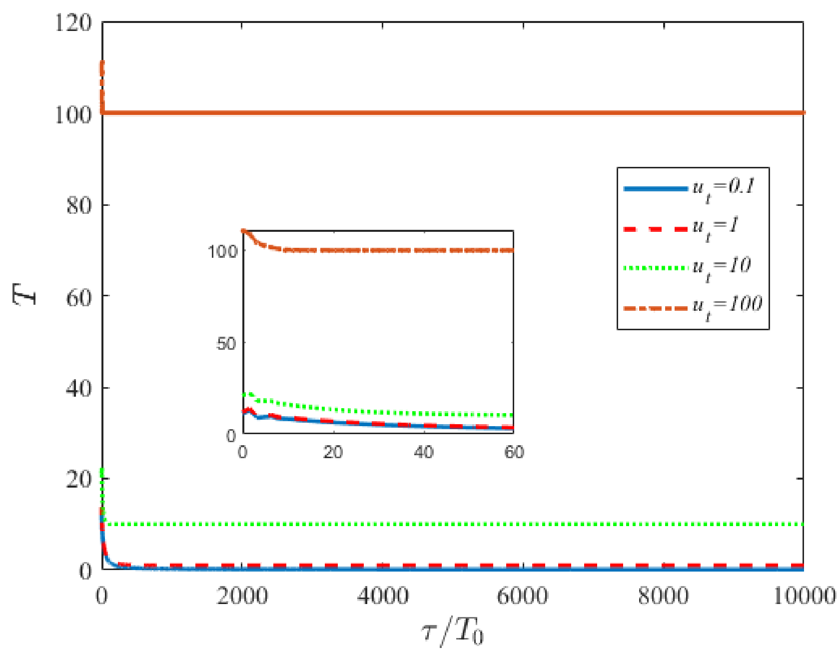
120
100
80
60
40
20
0
T
0
2000
4000
6000
8000
10000
τ/T_0
u_t=0.1
u_t=1
u_t=10
u_t=100
100
50
0
0
20
40
60

(d)

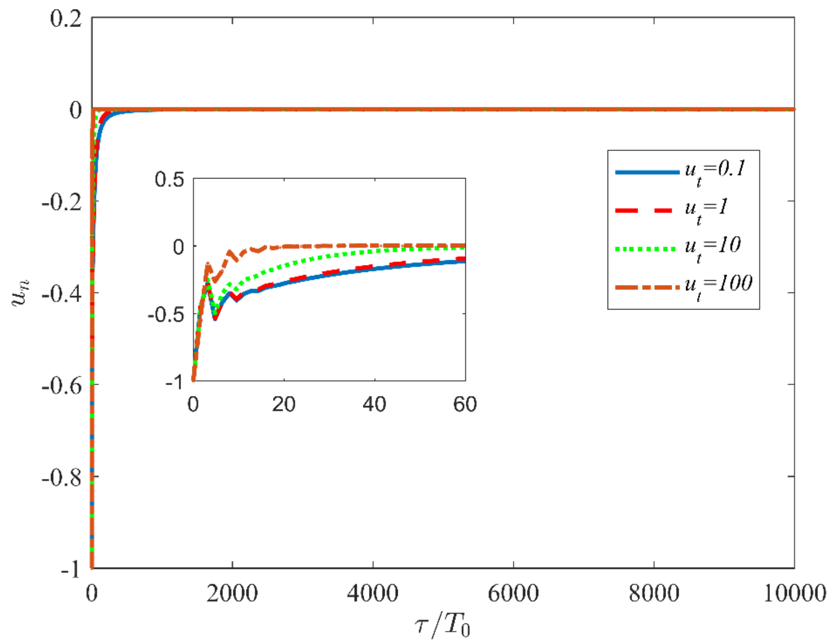

(e)

Figure 5.2 Effects of thrust u_t on despin.

5.1.2.2 Effect of Inertial Ratio λ

In this case, length ratio is $\xi = 10$ and tangent thrust is $u_t = 1$. Different inertial ratio $\lambda = 500$, 1000, 2000, 10000, 20000 are compared. As shown in Figure 5.3, all the states reduce to zero at the end of despin, and as the inertial ratio increases the despin time increases. Larger inertial ratio means the mass of target is much heavier, thus it requires much longer time to despin for same small tug. Figure 5.3(d) shows that all tether tensions converge to the given tangent thrust $u_t = 1$ similar in the previous case. As shown in Figure 5.3(e), the normal thrust peaks at the beginning with maximum less than 1 for all inertial ratios. The normal thrust gradually approaches to zero in the despin process. Thus, it is feasible to despin a massive target by TSS with a small thrust.

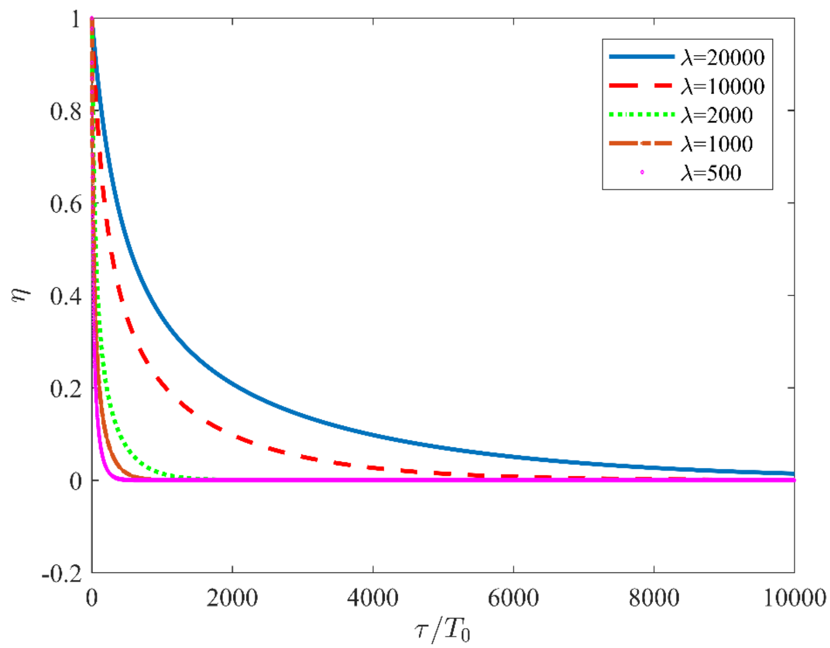

(a)

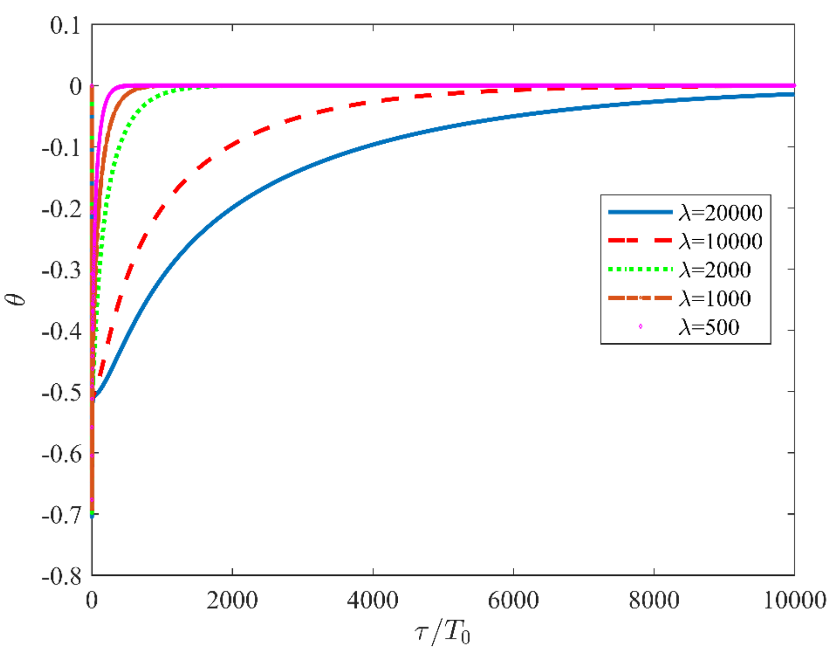

(b)

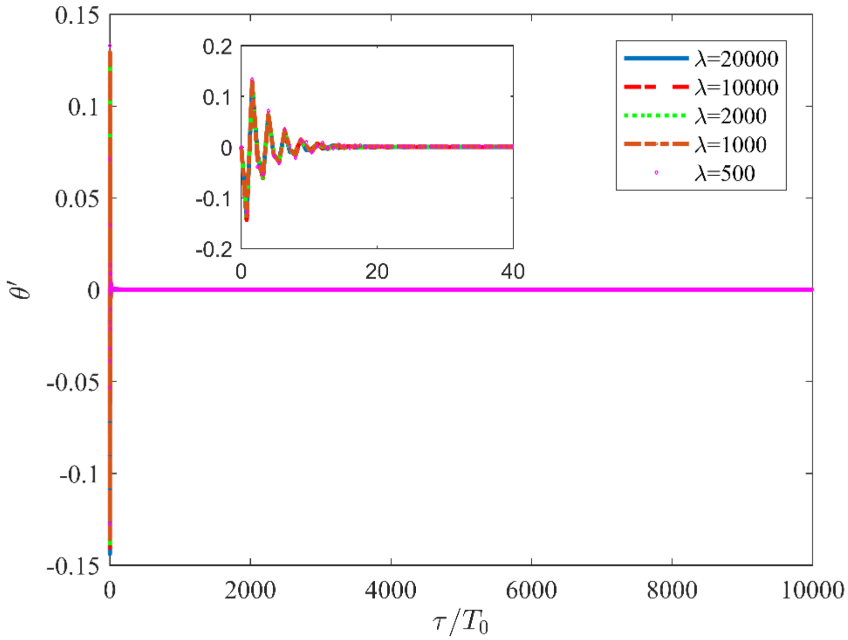

0.15
0.1
0.05
0
-0.05
-0.1
-0.15
θ'
0
2000
4000
6000
8000
10000
τ/T_0
0.2
0.1
0
-0.1
-0.2
0
20
40
λ=20000
λ=10000
λ=2000
λ=1000
λ=500

(c)

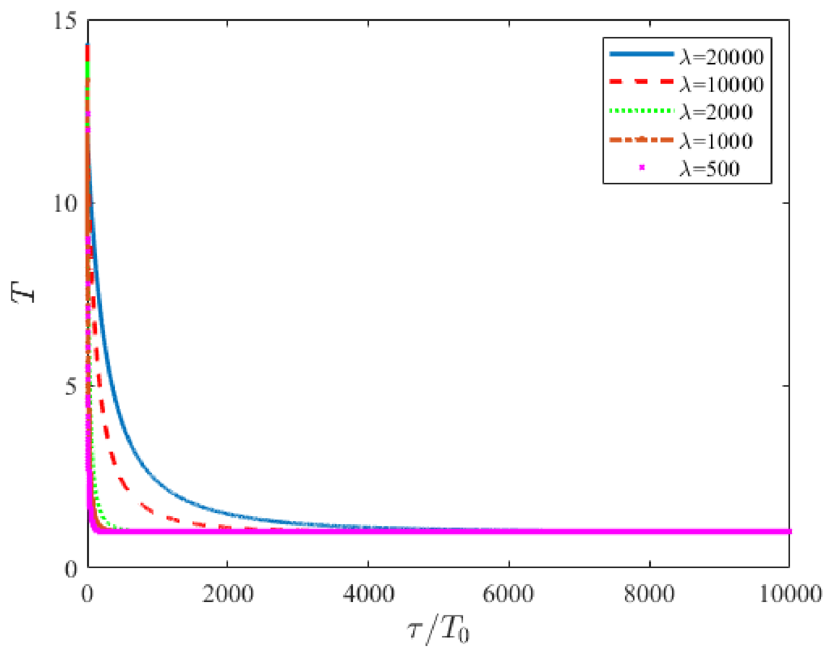

15
10
5
0
T
0
2000
4000
6000
8000
10000
τ/T_0
λ=20000
λ=10000
λ=2000
λ=1000
λ=500

(d)

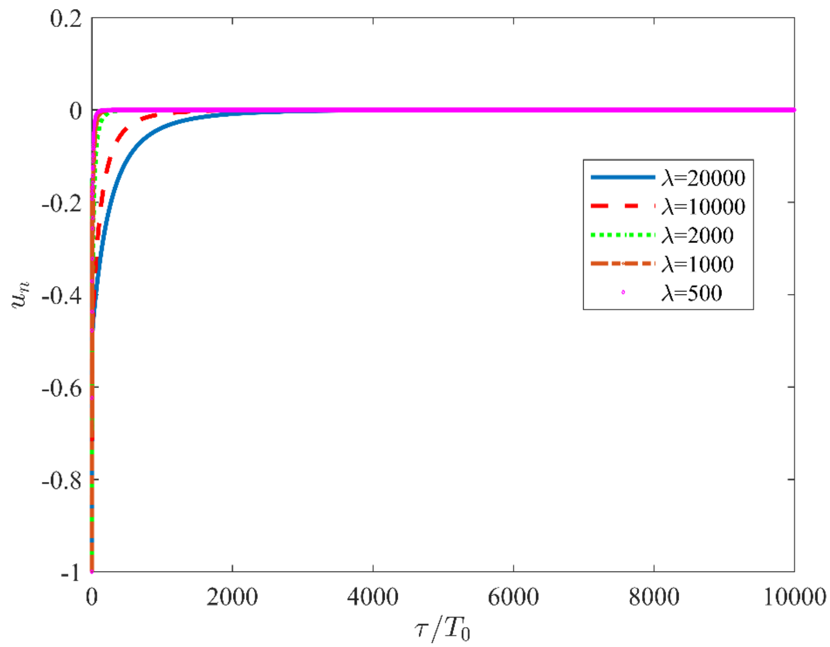

(e)

Figure 5.3 Effects of inertial ratio λ on despin.

5.1.2.3 Effect of Length Ratio ξ

In this case, different length ratios (tether length/target radius) are compared in the despin. Inertial ratio $\lambda = 2000$, tangent thrust $u_t = 1$, and the length ratios $\xi = 2, 5, 10, 100$ are used in the simulation. The results are plotted in the Figure 5.4. As shown in Figure 5.4 (a), despin of the large target is improved for larger length ratio. Because the system's inertial momentum increases with the increase of length ratio for given size of target, the same amount energy reduce will result in more decrease of the angular velocity for large target. Similar effect can be found for tether libration angle and angular velocity in Figure 5.4 (b) and (c). As the length ratio increases, the libration of tether converges faster. It should be noted that there exists a large oscillation for length ratio 100, which can be eliminated by increasing the control gain k_3. Seen in Figure 5.5, the oscillation of the libration is well suppressed for $k_3 = 10$. The maximum magnitude of tether libration reduces from 1 to 0.35 with the increase of length ratio. Figure 5.4(d), shows the maximum of tether tension is about 15 for the lower length ratio $\xi = 2$, but approaches to 120 for $\xi = 100$. This is caused by the centrifugal force term $\xi(\eta + \theta')^2$ in the tension.

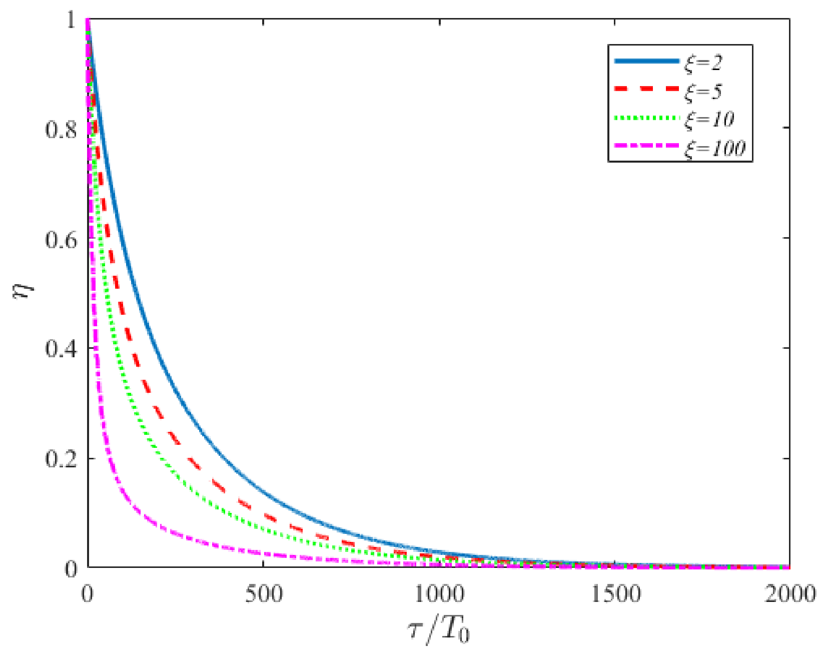

(a)

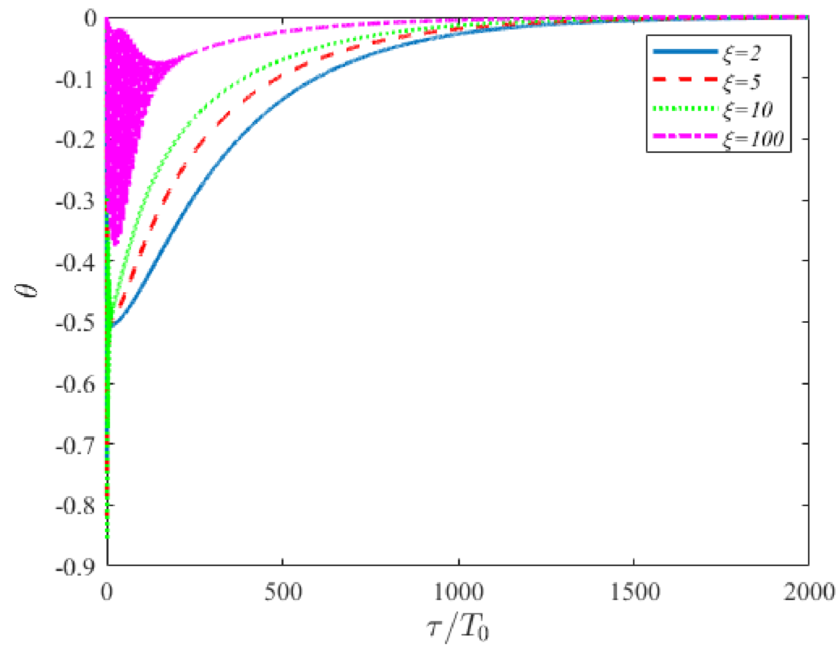

0
-0.1
-0.2
-0.3
-0.4
-0.5
-0.6
-0.7
-0.8
-0.9
θ
0
500
1000
1500
2000
τ/T0
ξ=2
ξ=5
ξ=10
ξ=100

(b)

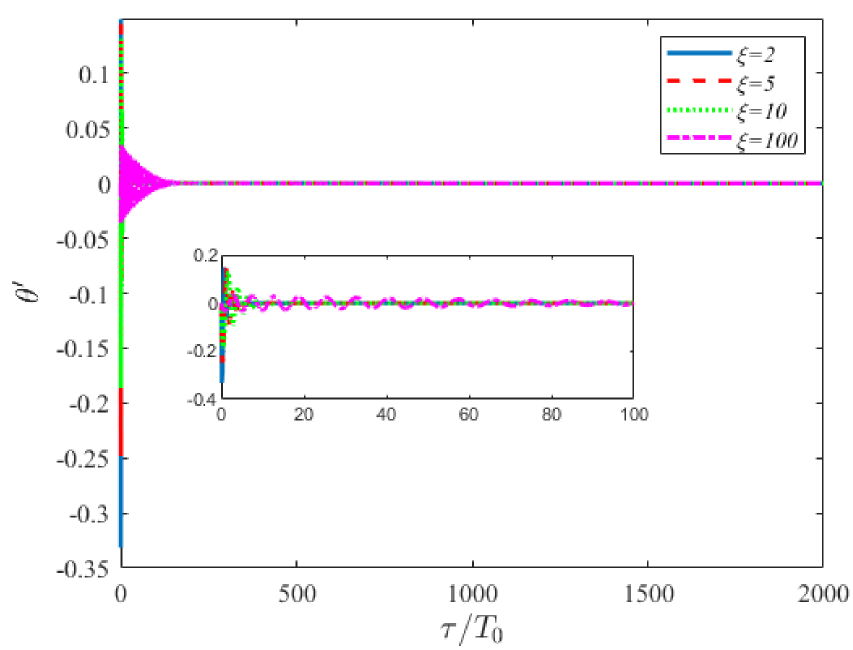

0.1
0.05
0
-0.05
-0.1
-0.15
-0.2
-0.25
-0.3
-0.35
θ'
0
500
1000
1500
2000
τ/T0
ξ=2
ξ=5
ξ=10
ξ=100
0.2
0
-0.2
-0.4
0
20
40
60
80
100

(c)

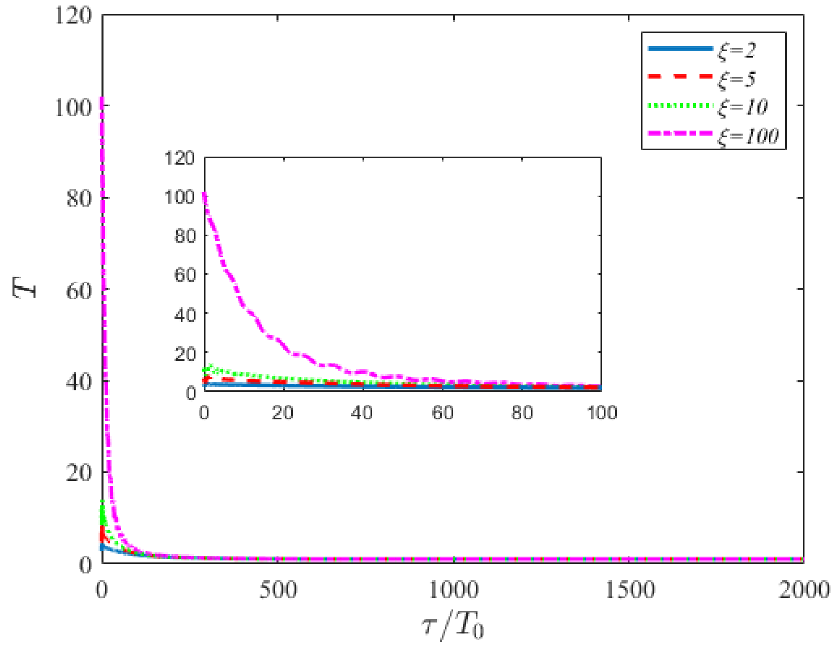

(d)

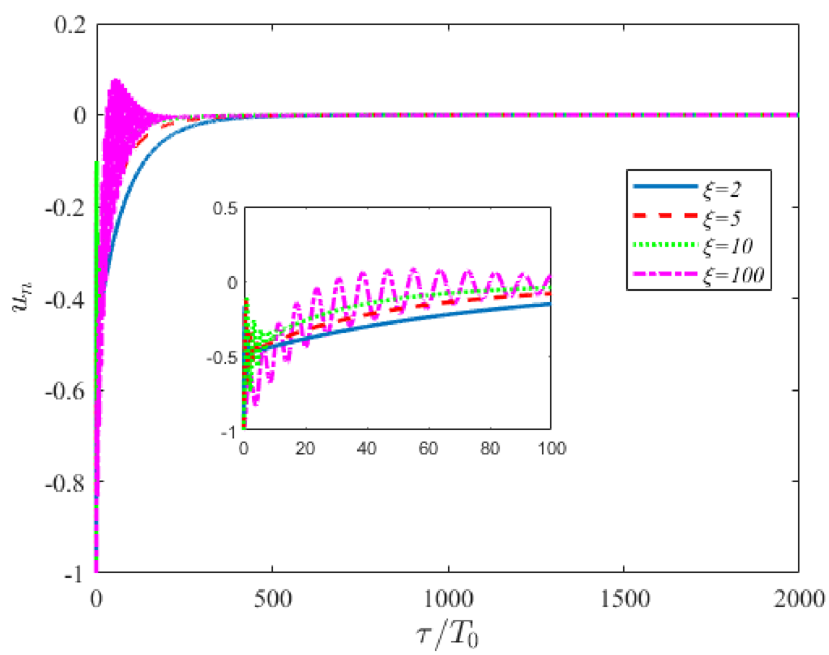

(e)

Figure 5.4 Effects of length ratio ξ on despin.

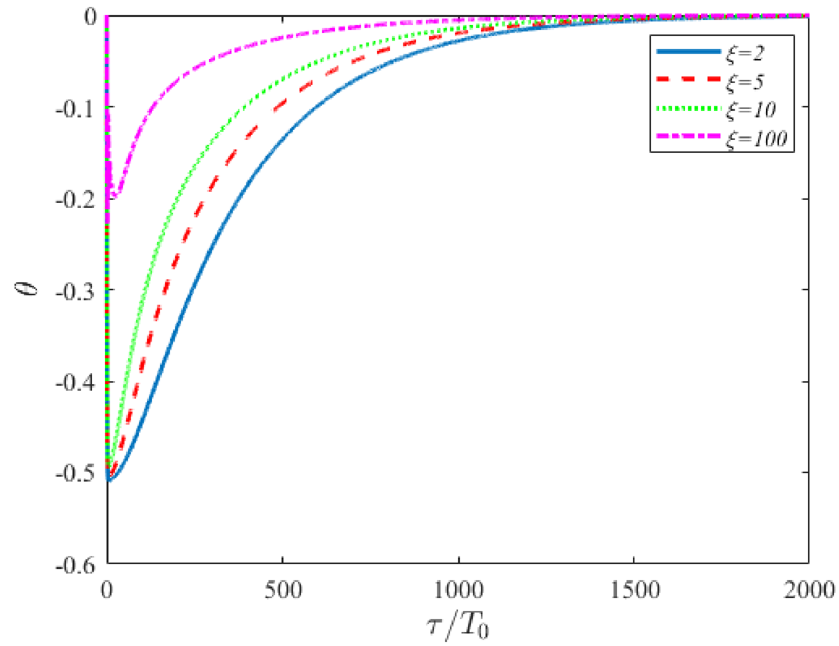

Figure 5.5 Libration angle for different length ratios at $k_3 = 10$

In conclusion, parametric study shows that tethered tug with small thrust can effectively despin the massive target. Longer tether can improve the despin efficiency, as well as the large tangential thrust that is along the tether.

5.2 Control Strategies Study of Despin

5.2.1 Control Strategies and Stability Analysis

This section is to study the control strategy to despin the target's rotation to a small level. All controllers are designed subject to the operational constraints: $T \geq 0$ and $|\theta| < \pi/2$.

a. Thrust Control

Frist, a thrust controller is designed to reduce the rotation of the massive target by thrusters on the small spacecraft for the fixed tether length. System's equations in Eq. (3.39) are written as follows,

$$\begin{aligned}
&\eta' = \frac{T\sin\theta}{\lambda} \\
&\theta'' = -\left(1+\frac{1}{\xi}\cos\theta\right)\frac{\sin\theta\left[\cos\theta\eta^2+\xi\left(\eta+\theta'\right)^2+u_t\right]}{\lambda+\sin^2\theta} - \frac{1}{\xi}\sin\theta\eta^2+\frac{u_n}{\xi} \\
&T = \frac{\lambda\left[\cos\theta\eta^2+\xi\left(\eta+\theta'\right)^2+u_t\right]}{\lambda+\sin^2\theta}
\end{aligned} \tag{5.9}$$

Equation (5.9) indicates the tether's libration angle θ is coupled with the large space target's rotational angular velocity η. Thus, it is easy find that one can despin the target if $T\sin\theta<0$. To this end, the libration angle of tether should satisfy $\sin\theta<0$ to reduce the angular velocity η due to tether tension T should be positive. Furthermore, the libration angle of the tether should be regulated by the normal thrust u_n to prevent the tether from wrapping around. One can design the thrust u_t to ensure the positive tether tension. Thus, a thrust controller similar to last section is designed as follows,

$$\begin{aligned}
&u_t = \mathrm{c} \\
&u_n = -\frac{1}{\xi}[(\xi+\cos\theta)\eta+\xi\theta'+k_\theta\frac{\theta}{\theta_{\max}^2-\theta^2}]
\end{aligned} \tag{5.10}$$

where k_θ denotes a positive control gain. $\theta_{\max}$ is set to $\pi/2$ to avoid the tether winding up. Notably, the thrust u_t is set as a constant thrust c, which is a positive constant to satisfy the positive tension from Eq. (5.9). u_n is a PD-like controller which has a barrier term to limit the tether libration angle.

b. Tension Control

Secondly, a tension controller is designed. The ideal is to accommodate the tether tension to regulate the tether length to dissipate the system's total kinetic energy, because the decrease of total kinetic energy leads rotating target despun. The controller is designed as following,

$$T = u_t + T_c + \sigma(k_{pt}\tilde{\xi} + k_{vt}\xi') \quad \text{and } T > 0 \tag{5.11}$$

where $\sigma(s)$ is strictly monotonously increasing saturation function defined as

$$\sigma(\mathrm{s}) = \begin{cases} s & \text{if } |s| < \varsigma \\ \varpi(s,\varsigma,\gamma) & \text{if } \varsigma \le |s| < \gamma \end{cases} \tag{5.12}$$

with $\varpi(s,\varsigma,\gamma) = \mathrm{sign}(s)\gamma + (\gamma - \varsigma)\tanh\left(\dfrac{s - \mathrm{sign}(s)\varsigma}{\gamma - \varsigma}\right)$ and $\gamma = T_c + u_t$, $\varsigma = 0.9\gamma$ [98].

T_c denotes the centrifugal force in the tether, $\tilde{\xi} = \xi - \xi_d$ denotes the error of tether length, k_{pt}, k_{vt} are the two positive control gains. The centrifugal force is positively definite, $T_c = \lambda[\eta^2 \cos\theta + \xi(\eta + \theta')^2]/(\sin^2\theta + \lambda) > 0$ and it is assumed to be slowly varying. Moreover, a thrust $u_t \ge 0$ is given to compare the efficiency of despin.

c. Hybrid Control

Finally, a hybrid control in combination of tension and thrust control is proposed to satisfy the constraints of positive tension and libration angle.

To study the closed-loop system's stability, we define the following energy-like Lyapunov function candidate, such that,

$$V = \tilde{K} + \int_0^{\tilde{\xi}} \sigma(k_{pt}\delta)\,\mathrm{d}\delta + \int_0^{\xi} T_c d\delta + V_b \tag{5.13}$$

where $\tilde{K} = K/(m_1 r\omega_0^2)$ denotes the dimensionless kinetic energy and $V_b = \frac{k_\theta}{2}\log\frac{\theta_{\max}^2}{\theta_{\max}^2 - \theta^2}$ is a barrier Lyapunov function to limit the tether angle within $\pi/2$ and V_b is bounded from below. Because of u_n with the opposite sign of the $\theta/\left(\theta_{\max}^2 - \theta^2\right)$, then $u_n \to -\infty$ if $\theta \to \pi/2$, which will result in tether angle to keep away with $\pi/2$. Similar results will be obtained if $\theta \to -\pi/2$.Thus, in this study the tether angle is considered to be less than $\pi/2$.

Taking the time derivative of the Lyapunov function and combing with the controllers in Eqs. (5.10) and (5.11) yield that

$$
\begin{aligned}
V' &= (u_t - T)\xi' + u_t r \sin\theta\eta + u_n[(\xi + \cos\theta)\eta + \xi\theta'] \\
&\quad + \sigma(k_{pt}\tilde{\xi})\xi' + T_c\xi' + k_\theta \frac{\theta\theta'}{\theta_{\max}^2 - \theta^2} \\
&= (u_t - T)\xi' + u_n[(\xi + \cos\theta)\eta + \xi\theta'] \\
&\quad + \sigma(k_{pt}\tilde{\xi})\xi' + T_c\xi' + cr\sin\theta\eta + k_\theta \frac{\theta\theta'}{\theta_{\max}^2 - \theta^2} \\
&= -[\sigma(k_{pt}\tilde{\xi} + k_{vt}\xi') - \sigma(k_{pt}\tilde{\xi})]\xi' - \frac{1}{l}[(\xi + \cos\theta)\eta + \xi\theta']^2 + W
\end{aligned}
\tag{5.14}
$$

where $W = -k_\theta \dfrac{\theta}{\theta_{\max}^2 - \theta^2}(\dfrac{\xi + \cos\theta}{\xi})\eta + cr\sin\theta\eta$. We know $[\sigma(k_{pt}\tilde{\xi} + k_{vt}\xi') - \sigma(k_{pt}\tilde{\xi})]$ has the same sign of ξ' due to the strictly increasing function σ . If η is bounded, W is bounded due to θ within $\pi/2$. Therefore, the closed-loop system under the hybrid controller will be ultimately bounded with suitable parameters selected.

5.2.2 Simulation and Discussion

In this section, numerical simulations are used to verify the effectiveness of these control strategies. The initial conditions of the system are set as $(\xi,\eta,\theta,\theta')|_{\text{initial}} = (1,1,0,0)$. The target's initial angular velocity is set to $\omega_0 = 0.02$ rad/s, same as in Section 5.1.2. Similar, time scale is normalized by the target's rotation period, $T_0 = 2\pi / \omega_0$.

5.2.2.1 Despin by Thrust Only

First, the thrust control is tested. System's parameters are chosen as inertial ratio $\lambda = 2000$ and length ratio $\xi = 10$. Controller is used with control gain $k_\theta = 10$ and thrust $u_t = 0, 0.1, 1, 10$ in the simulation. As shown in Figure 5.6 (a-e), all states converge to zero as expected. Figure 5.6 (a) illustrates the time to despin the target decreases significantly from about 5,000 to 50 for the increase of u_t. At the same time, the libration angle of tether is stabilized to zero as in Figure 5.6 (b) and the angular velocity of libration decreases much faster in 15, see Figure 5.6 (c). Furthermore, all tether tensions stabilize at the magnitude of u_t as shown in Figure 5.6 (d), and the thrust u_n converges to zero shown in Figure 5.6 (e) at the end of despin. It is worth noting that the magnitudes of u_n are always less than 1.2 ($|u_n| \leq 1.2$) during despin, see Figure 5.6 (e). Current simulation case indicates the thrust control strategy is effective to despin the target and the thrust u_t has significant effect on the despin efficiency.

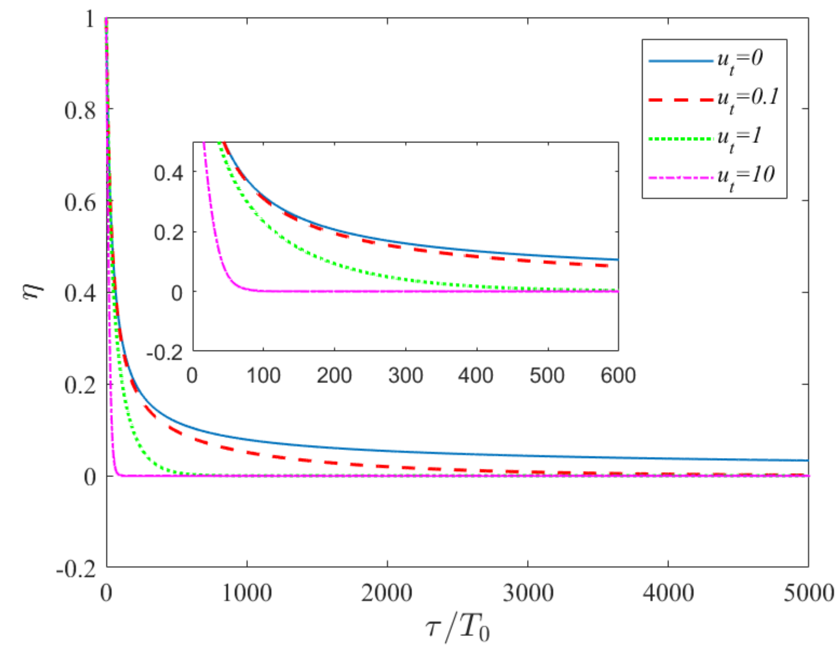

(a)

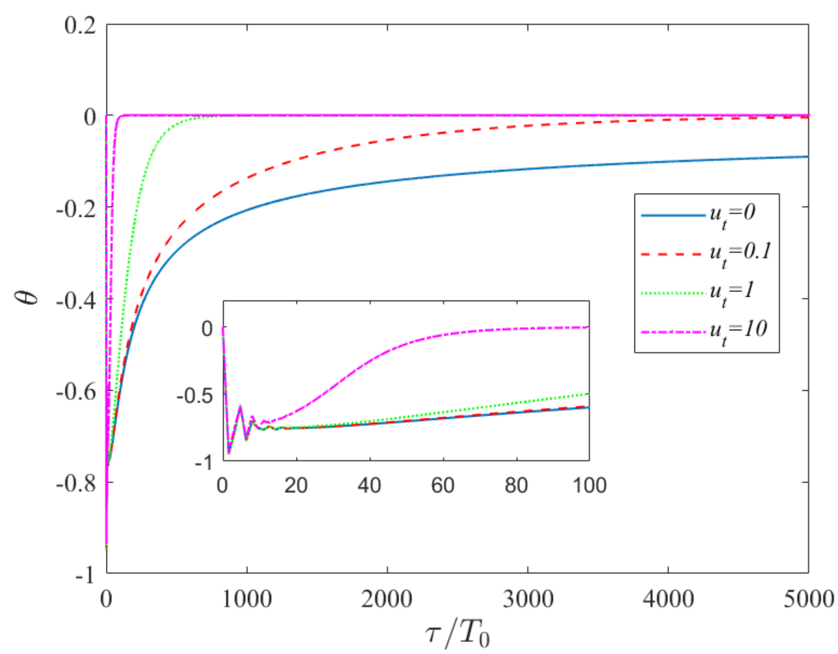

(b)

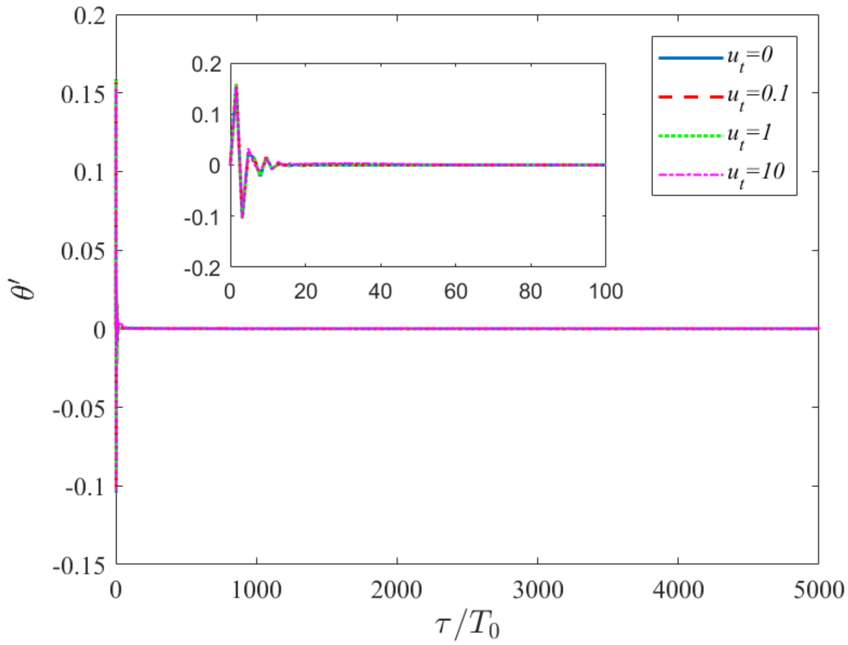

(c)

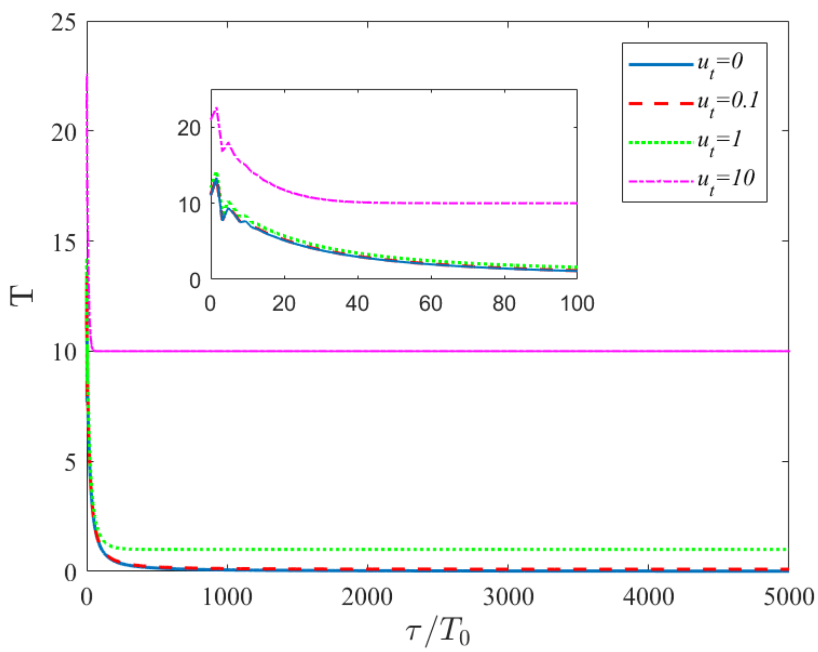

(d)

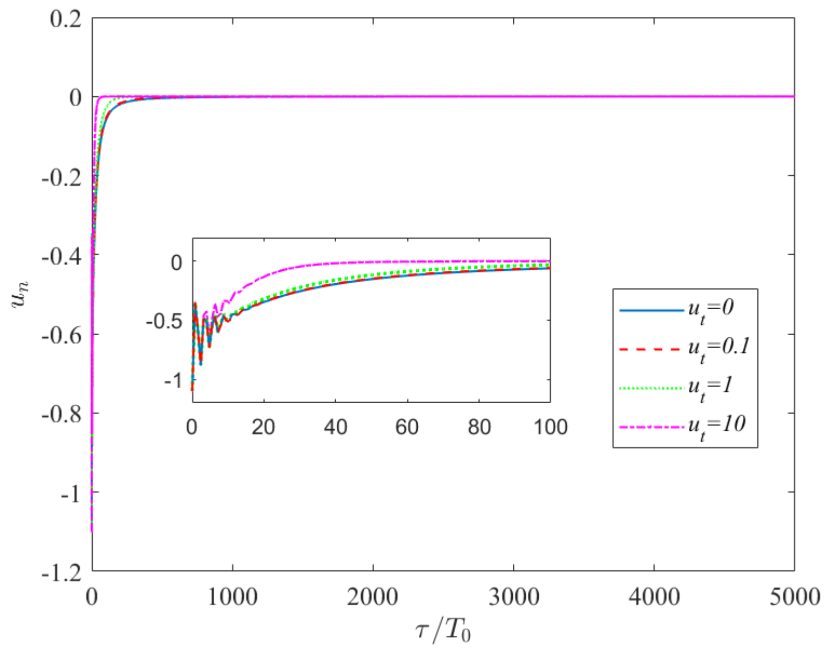

(e)

Figure 5.6 Despin process by thrust control.

5.2.2.2 Despin by Tension Control Only

Next, the tension control strategy is verified through simulation. In this section, we set the inertial ratio as $\lambda = 2000$ and the finial tether length as $\xi_d = 10, 50, 100, 200$, respectively. No thrust action will be applied, thus $u_t = u_n = 0$. Control gains $k_{pt} = 0.01$, $k_{vt} = 5$ are used for all cases. As shown in Figure 5.7 (a-e), the angular velocities of the target are decreasing as the tether deploys. Figure 5.7 (a) shows the angular velocity of target decreases from 1 to 0.95 and to 0.05 with the deployment of the tether. This is because the increase of the tether length means the increase system's inertial momentum, which will result in system's angular velocity decrease. However, the max magnitude of tether libration increases with the increase of the final tether length, see Figure 5.7 (b). This is because the induced Coriolis force by deployment results in the libration of tether as tether deploys. As is clear from Figure 5.7 (d), the tensions finally approach some constants which equal to the centrifugal force, because the target's angular velocities are not de-spun to zero.

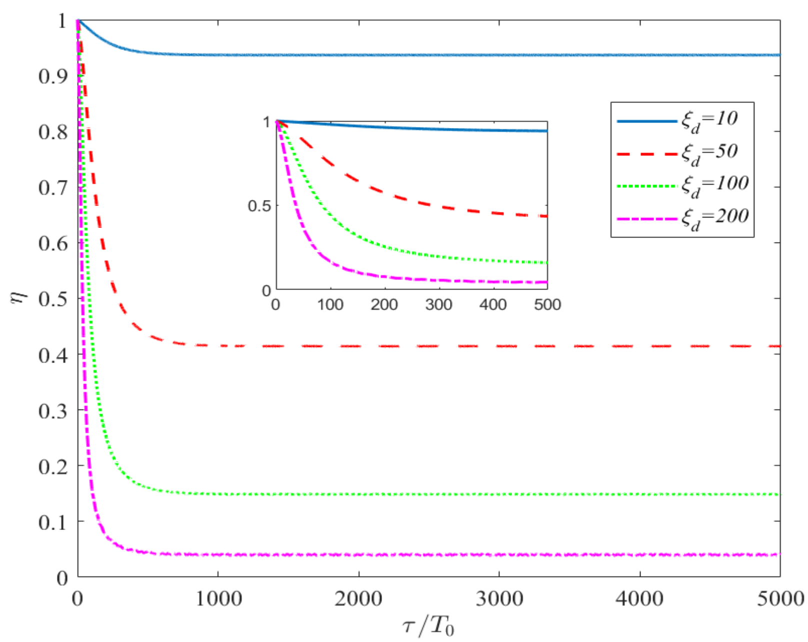

(a)

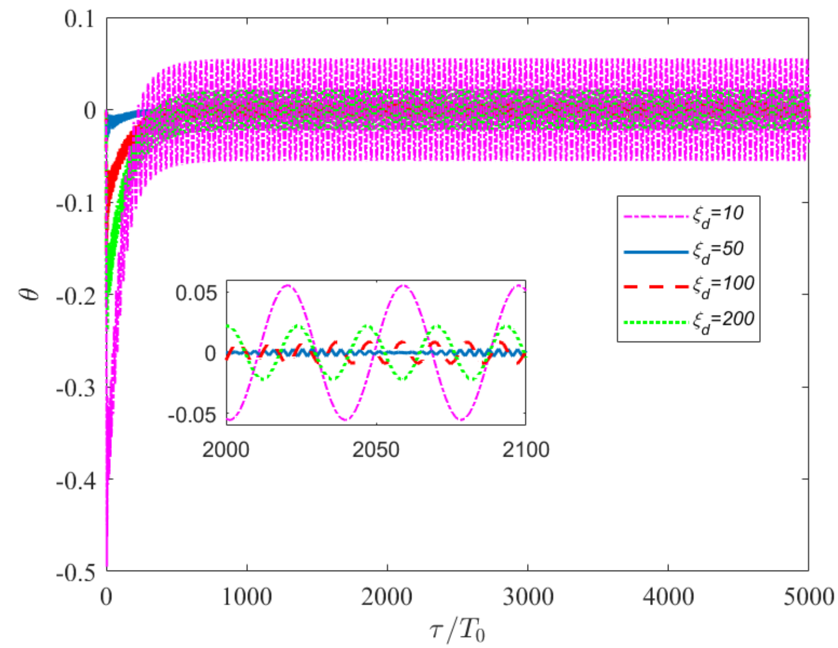

0.1
0
-0.1
-0.2
-0.3
-0.4
-0.5
θ
0
1000
2000
3000
4000
5000
τ/T_0
ξ_d=10
ξ_d=50
ξ_d=100
ξ_d=200
0.05
0
-0.05
2000
2050
2100

(b)

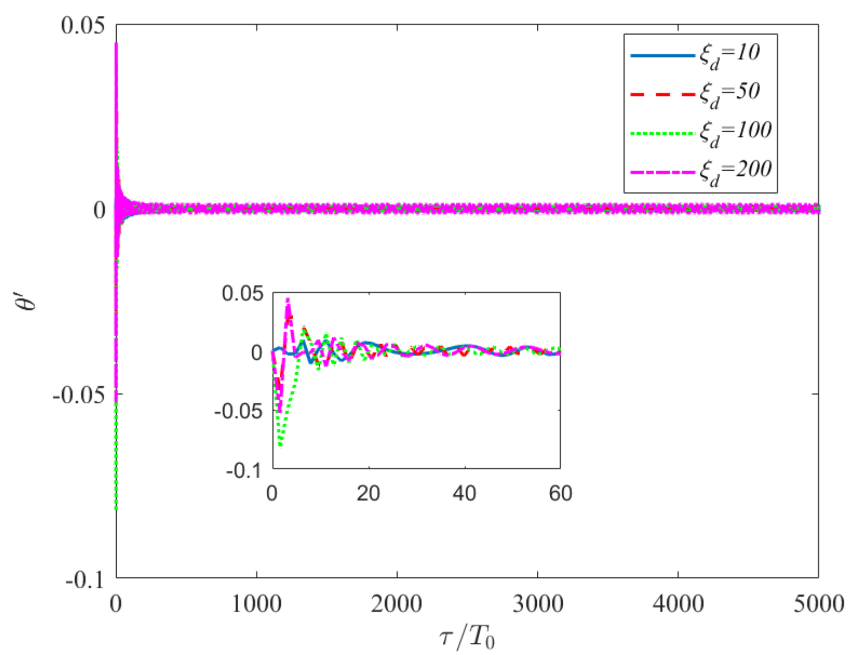

0.05
0
-0.05
-0.1
θ'
0
1000
2000
3000
4000
5000
τ/T_0
ξ_d=10
ξ_d=50
ξ_d=100
ξ_d=200
0.05
0
-0.05
-0.1
0
20
40
60

(c)

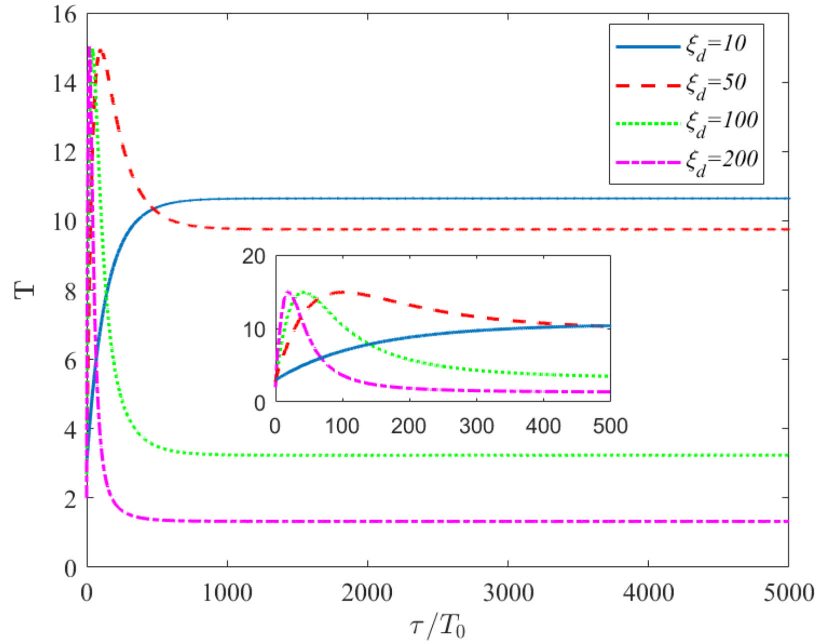

(d)

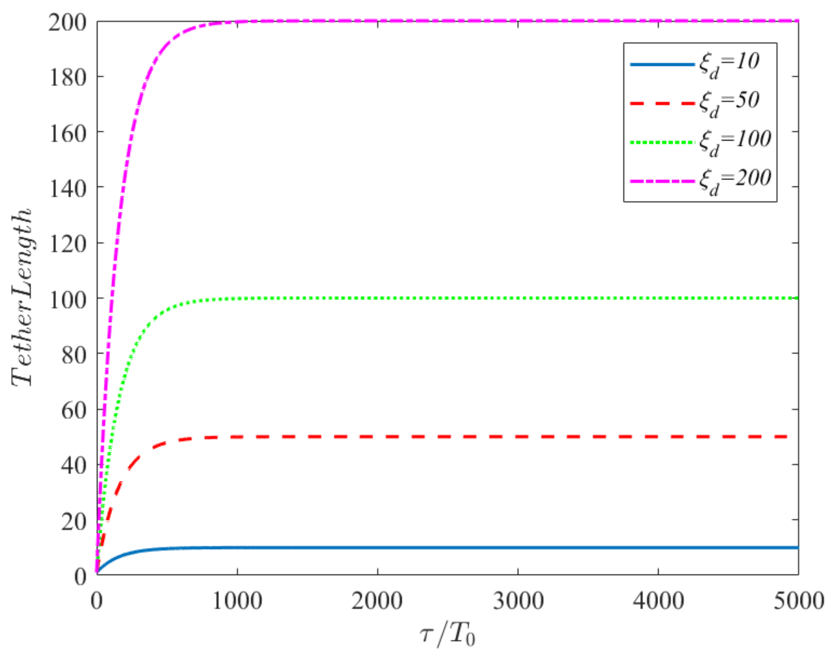

(e)

Figure 5.7 Despin process by tension control

5.2.2.3 Despin by Hybrid Control

In this section, the hybrid control strategy will be tested. The inertial ratio and the gains of tension controller are same as in Section 5.2.2.2. The desired tether length are set as $\xi_d = 10, 50, 100,\ 200$ and the thrust $u_t = 1$ in this simulation.

Simulation results are plotted in the Figure 5.8 (a-e). The target's angular velocity is despun quickly for the hybrid control. Figure 5.8 (a) shows the despin efficiency improves with the increase of. As from Figure 5.8 (b), the max libration angle of tether increases with the increase of ξ_d because of the effect of the Coriolis force. Notably, the libration constraint $\theta_{\max} < \pi / 2$ are satisfied in all profiles. Next, Figure 5.8 (c-d) shows the tether is regulated to the desired length as expect and tether tension is always positive at the end of despin. As is clear from Figure 5.8 (e), the required thrust u_n is slightly bigger than that in the Section 5.2.2.1.

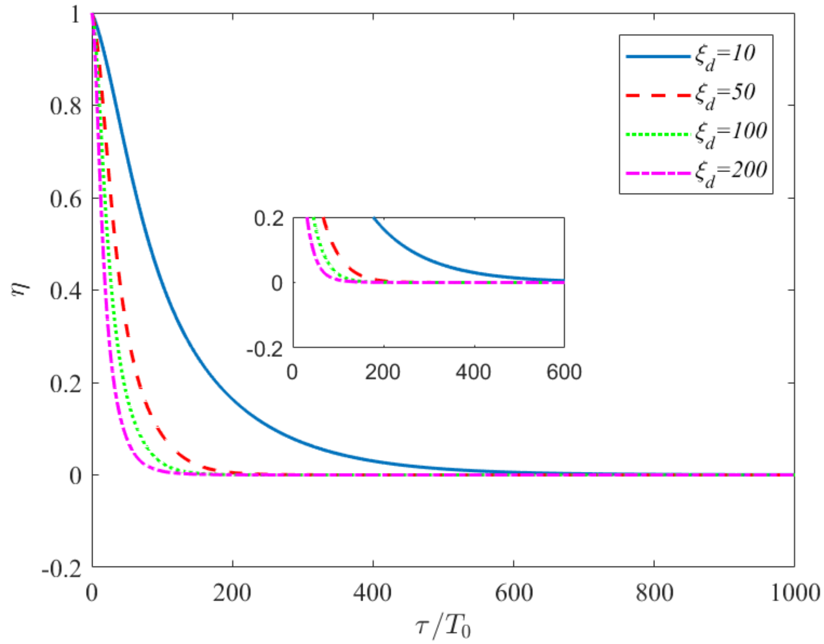

η
τ/T_0
ξ_d=10
ξ_d=50
ξ_d=100
ξ_d=200

(a)

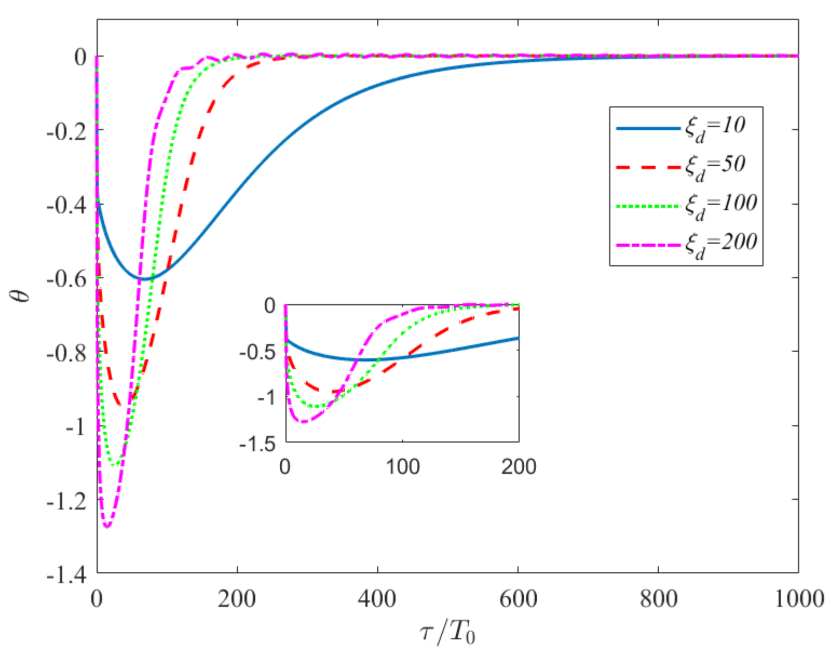

θ
τ/T_0
ξ_d=10
ξ_d=50
ξ_d=100
ξ_d=200

(b)

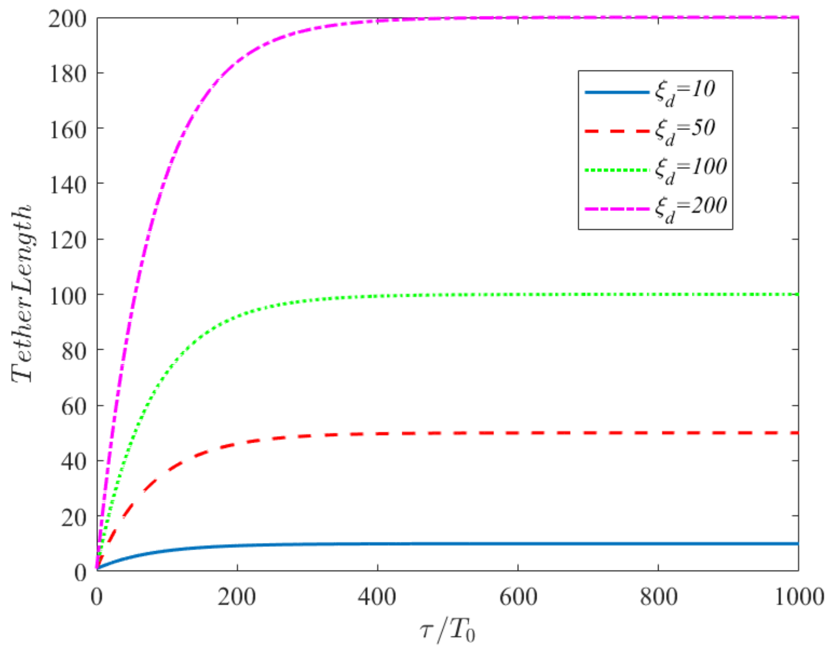

ξ_d=10
ξ_d=50
ξ_d=100
ξ_d=200
$Tether Length$
τ/T_0

(c)

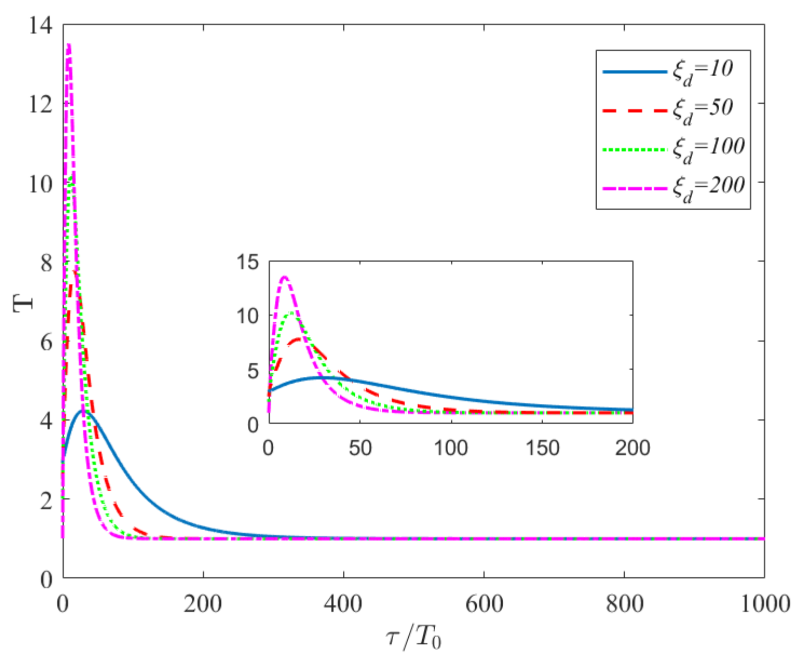

ξ_d=10
ξ_d=50
ξ_d=100
ξ_d=200
T
τ/T_0

(d)

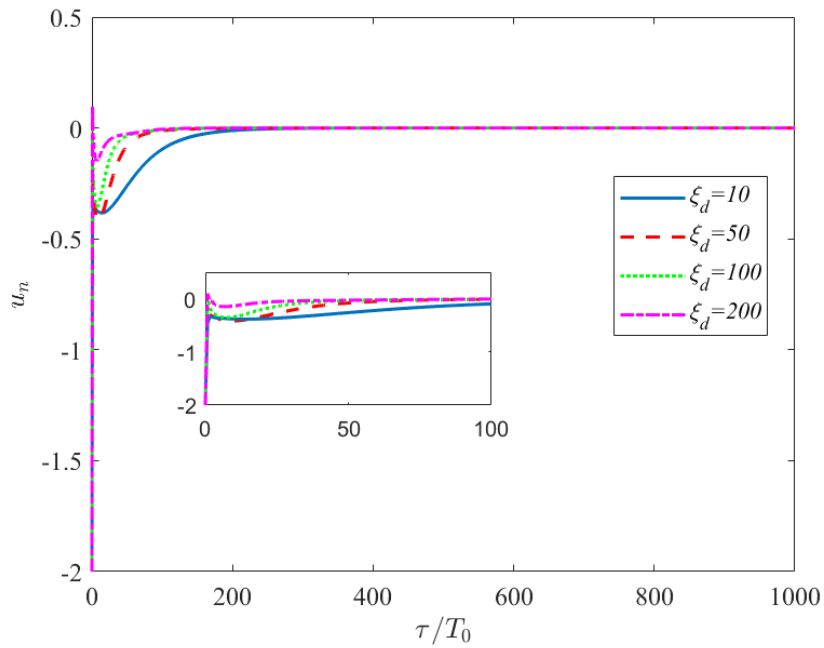

(e)

Figure 5.8 Despin process by hybrid control

According to the simulation comparison, we verify that the large rotating target could be de-spun by the designed control strategies. Thrust u_t has a positive effect on despinning the target and the libration angle can be limited by thrust u_n. Tension controllers require longer time to despin the target. Despin efficiency is enhanced with hybrid control, combination of thrust and tension. Thus, the hybrid control strategy is the best choice for the purpose of fast and complete despin.

5.3 Despin Large Target in Central Gravitational Filed

In this section, the dynamics behaviors and despin control are studied with consideration of the gravitational filed.

5.3.1 Equilibrium Configurations and Harmonic Motion

Considering the constant angular velocity α_0' and tether length, Eqs. (3.57)-(3.59) are reduced to

$$
\begin{aligned}
\beta'' = & \frac{\xi + \cos\beta}{\xi} \frac{\sin\beta}{\lambda + \sin^2\beta} \tilde{f}_\xi - \frac{1}{\xi} \sin\beta\alpha'^2 - \frac{2}{\xi} \sin\beta\bar{\Omega}\alpha' \\
& - \frac{3}{\xi} \bar{\Omega}^2 \cos\alpha \sin(\alpha + \beta) - 3\bar{\Omega}^2 \sin(\alpha + \beta) \cos(\alpha + \beta)
\end{aligned}
\tag{5.15}
$$

Figure 5.9(a-c) shows the phase portraits $\beta - \beta'$ for different ξ and α_0' with $\bar{\Omega} = 0.0036$ and $\lambda = 2{,}000$. It can be found that $(\beta, \beta') = (0,0)$ is a stable center equilibrium and $(\beta, \beta') = (\pm\pi, 0)$ are the unstable saddles. Further, the region of attraction is contracting with the increase of tether length. The similar trends for the region of attraction are found with the decrease of the angular velocity α_0'. Therefore, one can conclude that the system's stability will degenerate as the target's angular velocity reduces and tether deploys. To keep tether from wrapping around the target libration angle $|\beta| < \pi/2$, the only admissible equilibrium is at the origin.

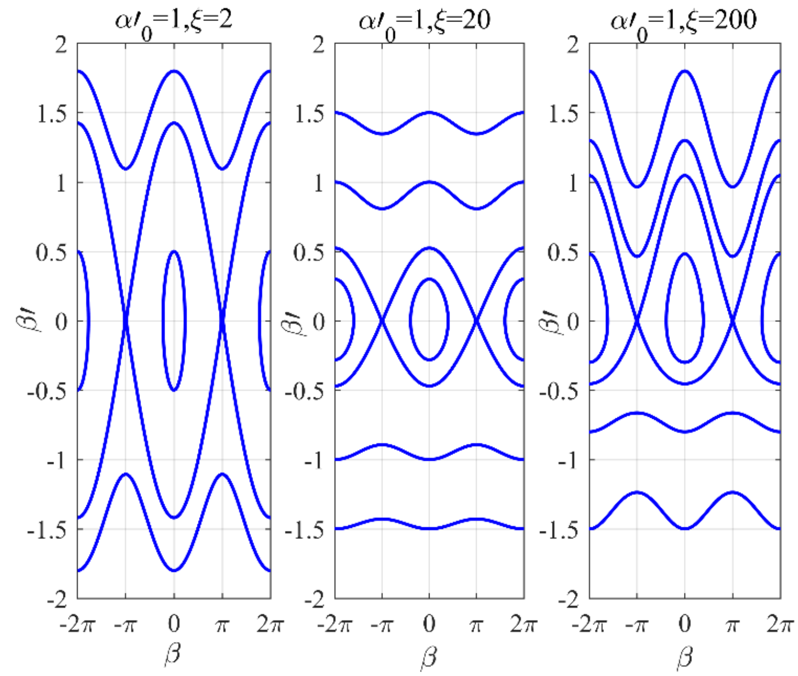

(a) Phase portraits of system with α_0'=1

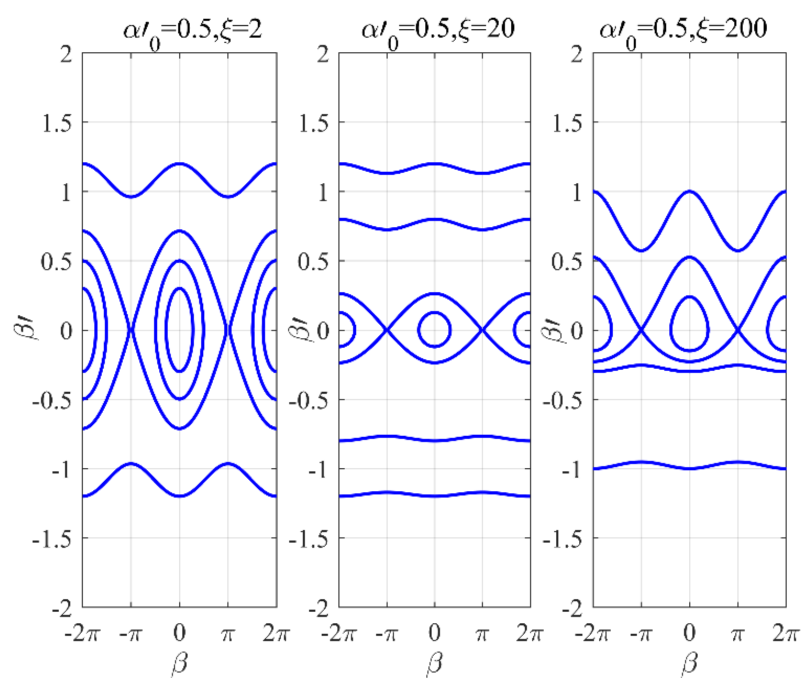

(b) Phase portraits of system with α_0'=0.5

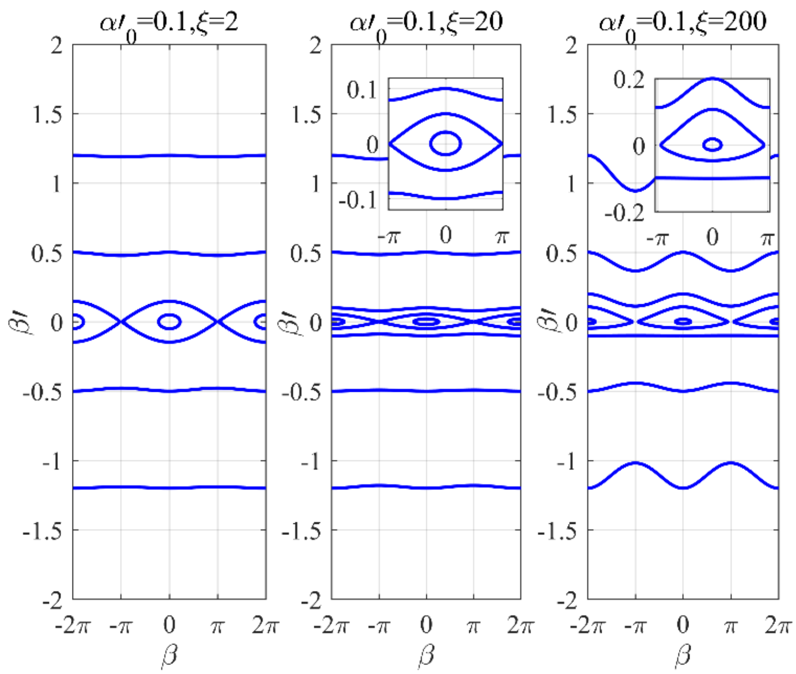

(c) Phase portraits of system with α_0'=0.1

Figure 5.9 Phase portraits of system with different α_0' and ξ

To find the equilibrium configuration of the tethered system, we set the first and second order derivatives to zero, $\xi' = \alpha' = \beta' = \xi'' = \alpha'' = \beta'' = 0$, $T = T_e = \text{constant}$ and $u = 0$ in Eqs. (3.57)-(3.59), such that,

$$-3\cos\alpha\cos(\alpha+\beta) - 3\xi\cos^2(\alpha+\beta) = -\frac{T}{\bar{\Omega}^2} \tag{5.16}$$

$$\begin{aligned} &3\sin\alpha\cos\alpha + 3\xi\sin\alpha\cos(\alpha+\beta) + \\ &3\xi\cos\alpha\sin(\alpha+\beta) + 3\xi^2\sin(\alpha+\beta)\cos(\alpha+\beta) = 0 \end{aligned} \tag{5.17}$$

$$3\xi\cos\alpha\sin(\alpha+\beta) + 3\xi^2\sin(\alpha+\beta)\cos(\alpha+\beta) = 0 \tag{5.18}$$

Simplify the above equations by,

$$(5.17)\text{-}(5.18)\times(1+\cos\beta/\xi)\text{-}(5.16)\times\sin\beta \tag{5.19}$$

Then we have,

$$T\sin\beta = 0 \tag{5.20}$$

Due to $|\beta| < \pi/2$ and $T > 0$, the admissible static equilibrium of tethered system exists only at $\beta = 0$.

In light of $\beta = 0$, Eq. (5.18) becomes,

$$\xi(1+\xi)\sin\alpha\cos\alpha = 0 \quad \Rightarrow \quad \alpha = n\pi/2, \quad n\in\mathbb{Z} \tag{5.21}$$

Thus, the equilibrium configurations of TSS are at $\alpha = n\pi/2, \beta = 0$. Illustrate these equilibrium configurations of tethered system in orbit as shown in Figure 5.10. There are two in local vertical (a) and (b) and two in local horizon (c) and (d). It should be pointed out such equilibrium configuration of TSS does not exist in free space.

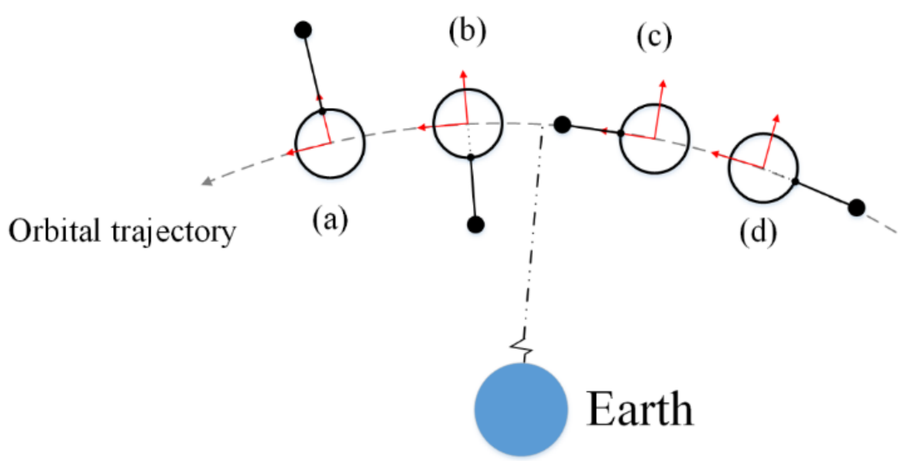

Figure 5.10 Equilibrium configurations at:

(a) $\alpha = 0$, (b) $\alpha = \pi$, (c) $\alpha = \pi/2$, and (d) $\alpha = 3\pi/2$.

The two equilibrium configurations in local vertical are stable while the two in local horizon are unstable. Therefore, the admissible equilibrium configurations of TSS are determined at (a) and (b) in local vertical direction. Then, one can obtain the tether tension T_e at the equilibrium configurations from Eq.(5.16) with $\alpha = n\pi, \beta = 0$, as follows,

$$T_e = 3\bar{\Omega}^2 (1+\xi) \tag{5.22}$$

Considering the constant tether length and setting control action to zero, i.e., $\xi' = \xi'' = 0$ and $u = 0$, then Eqs.(3.51)-(3.53) are reduced to

$$\begin{aligned} \alpha'' &= -\frac{\sin\beta}{\lambda + \sin^2\beta}\tilde{f}_\xi \\ \beta'' &= -\frac{1}{\xi}\begin{bmatrix} (\cos\beta + \xi)\alpha'' + \sin\beta\alpha'^2 + 2\sin\beta\,\bar{\Omega}\alpha' \\ +3\bar{\Omega}^2\cos\alpha\sin(\alpha+\beta) + 3\xi\,\bar{\Omega}^2\sin(\alpha+\beta)\cos(\alpha+\beta) \end{bmatrix} \end{aligned} \tag{5.23}$$

To solve the dynamic motions near the equilibrium state, one can linearize the Eq.(5.23) at the equilibrium state

$$\begin{bmatrix} \lambda & 0 \\ 1+\xi & \xi \end{bmatrix} \frac{\mathrm{d}^2}{\mathrm{d}\upsilon^2} \begin{bmatrix} \alpha \\ \beta \end{bmatrix} + 3(1+\xi) \begin{bmatrix} 0 & -1 \\ 1 & 1 \end{bmatrix} \begin{bmatrix} \alpha \\ \beta \end{bmatrix} = 0 \tag{5.24}$$

where $\upsilon = \Omega\, t$ denotes the dimensionless time, the true anomaly.

Assuming $(\alpha,\beta)^T = \mathbf{Z}e^{iw\upsilon}$ and putting into Eq. (5.24) yields

$$\left\{\begin{bmatrix}\lambda & 0\\ 1+\xi & \xi\end{bmatrix}w^2 - 3(1+\xi)\begin{bmatrix}0 & -1\\ 1 & 1\end{bmatrix}\right\}\mathbf{Z} = 0 \tag{5.25}$$

where $\mathbf{Z}$ is the complex amplitude.

Eq.(5.25) has non-trivial solutions, only when

$$\det\left\{\begin{bmatrix}\lambda & 0\\ 1+\xi & \xi\end{bmatrix}w^2 - 3(1+\xi)\begin{bmatrix}0 & -1\\ 1 & 1\end{bmatrix}\right\} = 0 \tag{5.26}$$

which leads to,

$$w^2_{1,2} = \frac{3\left[\xi+\lambda+1\pm\sqrt{(\lambda-\xi)^2+2\lambda+2\xi+1}\right](1+\xi)}{2\lambda\xi} \tag{5.27}$$

where $w_{1,2}$ denote the fast and slow frequencies of harmonic motion, respectively.

Then, the solution of α and β can be given as,

$$\begin{bmatrix}\alpha(\upsilon)\\ \beta(\upsilon)\end{bmatrix} = \left[A_1\cos(w_1\upsilon)+B_1\sin(w_1\upsilon)\right]\mathbf{b}_1 + \left[A_2\cos(w_2\upsilon)+B_2\sin(w_2\upsilon)\right]\mathbf{b}_2 \tag{5.28}$$

$$\mathbf{b}_{1,2} = \left[-\frac{2\xi}{\xi+\lambda+1\pm\sqrt{(\lambda-\xi)^2+2\lambda+2\xi+1}},\ 1\right]^{\mathrm{T}} \tag{5.29}$$

From Eq.(5.28), the TSS oscillates with pendular motions near the equilibrium. The amplitudes of harmonic motion ($A_{1,2}$, $B_{1,2}$) can be obtained with initial conditions.

Without loss of generality, the initial condition is assumed as $\alpha(0)=0$, $\frac{d\alpha}{d\upsilon}(0)=\delta$, $\beta(0)=0$, $\frac{d\beta}{d\upsilon}(0)=0$, where δ is a small constant. Substituting this initial condition into Eq. (5.28) leads to,

$$\begin{aligned} A_{1,2} &= 0 \\ B_{1,2} &= \pm\frac{\lambda\delta}{w_{1,2}\sqrt{(\lambda-\xi)^2+2\lambda+2\xi+1}} \end{aligned} \tag{5.30}$$

Then, the approximate solutions of Eq. (5.24) are obtained as,

$$\begin{bmatrix} \alpha(\upsilon) \\ \beta(\upsilon) \end{bmatrix} = B_1 \sin(w_1\upsilon)\mathbf{b}_1 + B_2 \sin(w_2\upsilon)\mathbf{b}_2 \tag{5.31}$$

5.3.2 Control Laws and Stability

Inspired from the previous study in section 5.3, two control laws are proposed here to despin the rotating target.

a. Tension Control Law

First, a pure tension control is proposed as follows,

$$T = T_e + k_p(\xi-\xi_d) + k_v\dot{\xi} \tag{5.32}$$

where T_e denotes the tether tension at the equilibrium given in Eq.(5.32). k_p, k_v

denotes the control gains to be determined and ξ_d denotes the desired tether length.

To analyze the closed-loop stability under the pure tension control law, a Lyapunov function V is defined as,

$$\begin{aligned} V &= \frac{1}{2}\mathbf{X}^{\mathrm{T}}\mathbf{H}\mathbf{X} + 3\xi\bar{\Omega}^2\left[1-\cos\alpha\cos\left(\alpha+\beta\right)\right] \\ &+\frac{3}{2}\bar{\Omega}^2\sin^2\alpha + \frac{3}{2}\xi^2\bar{\Omega}^2\sin^2\left(\alpha+\beta\right) + \frac{k_p}{2}\left(\xi-\xi_d\right)^2 \end{aligned} \tag{5.33}$$

where $\mathbf{X} = \mathrm{col}\left(\xi', \alpha', \beta'\right)$ and $\mathbf{H}$ is a positive definite matrix as

$$\mathbf{H} = \begin{bmatrix} 1 & \sin\beta & 0 \\ \sin\beta & \lambda+1+\xi^2+2\xi\cos\beta & \xi^2+\xi\cos\beta \\ 0 & \xi^2+\xi\cos\beta & \xi^2 \end{bmatrix}$$

It is easy to find $V \geq 0$ due to positive definiteness of $\mathbf{H}$ and $\xi > 0$.

Then, by taking the derivate of V with respect to the dimensionless time one has,

$$V' = -T\xi' + 3\xi'\bar{\Omega}^2 + 3\xi\xi'\bar{\Omega}^2 + k_p\left(\xi-\xi_d\right)\xi' \tag{5.34}$$

Putting the Eq. (5.32) into Eq. (5.34), we have

$$V' = -k_v\xi'^2 \tag{5.35}$$

Eq.(5.35) shows V is strictly decreasing if $\xi' \neq 0$. Thus, the target's angular velocity will have an upper bound because V is bounded.

Further, apply the operation,

$$\text{Eq. }(14)-\text{Eq. }(15)\times(1+\cos\beta/\xi)-\text{Eq. }(13)\times\sin\beta \tag{5.36}$$

one has

$$\lambda\alpha''=T\sin\beta \tag{5.37}$$

Thus, the angular velocity of target will keep decreasing if the libration angle $\beta<0$, which can be ensured in the tether deployment due to the induced Coriolis force $2\left(\bar{\Omega}+\alpha'+\beta'\right)\xi'$ acting in the negative direction of β.

Further, the proposed tension control law is modified as following to enhance the controller's performance,

$$T=T_e+\left(1+\xi\right)\left(\alpha'+\bar{\Omega}\right)^2+k_p\left(\xi-\xi_d\right)+k_v\dot{\xi} \tag{5.38}$$

b. Hybrid Control Law

To avoid the tether winding around the target, a thrust controller is given as,

$$u=-k_\beta\varphi\left(\beta\right)-k_{\beta'}\beta'-k_{\alpha'}\alpha' \tag{5.39}$$

where $k_\beta,k_{\beta'},k_{\alpha'}$ denote the control gains and $\varphi\left(\beta\right)=\dfrac{\beta}{1-\left(2\beta/\pi\right)^2}$ is a barrier term to limit the libration angle.

Put Eqs. (5.39) and (5.32) into Eqs.(3.57)-(3.59) and linearize the system at the equilibria $[\xi, \xi', \alpha, \alpha', \beta, \beta'] = [\xi_d, 0, n\pi, 0, 0, 0]$, such that

$$\mathbf{y}' = \mathbf{A}\mathbf{y} \tag{5.40}$$

where $\mathbf{y} = \left[(\xi - \xi_d), \xi', (\alpha - n\pi), \alpha', \beta, \beta' \right]^T$ denote the state vector and $\mathbf{A}$ is the Jacobin matrix.

$$\mathbf{A} = \begin{bmatrix} 0 & 1 & 0 & 0 & 0 & 0 \\ -k_p & -k_v & 0 & 2\xi_d + 2 & 0 & 2\xi_d \\ 0 & 0 & 0 & 1 & 0 & 0 \\ 0 & 0 & 0 & 0 & \dfrac{3\xi_d + 3}{\lambda} & 0 \\ 0 & 0 & 0 & 0 & 0 & 1 \\ 0 & -\dfrac{2}{\xi_d} & -\dfrac{3\xi_d + 3}{\xi_d} & -\dfrac{k_{\alpha'}}{\xi_d} & -\dfrac{k_\beta \lambda + 3(\xi_d + 1)\lambda + 3(\xi_d + 1)^2}{\xi_d \lambda} & -\dfrac{k_{\beta'}}{\xi_d} \end{bmatrix} \tag{5.41}$$

Then, to ensure the stability of the closed-loop system in Eq.(5.40), one can analyze the characteristic equation of $\mathbf{A}$, where obtains a sixth order characteristic equation which is hard to solve. Hence, a conservative way to determine the stable regions of the control gains is given as following.

1) Assume $u = 0$, i.e., $k_\beta = k_{\beta'} = k_{\alpha'} = 0$, then one can obtain tension control gains k_p, k_v should satisfy,

$$k_p > 0, k_v > 0 \tag{5.42}$$

2) Assume no tension control action, i.e., $k_p = k_v = 0$, then one can

obtain thrust control gains $k_\beta, k_{\beta'}, k_{\alpha'}$ should satisfy,

$$\begin{aligned}
&k_\beta > 0, k_{\beta'} > 0, k_{\alpha'} > 0 \\
&\lambda k_\beta k_{\beta'} + 3k_{\beta'} + 3\lambda k_{\beta'} + \xi_d\left(7\lambda k_{\beta'} + 6k_{\beta'} - 3k_{\alpha'}\right) + 3\xi_d{}^2\left(k_{\beta'} - k_{\alpha'}\right) > 0 \\
&3k_{\beta'}k_{\alpha'} + \lambda\left(k_\beta k_{\beta'}k_{\alpha'} - 7k_{\beta'}{}^2 + 3k_{\beta'}k_{\alpha'}\right) + \\
&\xi_d\left(7\lambda k_{\beta'}k_{\alpha'} + 6k_{\beta'}k_{\alpha'} - 3k_{\alpha'}{}^2 - 7\lambda k_{\beta'}{}^2\right) + 3\xi_d{}^2\left(k_{\beta'}k_{\alpha'} - k_{\alpha'}{}^2\right) > 0
\end{aligned} \tag{5.43}$$

3) After the gains of thrust control and tension control obtained, check if the eigenvalue of **A** locates in the left-plane. If not, reselect the gains from in 1) and 2).

For $\lambda = 2{,}000$ and $\xi_d = 100$, the gains of controllers are selected as $k_p = 0.5$, $k_v = 100$ and $k_\beta = 0.5, k_{\beta'} = 100, k_{\alpha'} = 100$.

5.3.3 Simulation and Discussion

In this section, the TSS's dynamic behaviors are first simulated to study the tether's libration motion. Then, two simulations are conducted to verify the effectiveness of the proposed two control laws. The simulations are ran in the Matlab 2017a with ODE 45 solver. TSS's physical parameters are listed as in Table 5.1.

Table 5.1 Physical parameters of system

Parameter	Value
m_1	250 kg
m_2	10^6 kg

R	42164 km
r	10 m
Ω	$7.291*10^{-5}$ rad/s
$\dot{\alpha}_0$	0.02 rad/s

5.3.3.1 Harmonic Motion

To simulate the harmonic motions, the inertial ratio $\lambda = 2000$ and length ratio $\xi = 10$ are used with the initial condition at $\left[\alpha_0, \frac{d\alpha_0}{d\upsilon}, \beta_0, \frac{d\beta_0}{d\upsilon}\right] = [0,\ 0.03,\ 0,\ 0]$.

From Eqs.(5.28)-(5.31), one can get the approximate solutions as,

$$\begin{bmatrix} \alpha(\upsilon) \\ \beta(\upsilon) \end{bmatrix} = \begin{bmatrix} -0.00008288\sin(1.81705\upsilon) + 0.23478108\sin(0.12842\upsilon) \\ 0.01658486\sin(1.81705\upsilon) - 0.23466316\sin(0.12842\upsilon) \end{bmatrix} \tag{5.44}$$

The profiles of α, β and tether tension are plotted in Figure 5.11 (a-e), where the states of system oscillate periodically around the equilibrium. As shown in Figure 5.11 (a) and (b), the approximate solutions are well consistent with the numerical solutions for the given initial condition. Figure 5.11 (c) shows the angular velocity of the target mainly performs the slow-mode motion because the magnitude of fast mode is very small, seen from Eq.(5.44). However, two modes of angular velocity of the tether libration are very clear in Figure 5.11 (d). As shown in Figure 5.11(e), the profile of the tether tension oscillates around 33 periodically. Figure 5.11 (f) shows the energy exchange between the target and spacecraft, where system's energy with respect to the initial value is defined by

$$\Delta E_{M,m} = E_{M,m}(\upsilon) - E_{M,m}(0) \tag{5.45}$$

Here $E_{M,m}$ are the normalized energies of target and spacecraft. As is clear from Figure 5.11 (f), the system's total mechanical energy is conservative and energy is periodically transferring between the target and the small spacecraft via tether.

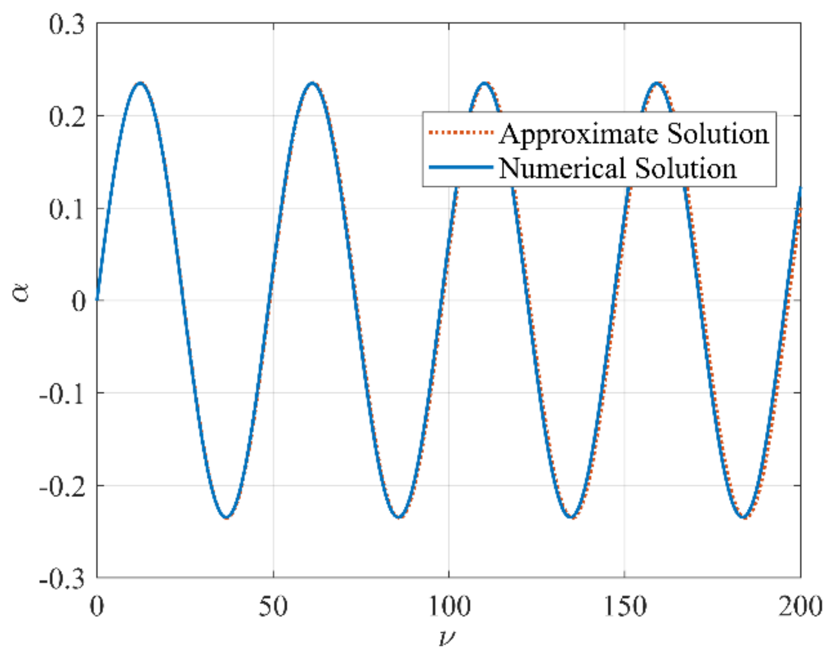

(a)

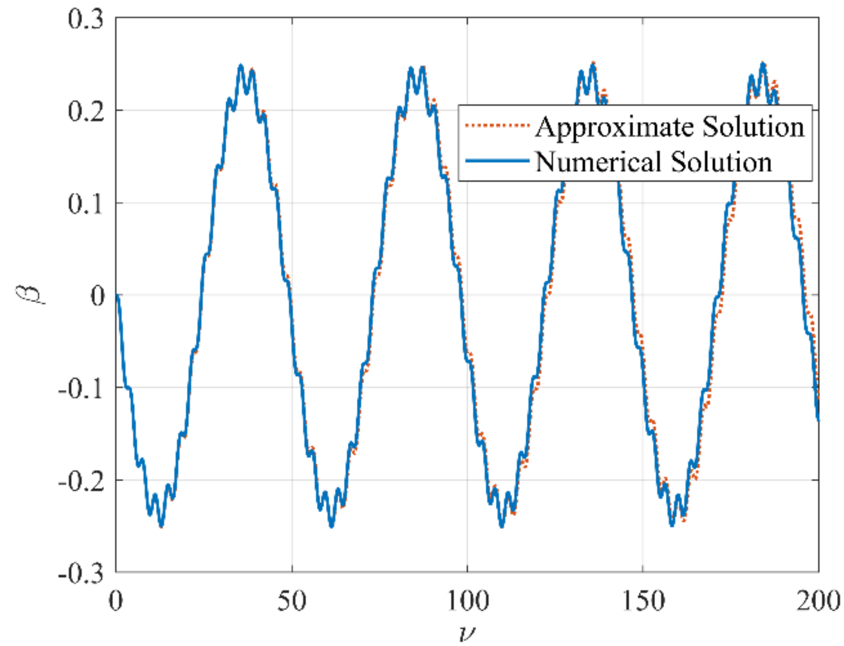
Approximate Solution
Numerical Solution
β
ν
0.3
0.2
0.1
0
-0.1
-0.2
-0.3
0
50
100
150
200

(b)

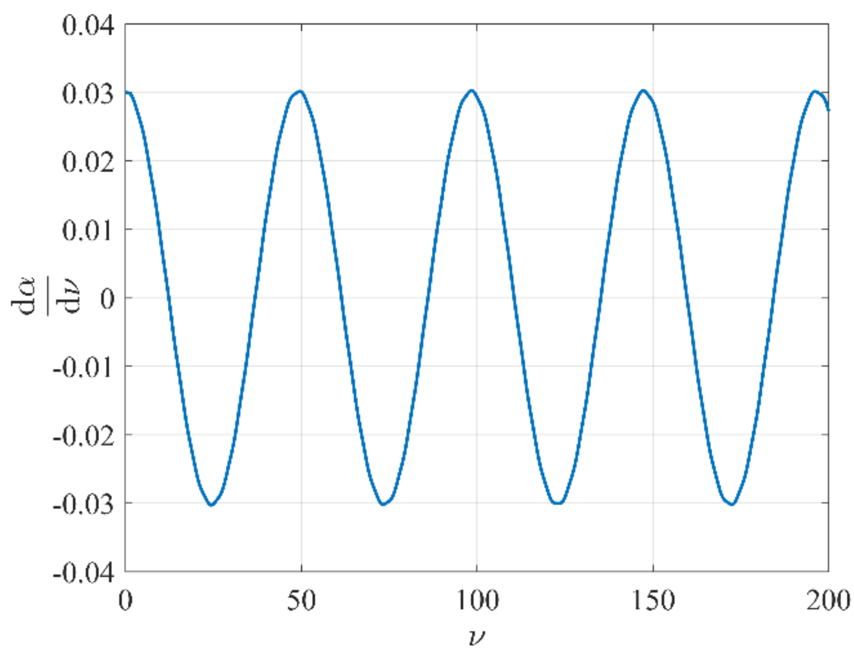
$\frac{d\alpha}{d\nu}$
ν
0.04
0.03
0.02
0.01
0
-0.01
-0.02
-0.03
-0.04
0
50
100
150
200

(c)

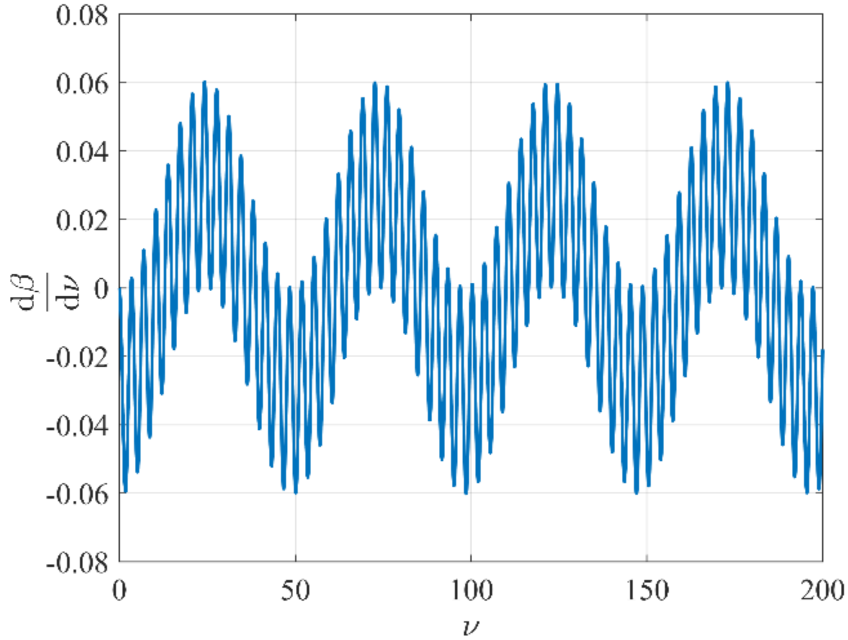
0.08
0.06
0.04
0.02
0
-0.02
-0.04
-0.06
-0.08
$\frac{d\beta}{d\nu}$
0
50
100
150
200
ν

(d)

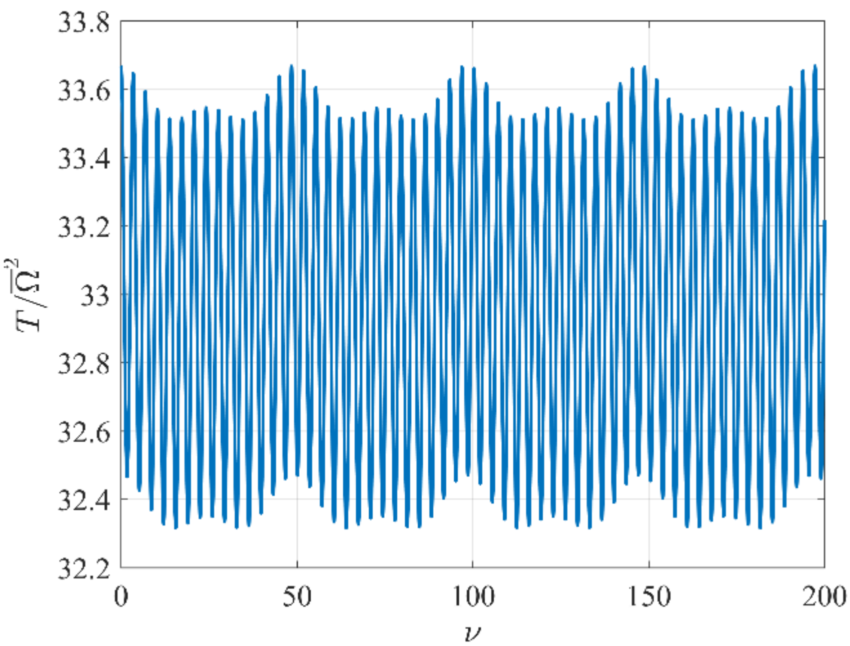
33.8
33.6
33.4
33.2
33
32.8
32.6
32.4
32.2
$T/\overline{\Omega}^2$
0
50
100
150
200
ν

(e)

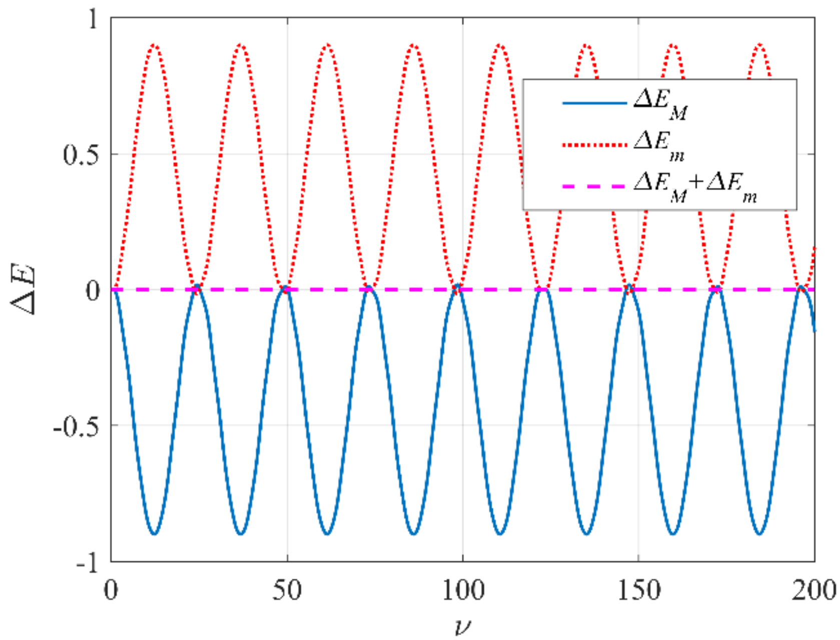

(f)

Figure 5.11 Time histories of state during despin process

5.3.3.2 Despin by Tension Control

In this case, the proposed tension control law to despin the target is first verified by numerical simulation with system's initial condition at $(\alpha_0, \alpha_0', \xi_0, \xi_0', \beta_0, \beta_0') = (0,\ 1,\ 0.01,\ 1,\ 0,\ 0)$, inertial ratio $\lambda = 2{,}000$, and the desired dimensionless tether $\xi_d = 100$.

The simulation results are plotted in Figure 5.12 (a-h). Figure 5.12 (b) shows that magnitude of target's angular velocity decreases very quickly with the increase of the tether length, and it finally stabilizes to a small number (< 0.165) as the tether length reaches $\xi_d = 100$. Consequently, the target's rotation angle increases persistently with time, as shown in Figure 5.12 (a). In the meantime, Figure 5.12 (c) and (d) show that libration of tether and its angular velocity, (β, β'), stabilize to zero as expected and the libration angle of tether (β) keeps negative during the despin process and less than $\pi / 2$. Figure 5.12 (f) illustrates the tether deployment velocity finally stabilizes to zero under the proposed tension control law. Furthermore, as shown in Figure 5.12 (g), the tether tension is always positive during the despin process and finally stabilizes to 2.74. This is because the target cannot be despun completely only by tension control. Figure 5.12 (h) presents the target's and spacecraft's energy variation, where the target's kinetic energy is dissipated by the tension control law, which acts like a damping-spring. There is a part of the energy transferred from large target to the small spacecraft. Moreover, the target's kinetic energy keeps decreasing for non-zero the tether deployment velocity. However, the target's total energy does not decrease to zero for the tension controller.

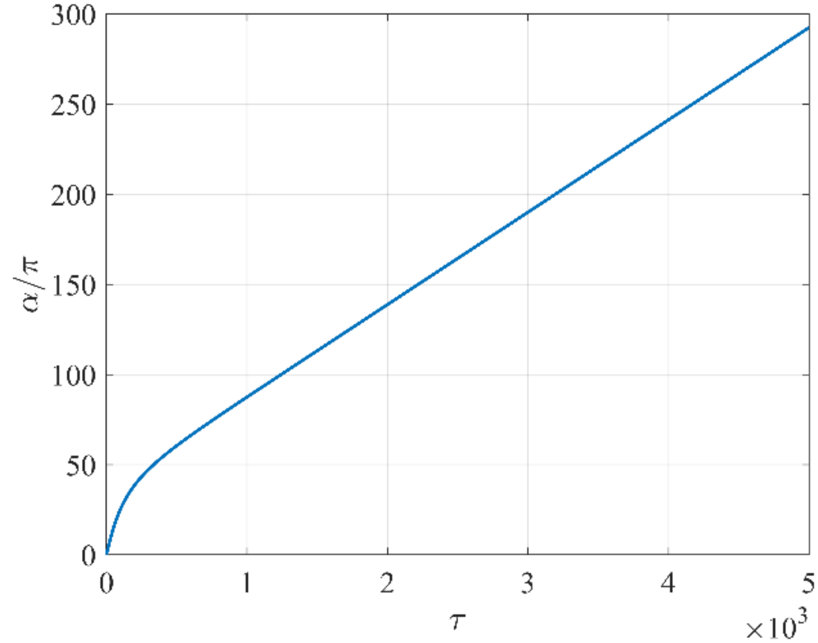

300
250
200
150
100
50
0
α/π
0
1
2
3
4
5
τ
$\times 10^3$

(a)

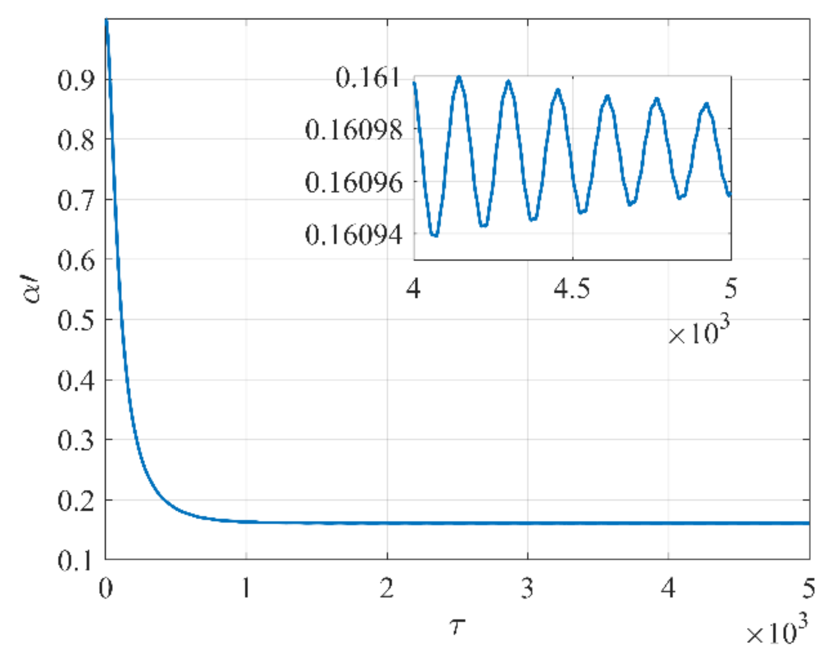

0.9
0.8
0.7
0.6
0.5
0.4
0.3
0.2
0.1
α'
0.161
0.16098
0.16096
0.16094
4
4.5
5
$\times 10^3$
0
1
2
3
4
5
τ
$\times 10^3$

(b)

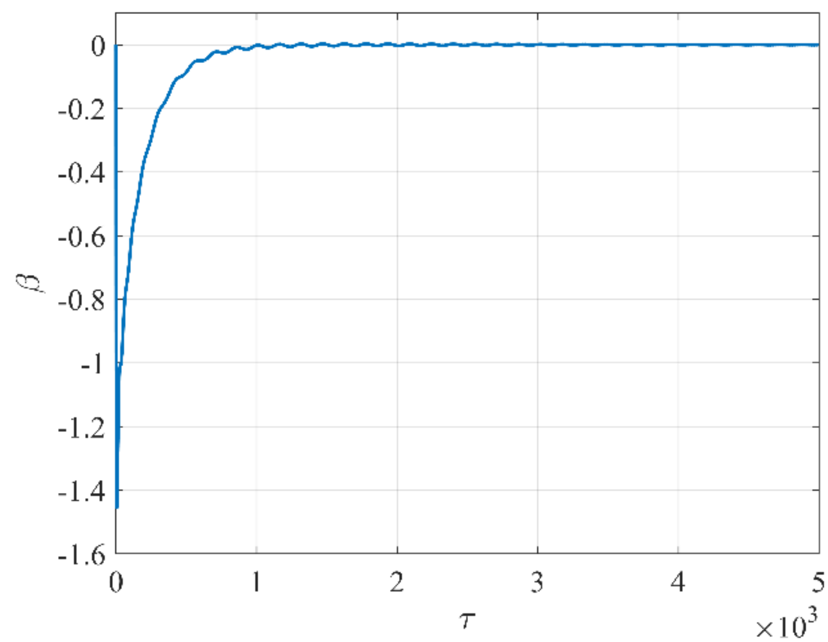

0
-0.2
-0.4
-0.6
-0.8
-1
-1.2
-1.4
-1.6
β
0
1
2
3
4
5
τ
×10^3

(c)

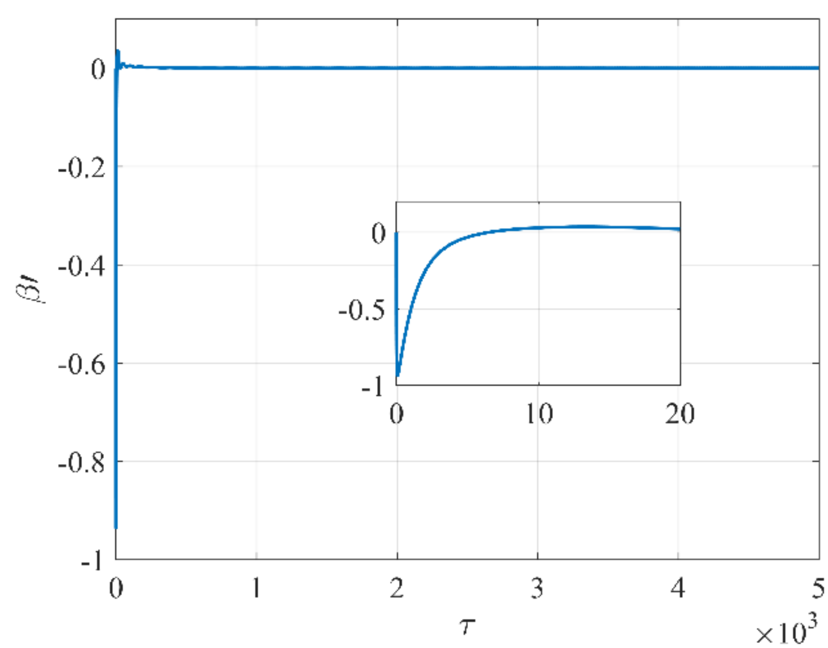

0
-0.2
-0.4
-0.6
-0.8
-1
βI
0
1
2
3
4
5
τ
×10^3
0
-0.5
-1
0
10
20

(d)

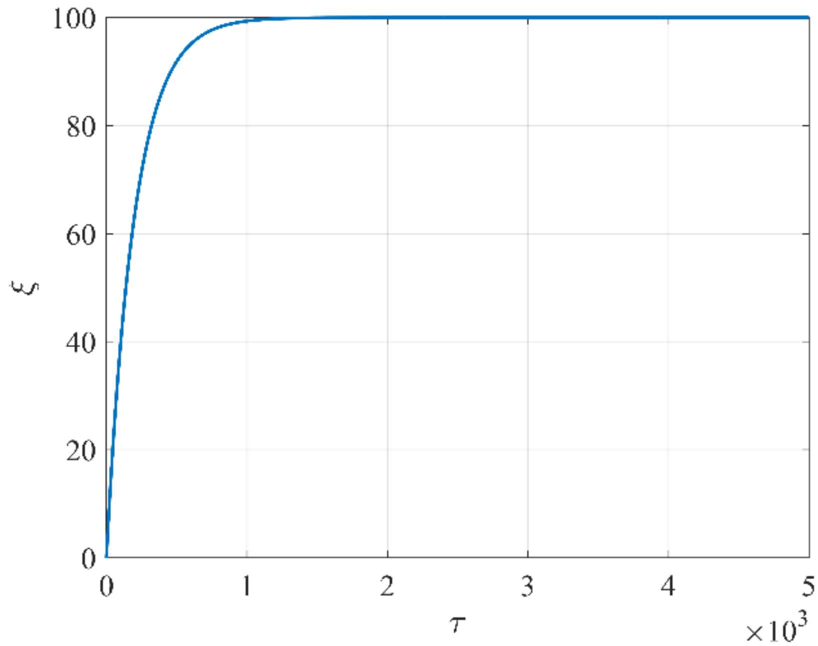

(e)

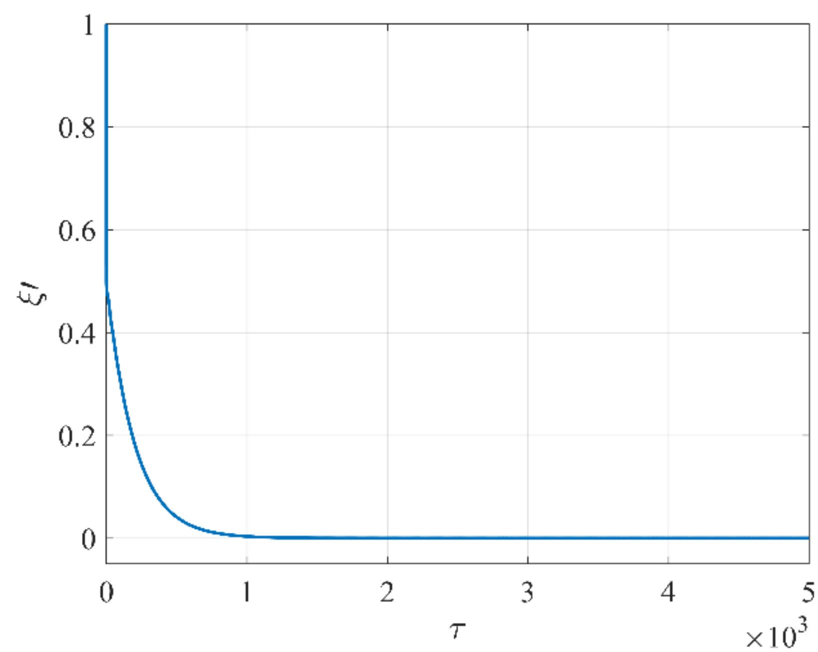

(f)

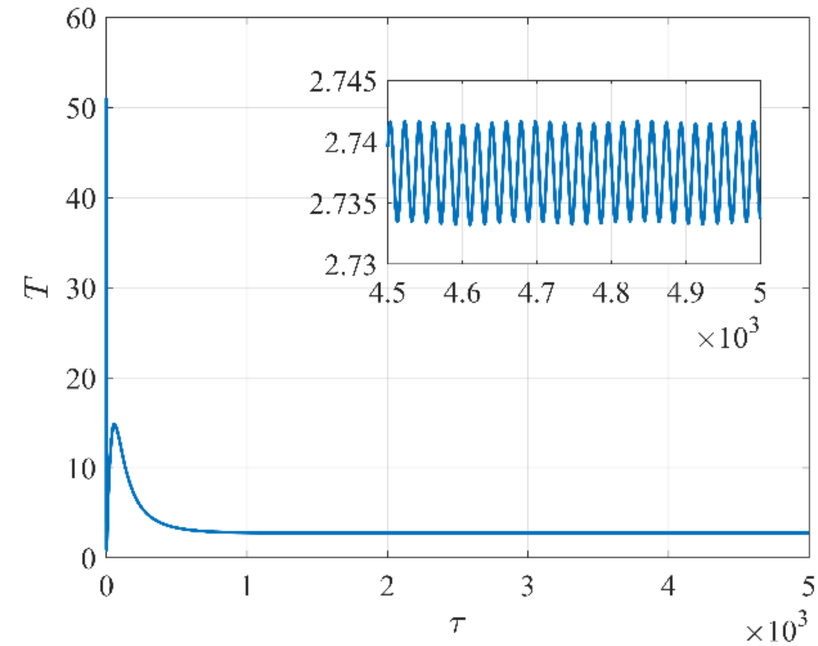

(g)

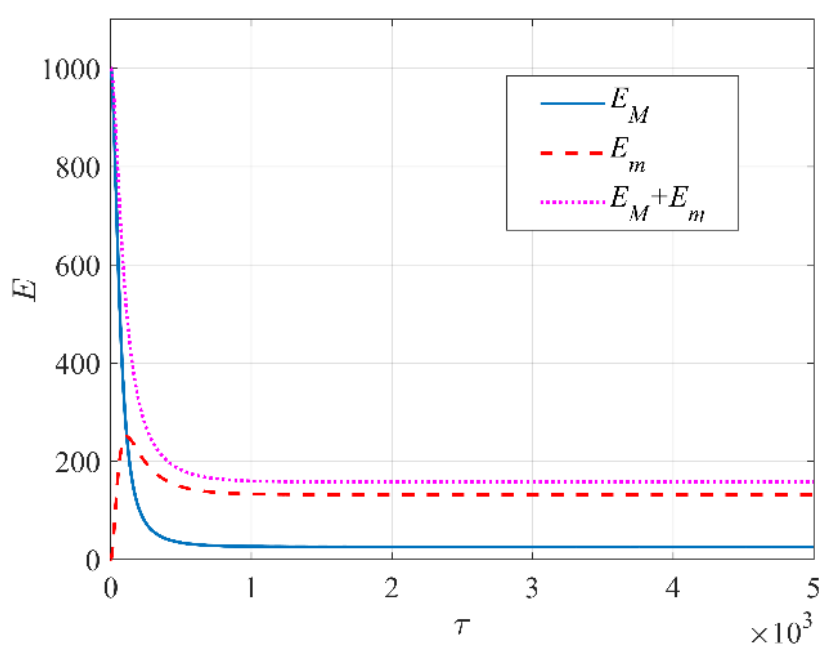

(h)

Figure 5.12 Time histories of states with tension control

5.3.3.3 Despin by Hybrid Control

In this section, the hybrid control law is used to completely despin the target' angular velocity to zero. Same physical parameters are used as those in Section 5.3.3.2 for comparison purpose.

The simulation results are plotted in the Figure 5.13(a-h). Figure 5.13 (a) shows the rotation angle of the target is stabilized to 55 π with the hybrid control law. Figure 5.13 (b) shows the angular velocity of target is completely despun to zero very quickly. The libration angle of tether β approaches close to $-\pi/2$ at the beginning of despin and then decreases to zero at the end, as shown in Figure 5.13 (c). The libration angle β is kept negative due to the induced Coriolis torque $-2\xi\xi'\left(\alpha'+\beta'+\bar{\Omega}\right)$ during the despin process. Figure 5.13 (d) indicates the angular velocity β' finally converges to the desired equilibrium, zero. As shown in Figure 5.13 (e-f), the tether is smoothly deployed to the desired length as expected and tether deployment velocity goes to zero. The tether tension is always positive and stabilized to $T_e = 3\left(1+\xi\right)\bar{\Omega}^2 \approx 0.004$, as shown in Figure 5.13 (g). Next, the thrust's magnitude, as shown in Figure 5.13 (h), is always less than 100 to prevent the tether from wrapping around the target. Finally, Figure 5.13 (i) the energy variation of the target and spacecraft, where the target's kinetic energy approaches to zero with the increase of time, which means that system finally stabilizes with $\alpha' = \beta' = 0$ under the hybrid controller. Therefore, compared with the only tension control, the hybrid control with adding a small thrust can achieve a complete despin of the target's angular velocity to zero.

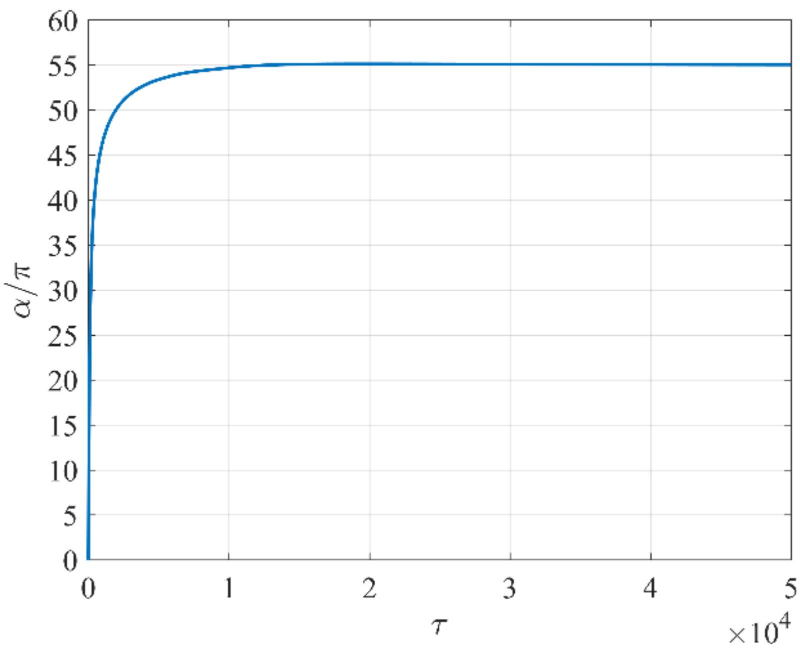

(a)

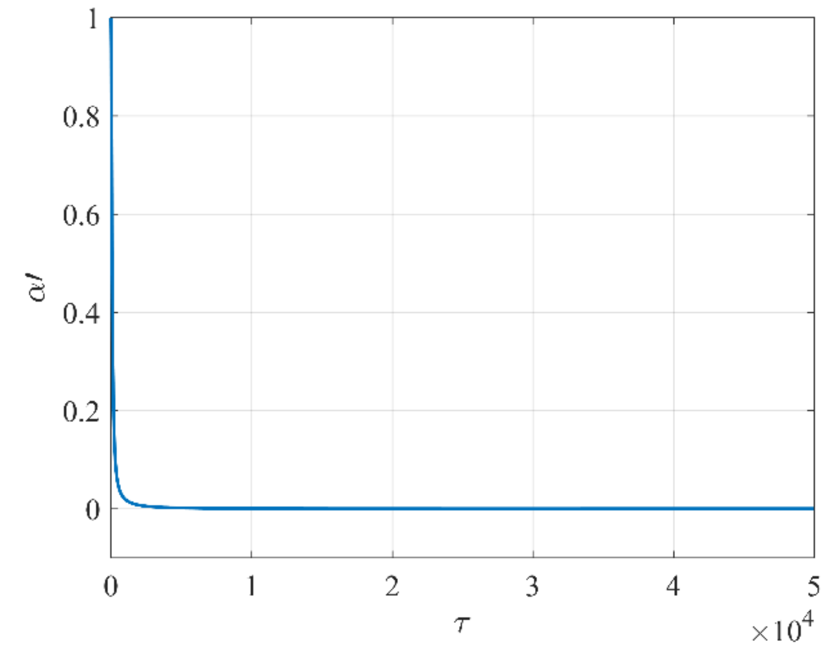

(b)

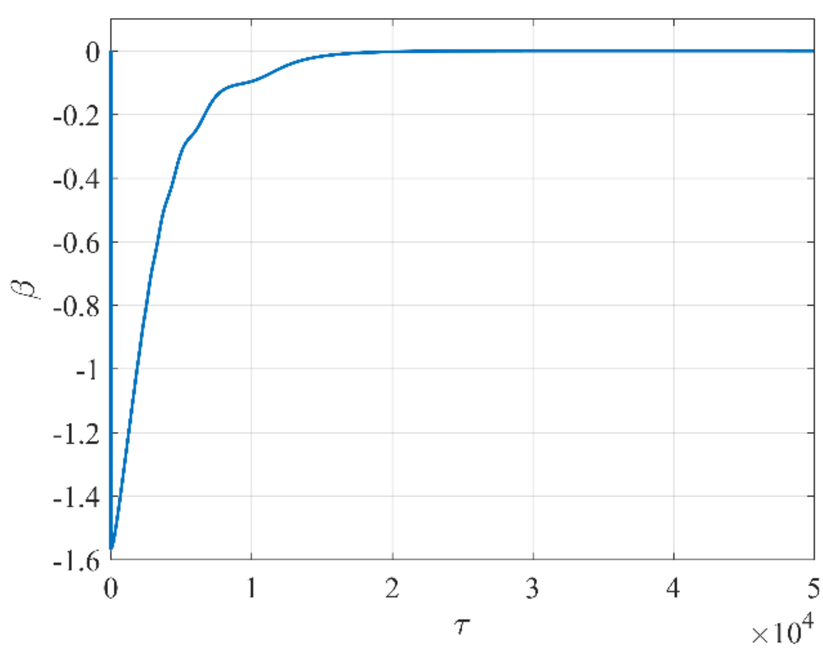

(c)

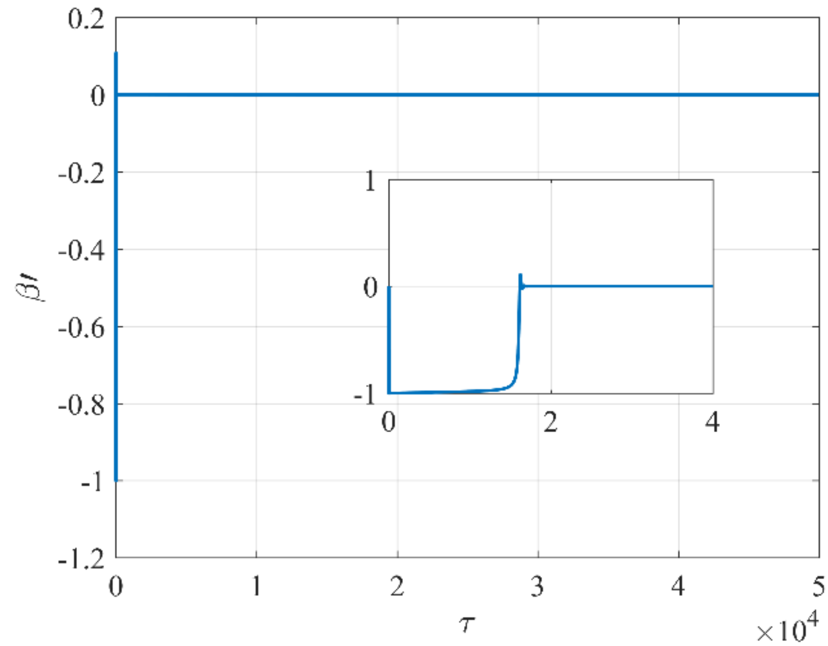
0.2
0
-0.2
-0.4
-0.6
-0.8
-1
-1.2
$\beta\prime$
1
0
-1
0
2
4
0
1
2
3
4
5
τ
$\times 10^4$

d)

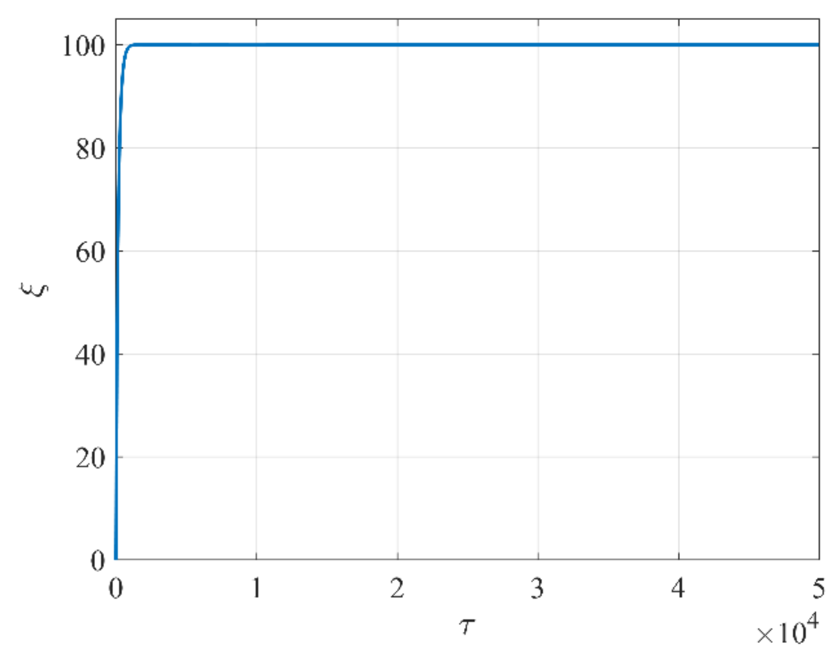
100
80
60
40
20
0
ξ
0
1
2
3
4
5
τ
$\times 10^4$

(e)

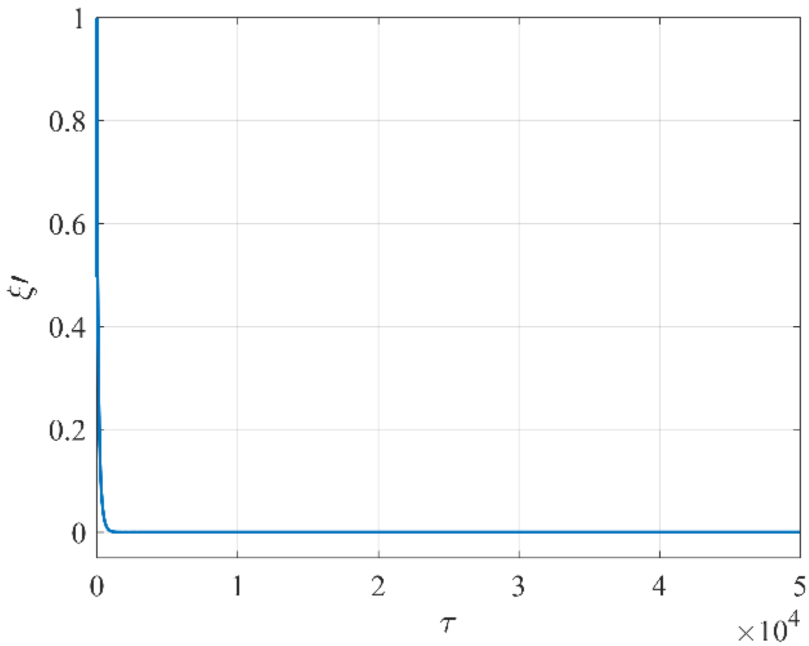
1
0.8
0.6
0.4
0.2
0
ξ_l
0
1
2
3
4
5
τ
$\times 10^4$

(f)

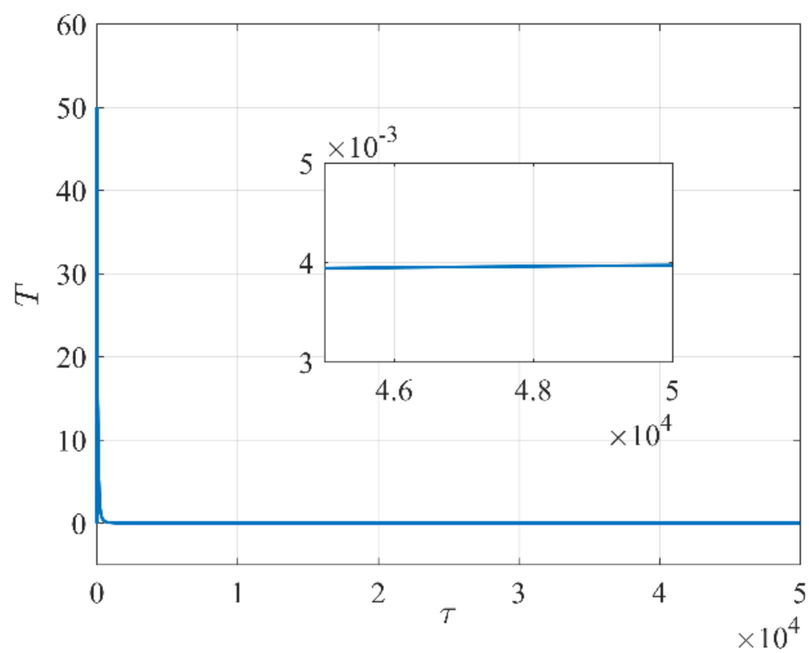
60
50
40
30
20
10
0
T
0
1
2
3
4
5
τ
$\times 10^4$
$\times 10^{-3}$
5
4
3
4.6
4.8
5
$\times 10^4$

(g)

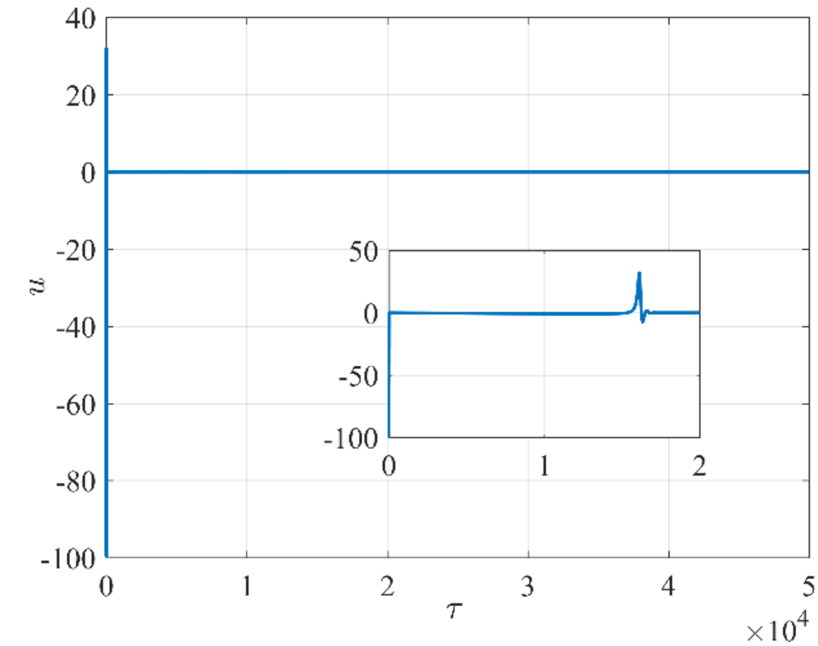

(h)

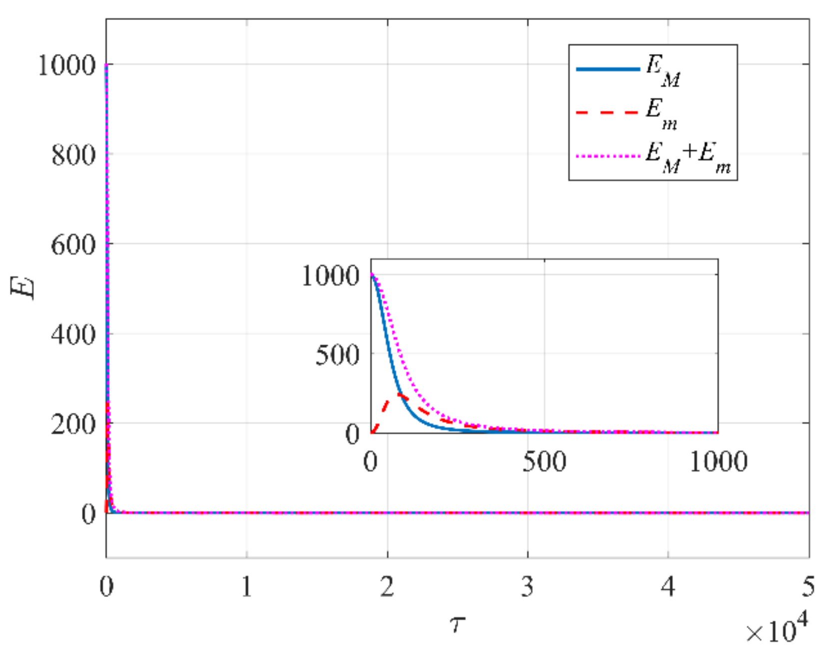

(i)

Figure 5.13 Time histories of states with hybrid control.

In the presence of the gravitational filed, the proposed strategies for a free-space in section 5.3 are modified and tested by the simulation studies. A tension controller can despin the target's angular velocity to a small bound, while hybrid control, with a thrust on the spacecraft, achieves the complete despin.

5.4 Passivity-Based Model Predictive Control

In this Section, the passivity based MPC controller is designed to solve the underactuated TSS control problem to despin the large target and, at the same time, maintain the constraints of positive tension and allowable operational libration angle.

5.4.1 Passivity Rendering

Recall the dynamic equations of tethered despin system in Section 3.2.2 and rewrite in the compact form,

$$M\ddot{q} + C\dot{q} + D\dot{q} + G = \eta \tag{5.46}$$

where the dimensionless variables

$$\xi = l / l_n, \gamma = r/l_n, \ \lambda = I\big/\left(ml_n^2\right), \ u_l = \tilde{u}_l\big/\left(ml_n\alpha_0'^2\right),$$

$$u_s = \tilde{u}_s\big/\left(ml_n\alpha_0'^2\right), \ \tau = \alpha_0' t, \ \bar{\omega}_o = \omega_o/\alpha_0', \ \dot{(\ )} = (\ )'/\alpha_0'.$$

l_n is the nominal tether length and α_0' is the initial rotating angular velocity of the space target. The matrixes are given as follows,

$$M = \begin{bmatrix} 1 & \gamma \sin\beta & 0 \\ \gamma \sin\beta & \lambda + \gamma^2 + \xi^2 + 2\gamma\xi\cos\beta & \xi^2 + \gamma\xi\cos\beta \\ 0 & \xi^2 + \gamma\xi\cos\beta & \xi^2 \end{bmatrix}$$

$$C = \begin{bmatrix} 0 & -(\xi + \gamma\cos\beta)(\dot{\alpha} + \dot{\beta} + 2\bar{\omega}_o) + \gamma\cos\beta\dot{\beta} & -\xi(\dot{\alpha} + \dot{\beta} + 2\bar{\omega}_o) \\ (\xi + \gamma\cos\beta)(\dot{\alpha} + \dot{\beta} + 2\bar{\omega}_o) & \xi\dot{\xi} + \gamma\cos\beta\dot{\xi} - \gamma\xi\sin\beta\dot{\beta} & \xi\dot{\xi} + \gamma\cos\beta\dot{\xi} - \gamma\xi\sin\beta(\dot{\alpha} + \dot{\beta} + 2\bar{\omega}_o) \\ \xi(\dot{\alpha} + \dot{\beta} + 2\bar{\omega}_o) & \xi\dot{\xi} + \gamma\xi\sin\beta(\dot{\alpha} + 2\bar{\omega}_o) & \xi\dot{\xi} \end{bmatrix}$$

$$G = \begin{bmatrix} -3\gamma\bar{\omega}_o^{\,2}\cos\alpha\cos(\alpha+\beta) - 3\xi\bar{\omega}_o^{\,2}\cos^2(\alpha+\beta) \\ 3\gamma^2\bar{\omega}_o^{\,2}\sin\alpha\cos\alpha + 3\gamma\xi\bar{\omega}_o^{\,2}\sin(2\alpha+\beta) + 3\xi^2\bar{\omega}_o^{\,2}\sin(\alpha+\beta)\cos(\alpha+\beta) \\ 3\gamma\xi\bar{\omega}_o^{\,2}\cos\alpha\sin(\alpha+\beta) + 3\xi^2\bar{\omega}_o^{\,2}\sin(\alpha+\beta)\cos(\alpha+\beta) \end{bmatrix}$$

$D = \mathrm{diag}(0, 0, f_\theta)$ is the damping matrix and f_θ denotes the pivot viscous damping and resistance terms affecting tether libration.

The generalized force/torque $\eta = Pu$, $P = \begin{bmatrix} 1 & 0 \\ 0 & \xi + \gamma\cos\beta \\ 0 & \xi \end{bmatrix}$ and $u = \begin{bmatrix} -u_l \\ u_s \end{bmatrix}$.

The following important properties, which will be exploited in the controller design, are summarized,

Property 1: M is positive definite and satisfies $\underline{m} \le \|M\| \le \bar{m}$. $\underline{m}$ and $\bar{m}$ are the lower and upper bounds of matrix M that are positive and bounded.

Property 2: The matrix $\dot{M} - 2C$ is skew-symmetric and $\dot{q}^T(\dot{M} - 2C)\dot{q} = 0$.

Remark 1: The positive definiteness of M can be easily verified by checking its principal minors with $0 < \lambda < \infty$, $\gamma > 0$ and $0 < \underline{\xi} \le \xi \le \bar{\xi} < \infty$. $\underline{\xi}$ and $\bar{\xi}$ is the lower and upper bound of the dimensionless tether length.

Remark 2: The skew-symmetry of the $\dot{M}-2C$ can be directly proved by using the above matrix M and specially chosen C. However, it is worth nothing that $\dot{q}^T\left(\dot{M}-2C\right)\dot{q}=0$ is always true even if the matrix $\dot{M}-2C$ is not skew-symmetric when matrix C is not specialized as above. Because $\dot{q}^T\left(\dot{M}-2C\right)\dot{q}=0$ reveals the conservation of energy property of Euler-Lagrange system.

For sake of simplicity of formulation, the dynamic model of the tethered system is represented into the form of general nonlinear as,

$$\dot{y}=\begin{bmatrix} v \\ M^{-1}\left(-Cv-Dv-G+\eta\right) \end{bmatrix}=f\left(y\right)+g\left(y\right)u \tag{5.47}$$

where the state is defined as $y=[q^T,v^T]^{\mathrm{T}}$, $q=[\xi,\alpha,\beta]^T$ and $v=\left[\dot{\xi},\dot{\alpha},\dot{\beta}\right]^T$.

Define the new variable as,

$$x=\begin{pmatrix}\xi & \dot{\xi} & \cos\alpha & \sin\alpha & \dot{\alpha} & \cos\beta & \sin\beta & \dot{\beta}\end{pmatrix}^T \tag{5.48}$$

Rewrite the system equations Eq.(5.46) with respect to the variable x as follows,

$$\begin{aligned}
\dot{x}_1 &= x_2 \\
\dot{x}_3 &= -x_4 x_5 \\
\dot{x}_4 &= x_3 x_5 \\
\dot{x}_6 &= -x_7 x_8 \\
\dot{x}_7 &= x_6 x_8 \\
\begin{pmatrix} \dot{x}_2 \\ \dot{x}_5 \\ \dot{x}_8 \end{pmatrix} &= M_x^{-1}\left(-C_x v_x - D_x v_x - G_x - \eta_x\right)
\end{aligned} \tag{5.49}$$

where $v_x = \left(x_2, x_5, x_8\right)^T$ is the velocity state of x.

Thus, the attainable equilibria can be written as,

$$\mathcal{U} = \left\{x \in \mathbb{R}^8 \mid x_2 = x_5 = x_8 = 0, x_1 = \xi_d, x_4 = x_7 = 0, x_3^2 = x_6^2 = 1\right\} \tag{5.50}$$

The passivity of system is revealed to apply control action directly based on the PBC theory. To guarantee the passive mapping from input to output $u \mapsto x$, the energy storage function V must have the minimum at the desired position $x_d \in \mathcal{U}$,such that,

$$x_d = \arg\min\left(U\right) \tag{5.51}$$

A non-negative energy storage function V is constructed by the energy shaping technique as follows,

$$V = \frac{1}{2} v_x^T M v_x + U_x \tag{5.52}$$

$$
\begin{aligned}
U_x &= 3\gamma x_1 \bar{\omega}_o^2 \left[1 - x_3\left(x_3 x_6 - x_4 x_7\right)\right] + \frac{3}{2}\gamma^2 \bar{\omega}_o^2 x_4^2 \\
&+ \frac{3}{2} x_1^2 \bar{\omega}_o^2 \left(x_4 x_6 + x_3 x_7\right)^2 + k_1 \int_0^{\tilde{x}_1} \sigma(\mathrm{s}) ds
\end{aligned}
\tag{5.53}
$$

where the function $\sigma\left(\tilde{x}_1\right)$ satisfies $\tilde{x}_1 \sigma\left(\tilde{x}_1\right) > 0$, $\forall \tilde{x}_1 \neq 0$, and $\sigma\left(\tilde{x}_1\right) = 0$ has the trivial solution at $\tilde{x}_1 = 0$. $\tilde{x}_1 = x_1 - x_{1d} = x_1 - \xi_d$ and $k_1 > 0$ is a positive number.

Remark 3: Seen from the storage function in Eq.(5.52), the first part is a kinetic energy, and the second is a potential energy. The kinetic energy and potential energy has the minimum at x_d. Thus, it arises a construction framework of the storage function based on system's energy. The kinetic energy term can be chosen as system's kinetic energy, and potential energy U_x can be rendered by energy shaping.

To identify the passivity mapping from $u \mapsto x$, one can take the derivative of Eq. (5.52) along the trajectory of system,

$$
\begin{aligned}
\dot{V} &= \frac{1}{2} v_x^T \dot{M}_x v_x + v_x^T M_x \dot{v}_x + \dot{U}_x \\
&= \left[k_1 \sigma\left(\tilde{x}_1\right) + u_{le} - u_l\right] x_2 + F\left[\left(x_1 + \gamma x_6\right) x_5 + x_1 x_8\right] - f_\theta x_8^2
\end{aligned}
\tag{5.54}
$$

It is clear to find the passive mapping $\upsilon \mapsto h$, if new input and output of system are selected as follows,

$$
\upsilon = \left[k_1 \sigma\left(\tilde{x}_1\right) + u_{le} - u_l, u_s\right]^T \text{ and } h = \left[x_2, \chi\right]^T \tag{5.55}
$$

where χ denotes a virtual output, $\chi = (x_1 + \gamma x_6) x_5 + x_1 x_8$.

Then, Eq.(5.54) can be represented as,

$$\dot{V} = \upsilon^T h - f_\theta x_8^2 \le \upsilon^T h \tag{5.56}$$

Obliviously, Eq.(5.56) satisfies the inequality of differential passivity.

Remark 4: We can naturally choose a passivity-based controller $\upsilon = -\phi(h)$ to ensure the closed-loop system stability. Here, $\phi(h)$ is a Lipschitz continuous function satisfying $\phi(h) = 0$ if $h = 0$, and $\phi(h)^T h > 0$ *for* $\forall h \ne 0$.

5.4.2 Merging Passivity into MPC

Recall the conventional MPC formulation for nonlinear system,

$$\begin{aligned} &\min \int_0^T \left(x^T Q x + \upsilon^T R \upsilon \right) ds \\ &\text{s.t. } \dot{x} = f(x) + g\upsilon \\ &\qquad x(0) = x(t_0) \end{aligned} \tag{5.57}$$

where T is the prediction horizon.

The passivity is merged into MPC as an additional constraint to guarantee the closed-loop stability. Then, the formulation of PB-MPC becomes,

$$
\begin{aligned}
&\min \int_0^T \left(x^T Q x + \upsilon^T R \upsilon \right) ds \\
&\text{s.t.} \quad \dot{x} = f(x) + g\upsilon \\
&\qquad 0 < x_6,\ x(0) \in \mathrm{X} \\
&\qquad 0 < u_l,\ |u_s| \le u_{s\max} \\
&\qquad \upsilon^T h \le -\phi(h)^T h - \varepsilon \|\upsilon\|^2
\end{aligned}
\tag{5.58}
$$

where ε is a positive number. $\phi(h)$ is a strictly increasing function which satisfies the properties as in Remark 4 and $\varsigma \|\phi(h)\|^2 \le \phi(h)^T h$. ς is a positive number. It should be noted that the last line in Eq.(5.58) is referred as the passivity constraint.

5.4.3 Stability Analysis

Choose the positive function V in Eq. (5.52) as the Lyapunov candidate and integrate both sides of Eq.(5.56), such that,

$$
\begin{aligned}
&V(\tau) - V(0) = -\int_0^\tau k_2 \upsilon^T h ds - \int_0^\tau f_\theta y_8^2 ds \\
&\le -\int_0^\tau k_2 \phi(h)^T h ds - \int_0^\tau f_\theta y_8^2 ds \le 0
\end{aligned}
\tag{5.59}
$$

Thus, we have $0 \le V(\tau) \le V(0)$, which indicates $V \in \mathcal{L}_\infty$.

Then, arranging the Eq.(5.59), one has that,

$$
\int_0^\tau k_2 \phi(h)^T h ds \le V(0) - V(\tau) < \infty \tag{5.60}
$$

$$\int_0^\tau f_\theta x_8^2 ds \le V(0) - V(\tau) < \infty \tag{5.61}$$

In regarding of $f_\theta > 0$, one can obtain $x_8 \in \mathcal{L}_2$.

Recall $\varsigma \|\phi(h)\|^2 \le \phi(h)^T h$, and combine with Eq.(5.60), one has

$$\int_0^\tau \varsigma \|\phi(h)\|^2 ds \le \int_0^\tau \varphi(h)^T h ds < \infty \tag{5.62}$$

Then, we have $\phi(h) \in \mathcal{L}_2$ for $\varsigma > 0$.

According to $V \in \mathcal{L}_\infty$, then one can obtain,

$$\{x_2, x_5, x_8\} \in \mathcal{L}_\infty \tag{5.63}$$

Further, according to the Property 1, and the definition of x_3, x_4, x_6, x_7 in Eq.(5.48), we have,

$$\sup\{x_3, x_4, x_6, x_7\} = 1 \quad \text{and} \quad x_1 \in \mathcal{L}_\infty \tag{5.64}$$

Thus,

$$x \in \mathcal{L}_\infty \quad \Rightarrow \quad \chi \in \mathcal{L}_\infty, h \in \mathcal{L}_\infty \tag{5.65}$$

This indicates $\phi(h) \in \mathcal{L}_\infty \cap \mathcal{L}_2$ and $x_8 \in \mathcal{L}_\infty \cap \mathcal{L}_2$.

Hence, according to the extended Barbalat Lemma, we have

$$\phi(h) \to 0,\ x_8 \to 0 \text{ as } \tau \to \infty \tag{5.66}$$

Therefore,

$$\phi(h) \to 0 \;\Rightarrow\; h \to 0 \tag{5.67}$$

To further analyze the stability, the following set $\mathcal{S}$ is defined,

$$\mathcal{S} \triangleq \left\{ x \in \mathbb{R}^8 \mid \dot{V} = 0, x_3^2 + x_4^2 = 1, x_6^2 + x_7^2 = 1 \right\} \tag{5.68}$$

and the largest invariant set $\mathcal{M}$ contained within $\mathcal{S}$ is given as,

$$\mathcal{M} \triangleq \left\{ x \in \mathbb{R}^8 \mid h = x_8 = 0, x_3^2 + x_4^2 = 1, x_6^2 + x_7^2 = 1 \right\} \tag{5.69}$$

Due to $h = 0$, we can obtain that

$$x_2 = 0 \quad \text{and} \quad \left(x_1 + x_6\right) x_5 = 0 \tag{5.70}$$

Thus, $x_5 = 0$ for $x_1 + x_6 > 0$.

Recalling Eq.(5.46), the dynamic equation of system, and setting $x_2 = x_5 = x_8 = 0$, one can have,

$$-3\gamma x_3 \left(x_3 x_6 - x_4 x_7 \right) - 3 x_1 \left(x_3 x_6 - x_4 x_7 \right)^2 = -u_l / \bar{\omega}_0^2 \tag{5.71}$$

$$\begin{aligned} &3\gamma^2 x_3 x_4 + 3\gamma x_1 \left[x_3 \left(x_4 x_6 + x_3 x_7 \right) + x_4 \left(x_3 x_6 - x_4 x_7 \right) \right] \\ &+ 3 x_1^2 \left(x_4 x_6 + x_3 x_7 \right) \left(x_3 x_6 - x_4 x_7 \right) = 0 \end{aligned} \tag{5.72}$$

$$3 x_1 x_3 \left(x_4 x_6 + x_3 x_7 \right) + 3 x_1^2 \left(x_4 x_6 + x_3 x_7 \right) \left(x_3 x_6 - x_4 x_7 \right) = 0 \tag{5.73}$$

Simplify the above equations by,

$$(5.72)\text{-}(5.71)\times\gamma x_7\text{-}(5.73)\times(1+\gamma x_3/x_1) \tag{5.74}$$

which leads to

$$\gamma x_7 u_l / \bar{\omega}_0^2 = 0 \tag{5.75}$$

Considering $u_l > 0$ and $x_6 > 0$, then we can obtain

$$x_7 = 0 \text{ and } x_6 = 1 \tag{5.76}$$

Recalling Eq.(5.73), and combing with Eq.(5.76), yields that,

$$x_3 x_4 \left(x_1 + x_6 \right) = 0 \tag{5.77}$$

Then, we have,

$$x_3 = 0, x_4^2 = 1 \text{ or } x_4 = 0, x_3^2 = 1 \tag{5.78}$$

Therefore, the invariant set $\mathcal{M}$ contains two subsets,

$$\mathcal{M}_1 \triangleq \left\{ x_2 = x_3 = x_5 = x_7 = x_8 = 0, x_4^2 = x_6 = 1 \right\}$$

and
$$\mathcal{M}_2 \triangleq \left\{ x_2 = x_4 = x_5 = x_7 = x_8 = 0, x_3^2 = x_6 = 1 \right\} \tag{5.79}$$

Furthermore, we can prove that the state in the subset $\mathcal{M}_2$ is stable while $\mathcal{M}_1$ is not stable, similar as in Section 4.12. Accordingly, we can conclude that the solution in the invariant set $\mathcal{M}$ will converge to the subset $\mathcal{M}_2$.

Substituting $\mathcal{M}_2$ into the Eq.(5.71) and combing with the Eq.(5.55) yield that,

$$
\begin{aligned}
&3(\gamma + x_1)\bar{\omega}_0^2 = k_1\sigma(\tilde{x}_1) + u_{le} \\
&\Rightarrow \quad \sigma(\tilde{x}_1) = 0 \quad \Leftrightarrow \quad x_1 = x_{1d}
\end{aligned}
\tag{5.80}
$$

Thus, by summarizing the results in Eqs.(5.79) and (5.80), we can finally obtain that, in the invariant set $\mathcal{M}$,

$$
\begin{aligned}
&x_1 = x_{1d}, x_3^2 = x_6 = 1 \\
&x_2 = x_4 = x_5 = x_7 = x_8 = 0
\end{aligned}
\tag{5.81}
$$

Thus, applying the Invariance theorem, one can directly obtain that the closed-loop system will converge to the desired state Eq. (5.81) asymptotically as time goes infinity.

Remark 5: Noting that the state in Eq. (5.81) actually represents the attainable configuration set $\mathcal{U}$ in Eq.(5.50), which shows the final stable configuration of the tethered system. They are locating at the local vertical direction.

5.4.4 Results and Discussion

In this section, the effectiveness of the proposed PBMPC is demonstrated by numerical simulation. The physical parameters of system for simulation validation are given as in Table 5.2.

Table 5.2 Physical parameters

Parameter	Value
m_1	500 kg
m_2	10^6 kg
r	10 m
R	7371 km
l_n	10 km
ω_0	$9.9761*10^{-4}$ rad/s
$\dot{\alpha}_0$	0.02 rad/s

Set initial conditions $\left(\alpha_0, \dot{\alpha}_0, \xi_0, \dot{\xi}_0, \beta_0, \dot{\beta}_0\right) = (0, 1, 0.01, 1, 0, 0)$. The desired final conditions after despin are $\left(\dot{\alpha}_d, \xi_d, \dot{\xi}_d, \beta_d, \dot{\beta}_d\right) = (0, 1, 0, 0, 0)$. The control input constraints are taken as $0 < u_l$ and $\max|u_s| = 5*10^{-4}$. The constraint of libration angle is given as $\max|\beta| = 1.3$ to prevent the tether from winding around the target. The designable function in Eq.(5.58) is chosen as $\phi(h) = \varsigma^T h$ and $\varsigma = \mathrm{diag}(200, 0.01)$. The parameters $\varepsilon = \mathrm{diag}\left(10^{-4}, 10^{-1}\right)$ and $f_\theta = 8*10^{-4}$. The NMPC tool 'acado' is used in Matlab to verify the proposed algorithm where the prediction horizon is set as 0.2 and the intervals are 2. The dimensionless simulation time is set as 2000.

The results of despinning process are shown in Figure 5.14 (a-d). As shown in Figure 5.14 (a), all the position states converges to the desired equilibrium very quickly. The magnitude of the libration angle is well limited within 1.3 (0.41π), smaller than $\pi/2$, which means tether does not wind around the target. Figure 5.14 (b) shows that the rotation of target is de-spun close to zero around 10 very quickly, and then gradually goes to zero. The velocity of tether length is within 0.1, and stabilizes to zero at the end of despin. At the same time, the angular velocity of libration converges zero as expected. Figure 5.14 (c) shows the variations of the control inputs of the tether tension and thrust. Tether tension is always positive during the despinning process, and finally stabilizes to the static equilibrium force $T_e = 3(1+\gamma)\bar{\omega}_0^2 \approx 7.472\mathrm{e}^{-3}$. Next, the magnitude of thrust u is always within the maximum bound, $5\mathrm{e}^{-4}$, to limit the libration of tether as shown in Figure 5.14 (c). Finally, the virtual output χ approaches to zero at the end of despin, see Figure 5.14 (d).

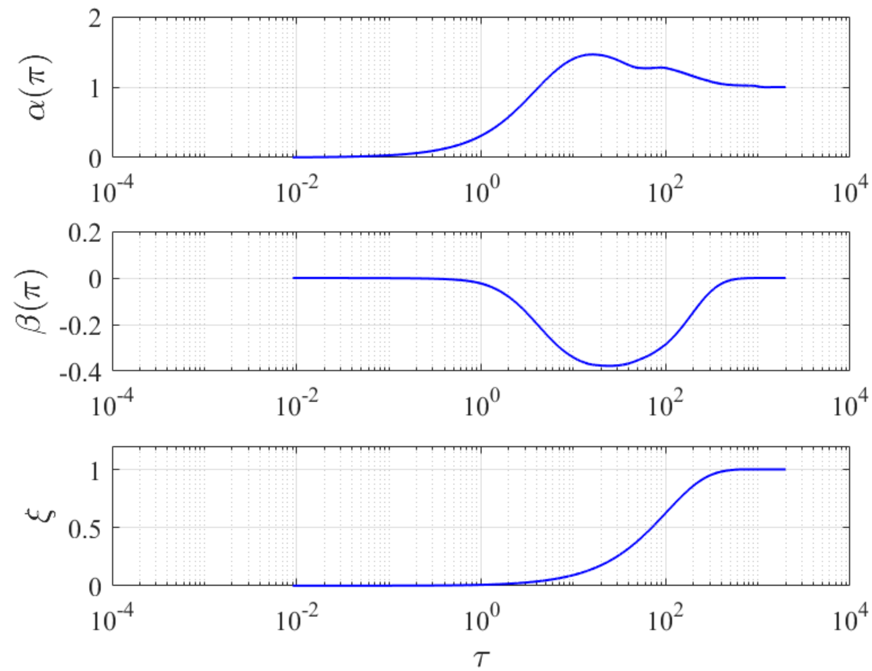

$\alpha(\pi)$
2
1
0
10^{-4}
10^{-2}
10^{0}
10^{2}
10^{4}
$\beta(\pi)$
0.2
0
-0.2
-0.4
ξ
1
0.5
0
τ

(a)

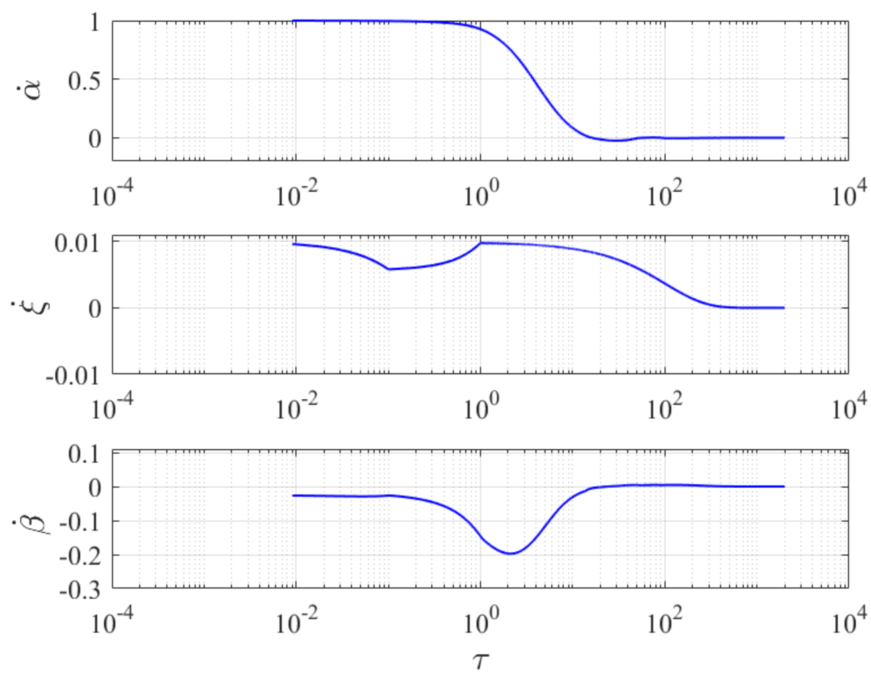

$\dot{\alpha}$
1
0.5
0
10^{-4}
10^{-2}
10^{0}
10^{2}
10^{4}
$\dot{\xi}$
0.01
0
-0.01
$\dot{\beta}$
0.1
0
-0.1
-0.2
-0.3
τ

(b)

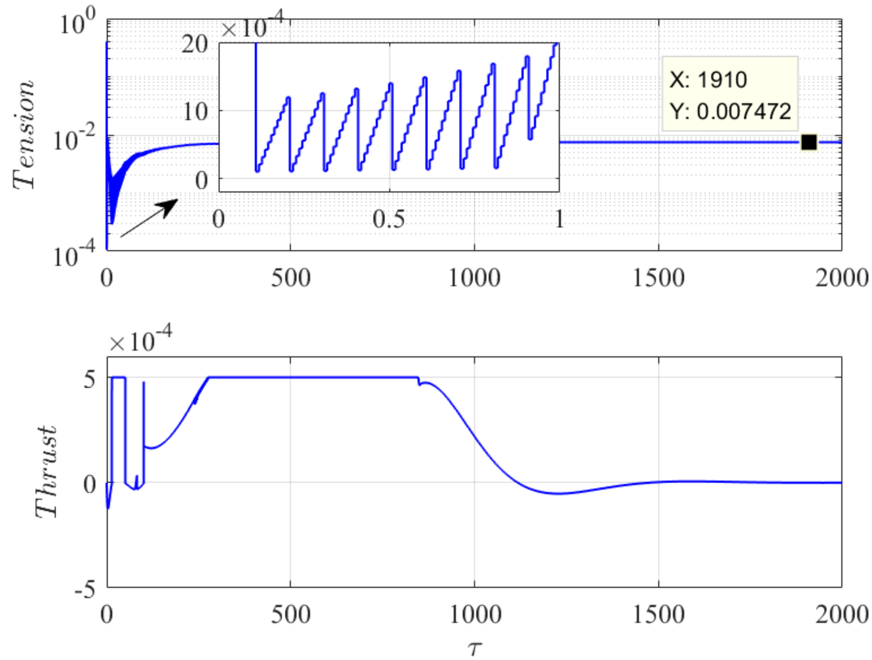

(c)

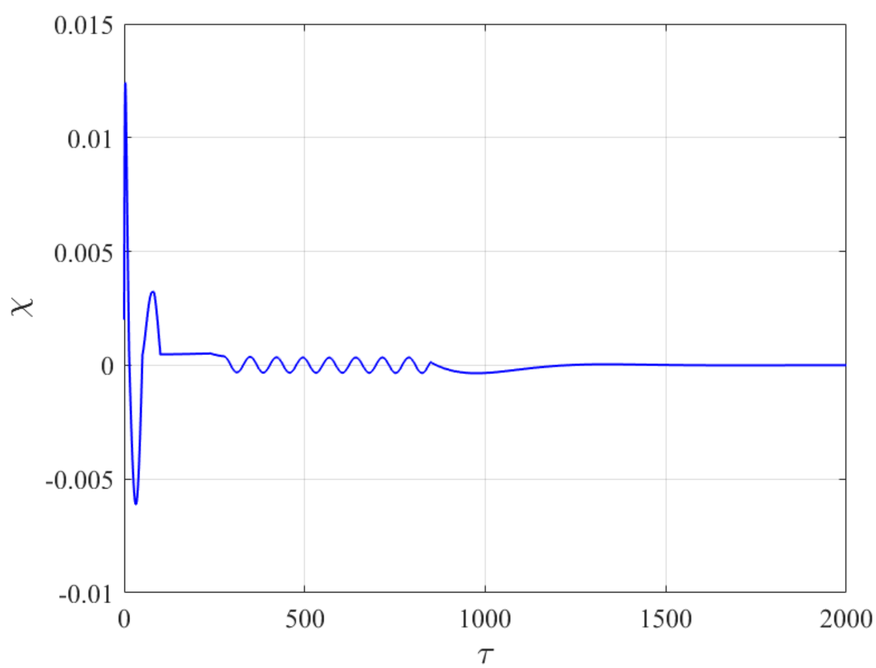

(d)

Figure 5.14 Time histories of system's states and control inputs

In this section, we proposed a new PBMPC scheme to despin the target subject to the input and state constraints. To guarantee the stability, the passivity was merged into MPC as an inequation constraint. Furthermore, PBMPC explicitly ensured the positive tension, and limited the libration angle. The stability of the proposed PBMPC was theoretically proved through the Extended Barbalat lemma and Invariance theorem. Simulation results demonstrated that proposed controller performed very well as expected.

Chapter 6 DYNAMICS AND CONTROL OF ROTATING TARGET DURING ORBITAL MANEUVERING

Summary: This chapter characterizes the dynamic behaviors of tethered rotating target during orbital maneuvering. To achieve the stable maneuver, the equilibria configurations and control strategies are studied. Then, numerical simulations are used to demonstrate the effectiveness of control strategies.

6.1 Attainable Configuration of Equilibrium

The libration motion of the TSS is stabilizable if the admissible equilibrium space is attainable with the given control action while the tether is kept taut and from warping the target. To find out the attainable configuration of equilibrium, we decompose the dynamic model of the TSS into two parts: the attitude motions of the tug and target in the body frame $\mathcal{F}_b$ and a two-body dumbbell model for the tether in the local-vertical-local-horizon of the orbital frame $\mathcal{F}_o$.

In Figure 6.1 (a), β_1 denotes the angle from the axis y_1 to the main tether and β_2 denotes the angle from the axis y_2 to the main tether. If $\beta_1 = \beta_2 = 0$, the system's configuration can be reduced as shown in Figure 6.1 (b), where β

denotes the libration angle of the dumbbell model of the TSS in the orbital frame $\mathcal{F}_o$.

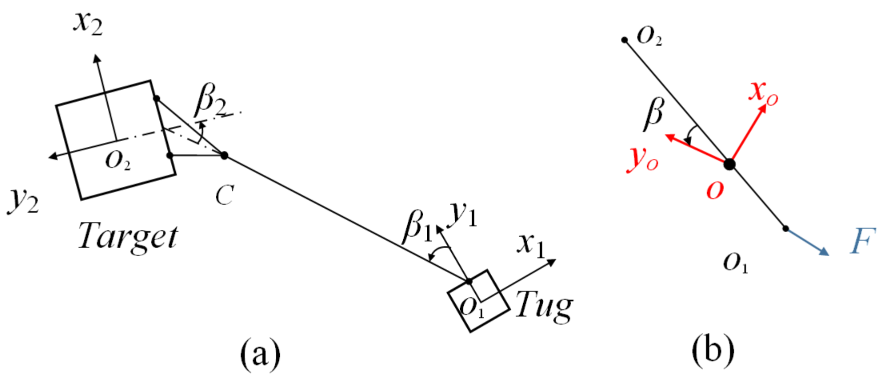

Figure 6.1 Sketch of decomposed configuration of TSS in orbital frame.

First, the attitude motion of the target, which equals to zero at the equilibrium, is derived as,

$$I_2\ddot{\theta}_2 = -T_{21}l_{21}\sin\left(\angle p + \angle 1\right) + T_{22}l_{22}\sin\left(\angle p + \angle 2\right) = 0 \tag{6.1}$$

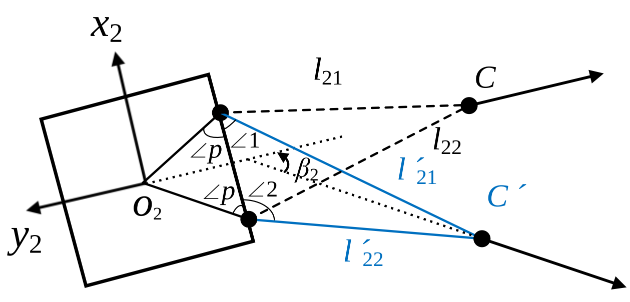

Figure 6.2 Geometrical configuration of the rotating target

As shown in Figure 6.2, the lengths of two auxiliary tethers $l'_{21} > l'_{22}$ if the target rotates anticlockwise and vice versa. Thus, the induced tether tensions must have $T_{21} > T_{22}$ at the equilibrium configuration. Then, there exists the relation $\angle 1 < \angle 2$.

Expanding Eq.(6.1) yields

$$\begin{aligned}&-T_{21}l_{21}\sin\left(\angle p+\angle 1\right)+T_{22}l_{22}\sin\left(\angle p+\angle 2\right)\\&=-\sin\angle p\left(T_{21}l_{21}\cos\angle 1-T_{22}l_{22}\cos\angle 2\right)-\cos\angle p\left(T_{21}l_{21}\sin\angle 1-T_{22}l_{22}\sin\angle 2\right)\end{aligned} \tag{6.2}$$

Considering the fact of $l_{21}\sin\angle 1 = l_{22}\sin\angle 2$, Eq.(6.2) will be negative if $l_{21} > l_{22}$ and positive if $l_{21} < l_{22}$. Equation (6.2) equals zero only if $l_{21} = l_{22}$. This is because the total torque acting on the target from the triangle connection of tethers is always against the rotation of target as a restore torque towards to the equilibrium $l_{21} = l_{22}$. Thus, one has $\beta_2 = 0$.

Next, the equilibrium configuration of the attitude of the tug can be obtained by setting $M_c = 0$ and $\alpha = 0$ in Eq. (3.77),

$$\ddot{\theta}_1 = T_1 \mathrm{P}_1 \sin\left(\beta_1\right)/I_1 = 0 \tag{6.3}$$

It should be pointed out that Eq. (6.3) implies the angle $\beta_1 = 0$ because the tension T_1 is positive.

Then, the TSS model can be reduced to a dumbbell model with perturbed forces at the equilibrium configuration as shown in Figure 6.1 (b). Then, the dynamic equations of system can be written in terms of local coordinates (l, β),

$$\begin{cases} \ddot{\beta} = -\alpha - 2\dfrac{\dot{l}}{l}\left(\dot{\beta} + \omega_o\right) + 3\omega_o^{\ 2}\sin\beta\cos\beta - \dfrac{F}{m_1 l}\sin\beta \\ \ddot{l} = l\dot{\beta}\left(\dot{\beta} + 2\omega_o\right) + 3l\omega_o^{\ 2}\sin^2\beta - \dfrac{T}{m_e} + \dfrac{F}{m_1}\cos\beta \end{cases} \tag{6.4}$$

where $m_e = (m_1 m_2)/(m_1 + m_2)$ is the equivalent mass of the dumbbell model and T denotes the tether tension. The direction of F is assumed as the opposite direction of $\overrightarrow{Oy_o}$ for the deorbit purpose.

Thus, the static equilibrium configuration can be obtained by setting $\dot{l} = \dot{\beta} = \ddot{l} = \ddot{\beta} = 0$ in Eq.(6.4), such that,

$$F\sin\beta + m_1 l\left(\alpha - 3\omega_o^{\ 2}\sin\beta\cos\beta\right) = 0 \tag{6.5}$$

$$3m_e m_1 l\omega_o^{\ 2}\sin^2\beta - m_1 T + m_e F\cos\beta = 0 \tag{6.6}$$

Compared with the orbital angular velocity ω_o, the angular acceleration α is much smaller due to the fact of slow orbit propagation. Thus, the slowly varying variable α can be assumed to be zero for searching the static equilibrium configuration. Accordingly, the solutions of Eq.(6.5) are $\beta = 0$ if $F > 3m_1 l\omega_o^{\ 2}$ and $\beta = 0, \pm\text{acos}\left(F/3m_1 l\omega_o^{\ 2}\right)$ if $0 < F \le 3m_1 l\omega_o^{\ 2}$. The corresponding configuration at $\beta = 0$ is stable if $F > 3m_1 l\omega_o^{\ 2}$. The configuration of $\beta = 0$ becomes unstable if $0 < F \le 3m_1 l\omega_o^{\ 2}$ while the configuration of $\beta = \pm\arccos\left(F/3m_1 l\omega_o^{\ 2}\right)$ becomes stable as per [99]. Here, the attainable configuration denotes the stable equilibrium configuration at $\beta = 0$ while the thrust $F > 3m_1 l \omega_o^2$.

Substituting $\beta = 0$ into Eq.(6.6) yields,

$$T_s = F\frac{m_e}{m_1} = F\frac{m_2}{m_1 + m_2} \tag{6.7}$$

where T_s is the tension in the main tether at the static equilibrium configuration.

Finally, the equilibria of the target's and tug's attitudes are $\theta_1 = \theta_2 = \beta = 0$ because the angles $\beta_1 = \beta_2 = 0$. Therefore, the attainable equilibrium configuration of the TSS is along the direction of the local horizon $\overrightarrow{Oy_o}$.

6.2 Controller Design and Stability Analysis

In this section, different control strategies are studied to suppress the tether libration motion and stabilize the attitude motions of the uncooperative target and tug towards to the attainable equilibrium configuration.

6.2.1 Tether Tension Control

Actively adjust tether length by tension control using reel in/out mechanism has been confirmed as an effective approach in space tethered systems. Adjusting the tether length to suppress the rotation motion of the tethered system has been proposed in the previous Section 5.2. The idea is to extract the angular momentum by deploying tether, where the tension does negative work to dissipate system's energy. As well, the system's rotation speed will decrease due to the increase of tether length. This is because the system's inertia momentum will increase as the tether length increases.

Hereby, to adjust the length of the main tether, a simple tension controller is given as below,

$$T_1 = T_s + k_1\left(l_1 - l_{1d}\right) + k_2\dot{l}_1 \tag{6.8}$$

where k_1 and k_2 are the positive control parameters. l_{1d} is desired length of the main tether.

6.2.2 Attitude Control of Tug

From Eq. (3.77), space tug's attitude motion will persistently oscillate due to the tether's libration which is caused by rotation of the uncooperative space target. Thus, the torquer or induced by thrust on the tug should be used to stabilize the space tug's attitude motion. An attitude controller is given as below,

$$M_c = -k_3\theta_1 - k_4\dot{\theta}_1 \tag{6.9}$$

where k_3 and k_4 are positive control parameters.

Further, to conduct the stability analysis, recall the Eq. (3.77) and combine with Eq.(6.9), then write into state space form,

$$\dot{\Theta} = A\Theta + d \tag{6.10}$$

where $\Theta = \mathrm{col}(\theta_1, \dot{\theta}_1)$ and A is a Hurwitz matrix given below. $d = -\alpha + \left(\mathbf{P}_1 \times \mathbf{T}_1\right)/I_1$ denotes the total perturbation caused by the system's libration and orbital propagation. Here, d has the upper bound $\bar{d}$.

$$A = \begin{bmatrix} 0 & 1 \\ -k_3 & -k_4 \end{bmatrix} \tag{6.11}$$

Then, a Lyapunov candidate function can be defined as following,

$$V = \Theta^T P \Theta \tag{6.12}$$

where matrix P is the solution of the Lyapunov Equation,

$$PA + AP^T = -Q \tag{6.13}$$

Here, $Q = Q^T > 0$ is positive symmetry matrix. Then, Eq.(6.13) has a unique solution for Hurwitz matrix A.

Then, the derivative of V along the trajectories of the perturbed Eq.(6.10) is,

$$\begin{aligned}\dot{V} &= \dot{\Theta}^T P\Theta + \Theta^T P\dot{\Theta} \\ &\le -\Theta^T Q\Theta + 2\lambda_{\max}(P)\bar{d}\,\|\Theta\| \\ &\le -\lambda_{\min}(Q)\|\Theta\|^2 + 2\lambda_{\max}(P)\bar{d}\,\|\Theta\|\end{aligned} \tag{6.14}$$

where $\lambda_{\min}(Q)$ and $\lambda_{\max}(Q)$ are the minimum and maximum eigenvalue of matrix Q and P, respectively.

Eq.(6.14) can be further written as follows,

$$\begin{aligned}\dot{V} &\le -(1-\varepsilon)\lambda_{\min}(Q)\|\Theta\|^2 - \varepsilon\lambda_{\min}(Q)\|\Theta\|^2 + 2\lambda_{\max}(P)\bar{d}\,\|\Theta\| \\ &\le -(1-\varepsilon)\lambda_{\min}(Q)\|\Theta\|^2\end{aligned} \tag{6.15}$$

when $\|\Theta\| > \dfrac{2\lambda_{\max}(P)\bar{d}}{\varepsilon\lambda_{\min}(Q)}$ and the parameter $\varepsilon \in (0,1)$. Thus, one can conclude that the system Eq. (6.10) is uniformly ultimate bounded stable.

Further, the combined tethered system has the equilibrium at $\|\Theta\| = 0$ as indicated in Section 6.1. Then, the total perturbation d can be considered as a vanishing perturbation which satisfies $\|d\| \le \eta\|\Theta\|$, where η is small positive number, because α is smaller enough.

Consequently, Eq. (6.15) can be represented as,

$$\begin{aligned}\dot{V} &\le -\lambda_{\min}(Q)\|\Theta\|^2 + 2\lambda_{\max}(P)\eta\|\Theta\|^2 \\ &= -\left[\lambda_{\min}(Q) - 2\lambda_{\max}(P)\eta\right]\|\Theta\|^2\end{aligned} \tag{6.16}$$

Thus, the origin of the closed-loop system Eq. (6.10) is exponentially stable if η satisfies the relation $\eta < \dfrac{\lambda_{\min}(Q)}{2\lambda_{\max}(P)}$. This bound depends on the minimum and maximum eigenvalue of matrix Q and P.

6.2.3 Output Feedback Hybrid Control

The hybrid control strategy combines both tether length control strategy and attitude control strategy together. Accordingly, the hybrid controller can be represented as,

$$u = -K_1 x - K_2 \dot{x} \tag{6.17}$$

where $u = \text{col}(u_1, u_2)$ denotes the virtual input, which has the relation with input tension and torque as $T_1 = u_1 + T_s$ and $M_c = u_2$. x denotes the state vector $x = \text{col}(l_{1d} - l_1, \theta_1)$. K_1 and K_2 are the positive diagonal matrixes, such as $K_1 = \text{diag}(k_1, k_3)$ and $K_2 = \text{diag}(k_2, k_4)$.

Further, the controller Eq. (6.17) can be improved to a output feedback view as follows,

$$u = -K_1 x - K_2 z \tag{6.18}$$

$$\begin{aligned} \dot{\chi} &= -A_c \chi - B_c \dot{x} \\ z &= C_c \chi \end{aligned} \tag{6.19}$$

Thus, the new variable $z = -C(s)\dot{x} = -sC(s)x$ has relation with x and

$C(s)=\dfrac{C_cB_c}{s+A_c}$. If the transfer function $C(s)$ is a linear time invariant, strictly positive real, and proper, Eq. (6.19) performs as a linear filter to estimate the velocity term $\dot{x}$ in the hybrid controller. Matrices A_c, B_c and C_c are all the positive diagonals and belong to $\mathbb{R}^2$.

Further, a realization of the estimator Eq.(6.19) can be given as,

$$\begin{aligned} \dot{\chi}_1 &= -A_c\chi_1 - B_c x \\ z &= C_c\left(-A_c\chi_1 - B_c x\right) \end{aligned} \tag{6.20}$$

Obviously, the velocity measurement is avoided in Eq.(6.20). Combing with the Eqs. (6.18) and (6.20), the output feedback hybrid control could be employed to replace the controller Eq.(6.17).

6.3 Simulation and Discussion

The simulation parameters of system are given in Table 6.1,

Table 6.1 Parameters of the tethered space system

Paramet	Description	Value
m_1	Mass, tug (kg)	500
m_2	Mass, target (kg)	1,500
m_c	Mass, connection point (kg)	0.1
I_1, I_2	Momentum of inertia, tug, and target	(333.3, 1000)
l_{10}	Length of main tether, undeformed (m)	197
l_{20}	Lengths of auxiliary tethers,	1.4

P_1	(X, Y) coordinates of attachment in $\mathcal{F}_{b1}$	(0, 1)
P_{21}	(X, Y) coordinates of attachment in $\mathcal{F}_{b2}$	(1, -1)
P_{22}	(X, Y) coordinates of attachment in $\mathcal{F}_{b2}$	(-1, -1)
c_k	Stiffness, auxiliary tethers (N/m)	300
c_v	Damping, auxiliary tether (Ns/m)	15
F	Thrust, tug (N)	20

The system's orbit starts from $(a, e, i, \Omega, \omega, \theta) = \left(42164\,km, 0\,, 0\,, 0\,, 0\,, 0\right)$, which is assumed at the geostationary orbit. The classical orbital elements are substituted into Eq.(3.65) to obtain the initial values of the non-singular orbital elements for orbital propagation.

Five simulation cases are the listed in the Table 6.2 as below under the control strategies with own control parameters. In the first case, the tethered system's dynamics behavior is studied without implementing any control effort. From case 2 to 4, the attitude control, length control, and hybrid control strategies are studied, respectively. In case 5, the output feedback hybrid controller is used for simulation. The initial values of all simulation cases are all given as same, such as the space tug $\left(x_1, y_1, \theta_1, \dot{x}_1, \dot{y}_1, \dot{\theta}_1\right) = \left(0, -150, 0, 0, 0, 0\right)$, the rotating uncooperative space target $\left(x_2, y_2, \theta_2, \dot{x}_2, \dot{y}_2, \dot{\theta}_2\right) = \left(0, 50, 0, 0, 0, 0.1\right)$, and the connection $\left(x_c, y_c, \dot{x}_c, \dot{y}_c\right) = \left(0, 48, 0, 0\right)$, where the units of all variable are taken as international system of units.

Table 6.2 Case studies

Case #	Control strategy	Controller parameter
1	No control	N/A
2	Tug's attitude control	$(k_3, k_4) = (2, 10)$
3	Tether tension control	$(k_1, k_2) = (0.02, 5)$, $l_{1d} = 250\ m$
4	Hybrid control (6.17)	$K_1 = \text{diag}(k_1, k_3)$, $K_2 = \text{diag}(k_2, k_4)$, $l_{1d} = 250\ m$
5	Output feedback hybrid control (6.18)	$A_c = \text{diag}(6, 6)$, $B_c = \text{diag}(36, 36)$, $C_c = \text{diag}(1/6, 1/6)$,

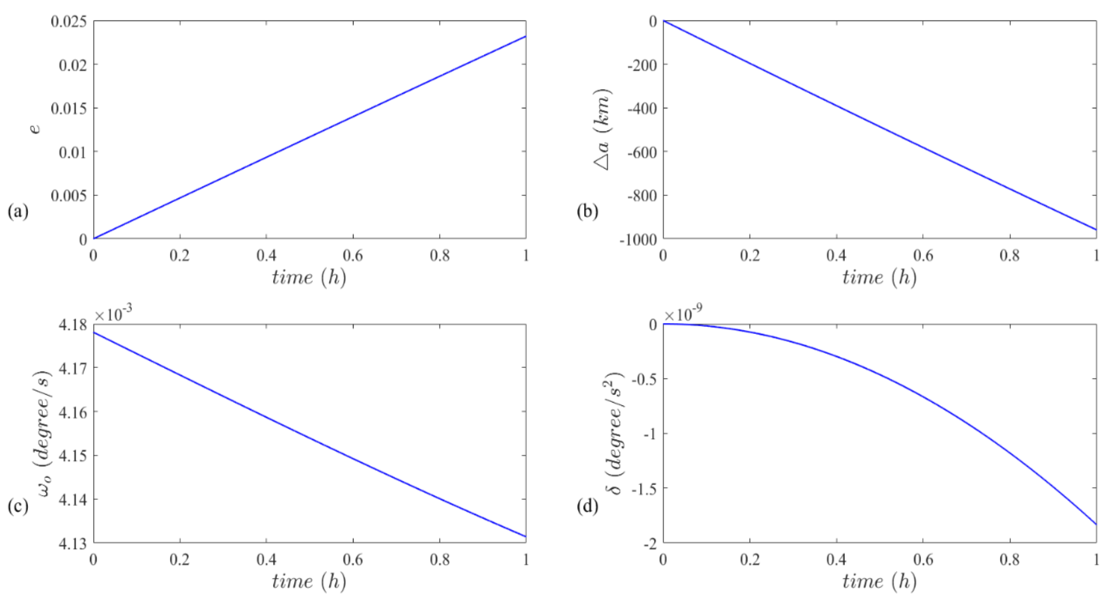

Figure 6.3 Orbital Propagation of TSS: (a) eccentricity; (b) variation of semimajor axis; (c) orbit angular velocity; and d) orbit angular acceleration.

Tethered system's orbital propagation under perturbation is illustrated in Figure 6.3. The variations of orbit are same in all case due to the equal perturbation force. As shown in Figure 6.3 (a) and (b), the system's eccentricity is keeping increasing from 0 to 0.22 and on the contrary the semi-major axis is decreasing as time elapses. This indicates that system's orbital is descending as a spiral while direction of the perturbation force is opposite to the direction of the orbital velocity. Although the length of the orbital semi-major axis is decreasing, the angular velocity is decreasing as well, see Figure 6.3 (c). This is because the eccentricity is also increasing. Figure 6.3 (d) shows the variation of the angular acceleration of the orbit over time and its magnitude is very small. Thus, it is reasonable to assume $\alpha = 0$ for equilibrium and stability analysis as in Sections 6.2.

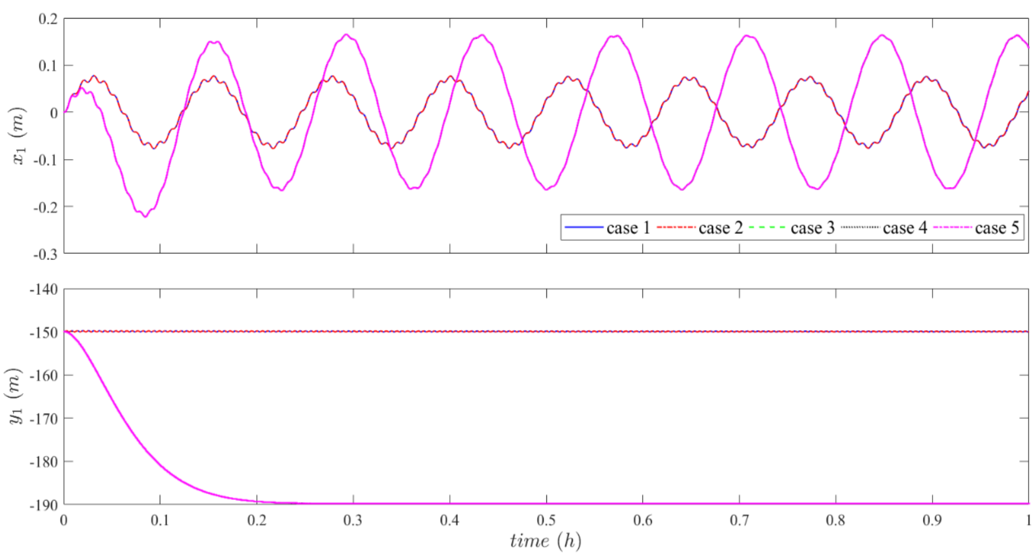

Figure 6.4 Space tug's positions for all cases

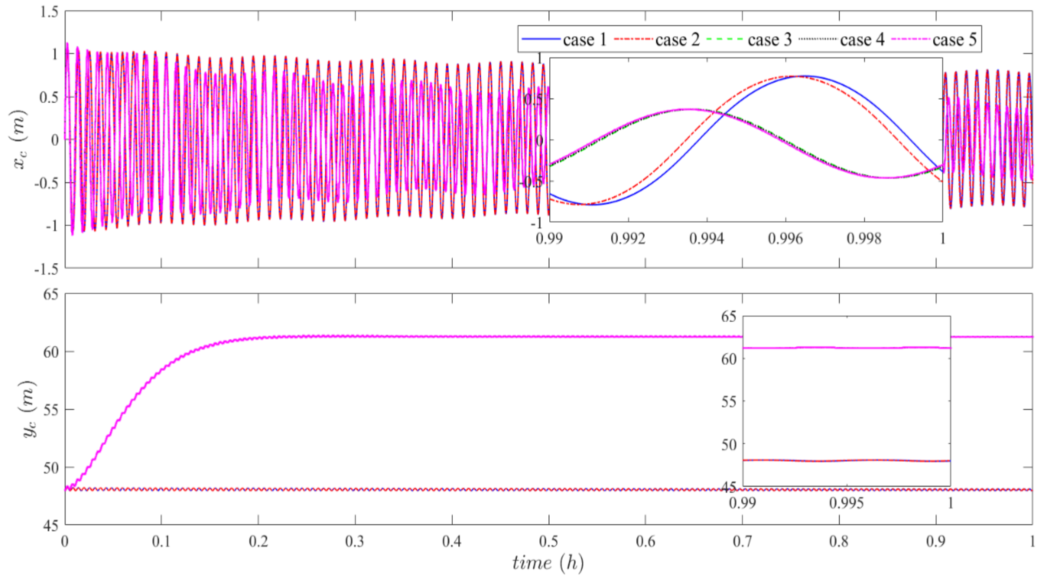

Figure 6.5 Connection point's positions for all cases

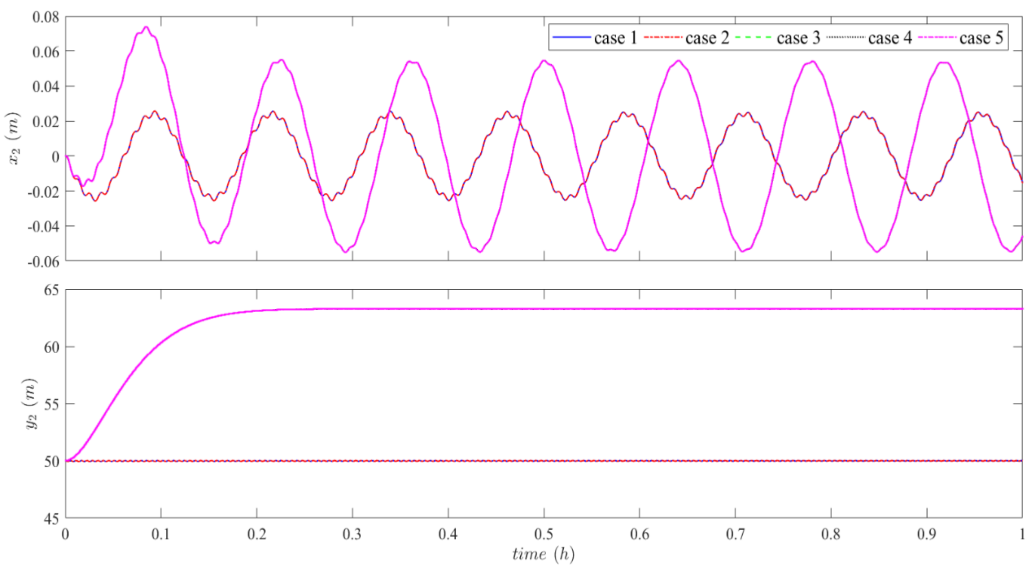

Figure 6.6 Target's positions for all cases

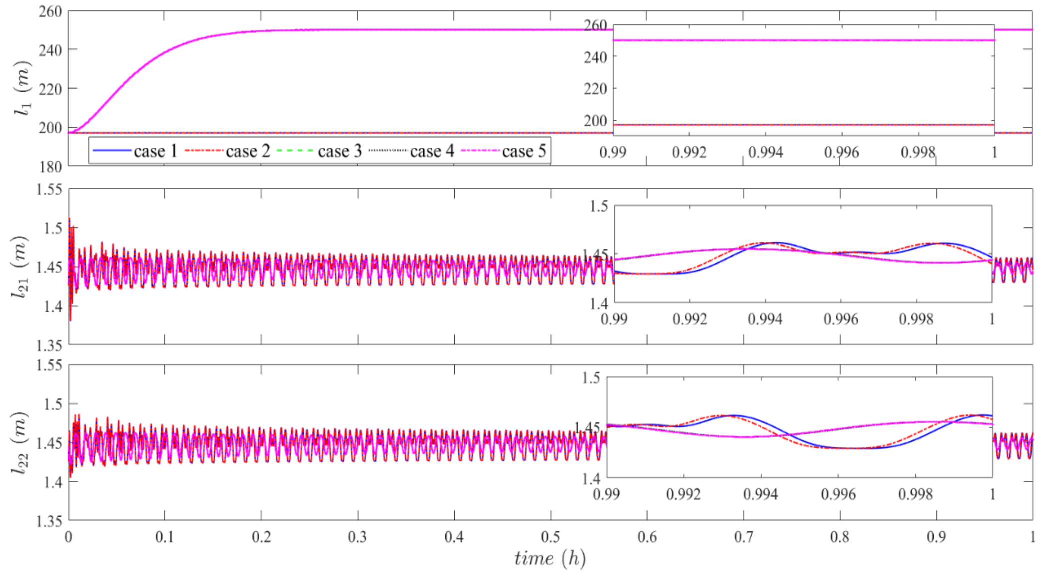

Figure 6.7 Tether lengths for all cases

The positions of the space tug, connection point and target are shown in Figure 6.4-Figure 6.6. The length of all tethers are illustrated as in Figure 6.7. From cases 1 and 2, one can find that the curves of the positions are all oscillating periodically around the initial value because the main tether length l_1 is set as fixed, see Figure 6.7. Form cases 3-5, that the magnitude of oscillation of x are slighter larger than in cases 1-2. This is caused by the active deployment of the tether, see Figure 6.7, where the main tether length is deployed from 197 to 250 m in case 3-5. It will cause the system's libration due to the Coriolis force as in Eq.(16) and the magnitude of the libration will decay to zero even slightly as the analysis of the attainable equilibrium, which is only located at the local horizon direction. The length of the two tethers of triangle connection are oscillating around the final value about 1.45.

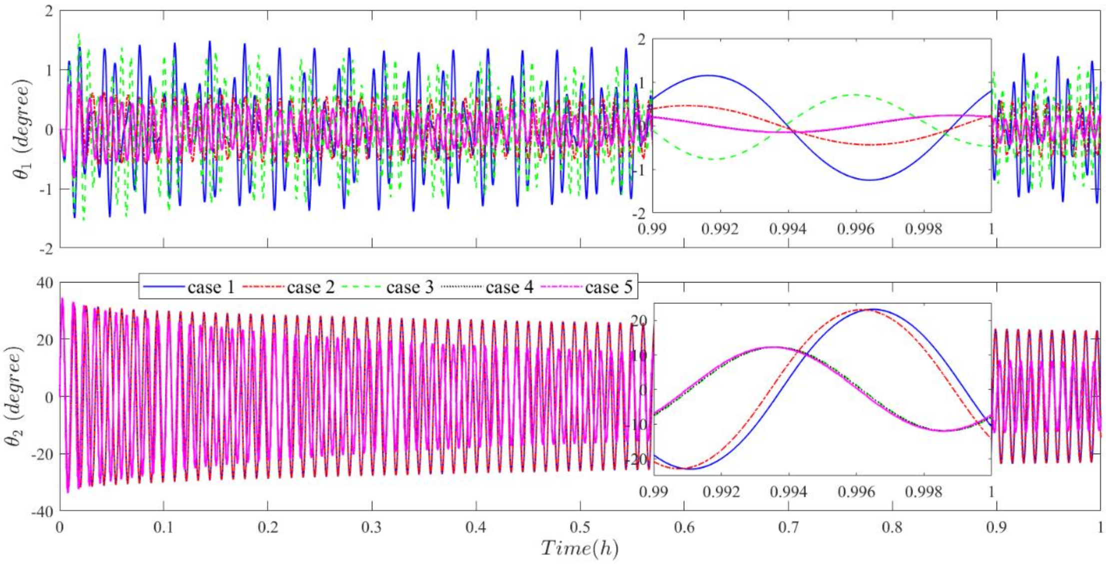

Figure 6.8 Space tug and target's attitudes for all cases

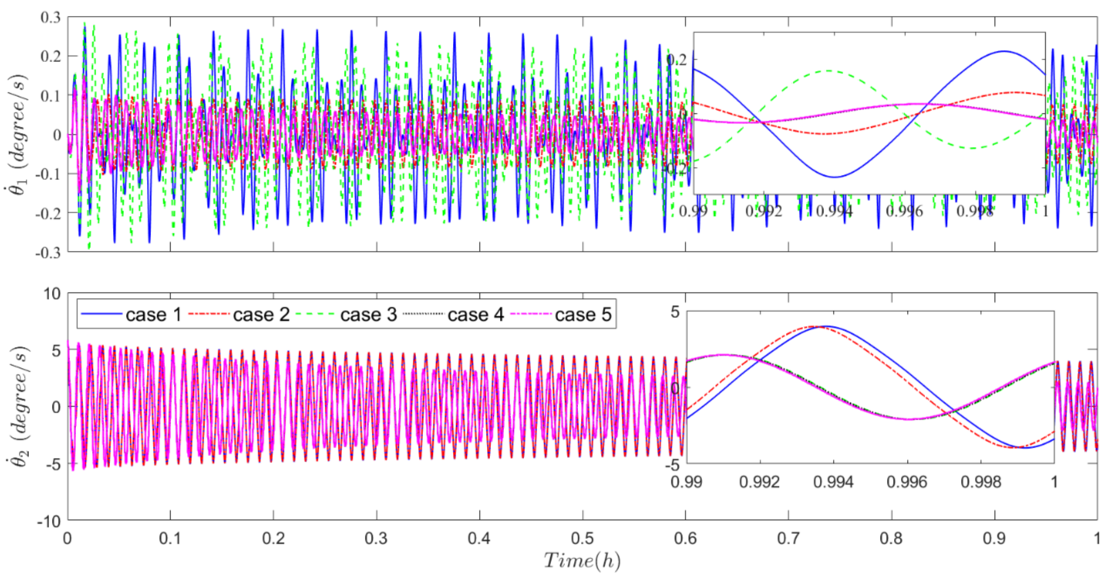

Figure 6.9 Space tug and target's spin rates for all cases

The attitude motion of the space tug and target are drawn in the Figure 6.8 and Figure 6.9. Figure 6.8 depicts that the attitude angles of the tug and target are periodically oscillating while the magnitudes of the oscillation are decaying in all cases. It is worth nothing that the significant trend of decay of target's attitude motion (θ_2 and $\dot{\theta}_2$) can be found in Figure 6.8 and Figure 6.9 for cases 3-5. Cases 1 and 2 show only half decaying trends of cases 3-5, where the magnitude of the θ_2 is around 25 degree and $\dot{\theta}_2$ around 4 degree/s for cases 1 and 2, but θ_2 is around 12 degree and $\dot{\theta}_2$ around 2 degree/s for cases 3-5. Though it looks remarkably close for case 1 and case 2, there is a smaller superiority in case 2 than in case 1. It is further interested to point out that, in case 2, 4 and 5 the attitude motions of the space tug (θ_1 and $\dot{\theta}_1$) are smaller than in cases 1 and 3. This is because that attitude control action in case 2 4, 5. Thus, the attitude motion of the space tug is well controlled with very small attitude angle. In summary, the attitude motions under any control strategies are better than case 1. The attitude control can guarantee the smaller attitude of the space tug. The length control helps to decay the attitude motion of the uncooperative target while it will cause a slight increase on the magnitude of the attitude of the space tug. Notably, the hybrid control can not only achieve the well control of the attitude of space tug but also make the attitude of the space target decay quickly.

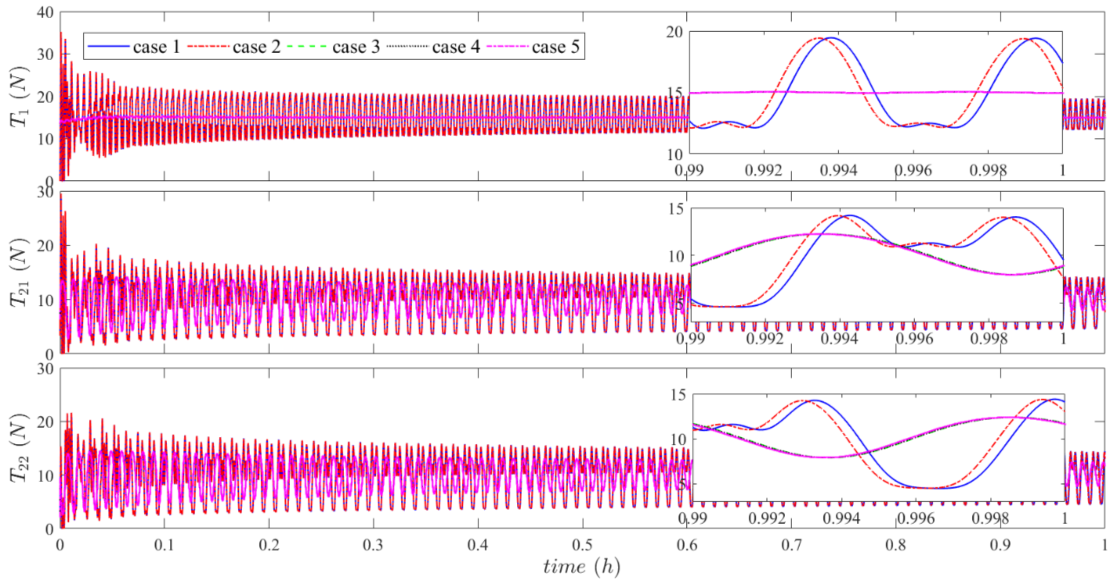

Figure 6.10 Tether tensions for all cases

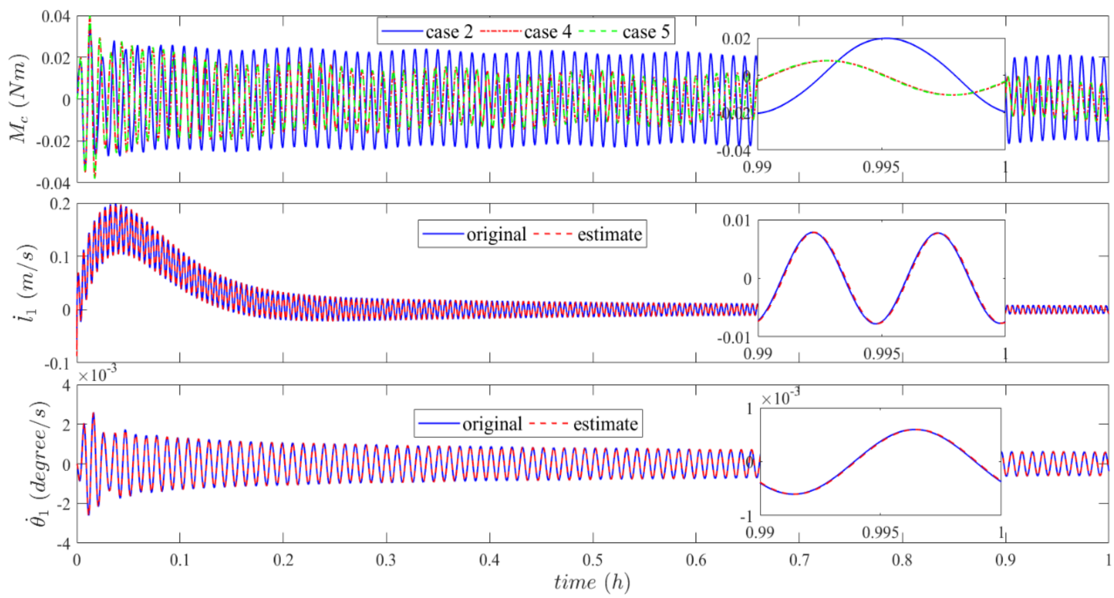

Figure 6.11 Control torque and estimated velocities

Figure 6.10 shows the tension profiles for all cases. The main tether tension T_1 is periodically changing around the static equilibrium force 15 N.

Without length control, the magnitude of the oscillations is larger in case 1 and 2. With length control applied in cases 3-5, the tension of main tether is converged to the final static equilibrium force. For the other two tensions of the triangle tether, they have the similar phenomenon that the magnitude of the oscillations is smaller in cases 3-5 than in case 1 and 2. Figure 6.11 depicts that control torques in cases 2, 4 and 5 and the estimated velocities $\dot{l}_1$ and $\dot{\theta}_1$ used in case 5. It can be seen that the control torque is keeping oscillating with bounded of 0.04 Nm, and the estimated velocities $\dot{l}_1$ and $\dot{\theta}_1$ are very close to the original velocities. Thus, the proposed output feedback hybrid controller in Eq. (6.18) can replace the hybrid controller to ease the requirement for velocity feedback.

Chapter 7 EXPERIMENTAL SETUP AND VALIDATION

Summary: In this chapter, experimental system of tethered space tug is set up on the zero-gravity air-bearing testbed to examine the concept of large debris removal after despin. The main scope is to validate the feasibility of the target maneuver by tethered tug and proposed tug's attitude control strategy in Chapter 6 for system stabilization.

7.1 Spacecraft Simulator Air-bearing Testbed Overview

The Spacecraft Simulator Air-bearing Testbed (SSABT) in the Space Engineering Design Lab contains two identical air-bearing spacecraft simulators, a smooth surface granite table, and a pseudo-galactic star system, see Figure 7.1. The SSABT was originally developed by Tsinghua University [100] and was advanced by Peng Li, with help of the visiting professor Ning Chen, for the attitude stabilization control during his PhD study [101] and Joshua Cookson for the autonomous rendezvous and docking during his master study [102]. It was further expanded and equipped with a robotic arm by Lucas Santaguida for capturing and detumbling the non-cooperative target during his master study [103]. The granite table is to provide a flat and smooth surface for the good function of the air-bearing simulator floating steadily and performing 'zero friction' capacity. The granite table is 4 m × 2m and the simulators are 0.42m × 0.42m × 0.37m. The pseudo-galactic star system is consisted of 52 randomly distributed IR (infrared) LED lights (935nm wavelength) mounted on the ceiling [102]. Camera with narrow band IR optical filter on the top of each spacecraft simulator looks at the IR LEDs to calculate the position and orientation of spacecraft simulator with respect to the granite table by the onboard computer (OBC) in real time. The experimental software system is designed in the Lab VIEW software for data acquisition, processing, and commands generation.

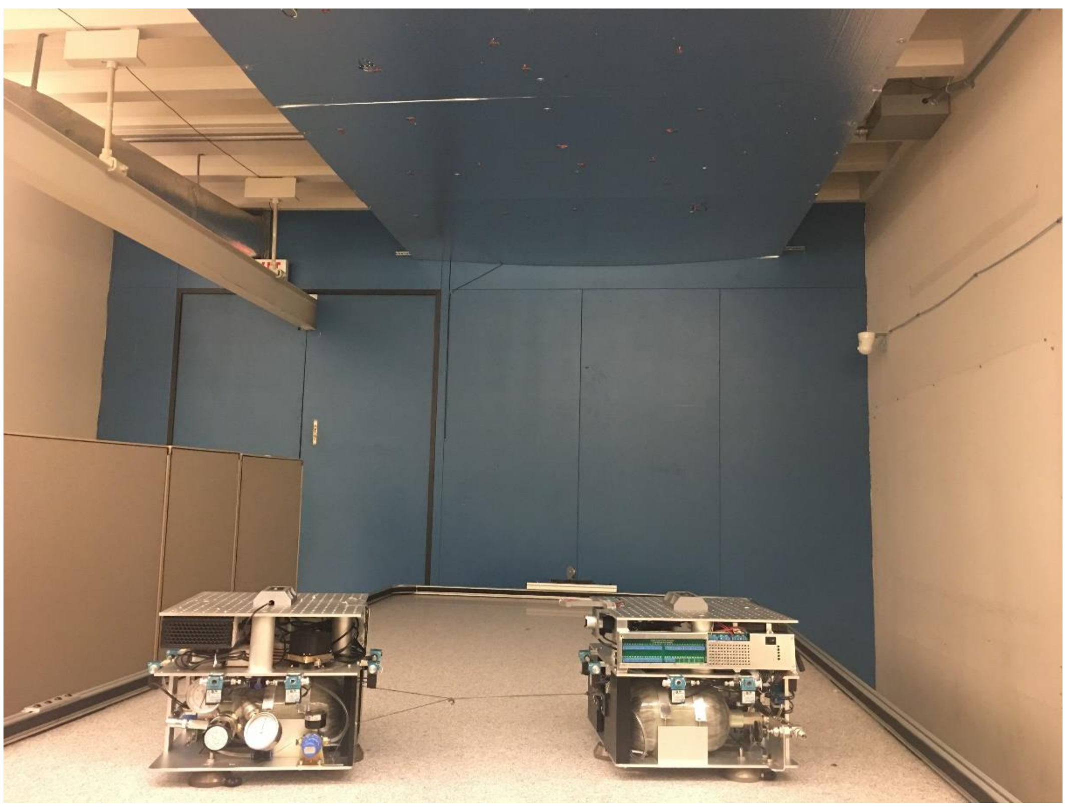

Figure 7.1 Picture of the SSABT

7.1.1 Spacecraft Simulators

The spacecraft simulator (SS) has a two-layer structure. In the first (bottom) layer, two air tanks are placed. In the second (up) layer, most of the components are mounted, as listed as in Table 7.1. Each SS is designed with 3 degrees of freedom (DOF) motion capacity: 2 DOF translational motion in the table plane and 1 DOF rotational motion perpendicular to the table plane. Three air-bearing feet mounted at the bottom of each SS produce a film of pressurized air between the smooth table and feet surface to achieve the floatation, which provides the 'zero friction' environment [102].

Table 7.1 Major components on each simulator

Name	Description	Quantity
Air-Bearing Foot	Provide 'zero friction' between surfaces by a film of the pressurized air	3
Air Tank	Store the high-pressure air (20 MPa); Volume 2L	2
Battery	LiFePO4, 12V, 150Wh	1

Camera	Capture the LEDs in the star fields; 1080p Logitech C920 webcam	1
Data Acquisition Device	Acquire Data and digitalize for computer read; NI 6112 DAQ	1
Fiber-Optic Gyroscope	Measure the angular velocity; Fizoptika VG103PT	1
Gas Thruster	Supply the thruster force by regulating the high-pressure air; MAC 35A-AAA-DDBA-1BA Solenoid Valve	8
Onboard Computer	Run simulation software and deal with all commands; Zotac CI660-nano, i7-8550U, 16GB RAM	1
Pressure Regulator (large)	Regulate the 20 MPa incoming air to 1Mpa; (Xiongchuan Valves)	1
Law Pressure Regulator	Covert the 1 MPa incoming air into 0.4 Mpa; (Xiongchuan Valves)	1

Reaction Wheel	Provide the control torque for the simulator’s attitude control; Sinclair RW-0.01	1

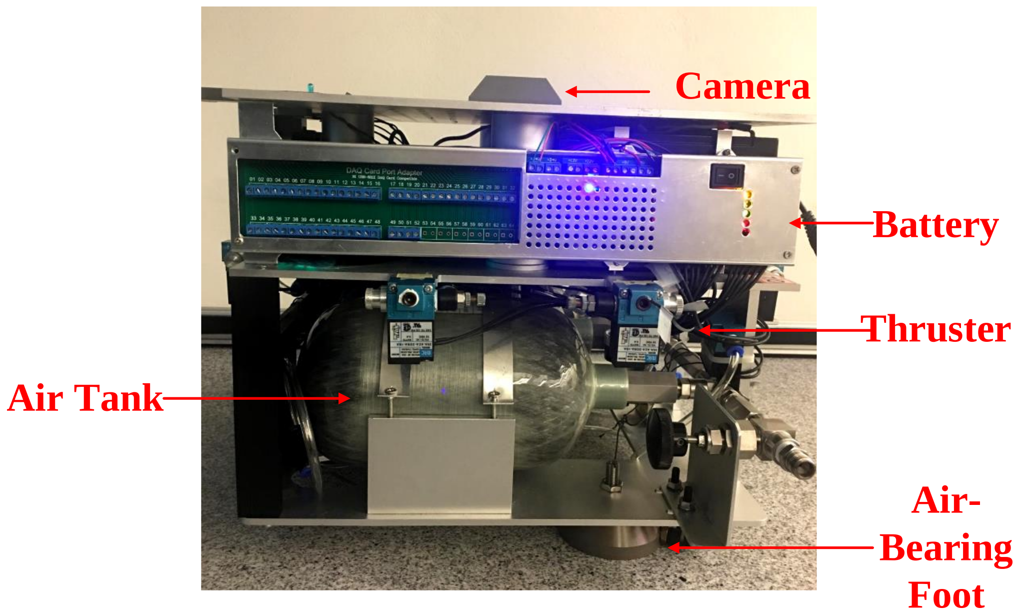

(a)

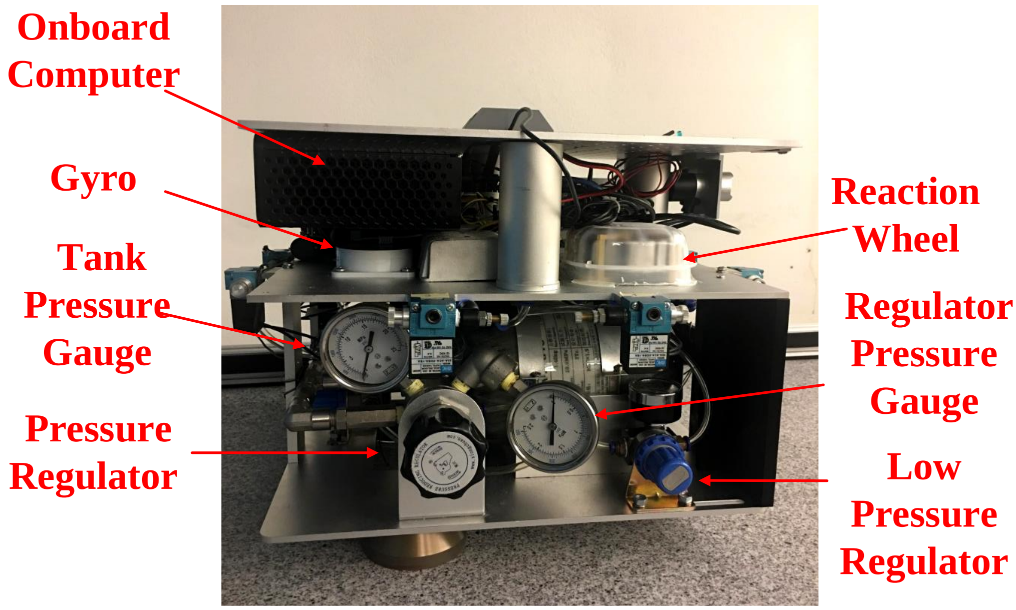

(b)

Figure 7.2 Simulator structure and payloads

7.1.2 Measurement System

The star tracker system is designed to measure each SS's position and single axis attitude. The system contains one Logitech C920 USB web camera mounted on the top of each SS and the 52 randomly distributed Infrared (IR) LED maps on the ceiling of room, see Figure 7.3. An IR Lens is added on the top of the camera to observe the Infrared spectrum of LEDs which can reduce the interference from external environments compared with visible spectrum. The view of the LEDs' points is shown in Figure 7.4. [102]

Figure 7.3 IR LEDs map of Star Tracker system

Figure 7.4 Stars positions in Camera view

To compute the position and attitude information of the SS, the LED positions in the star map are stored with identifier. Using the geometrical relationship of any groups of 5 stars, the absolute position and attitude information of SS can be computed as SS moves. To increase the accuracy of measurements, the 3-point moving average filter algorithm is applied in the software system. [103] The velocity and angular velocity information is obtained by the finite difference in the software system as well. However, the angular velocity information is very sensitive to the noise and sampling time. The finite difference will cause the sharp jumps, see Figure 7.5. Therefore, the Fiber-Optic Gyroscope sensor should be used to measure the angular velocity while SS is fast rotating.

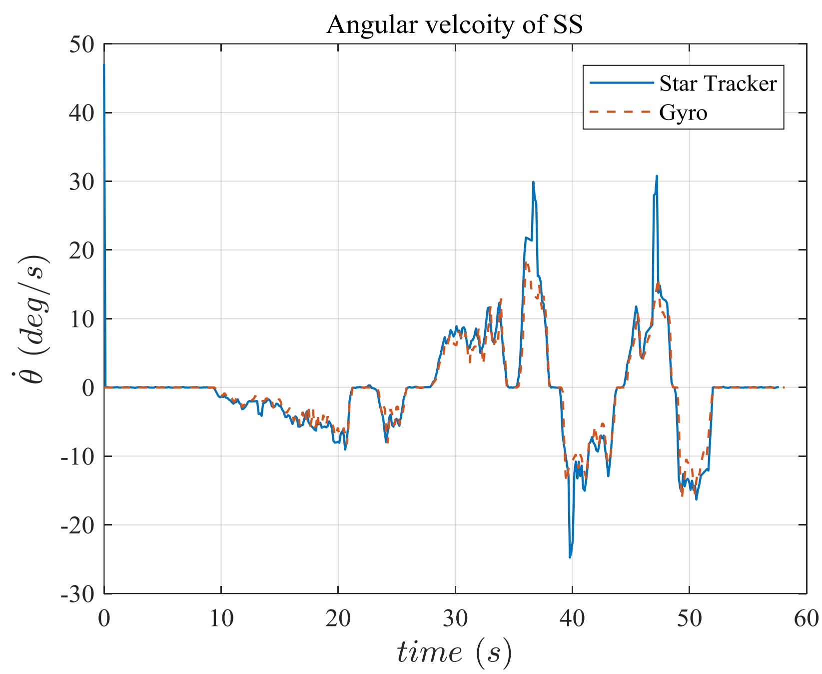

Figure 7.5 Angular velocity measured by Star Tracker and Gyro

7.1.3 Control System

Eight thrusters of each SS are designed to maintain the SS's attitude motion or achieve the docking operation during maneuvering, see Figure 7.6. Each thruster provides a unidirectional constant force of $u_o = 0.065N$ at a pressure of 0.4 MPa controlled by a solenoid valve and supplies the control force F_x, F_y for translational motion and the control torque M for single axis rotation. The produced force and torque in the inertial frame OXY can be obtained by the control allocation relation, as follows,

$$\begin{bmatrix} F_x \\ F_y \\ M \end{bmatrix} = \begin{bmatrix} -c\theta & s\theta & c\theta & -s\theta \\ -s\theta & -c\theta & s\theta & c\theta \\ d_u & d_u & d_u & d_u \end{bmatrix} \begin{bmatrix} u_1 \\ u_2 \\ u_3 \\ u_4 \end{bmatrix} \tag{7.1}$$

where the u_1 - u_4 denote the bidirectional thruster force which the directional of positive direction is defined in clockwise turns. θ is the angle of rotation of the SS, which is defined as the angle from the inertial frame OXY to the body frame oxy. $d_u = 0.21m$ is the thruster's arm of the momentum. Therefore, the required thruster force for system control can be computed by,

$$\begin{bmatrix} u_1 \\ u_2 \\ u_3 \\ u_4 \end{bmatrix} = \begin{bmatrix} -c\theta & s\theta & c\theta & -s\theta \\ -s\theta & -c\theta & s\theta & c\theta \\ d_u & d_u & d_u & d_u \end{bmatrix}^{+} \begin{bmatrix} F_x \\ F_y \\ M \end{bmatrix} \tag{7.2}$$

where $(\ )^{+}$ denotes the Moore–Penrose inverse for the 4×3 matrix. The corresponding solenoid valves are turned on when the required thrust is greater than the threshold value, i.e., $|u_i| \geq 0.065N$, and otherwise are kept off.

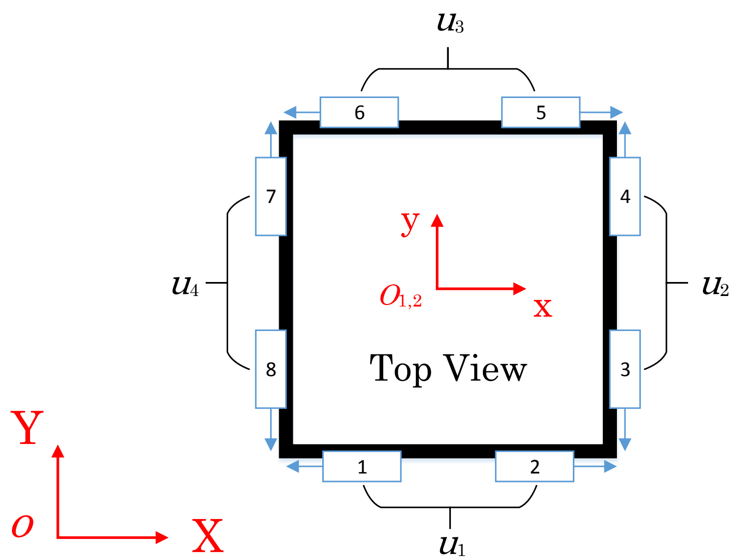

Figure 7.6 Thrusters distribution in the top view of SS

7.2 Experimental Setup

In this section, the SSABT is set up to validate the rotating target maneuver by the tethered space tug. The main work of my thesis on the experimental validation is focused on the design and setup of tethered tug system, the plan of experimental scenarios, attitude controller design and implementation, and angular velocity measurement by Fiber-Optic Gyroscope. Moreover, an auxiliary pulley mechanism is developed to supply the sufficient towing force. This is because unlike the previous actively attitude control experiment and the autonomous docking/rendezvous [101, 102], the main interest of my study is on the stabilization of rotating passive target maneuver by tethered tug. This is our first attempt to experimentally validate the tethered tug concept on the custom-built air-bearing table.

One simulator is considered as a space tug, and the other one is considered as an uncooperative and passive space target. The target is considered to be rotating around its primary axis. In practical tether mission, it is very difficult to install an active actuator on the target through the flexible tether to control the target's attitude motion. In current experiment setup, only the tug is considered to be actuated while the target is passive to operate (floating only). No communication between the tug and target is available. The current experimental setup is more difficult than the previous fully actuated docking and attitude control experiment. Besides, the originally designed thrust capacity of simulator is very limited (maximum 0.13 N) to maneuver the total mass of 40 kg. Consequently, in order to successfully set up the TSS experimental system based on the existing SSABT, we raised the idea of an auxiliary pulley-weight mechanism aided tethered tug system, as shown in Figure 7.7, where the target is connected to two auxiliary tethers in a triangle first and the latter is connected to the tug via a main tether.

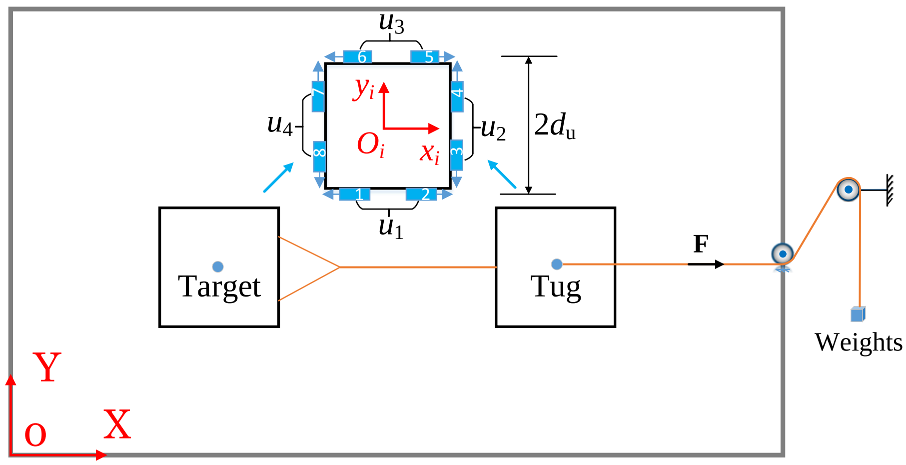

Figure 7.7 Sketch of experiment system setup

Additionally, solving the expected and unexpected problems are also the critical part of my research during the tethered experiment system setup. Two typical problems were found in the design and setup, as shown in Figure 7.8 (a) and (b). First, the selection of elastic tethers for experiment. At the beginning, we connected a 'rigid' (high stiffness) and heavy tether (rubber rope) to the rotating target. However, the SS becomes very unstable because heavy stiff tethers, under large gravity force, pull the target together, and it becomes worse when the target rotates. Thus, in the experiment, the material of tethers should be chosen with lightweight and low stiffness. The tether information will be given in subsequent section. Secondly, it is not able to stably maneuver the whole system by the tug's thrust because the max magnitude of the tug's thrust is only 0.13 N, which is not sufficient for the whole system with 40 kg. To supply the enough towing force, an auxiliary pulley-weight mechanism is designed and built as an alternation, seen in Figure 7.8 (c). The towing force is provided by the gravity of the given weight, which is adjustable and constant.

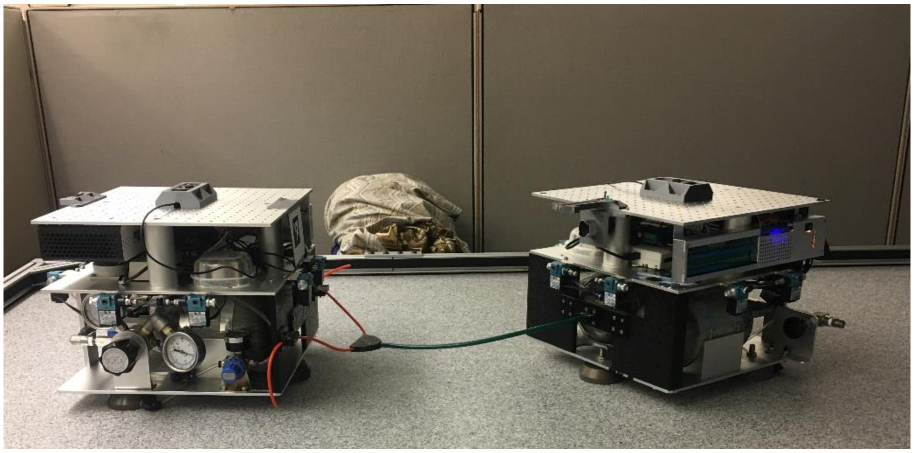

(a)

(b)

(c)

Figure 7.8 Problems found in experimental setup

(a) Rubber tether Connection (b) No external actuation
(c) With auxiliary towing force

As shown in Figure 7.9, the experiment system's configuration is well set up under the auxiliary pulley-weight mechanism. It is worth noting that despite the tether material, the tether length selection also affects the experimental validation during the experimental setup. It is better to use the short thin string with low stiffness of the auxiliary elastic tethers. The length of the main tether could be set slightly longer than the auxiliary elastic tether, and ensures the distance between the two simulators over the simulator's size. Then, two simulators have a safety region to avoid the collision from the rotation. Due to the 4 m length of the air-bearing table, the total tether length doesn't exceed 1 m. Otherwise, we can only run experimental tests for a short time. One appropriate set of parameters are for successful experimental setup is listed as in Table 7.2.

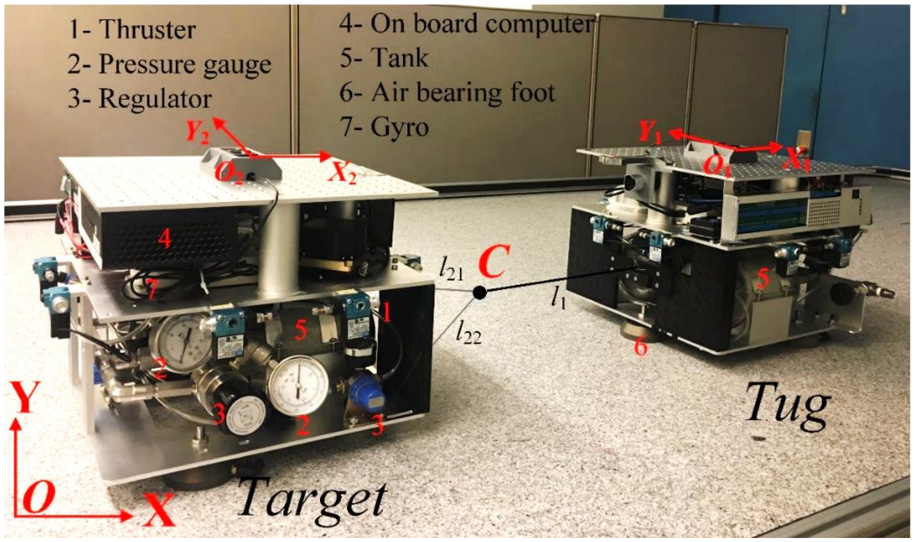

Figure 7.9 The experiment system on the SSABT

Table 7.2 Parameters of the experiment system

Parameter	Description	Value
m_1	Space tug's mass	20 kg
m_2	Space target's mass	20 kg
m_c	Connection's mass	0.01 kg
I_1, I_2	Tug and target's momentums of inertia	0.456 kgm^2
l_{10}	Original length of main tether	27 cm
l_{20}	Original lengths of elastic tethers	22 cm
P_1	Coordinates of attachment in $X_1O_1Y_1$	(-0.185, 0) m
P_{21}	Coordinates of attachment in $X_2O_2Y_2$	(0.185,0.15) m
P_{22}	Coordinates of attachment in $X_2O_2Y_2$	(0.185,-0.15) m
F	Thruster force	(0.4, 0) N

7.3 Formulation of Experimental System

To formulate the model of the system as shown in Figure 7.9, the following coordinates of frame are defined. The inertial frame is defined XOY, where the origin is fixed at the corner of the table, OX along the length of the table, OY along the width of the table. Two body frames $X_1O_1Y_1$ and $X_2O_2Y_2$ are defined for tug and target, respectively. The subscript 1 and 2 denote the tug and target, respectively.

Similar as in Eqs. (3.73)-(3.75), the dynamic equations of the experimental system are derived as,

$$\begin{bmatrix} \ddot{x}_1 \\ \ddot{y}_1 \end{bmatrix} = \begin{bmatrix} \dfrac{\mathbf{T}_1 + \mathbf{F}\left(m_2 + m_c\right) / \left(m_1 + m_2 + m_c\right)}{m_1} \cdot \mathbf{e}_x \\ \dfrac{\mathbf{T}_1 + \mathbf{F}\left(m_2 + m_c\right) / \left(m_1 + m_2 + m_c\right)}{m_1} \cdot \mathbf{e}_y \end{bmatrix} \tag{7.3}$$

$$\begin{bmatrix} \ddot{x}_2 \\ \ddot{y}_2 \end{bmatrix} = \begin{bmatrix} -\dfrac{\mathbf{T}_{21} + \mathbf{T}_{22} + \mathbf{F} m_2 / \left(m_1 + m_2 + m_c\right)}{m_2} \cdot \mathbf{e}_x \\ -\dfrac{\mathbf{T}_{21} + \mathbf{T}_{22} + \mathbf{F} m_2 / \left(m_1 + m_2 + m_c\right)}{m_2} \cdot \mathbf{e}_y \end{bmatrix} \tag{7.4}$$

$$\begin{bmatrix} \ddot{x}_c \\ \ddot{y}_c \end{bmatrix} = \begin{bmatrix} \dfrac{\mathbf{T}_{21} + \mathbf{T}_{22} - \mathbf{T}_1 - \mathbf{F} m_c / \left(m_1 + m_2 + m_c\right)}{m_c} \cdot \mathbf{e}_x \\ \dfrac{\mathbf{T}_{21} + \mathbf{T}_{22} - \mathbf{T}_1 - \mathbf{F} m_c / \left(m_1 + m_2 + m_c\right)}{m_c} \cdot \mathbf{e}_y \end{bmatrix} \tag{7.5}$$

$$\begin{bmatrix} \ddot{\theta}_1 \\ \ddot{\theta}_2 \end{bmatrix} = \begin{bmatrix} (\mathbf{P}_1 \times \mathbf{T}_1)/I_1 + M \\ (\mathbf{P}_{21} \times \mathbf{T}_{21} + \mathbf{P}_{22} \times \mathbf{T}_{22})/I_2 \end{bmatrix} \tag{7.6}$$

where θ_1 and θ_2 are the angle between the inertial frame and the body frame of tug and target, respectively, x and y denote the positions of the mass center of the tug and target, $\mathbf{P}_1$, $\mathbf{P}_{21}$, and $\mathbf{P}_{22}$ are moment arms of tension in the corresponding tethers, and $\mathbf{T}_1$, $\mathbf{T}_{21}$ and $\mathbf{T}_{22}$ are the tensions in the main tether and two auxiliary tethers.

To calculate the tension, tether is modeled as a 'spring-damper', as shown in Figure 7.10,

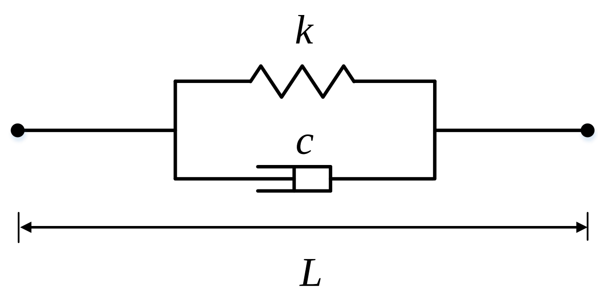

Figure 7.10 Sketch of the tether model

Thus, the tensions in the tethers can be computed by,

$$T = \begin{cases} k(L - L_0) + c\dot{L} & ,T > 0 \,\&\, L > L_0 \\ 0 & ,else \end{cases} \tag{7.7}$$

where k and c represent the stiffness and damping of the tether, L_0 denotes the undeformed tether length, and L denotes the instantaneous tether length.

The controller of torque used in the experiment is same as in Eq.(6.18),

$$M = -k_1\theta_1 - k_2\vartheta \tag{7.8}$$

where k_1 and k_2 are control parameters. ϑ is estimated value angular velocity $\dot{\theta}_1$. ϑ is obtained by the following estimator,

$$\begin{aligned} \vartheta &= \rho + b\theta_1 \\ \dot{\rho} &= -a\vartheta \end{aligned} \tag{7.9}$$

where a and b are the parameters for the estimator.

7.4 Results and Discussion

In this section, the simulation and experiment of maneuvering a rotating space target by tethered space tug are carried out. There is no communication between space target and tug since the target is passive and uncooperative. In current experiment validation, only the tug's attitude control strategy is tested. The control system on space tug only has its own position and attitude information.

7.4.1 Tether Stiffness Measurement

The auxiliary tether for triangle connection used in the experiment is a lightweight elastic string. The stiffness of the string is measured with the

Nidec FG-7000 Digital Force Gauge as shown in Figure 7.11. The custom-built equipment contains the Vernier scale, which is mounted on a guide rail, and two claws for the tether fixation. The deformation of the tether can be recorded by Vernier scale, and the corresponding force is measured by Force Gauge.

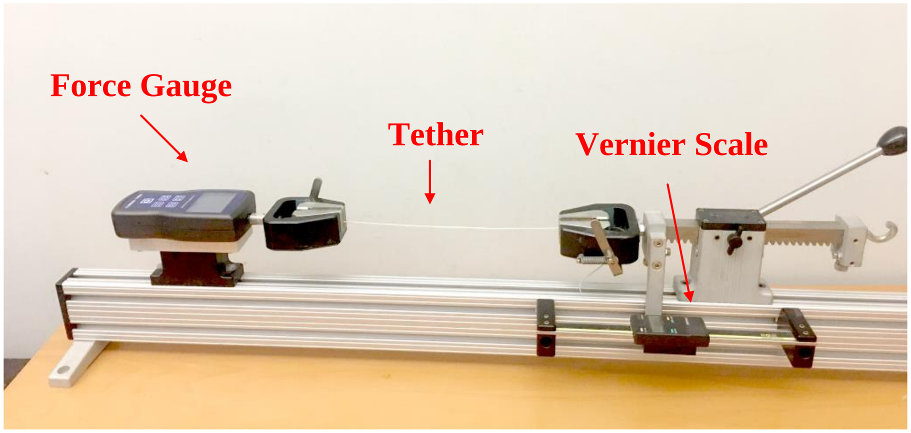

Figure 7.11 Tether stiffness test equipment

To start the test, the equipment is placed on a level table. Undeformed tether length is set as 0.22 m same as the experimental parameter in Table 7.2. Once the length and force are measured, the stiffness can be directly calculated with the measured force and deformation data by the Hooke's law. By taking the average of many tests results, a high measurement accuracy can be ensured. As shown in Figure 7.12, 40 times measurement results are plotted with an error-bar. Note that the average of 40 times measurements is 30 N/m, which will be used in the simulation for comparison purpose.

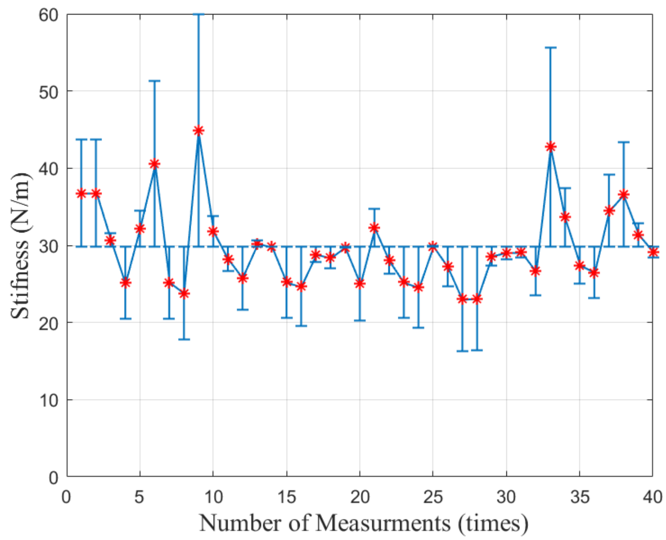

Figure 7.12 Measured tether stiffness

7.4.2 Numerical Simulation

In the simulation case, the initial condition of the system is set as $\left(\theta_1,\dot{\theta}_1,\theta_2,\dot{\theta}_2\right)=\left(0,0,-2\,\mathrm{deg},6\,\mathrm{deg/s}\right)$, which is measured in the experiment, and other parameters are given in Table 7.2. The stiffness of the auxiliary tether is $k=30$ N/m. The material damping of tether is chosen as 3 Ns/m, which is estimated based on the damping ratio of natural rubber (0.01~0.1). To keep the validity of the rigid main tether in simulation, the stiffness of the main tether is about seven times greater than that of the auxiliary tethers. The towing force is 0.4N on the space tug along the OX direction. The parameters in the controller are $k_1=0.1$ and $k_2=2$, and parameters of estimator are $a=6$ and

$b = 6$. The simulation are carried out for 500 seconds and the results are shown in Figure 7.13 (a-h). Figure 7.13 (a) shows the attitude motion of the tug, one can find that the attitude motion of the tug is well controlled with small oscillation around 0 and the magnitude of rotation of tug is decaying towards 0. The attitude motion of the target is oscillating around 0 with significant decaying trend over time, as shown in Figure 7.13 (b). The max rotation angle of target drops from 10 to 2 degree. The angular velocity of the tug is shown in Figure 7.13 (c), the curve of the estimated angular velocity coincides with the original angular velocity. Figure 7.13 (d) shows that the magnitude of the target's angular velocity decreases from 6 to 1 degree/s after 500s. Notably, it indicates that the uncooperative target's angular velocity is well de-spun during maneuver process towed by tug. The tether lengths and tensions are plotted in Figure 7.13 (e) and (f), they all are converging towards the zero equilibrium. The required control torque on the tug is drawn in Figure 7.13 (g), which is within 0.1 Nm and small than the maximum torque can produced by the thrusters. Thus, the simulation indicates that the attitude motion can be well stabilized and controlled while the tethered tug system tows the uncooperative rotating target with triangle connection.

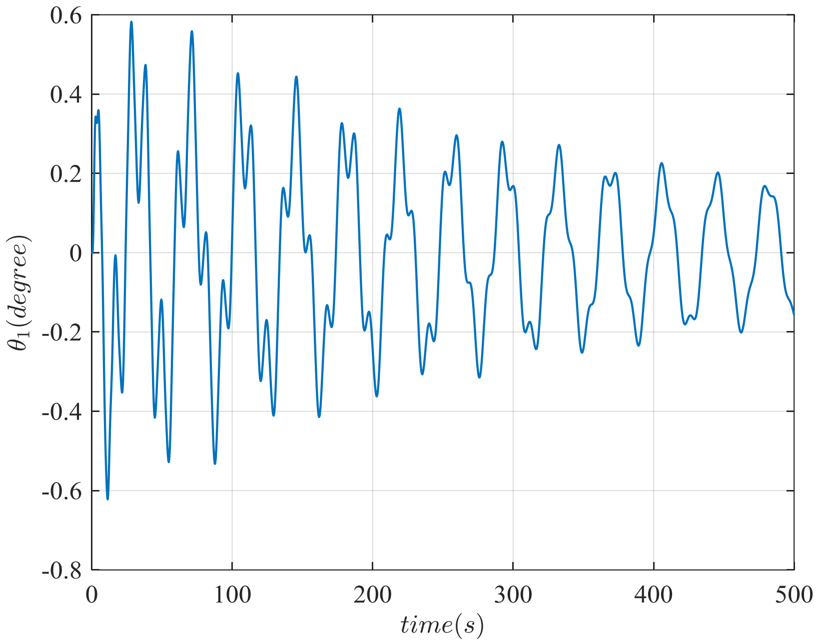
0.6
0.4
0.2
0
-0.2
-0.4
-0.6
-0.8
$\theta_1(degree)$
0
100
200
300
400
500
$time(s)$

(a)

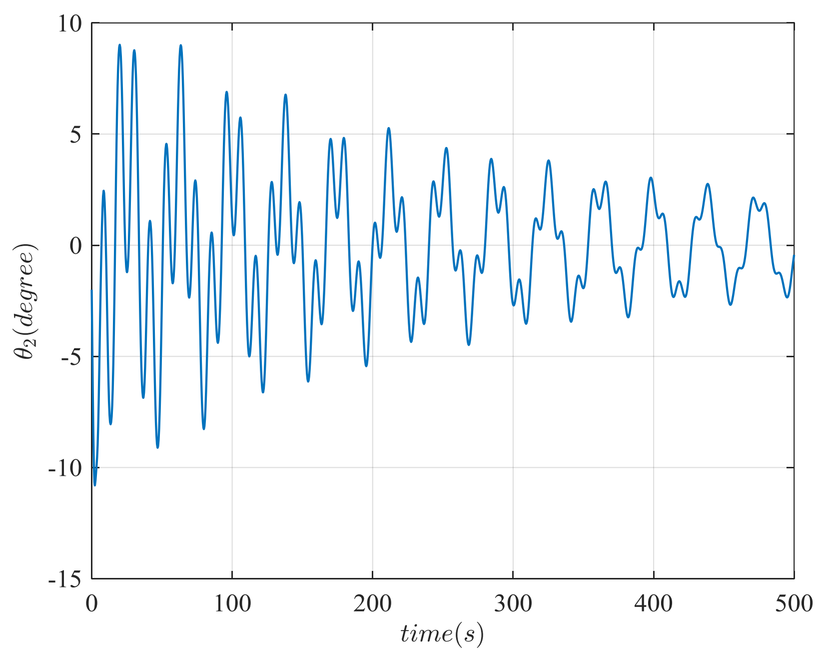
10
5
0
-5
-10
-15
$\theta_2(degree)$
0
100
200
300
400
500
$time(s)$

(b)

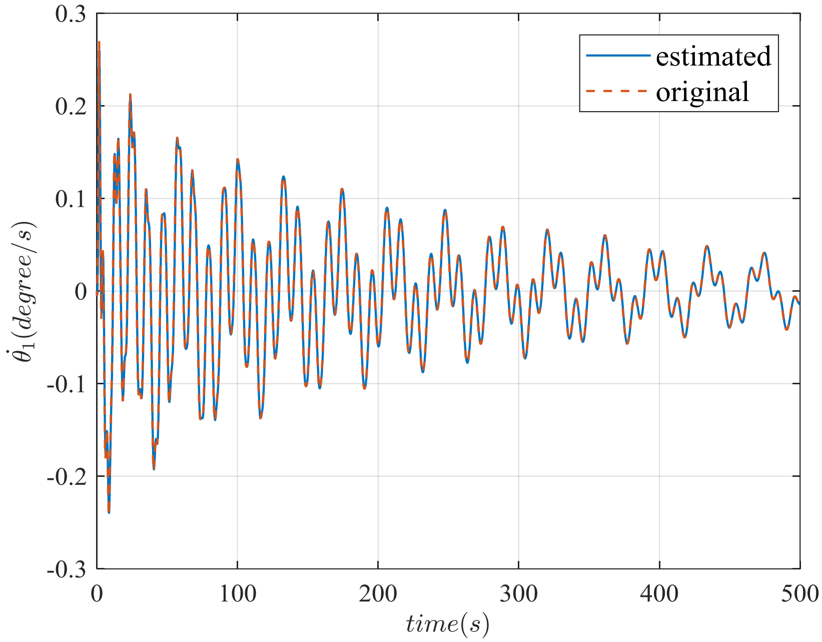
estimated
original
0.3
0.2
0.1
0
-0.1
-0.2
-0.3
0
100
200
300
400
500
$\dot{\theta}_1(degree/s)$
$time(s)$

(c)

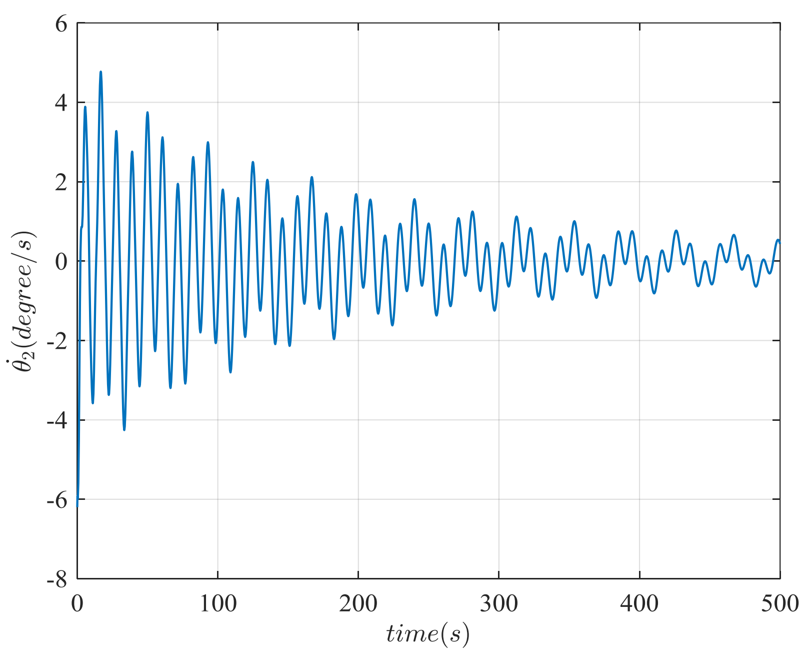
6
4
2
0
-2
-4
-6
-8
0
100
200
300
400
500
$\dot{\theta}_2(degree/s)$
$time(s)$

(d)

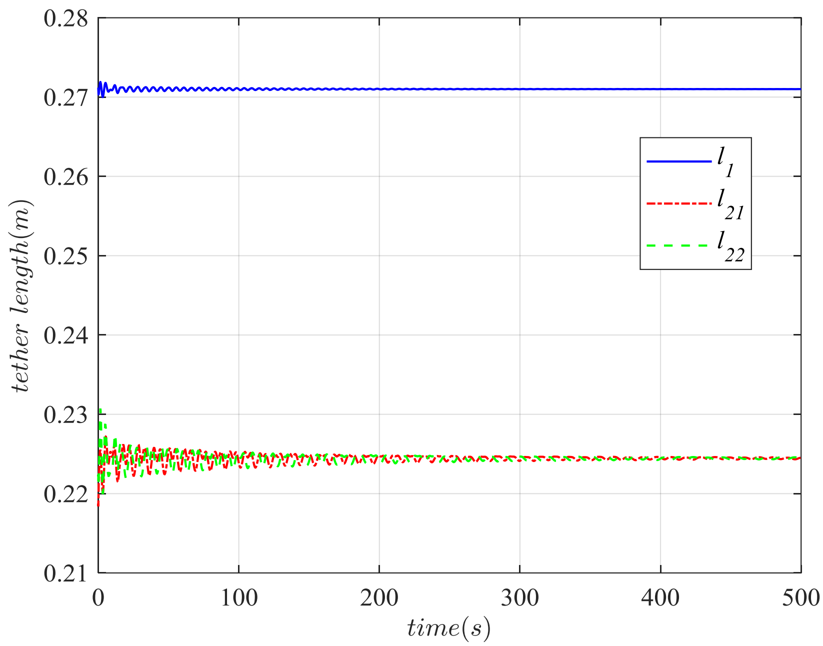

0.28
0.27
0.26
0.25
0.24
0.23
0.22
0.21
tether length(m)
0
100
200
300
400
500
time(s)
l_1
l_{21}
l_{22}

(e)

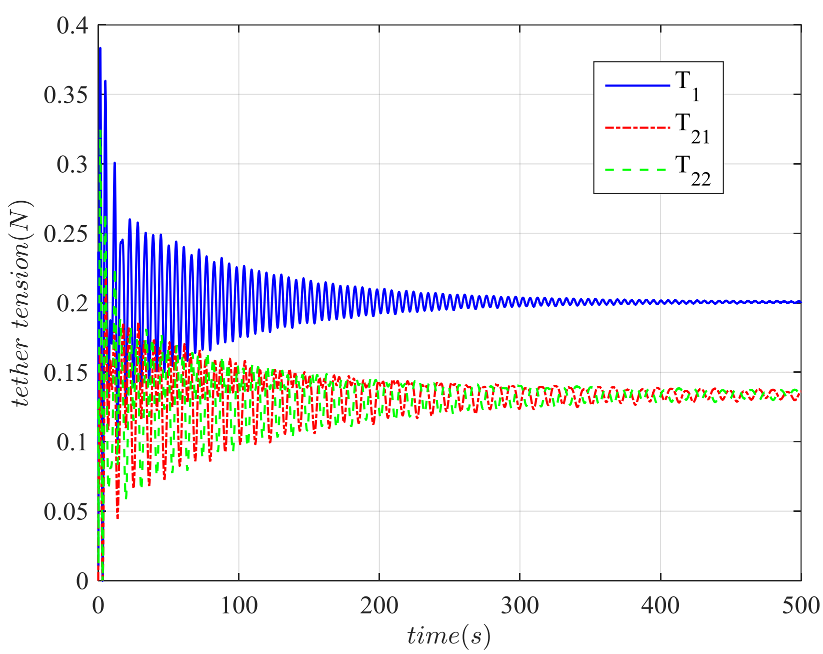

0.4
0.35
0.3
0.25
0.2
0.15
0.1
0.05
0
tether tension(N)
0
100
200
300
400
500
time(s)
T_1
T_{21}
T_{22}

(f)

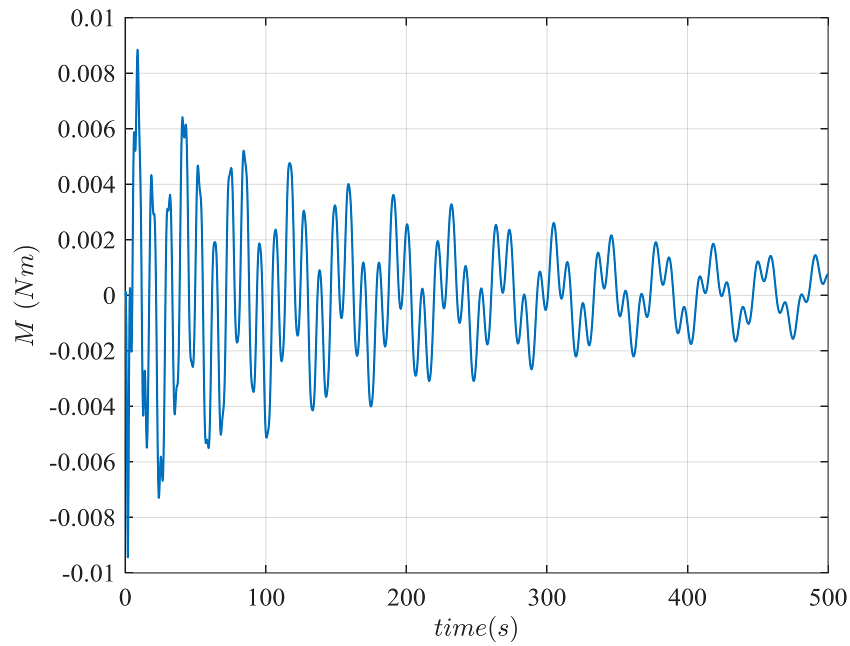

(g)

Figure 7.13 Simulation results of experiment system

7.4.3 Experimental Results

In this section, the experimental validation of the tethered system tug is carried on the SSABT with manually applying an initial spin rate on the target. The output feedback attitude control strategy in Eq. (7.8) is used the same parameters in the simulation. Configurations of the experimental system with respect to time are shown in Figure 7.14. The target is towed towards right- direction with constant force 0.4 N supplied by the auxiliary pulley device. Target is initially spun with a negative spinning rate, 6 degree/s, and then it performs a periodical oscillation during the maneuvering process.

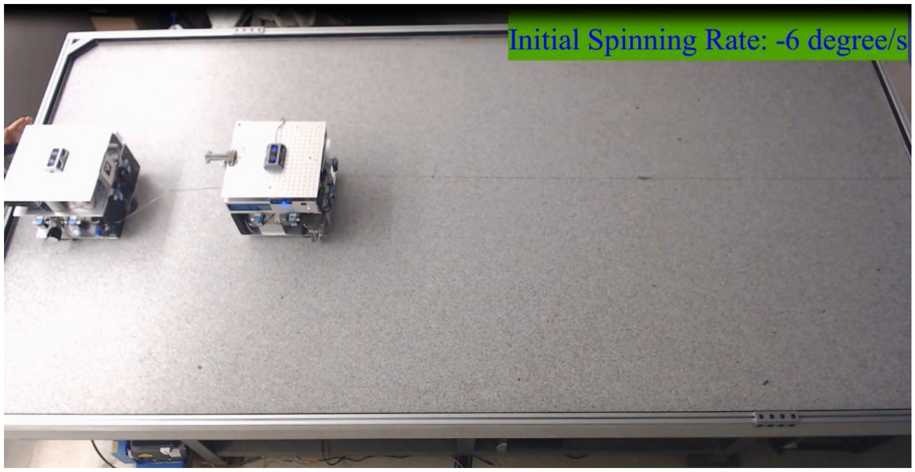
Initial Spinning Rate: -6 degree/s

t=1s

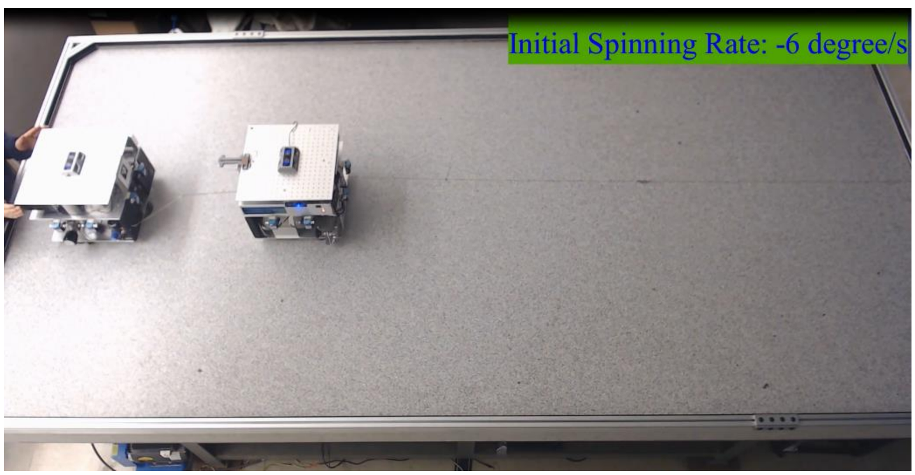
Initial Spinning Rate: -6 degree/s

t=3s

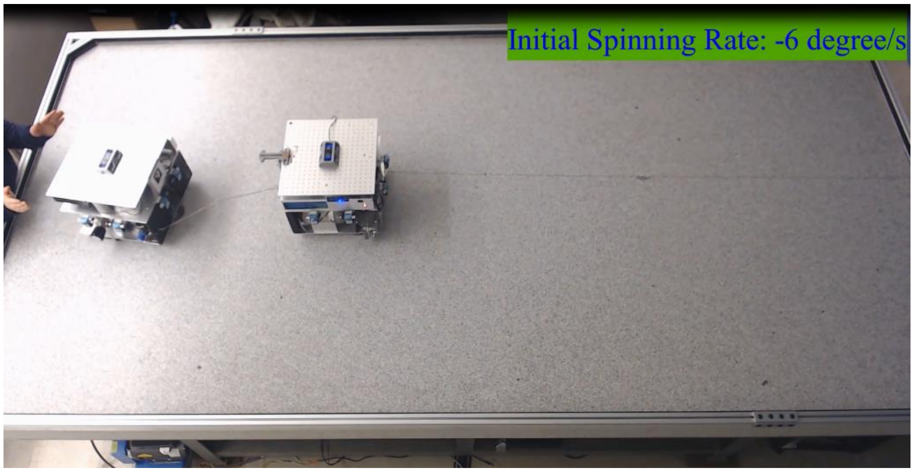
Initial Spinning Rate: -6 degree/s

t=5s

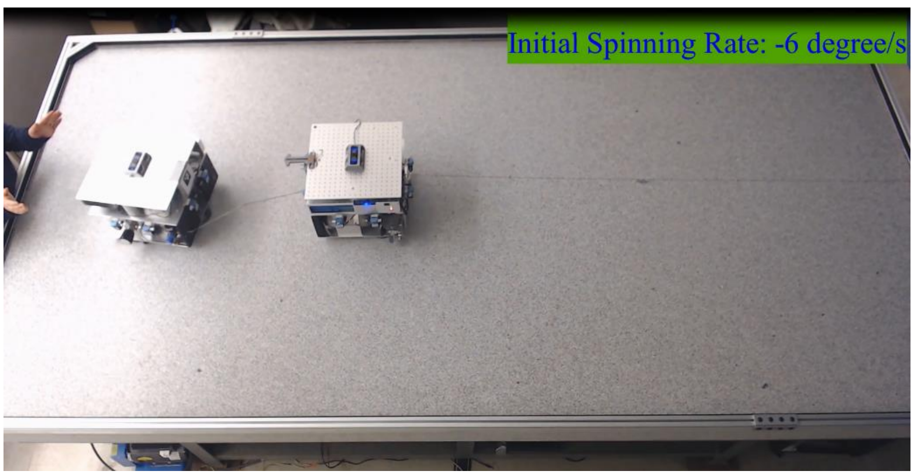
Initial Spinning Rate: -6 degree/s

t=7s

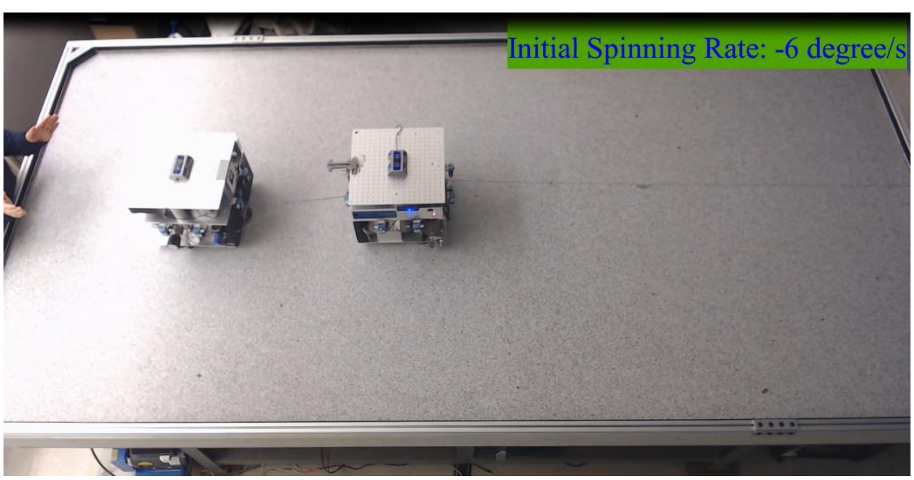
Initial Spinning Rate: -6 degree/s

t=9s

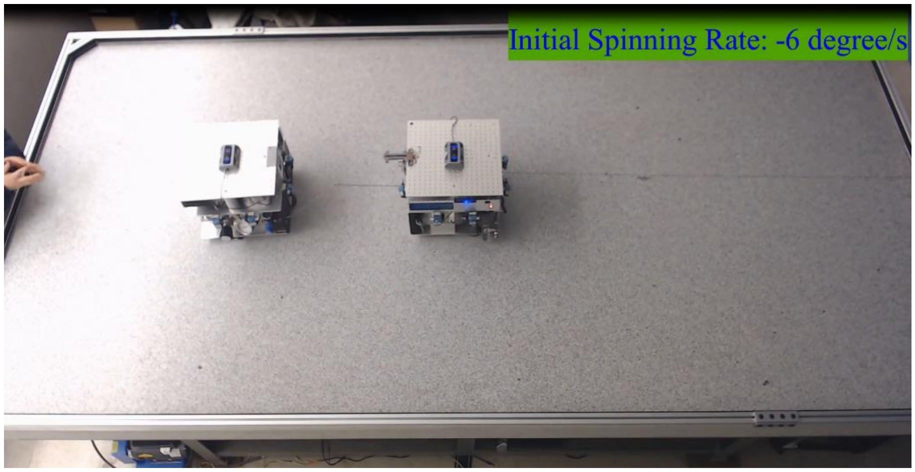

t=11s

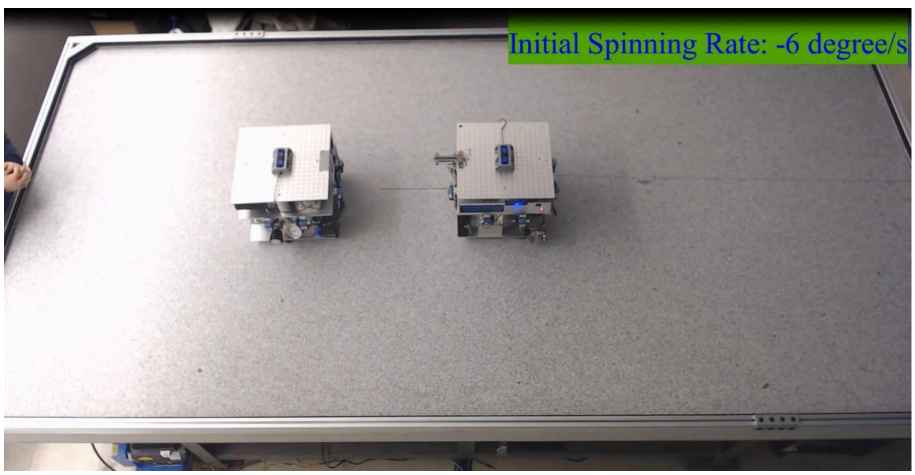

t=13s

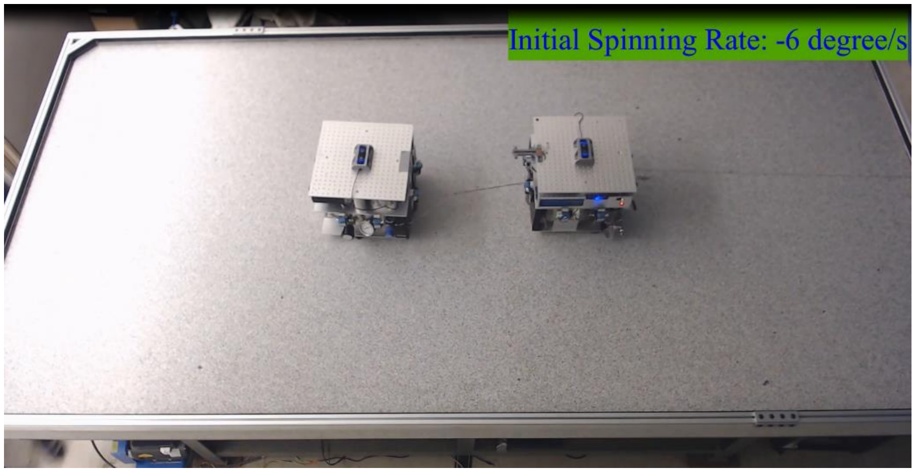

t=15s

Figure 7.14 Time history of configurations in experiment

(Left SS-Target; Right SS-Tug)

The experiment results of the target are drawn in Figure 7.15. Notably, the experiment is running for 18 s due to the length limitation of the air bearing platform. The positions of the target are given in Figure 7.15 (a) and (b), one can find that the translational motion of the target is mainly moving along OX direction while it is oscillating in the OY direction. Seen from Figure 7.15 (c) and (d), the attitude motion of the uncooperative target is slowly decreasing with the magnitude of angular velocity from 6 to 5 degree/s and the magnitude of the rotation angle from 12 to 8 degrees within one period. Furthermore, it is worth noting that the results in the simulation are coincident within the experiment, which validates the simulation results in Section 7.4.2 and demonstrates that the maneuvering a rotating target by the tethered tug system is feasible with proposed design and control strategy.

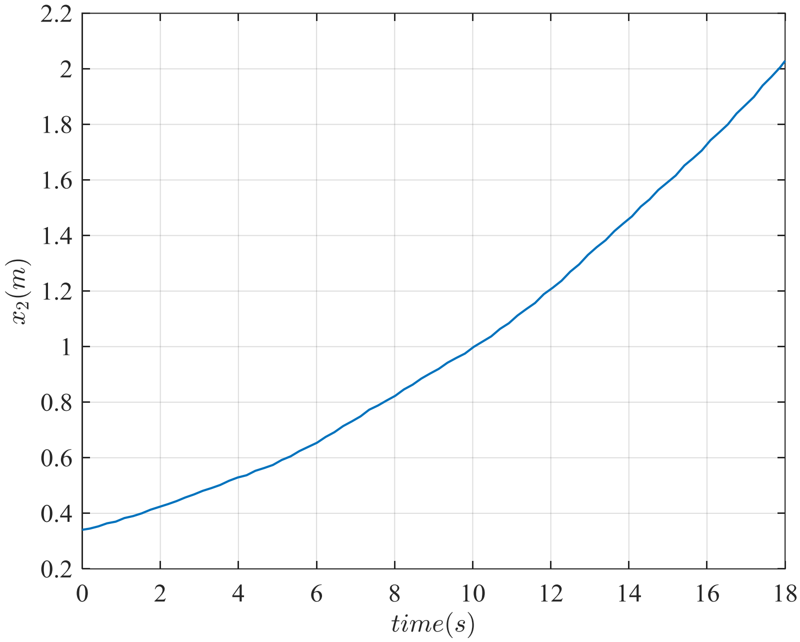

2.2
2
1.8
1.6
1.4
1.2
1
0.8
0.6
0.4
0.2
$x_2(m)$
0
2
4
6
8
10
12
14
16
18
$time(s)$

(a)

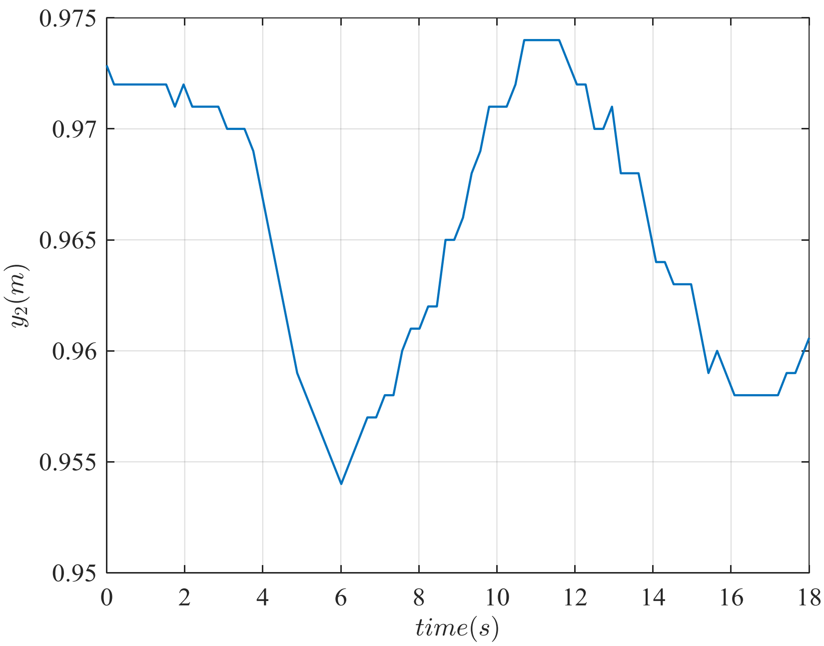

0.975
0.97
0.965
0.96
0.955
0.95
$y_2(m)$
0
2
4
6
8
10
12
14
16
18
$time(s)$

(b)

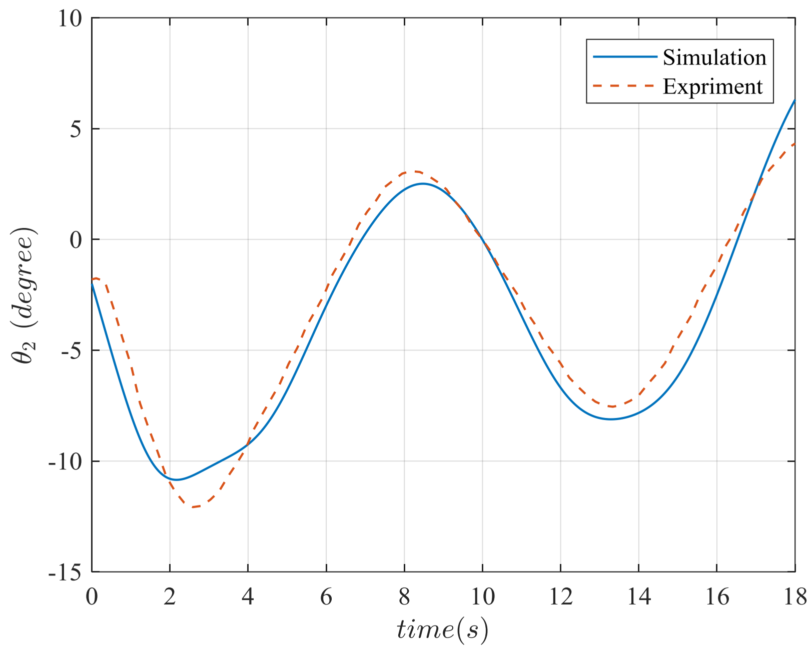

(c)

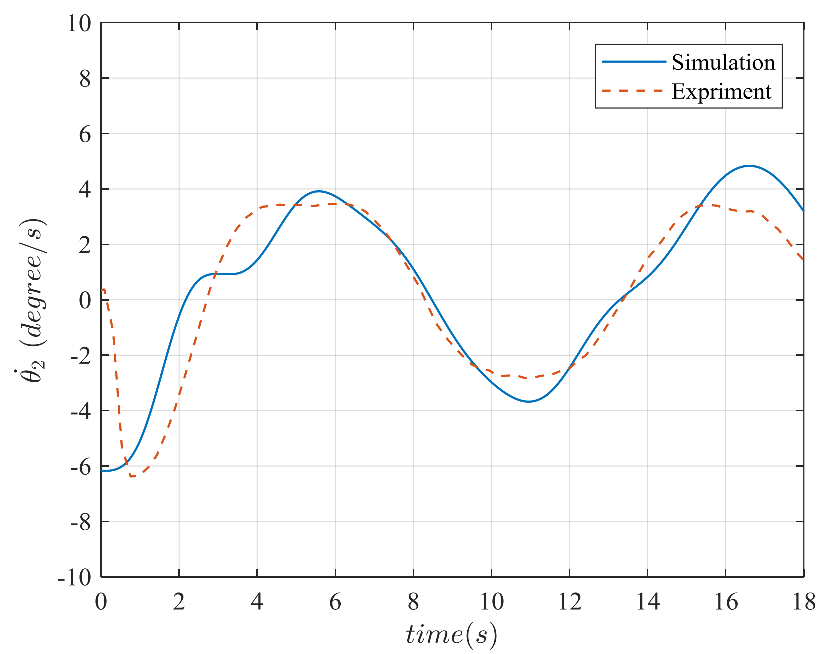

(d)

Figure 7.15 Target's results of experiment

Next, another two experimental tests with different initial spinning rates (10 degree/s and 3 degree/s) are run on the air-bearing testbed to further demonstrate the validity of maneuvering the rotating target by the space-tug. The experimental results of the target's angular velocity are plotted in Figure 7.16, where the angular velocities of the target of both two cases are periodically oscillating and the magnitudes are decreasing slowly. For the 10 degree/s case, it decreases to 9 degree/s after 1.5 periods. It should be noted that, in the 10 degree/s case, the tether slackness occurs at t=5 s because the initial angular velocity of the target is too large to maneuver for a 0.4 N thrust force. The slackness does not appear in the 3 degree/s case, where the angular velocity varies uniformly and decrease to 2 degree/s after 16 s. Two snapshots of these two cases are presented in Figure 7.17 to show the system's configuration. The time history of system's configuration is similar to Figure 7.14, thus it is not presented here.

According to the theoretical analysis, numerical simulations, and experimental tests, it can be concluded that the tethered space tug is feasible to maneuver a rotating space target. Note that the despin of target has to be conducted before orbital maneuver if the space target is with huge kinetic energy compared to the capacity of the thrust. Otherwise, the tether will become slack or wrap around the target or tug, and further destabilize the whole system and result in a failure of the mission. After the target's rotation is despun to a small level that the tug's thrust can compete, the tethered space tug can maneuver an uncooperative target, effectively to the desired orbit.

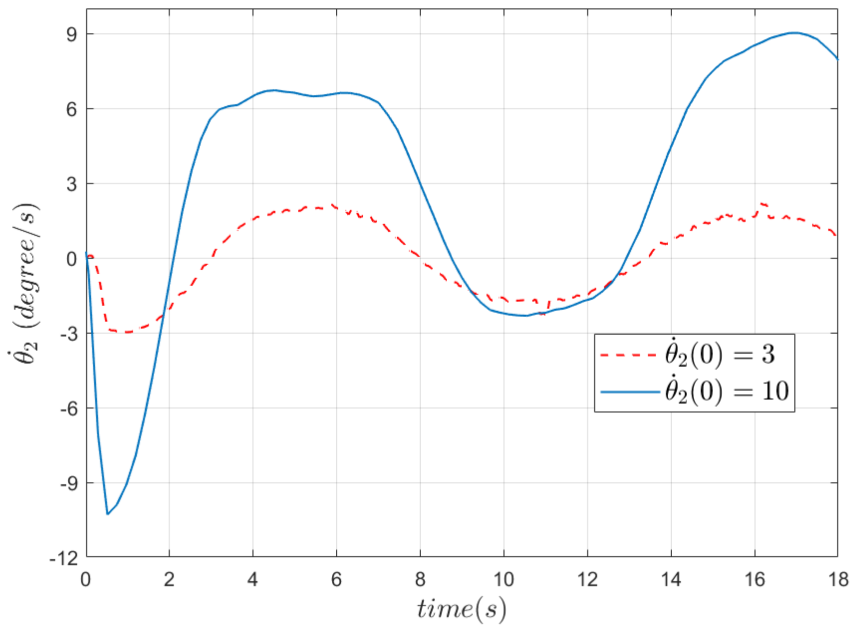

Figure 7.16 Angular velocity of target

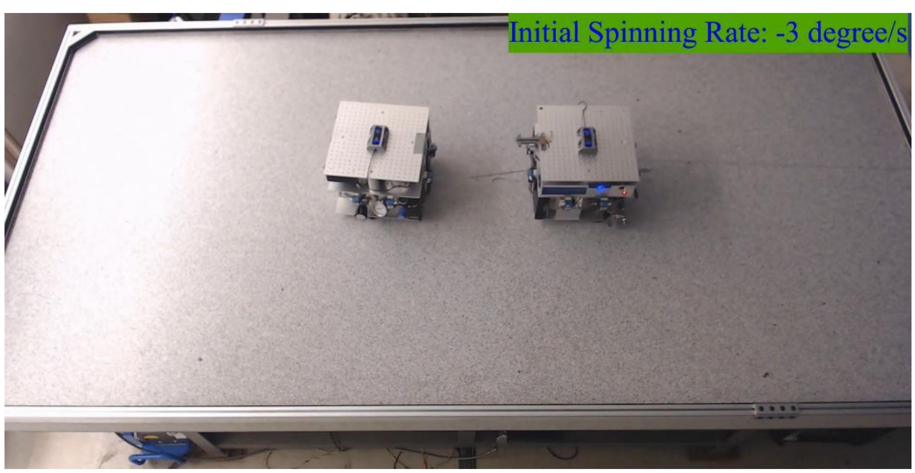

(a)

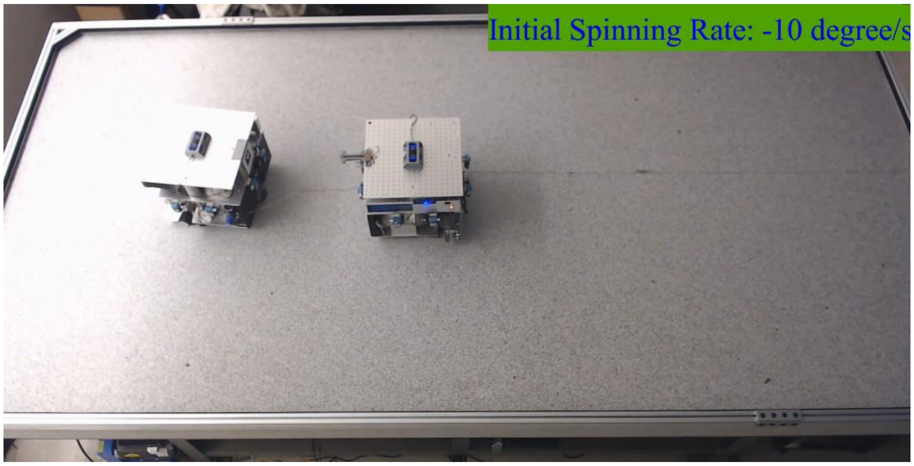

(b)

Figure 7.17 Configurations of tethered system

(a) 3 degrees/s case (b) 10 degree/s case

In this section, we built an auxiliary-pulley mechanism aided tethered tug experimental system on the air-bearing to supply the sufficient towing force for the simulator in experimental setup and validate the tug's attitude control strategy experimentally through the LabVIEW Real-Time Module. Three tests of different initial spinning rate of targets are conducted and the results demonstrate the feasibility and effectiveness of the proposed concept of tether tug maneuver.

Chapter 8 CONCLUSIONS AND FUTURE WORK

Summary: This chapter summarizes the contributions and future research directions for the continuation of the current study.

8.1 Contributions

This dissertation focuses on the control of the underactuated TSS and the dynamics and control of massive rotating space target removal. To best of my knowledge, this research systematically investigated the dynamics and control of the massive rotating target despin by small tethered tug, including the concept design, control strategy, and experimental validation after despin. The main contributions of this research are summarized as follows.

8.1.1 Tension Control for TSS Deployment/Retrieval

The current work develops a unified energy-based framework for tension controller to achieve fast, stable, and precise deployment/retrieval of underactuated TSS. As a systematic approach, the control objectives and stability requirement for closed-loop system are transformed into the necessary and sufficient conditions for the artificial potential energy function and the dissipative functions. The asymptotic stability of the energy-based tension control framework has been proven rigorously by the Lyapunov technique and the LaSalle's Invariance Principle.

Furthermore, to address the challenge arising from engineering where the unknown and unexpected disturbances occurring in the TSS missions, a fractional order sliding mode controller is designed to address the disturbances. The effectiveness and robustness of the proposed FOSMC are demonstrated by comparing with existing conventional control methods. Fractional order sliding mode control law demonstrates excellent disturbance rejection capability in a wide frequency range.

8.1.2 Dynamics and Despin Control of Large Rotating Target

Dynamics and control of large rotating targets captured by small tethered spacecraft are studied. The dynamic model is established in both the free-floating space and the central gravitational field. The physical parameters of the system's effect on the dynamic behaviors are compared, and control strategies are proposed with considering the operational constraints and attainable configurations of equilibrium. Furthermore, to analytically tackle the problem of the constraint and guarantee the stability of the despin control for the nonlinear underactuated target with TSS, a novel MPC approach based on passivity-based control is proposed. The approach of the PBMPC is theoretically proved in an elegant framework by the nonlinear stability analysis without linearization, and the asymptotic stability of the system with PBMPC is ensured without using the terminal cost.

8.1.3 Uncooperative Target Maneuvering and Experimental Verification

The dynamic model of the tethered captured uncooperative target during orbit maneuvering is established to study the system's dynamic behaviors. The orbital dynamics, attitude motions of the space tug and uncooperative target are included in this dissertation. Control strategies are then designed to achieve the attitude stabilization for both tug and target and to suppress the tether libration motion. Furthermore, to demonstrate the effectiveness of the concept of the tethered space tug and validate the proposed control strategy, an experimental system is set up on the air-bearing platform to mimic the zero-gravity environment in space.

8.2 Conclusions

Deployment/retrieval control of the tethered space system is challenging due to the underactuation and partial state measurement. Energy shaping control can deal with these restrictions on controller design by constructing an artificial function with only the actuated state to render the TSS stable. Additionally, positive tension and libration angle constraints can be effectively handled by tuning the control gains. Moreover, the total external disturbances, orbital perturbations, and other potential uncertainties may degrade the conventional controller's performance and stability. Thus, a stable and robust controller is needed for TSS, such as SMC and adaptive control.

Large space debris removal and small asteroid retrieval attract much attention due to its scientific and commercial interests. Tethered space tug is an appealing and low-cost approach with broad applicability on different sizes of targets. However, capturing the sizeable rotating target or attaching the tether to the target is still a particularly challenging problem. Moreover, TSS's dynamic motions are extremely complicated due to the uncooperative rotating target in the post-capture phase. The large target's rotation is with substantial kinetic energy, which must be damped before the next operation.

Consequently, a de-tumbling process should be executed to reduce the rotation to an admissible level. According to the comparison, the hybrid control strategy is appealing to implement in future mission for its fast and good despin performance. Then, in the orbit maneuvering process, it still needs to pay attention to the residual rotation. It might cause the tether wrapping around the target and tug. The ground experimental facilities should be made to simulate the orbital maneuvering of TSS in the space environment. The air-bearing table experimental facility provides a preferable zero-gravity environment to verify the concept of TSS and control strategy. However, it is not enough to examine the large-scale tethered system's long-term motion due to its limited dimensions.

8.3 Future Work

The following research is summarized as follows to continue and expand the current work.

(i) Consider the model uncertainties of tether system for deployment/retrieval. Such as, capture an unknown mass of target and relocate it.

(ii) Extend the current work of space target despinning to de-tumbling because the space target might tumble in space.

(iii) Investigate the parameter optimization of tethered system to improve the despin efficiency of a specified target.

(iv) Verify TSS deployment/retrieval and the tension control and hybrid control strategy for rotating target maneuvering by tethered space tug on the air-bearing table experimentally.

(v) Improve current experimental setup on air-bearing table for long-time maneuver validation. One feasible way is to maneuver the experimental system in circles, thus we can get rid of the size limitation of air-table. However, this requires the sufficient thrust capacity of simulator to tow the passive target and ensure tether taut.

Bibliography

[1]. "Space environment statistics," https://sdup.esoc.esa.int/discosweb/statistics/. Accessd on August 30, 2020.

[2]. Anz-Meador, P. D., Opiela, J. N., Shoots, D., and Liou, J.-C. "History of on-orbit satellite fragmentations." 2018.

[3]. Council, N. R. Orbital debris: A technical assessment: National Academies Press, 1995.

[4]. Rumpf, C. M., Lewis, H. G., and Atkinson, P. M. "Asteroid impact effects and their immediate hazards for human populations," Geophysical Research Letters, Vol. 44, No. 8, 2017, pp. 3433-3440. doi: 10.1002/2017gl073191

[5]. "Discovery statistics," https://cneos.jpl.nasa.gov/stats/totals.html. Accessd on September 1, 2020.

[6]. Granvik, M., Morbidelli, A., Jedicke, R., Bolin, B., Bottke, W. F., Beshore, E., Vokrouhlický, D., Nesvorný, D., and Michel, P. "Debiased orbit and absolute-magnitude distributions for near-earth objects," Icarus, Vol. 312, 2018, pp. 181-207. doi: 10.1016/j.icarus.2018.04.018

[7]. "Asteroid initiative ideas synthesis workshop," https://www.nasa.gov/content/asteroid-initiative-idea-synthesis-workshop/#.XwC3lG1KjX4. Accessd on July 1, 2020.

[8]. Brophy, J. R., and Muirhead, B. "Near-earth asteroid retrieval mission (arm) study." 2013.

[9]. "Osiris-rex," https://solarsystem.nasa.gov/missions/osiris-rex/in-depth/. Accessd on September 1, 2020.

[10]. Bonnal, C., Ruault, J.-M., and Desjean, M.-C. "Active debris removal: Recent progress and current trends," Acta Astronautica, Vol. 85, 2013, pp. 51-60. doi: 10.1016/j.actaastro.2012.11.009

[11]. Shan, M., Guo, J., and Gill, E. "Review and comparison of active space debris capturing and removal methods," Progress in Aerospace Sciences, Vol. 80, 2016, pp. 18-32. doi: 10.1016/j.paerosci.2015.11.001

[12]. Mazanek, D. D., Brohpy, J. R., and Merrill, R. G. "Asteroid retrieval mission concept-trailblazing our future in space and helping to protect us from earth impactors," IAA Planetary Defense Conference. Flagstaff, AZ., 2013.

[13]. Chen, Y., Huang, R., Ren, X., He, L., and He, Y. "History of the tether concept and tether missions: A review," ISRN Astronomy and

Astrophysics, 2013.
doi: 10.1155/2013/502973
[14]. Kruijff, M. "Tethers in space: A propellantless propulsion in-orbit demonstration." Doctoral Thesis, Delft University of Technology, Netherlands, 2011.
[15]. "Space tethers," https://earth.esa.int/web/eoportal/satellite-missions/s/space-tethers. Accessd on September 1, 2020.
[16]. Yu, B. S., Wen, H., and Jin, D. P. "Review of deployment technology for tethered satellite systems," Acta Mechanica Sinica, Vol. 34, No. 4, 2018, pp. 754-768.
doi: 10.1007/s10409-018-0752-5
[17]. Kumar, K. D. "Review on dynamics and control of nonelectrodynamic tethered satellite systems," Journal of Spacecraft and Rockets, Vol. 43, No. 4, 2006, pp. 705-720.
doi: 10.2514/1.5479
[18]. Wen, H., Jin, D. P., and Hu, H. Y. "Advances in dynamics and control of tethered satellite systems," Acta Mechanica Sinica, Vol. 24, No. 3, 2008.
doi: 10.1007/s10409-008-0159-9
[19]. Hoyt, R. P., and James, K. "Wrangler: Nanosatellite architecture for tethered de-spin of massive asteroids," AIAA SPACE 2015 Conference and Exposition.
[20]. Yudintsev, V., and Aslanov, V. "Detumbling space debris using modified yo-yo mechanism," Journal of Guidance, Control, and Dynamics, Vol. 40, No. 3, 2017, pp. 714-721.
doi: 10.2514/1.g000686
[21]. Jasper, L. E. "Open-loop thrust profile development for tethered towing of large space objects." University of Colorado at Boulder, 2014.
[22]. Kang, J., and Zhu, Z. H. "Dynamics and control of de-spinning giant asteroids by small tethered spacecraft," Aerospace Science and Technology, Vol. 94, 2019, p. 105394.
doi: 10.1016/j.ast.2019.105394
[23]. Zhang, J., Yang, K., and Qi, R. "Dynamics and offset control of tethered space-tug system," Acta Astronautica, Vol. 142, 2018, pp. 232-252.
doi: 10.1016/j.actaastro.2017.10.020
[24]. Puig-Suari, J., Logunski, J. M., and Tragesser, S. G. "Aerocapture with a flexible tether," Journal of Guidance, Control, and Dynamics, Vol. 18, No. 6, 1995, pp. 1305-1312.
doi: 10.2514/3.21546
[25]. Rupp, C. C. "A tether tension control law for tethered subsatellites deployed along local vertical," STIN. Vol. 76, 1975, p. 11194.
[26]. Fujii, H., and Ishijima, S. "Mission function control for deployment and retrieval of a subsatellite," Journal of Guidance, Control, and Dynamics,

Vol. 12, No. 2, 1989, pp. 243-247.
doi: 10.2514/3.20397

[27]. Vadali, S. R. "Feedback tether deployment and retrieval," Journal of Guidance, Control, and Dynamics, Vol. 14, No. 2, 1991, pp. 469-470.
doi: 10.2514/3.20662

[28]. Kim, E., and Vadali, S. R. "Nonlinear feedback deployment and retrieval of tethered satellite systems," Journal of Guidance, Control, and Dynamics, Vol. 15, No. 1, 1992, pp. 28-34.
doi: 10.2514/3.20797

[29]. Pradeep, S. "A new tension control law for deployment of tethered satellites," Mechanics Research Communications, Vol. 24, No. 3, 1997, pp. 247-254.
doi: 10.1016/S0093-6413(97)00021-9

[30]. Kumar, K., and Pradeep, S. "Strategies for three dimensional deployment of tethered satellites," Mechanics Research Communications, Vol. 25, No. 5, 1998, pp. 543-550.
doi: 10.1016/S0093-6413(98)00071-8

[31]. Sun, G., and Zhu, Z. H. "Fractional-order tension control law for deployment of space tether system," Journal of Guidance, Control, and Dynamics, Vol. 37, No. 6, 2014, pp. 2057-2062.
doi: 10.2514/1.g000496

[32]. Sun, G., and Zhu, Z. H. "Fractional order tension control for stable and fast tethered satellite retrieval," Acta Astronautica, Vol. 104, No. 1, 2014, pp. 304-312.
doi: 10.1016/j.actaastro.2014.08.012

[33]. Ma, Z., and Sun, G. "Adaptive sliding mode control of tethered satellite deployment with input limitation," Acta Astronautica, Vol. 127, 2016, pp. 67-75.
doi: 10.1016/j.actaastro.2016.05.022

[34]. Wang, C., Wang, P., Li, A., and Guo, Y. "Deployment of tethered satellites in low-eccentricity orbits using adaptive sliding mode control," Journal of Aerospace Engineering, Vol. 30, No. 6, 2017, p. 04017077.
doi: doi:10.1061/(ASCE)AS.1943-5525.0000793

[35]. Ma, Z., Sun, G., Cheng, Z., and Li, Z. "Pure-tension non-linear sliding mode control for deployment of tethered satellite system," Proceedings of the Institution of Mechanical Engineers, Part G: Journal of Aerospace Engineering, Vol. 232, No. 13, 2018, pp. 2541-2551.
doi: 10.1177/0954410017718002

[36]. Xu, S., Sun, G., Ma, Z., and Li, X. "Fractional-order fuzzy sliding mode control for the deployment of tethered satellite system under input saturation," IEEE Transactions on Aerospace and Electronic Systems, Vol. 55, No. 2, 2019, pp. 747-756.

doi: 10.1109/TAES.2018.2864767
[37]. Wen, H., Zhu, Z. H., Jin, D., and Hu, H. "Space tether deployment control with explicit tension constraint and saturation function," Journal of Guidance, Control, and Dynamics, Vol. 39, No. 4, 2016, pp. 916-921.
doi: 10.2514/1.g001356
[38]. Wen, H., Zhu, Z. H., Jin, D., and Hu, H. "Constrained tension control of a tethered space-tug system with only length measurement," Acta Astronautica, Vol. 119, 2016, pp. 110-117.
doi: 10.1016/j.actaastro.2015.11.011
[39]. Kang, J., Zhu, Z. H., Wang, W., Li, A., and Wang, C. "Fractional order sliding mode control for tethered satellite deployment with disturbances," Advances in Space Research, Vol. 59, No. 1, 2017, pp. 263-273.
doi: 10.1016/j.asr.2016.10.006
[40]. Steindl, A., and Troger, H. "Optimal control of deployment of a tethered subsatellite," Nonlinear Dynamics, Vol. 31, No. 3, 2003, pp. 257-274.
doi: 10.1023/A:1022956002484
[41]. Wen, H., Jin, D. P., and Hu, H. Y. "Optimal feedback control of the deployment of a tethered subsatellite subject to perturbations," Nonlinear Dynamics, Vol. 51, No. 4, 2008, pp. 501-514.
doi: 10.1007/s11071-007-9240-3
[42]. Williams, P., Hyslop, A., Stelzer, M., and Kruijff, M. "Yes2 optimal trajectories in presence of eccentricity and aerodynamic drag," Acta Astronautica, Vol. 64, No. 7, 2009, pp. 745-769.
doi: 10.1016/j.actaastro.2008.11.007
[43]. Jin, D. P., and Hu, H. Y. "Optimal control of a tethered subsatellite of three degrees of freedom," Nonlinear Dynamics, Vol. 46, No. 1, 2006, pp. 161-178.
doi: 10.1007/s11071-006-9021-4
[44]. Kang, J., and Zhu, Z. H. "A unified energy-based control framework for tethered spacecraft deployment," Nonlinear Dynamics, Vol. 95, No. 2, 2019, pp. 1117-1131.
doi: 10.1007/s11071-018-4619-x
[45]. Liu, M., Zhan, X., Zhu, Z. H., and Liu, B. "Space tether deployment with explicit non-overshooting length and positive velocity constraints," Journal of Guidance, Control, and Dynamics, Vol. 40, No. 12, 2017, pp. 3313-3318.
doi: 10.2514/1.g002829
[46]. Strange, N., Landau, D., Longuski, J., and Chodas, P. "Redirection of asteroids onto earth-mars cyclers," AAS Spaceflight Mechanics Meeting. 2015.

[47]. Debus, T., and Dougherty, S. "Overview and performance of the front-end robotics enabling near-term demonstration (frend) robotic arm," AIAA Infotech@Aerospace Conference. Seattle,Washington USA, 2009.
[48]. Flores-Abad, A., Ma, O., Pham, K., and Ulrich, S. "A review of space robotics technologies for on-orbit servicing," Progress in Aerospace Sciences, Vol. 68, 2014, pp. 1-26.
doi: 10.1016/j.paerosci.2014.03.002
[49]. Shan, M., Guo, J., and Gill, E. "Contact dynamics on net capturing of tumbling space debris," Journal of Guidance, Control, and Dynamics, Vol. 41, No. 9, 2018, pp. 2063-2072.
doi: 10.2514/1.g003460
[50]. Zinner, N., Williamson, A., Brenner, K., Curran, J., Isaak, A., Knoch, M., Leppek, A., and Lestishen, J. "Junk hunter: Autonomous rendezvous, capture, and de-orbit of orbital debris," AIAA SPACE 2011 Conference & Exposition. Long Beach, CA, USA, 2011.
[51]. Bischof, B. "Roger-robotic geostationary orbit restorer," 54th International Astronautical Congress of the International Astronautical Federation, the International Academy of Astronautics, and the International Institute of Space Law. 2003, p. IAA. 5.2. 08.
[52]. Huang, P., Zhang, F., Cai, J., Wang, D., Meng, Z., and Guo, J. "Dexterous tethered space robot: Design, measurement, control, and experiment," IEEE Transactions on Aerospace and Electronic Systems, Vol. 53, No. 3, 2017, pp. 1452-1468.
doi: 10.1109/TAES.2017.2671558
[53]. Grip, H. F., Ono, M., Balaram, J., Cameron, J., Jain, A., Kuo, C., Myint, S., and Quadrelli, M. "Modeling and simulation of asteroid retrieval using a flexible capture mechanism," 2014 IEEE Aerospace Conference. 2014, pp. 1-14.
[54]. Fedor, J. Theory and design curves for a yo-yo de-spin mechanism for satellites: National Aeronautics and Space Administration, 1961.
[55]. Hoyt, R. P., and James, K. "Wrangler: Nanosatellite architecture for tethered de-spin of massive asteroids," AIAA SPACE 2015 Conference and Exposition. Pasadena, California,USA, 2015.
[56]. Aslanov, V. S., and Yudintsev, V. V. "Dynamics of large debris connected to space tug by a tether," Journal of Guidance, Control, and Dynamics, Vol. 36, No. 6, 2013, pp. 1654-1660.
doi: 10.2514/1.60976
[57]. Aslanov, V., and Yudintsev, V. "Dynamics of large space debris removal using tethered space tug," Acta Astronautica, Vol. 91, 2013, pp. 149-156.
doi: 10.1016/j.actaastro.2013.05.020
[58]. Aslanov, V. S., and Ledkov, A. S. "Dynamics of towed large space debris taking into account atmospheric disturbance," Acta Mechanica, Vol. 225,

No. 9, 2014, pp. 2685-2697.
doi: 10.1007/s00707-014-1094-4

[59]. Aslanov, V. S., and Yudintsev, V. V. "Dynamics, analytical solutions and choice of parameters for towed space debris with flexible appendages," Advances in Space Research, Vol. 55, No. 2, 2015, pp. 660-667.
doi: 10.1016/j.asr.2014.10.034

[60]. Cleary, S., and O'Connor, W. J. "Control of space debris using an elastic tether and wave-based control," Journal of Guidance, Control, and Dynamics, Vol. 39, No. 6, 2016, pp. 1392-1406.
doi: 10.2514/1.g001624

[61]. O'Connor, M., Clearly, S., and Hayden, D. "Debris de-tumbling and de-orbiting by elastic tether and wave-based control," 6th International Conference on Astrodynamics Tools and Techniques. Darmstadt, Germany, 2016, pp. 14-17.

[62]. Meng, Z., Wang, B., and Huang, P. "Twist suppression method of tethered towing for spinning space debris," Journal of Aerospace Engineering, Vol. 30, No. 4, 2017, p. 04017012.
doi: 10.1061/(ASCE)AS.1943-5525.0000708

[63]. Wang, B., Meng, Z., and Huang, P. "Attitude control of towed space debris using only tether," Acta Astronautica, Vol. 138, 2017, pp. 152-167.
doi: 10.1016/j.actaastro.2017.05.012

[64]. Chu, Z., Di, J., and Cui, J. "Analysis of the effect of attachment point bias during large space debris removal using a tethered space tug," Acta Astronautica, Vol. 139, 2017, pp. 34-41.
doi: 10.1016/j.actaastro.2017.06.028

[65]. Sun, X., and Zhong, R. "Tether attachment point stabilization of noncooperative debris captured by a tethered space system," Acta Astronautica, 2019.
doi: 10.1016/j.actaastro.2019.12.012

[66]. Sun, X., and Zhong, R. "Nutation damping and spin orientation control of tethered space debris," Acta Astronautica, Vol. 160, 2019, pp. 683-693.
doi: 10.1016/j.actaastro.2019.03.019

[67]. Liu, H., Zhang, Q., Yang, L., Zhu, Y., and Zhang, Y. "Dynamics of tether-tugging reorbiting with net capture," Science China Technological Sciences, Vol. 57, No. 12, 2014, pp. 2407-2417.
doi: 10.1007/s11431-014-5717-8

[68]. Yang, K., Misra, A. K., Zhang, J., Qi, R., Lu, S., and Liu, Y. "Dynamics of a debris towing system with hierarchical tether architecture," Acta Astronautica, 2019.
doi: 10.1016/j.actaastro.2019.10.048

[69]. Qi, R., Misra, A. K., and Zuo, Z. "Active debris removal using double-tethered space-tug system," Journal of Guidance, Control, and

Dynamics, Vol. 40, No. 3, 2017, pp. 722-730.
doi: 10.2514/1.g000699

[70]. Hovell, K., and Ulrich, S. "Attitude stabilization of an uncooperative spacecraft in an orbital environment using visco-elastic tethers," AIAA Guidance, Navigation, and Control Conference. San Diego, California, USA, 2016.

[71]. Hovell, K., and Ulrich, S. "Experimental validation for tethered capture of spinning space debris," AIAA Guidance, Navigation, and Control Conference. Grapevine, Texas, USA, 2017.

[72]. Hovell, K., and Ulrich, S. "Postcapture dynamics and experimental validation of subtethered space debris," Journal of Guidance, Control, and Dynamics, Vol. 41, No. 2, 2018, pp. 519-525.
doi: 10.2514/1.g003049

[73]. Kang, J., Zhu, Z. H., Wang, W., Wang, C., and Li, A. "Dynamics and de-spin control of massive target by single tethered space tug," Chinese Journal of Aeronautics, Vol. 32, No. 3, 2019, pp. 653-659.
doi: 10.1016/j.cja.2019.01.002

[74]. Kang, J., and Zhu, Z. H. "De-spin of massive rotating space object by tethered space tug," Journal of Guidance, Control, and Dynamics, Vol. 41, No. 11, 2018, pp. 2463-2469.
doi: 10.2514/1.g003584

[75]. Wen, H., and Jin, D. "De-spinning of tethered space target via partially invariable deployment with tension control," Nonlinear Dynamics, Vol. 96, No. 1, 2019, pp. 637-645.
doi: 10.1007/s11071-019-04811-2

[76]. Mayne, D. Q., Rawlings, J. B., Rao, C. V., and Scokaert, P. O. M. "Constrained model predictive control: Stability and optimality," Automatica, Vol. 36, No. 6, 2000, pp. 789-814.
doi: 10.1016/S0005-1098(99)00214-9

[77]. Wen, H., Zhu, Z. H., Jin, D., and Hu, H. "Tension control of space tether via online quasi-linearization iterations," Advances in Space Research, Vol. 57, No. 3, 2016, pp. 754-763.
doi: 10.1016/j.asr.2015.11.037

[78]. Meng, Z., Wang, B., and Huang, P. "Mpc-based anti-sway control of tethered space robots," Acta Astronautica, Vol. 152, 2018, pp. 146-162.
doi: 10.1016/j.actaastro.2018.07.050

[79]. Raff, T., Ebenbauer, C., and Allgöwer, P. "Nonlinear model predictive control: A passivity-based approach," Assessment and future directions of nonlinear model predictive control. Springer Berlin Heidelberg, Berlin, Heidelberg, 2007, pp. 151-162.

[80]. Tahirovic, A., and Magnani, G. "General framework for mobile robot navigation using passivity-based mpc," IEEE Transactions on

Automatic Control, Vol. 56, No. 1, 2011, pp. 184-190.
doi: 10.1109/TAC.2010.2089654
[81]. Jasper, L., and Schaub, H. "Input shaped large thrust maneuver with a tethered debris object," Acta Astronautica, Vol. 96, 2014, pp. 128-137.
doi: 10.1016/j.actaastro.2013.11.005
[82]. Jasper, L., and Schaub, H. "Tethered towing using open-loop input-shaping and discrete thrust levels," Acta Astronautica, Vol. 105, No. 1, 2014, pp. 373-384.
doi: 10.1016/j.actaastro.2014.10.001
[83]. Linskens, H. T. K., and Mooij, E. "Tether dynamics analysis and guidance and control design for active space-debris removal," Journal of Guidance, Control, and Dynamics, Vol. 39, No. 6, 2016, pp. 1232-1243.
doi: 10.2514/1.g001651
[84]. Liu, H., He, Y., Yan, H., and Tan, S. "Tether tension control law design during orbital transfer via small-gain theorem," Aerospace Science and Technology, Vol. 63, 2017, pp. 191-202.
doi: 10.1016/j.ast.2017.01.001
[85]. Zhong, R., and Zhu, Z. H. "Attitude stabilization of tug–towed space target by thrust regulation in orbital transfer," IEEE/ASME Transactions on Mechatronics, Vol. 24, No. 1, 2019, pp. 373-383.
doi: 10.1109/TMECH.2019.2892331
[86]. Li, P., Zhong, R., and Lu, S. "Optimal control scheme of space tethered system for space debris deorbit," Acta Astronautica, Vol. 165, 2019, pp. 355-364.
doi: 10.1016/j.actaastro.2019.09.031
[87]. Zhong, R., and Zhu, Z. H. "Timescale separate optimal control of tethered space-tug systems for space-debris removal," Journal of Guidance, Control, and Dynamics, Vol. 39, No. 11, 2016, pp. 2540-2545.
doi: 10.2514/1.g001867
[88]. Sun, X., and Zhong, R. "Libration control for the low-thrust space tug system using electrodynamic force," Journal of Guidance, Control, and Dynamics, Vol. 41, No. 7, 2018, pp. 1602-1609.
doi: 10.2514/1.g003375
[89]. Rybus, T., and Seweryn, K. "Planar air-bearing microgravity simulators: Review of applications, existing solutions and design parameters," Acta Astronautica, Vol. 120, 2016, pp. 239-259.
doi: 10.1016/j.actaastro.2015.12.018
[90]. Chung, S.-J., and Miller, D. W. "Propellant-free control of tethered formation flight, part 1: Linear control and experimentation," Journal of Guidance, Control, and Dynamics, Vol. 31, No. 3, 2008, pp. 571-584.
doi: 10.2514/1.32188
[91]. Chung, S.-J., Slotine, J.-J. E., and Miller, D. W. "Propellant-free control

of tethered formation flight, part 2: Nonlinear underactuated control," Journal of Guidance, Control, and Dynamics, Vol. 31, No. 5, 2008, pp. 1437-1446.
doi: 10.2514/1.32189

[92]. Yu, B. S., Geng, L. L., Wen, H., Chen, T., and Jin, D. P. "Ground-based experiments of tether deployment subject to an analytical control law," Acta Astronautica, Vol. 151, 2018, pp. 253-259.
doi: 10.1016/j.actaastro.2018.06.013

[93]. Pang, Z., and Jin, D. "Experimental verification of chaotic control of an underactuated tethered satellite system," Acta Astronautica, Vol. 120, 2016, pp. 287-294.
doi: 10.1016/j.actaastro.2015.12.016

[94]. Kang, J., and Zhu, Z. H. "Hamiltonian formulation and energy-based control for space tethered system deployment and retrieval," Transactions of the Canadian Society for Mechanical Engineering, Vol. 43, No. 4, 2019, pp. 463-470.
doi: 10.1139/tcsme-2018-0215

[95]. Battin, R. H. An introduction to the mathematics and methods of astrodynamics, revised edition: American Institute of Aeronautics and Astronautics, 1999.

[96]. Aghababa, M. P. "A lyapunov-based control scheme for robust stabilization of fractional chaotic systems," Nonlinear Dynamics, Vol. 78, No. 3, 2014, pp. 2129-2140.
doi: 10.1007/s11071-014-1594-8

[97]. Chen, Y., Petras, I., and Xue, D. "Fractional order control - a tutorial," 2009 American Control Conference. 2009, pp. 1397-1411.

[98]. Zavala-Rio, A., and Santibanez, V. "A natural saturating extension of the pd-with-desired-gravity-compensation control law for robot manipulators with bounded inputs," IEEE Transactions on Robotics, Vol. 23, No. 2, 2007, pp. 386-391.
doi: 10.1109/TRO.2007.892224

[99]. Aslanov, V. S. "Chaos behavior of space debris during tethered tow," Journal of Guidance, Control, and Dynamics, Vol. 39, No. 10, 2016, pp. 2399-2405.
doi: 10.2514/1.g001460

[100]. Yao, H., Wang, Y., Cui, J., Bao, J., Yang, H., Zhu, Z., Zheng, G., and Zhu, Z. H. "Implementation of three dofs small satellite ground simulation system," 54th AIAA Aerospace Sciences Meeting.

[101]. Li, P. "Dynamics and control of spacecraft rendezvous by nonlinear model predictive control." Doctoral Thesis, York University, Canada, 2018.

[102]. COOKSON, J. "Experimental investigation of spacecraft rendezvous

and docking by development of a 3 degree of freedom satellite simulator testbed." Master Thesis, York University, Canada, 2019.

[103]. Santaguida, L. "Study of autonomous capture and detumble of non-cooperative target by a free-flying space manipulator using an air-bearing platform." Master Thesis,York University, Canada, 2020.